SUBTIDAL CIRCULATION, HYDROGRAPHY, SEA ICE AND ASSOCIATED VARIABILITY OVER THE EASTERN CANADIAN SHELF USING A COUPLED OCEAN-ICE MODEL

by

Jorge R. Urrego-Blanco

Submitted in partial fulfilment of the requirements
for the degree of Doctor of Philosophy

at

Dalhousie University
Halifax, Nova Scotia
September 2014

To my parents

TABLE OF CONTENTS

LIST OF TABLES

LIST OF FIGURES

ABSTRACT

The subtidal circulation, hydrography, sea ice and associated variability over the eastern Canadian shelf (ECS) are examined using 17-years of model results produced by a coupled ocean-ice model. The coupled model has a fine-resolution child model (~1/12°) embedded inside a coarse-resolution parent model (~1/4°) of the northwest Atlantic. A combination of the semi-prognostic method and the spectral nudging method is used to reduce the model seasonal bias and drift. The model reproduces general features of the observed subtidal circulation and hydrography over the ECS. Analysis of model results demonstrates that the temporal variability in atmospheric forcing significantly affects the strength of the time-mean cyclonic circulation over the Gulf of Maine (GOM) and the outflow from the Gulf of St. Lawrence (GSL) through western Cabot Strait. The seasonal variability of salinity in the top 30 m of the Gulf of St. Lawrence, the Scotian Shelf and the Gulf of Maine (GSL-SS-GOM) is mainly affected by equatorward advection of low salinity waters from the lower St. Lawrence Estuary onto the GOM through the SS. Model results also reveal that there are significant regional differences in the interannual variability of circulation and hydrography over the ECS. Interannual variability on the Labrador Shelf is mainly affected by the advection of variability from high latitudes by the Labrador Current. Over the Newfoundland Shelf and the Grand Banks, the interannual variability is significantly affected by the non-linear interaction between the Labrador Current and the Gulf Stream. Over the Scotian Shelf and the Gulf of St. Lawrence, the interannual variability is significantly affected by advection of anomalies produced over the Tail of the Grand Banks. Net production of sea ice in the GSL during winter mainly occurs over shallow areas in the northern and southwestern Gulf. By contrast, net melting of sea ice during winter occurs over the central GSL, the eastern side of Esquiman Channel, and waters near Cabot Strait. Advection plays an important role in redistributing sea ice over different regions in the GSL. The sea ice also plays an important role in modulating the strength of winter currents in the GSL.

LIST OF ABBREVIATIONS AND SYMBOLS USED

Abbreviation	Definition
AAD	Average Absolute Difference
AC	Avalon Channel
ACENET	Atlantic Computational Excellence Network
AG	Anticosti Gyre
AGRIF	Adaptive Grid Refinement in FORTRAN
AZMP	Atlantic Zone Monitoring Program
BB	Browns Bank
BIB	Belle Isle Bank
BIC	Baffin Island Current
CEOF	Complex Empirical Orthogonal Function
CH	Cape Hatteras
CIL	Cold Intermediate Layer
CLSW	Classical Labrador Sea Water
CM	Child Model
CS	Cabot Strait
CTD	Conductivity-Temperature-Depth
DFO	Department of Fisheries and Oceans
DSO	Denmark Strait Overflow
ECS	Eastern Canadian Shelf
ENFS	Eastern Newfoundland Shelf
EOF	Empirical Orthogonal Function
ESS	Eastern Scotian Shelf
ETOPO	Earth Topography and Bathymetry
FIZ	Feedback Interface Zone
FC	Flemish Cap
FP	Flemish Pass
GB	Grand Banks
GC	Gaspé Current

Abbreviation	Definition
GOM	Gulf of Maine
GRACE	Gravity Recovery and Climate Experiment
GS	Gulf Stream
GsB	Georges Bank
GSC	Great South Channel
GSL	Gulf of St. Lawrence
GSP	Gulf Stream Position
HB	Hamilton Bank
HS	Hudson Strait
ILC	Inflow of the Labrador Current
ISBI	Inflow through the Strait of Belle Isle
LC	Labrador Current
LIM	Louvain-La-Neuve Ice Model
LRF	Lloyds Register Foundation
LS	Labrador Shelf
ME	Mann Eddy
MSST	Mean Sea Surface Topography
NAC	North Atlantic Current
NAO	North Atlantic Oscillation
NEMO	Nucleus for European Modelling of the Ocean
NES	New England Shelf
NFS	Newfoundland Shelf
NNFS	Northern Newfoundland Shelf
NSC	Nova Scotia Current
NSh	Nantucket Shoals
OB	Open Boundary
OHS	Outflow from Hudson Strait
OPA	Océan PArallélisé
OWN	One-way nesting
PM	Parent Model

Abbreviation	Definition
SBI	Strait of Belle Isle
SLR	St. Lawrence River
SS	Scotian Shelf
SSF	Shelf Slope Front
SST	Sea Surface Temperature
SToGB	Southern Tip of the Grand Banks
SW	Slope Water
SWJ	Slope Water Jet
TWN	Two-way nesting
ULSW	Upper Labrador Sea Water
WGC	West Greenland Current
WNFS	Western Newfoundland Shelf
WSS	Western Scotian Shelf

Symbol	Description	Units
$\vec{\tau}$	Stress at the ocean surface	Pa
$\vec{\tau}_{io}$	Stress at the ice-ocean interface	Pa
$\vec{\tau}_{ao}$	Stress at the air-ocean interface	Pa
f_i	Fraction of ocean surface covered by ice	
Q	Net heat flux	W m^{-2}
Q_{io}	Ice-ocean heat flux	W m^{-2}
Q_{sw}	Shortwave radiation	W m^{-2}
Q_{lw}	Longwave radiation	W m^{-2}
Q_s	Sensible heat flux	W m^{-2}
Q_l	Latent heat flux	W m^{-2}
F	Net freshwater flux	kg m^{-2} s^{-1}
E	Evaporation	kg m^{-2} s^{-1}
P	Precipitation	kg m^{-2} s^{-1}
F_r	Sea surface salinity restoring term	kg m^{-2} s^{-1}

Abbreviation	Definition	
F_{io}	Freshwater flux between ice and ocean	kg m^{-2} s^{-1}
p	Pressure	Pa
z	Vertical coordinate	m
g	Acceleration of gravity	m s^{-2}
ρ_m	Parent model density	kg m^{-3}
ρ_c	Child model density	kg m^{-3}
Ψ	Complex time series in CEOF	
x,y,z	Spatial coordinates	m
t	Time	s
H	Hilbert transform in CEOF	
T	Real time series in CEOF	
A_n	Mode coefficients of Ψ	
E_n	Eigenfunctions of Ψ	
R_n	Temporal amplitude function	
ϕ_n	Temporal phase function	
S_n	Spatial amplitude function	
θ_n	Spatial phase function	
ε^2	Score	
U,V	Eastward, northward velocities	m s^{-1}
O,M	Observed and modeled variables	
ϕ	Unfiltered time series	
$\overline{\phi}$	Time-mean component of a time series	
$\hat{\phi}$	Interannual component of ϕ (periods greater than 12 months)	
$\widetilde{\phi}$	Seasonal component of ϕ	
ϕ'	High-frequency component of ϕ (periods less than 12 months)	
m	Ice mass per unit area	kg m^{-2}

Abbreviation	Definition	
$\vec{u}$	Horizontal velocity	m s^{-1}
A	Ice concentration	
f	Coriolis parameter	radians s^{-1}
$\vec{k}$	Upward unit vector	
η	Sea surface elevation	m
$\vec{\sigma}$	Internal stress tensor	N m^{-1}
Q_{swio}	Shortwave radiation at the bottom of ice	W m^{-2}
i_o	Fraction of shortwave penetrating snow-ice	
α	Snow-ice albedo	
h_i	Mean sea ice thickness	m
Q_{sio}	Sensible heat flux from ice to ocean	W m^{-2}
ρ_0	Reference density of seawater	kg m^{-3}
C_w	Specific heat of seawater	J K^{-1}
C_{io}	Exchange coefficient of heat	
C_{ao}	Air-ocean drag coefficient	
u_{io}^{*}	Friction velocity between ice-ocean	m s^{-1}
T_0	Temperature of the oceans surface layer	°C
T_f	Freezing point of seawater	°C
R	Freshwater flux from river runoff	kg m^{-2} s^{-1}
S_m	Reference seawater salinity	
S_i	Sea ice salinity	
m_s	Mass of snow per unit area	kg m^{-2}
m_i	Mass of ice per unit area	kg m^{-2}
C_{Dio}	Drag coefficient between ice and ocean	
$\vec{u}_i$	Horizontal ice velocity	m s^{-1}
$\vec{u}_o$	Horizontal ocean surface velocity	m s^{-1}
$\vec{W}$	Wind velocity vector	m s^{-1}
σ_w	Standard deviation of the wind speed	m s^{-1}

Abbreviation	Definition	
ε	Reanalysis error	
K	Weighting function	
$\hat{f}$	Probability density function estimate	
ΔV^{CR}	Time change of ice volume in Exp-Control per unit area	m
ΔV^{NoDYN}	Time change of ice volume in Exp-noDYN per unit area	m
V_p^{CR}	Production of sea ice in Exp-Control	m
V_a^{CR}	Advection of sea ice in Exp-Control	m
V_p^{NoDYN}	Production of sea ice in Exp-NoDYN	m
$V_p^{CR\|DYN}$	Production of sea ice associated with dynamics	m
I	Index relating thermodynamics and dynamics of sea ice	
β	Strength of feedback from CM to PM	

ACKNOWLEDGEMENTS

I would like to thank my supervisor Jinyu Sheng, for his guidance and support during all these years. Thanks go to my supervisory committee, Keith Thompson, Hal Ritchie and Tetjana Ross for their useful comments and support. Thanks go to my external examiner, Kevin Horsburg, for carefully reading my thesis and making useful and constructive comments. I also want to thank to the members of the Ocean Modelling Group, Shiliang Shang, Kyoko Ohashi, Heng Zhang, Daisuke Hasegawa and Andy Lin. Thanks to Daniel Morrison and Jackie Hurst. Thanks go to Frederic Dupont for help with the NEMO model. Thanks go to Greg Smith, Simon Higginson and Lee Titus for providing data used in this work.

I want to thank specially my brother Juan Pablo, without his help and guidance it would have been impossible to complete this endeavor. Thanks go to my little sister Diana, for your moral support, friendship and laughs. Thanks go to my parents, for giving us love, advice, freedom, and hope, for always being there. Thanks go to Pilar and Teresa for your help and encouragement. Thanks go to Ramon and Catalina for your friendship.

This PhD work was supported by the Global Ocean-Atmosphere Prediction and Predictability project (GOAAP), Lloyd's Register Foundation (LRF), the Ocean Tracking Network (OTN), Marine Environmental Observation Prediction and Response Network (MEOPAR) and the Natural Sciences and Engineering Research Council of Canada (NSERC). This research used ACEnet computational resources.

CHAPTER 1

INTRODUCTION

The eastern Canadian shelf (ECS) considered in this thesis consists of coastal and shelf waters of the Labrador Shelf (LS), the Newfoundland Shelf (NFS), the Gulf of St. Lawrence (GSL), the Scotian Shelf (SS), and the Gulf of Maine (GOM) (Fig. 1.1). This region is characterized by complex bathymetry, highly variable atmospheric conditions, high riverine input, oceanic forcing from high latitudes and from the Atlantic Ocean, and presence of sea ice over the LS, NFS, and the GSL. The hydrographic variability in this region has been demonstrated to be among the largest in the North Atlantic and Pacific Oceans (Thompson et al., 1988). The water temperatures over the Scotian Shelf, for example, have a large seasonal cycle with a mean range of about 16^{o}C. There is evidence that variability in the freshwater discharge from the Gulf of St. Lawrence affects fisheries on the Scotian Shelf and the Gulf of Maine, indicating the importance of the links among different regions in the ECS (Gagné and Sinclair, 2013). Previous studies have also suggested that tilefish mortality events over the Middle Atlantic Bight were caused by enhanced equatorward transport of cold water in the Labrador Current (Marsh et al., 1999), indicating the importance of interactions between the shelf and oceanic waters in the region. It is, therefore, important to understand what are the key factors affecting the circulation and associated variability over this region, including the dynamical connections among different subregions and interactions between oceanic and shelf waters.

Significant efforts have been made in the past in determining the general circulation, hydrographic distributions and associated variability over the ECS. In particular, there have been characterizations of the seasonal variability (Smith and Schwing, 1991; Sheng and Thompson, 1996; Lynch et al., 1996; Colbourne et al., 1997; Loder et al., 1998; Xue et al., 2000; Sheng et al., 2001) and the interannual variability over the ECS (Thompson et al., 1988; Petrie et al., 1992; Petrie and Drinkwater, 1993; Han and Tang, 2001; Han, 2007). Studies have also been made of sea ice distributions over the Gulf of St. Lawrence

(Saucier et al., 2003 and Drinkwater et al., 1999). Nevertheless, we do not fully understand the temporal and spatial variability of circulation and sea ice over the region.

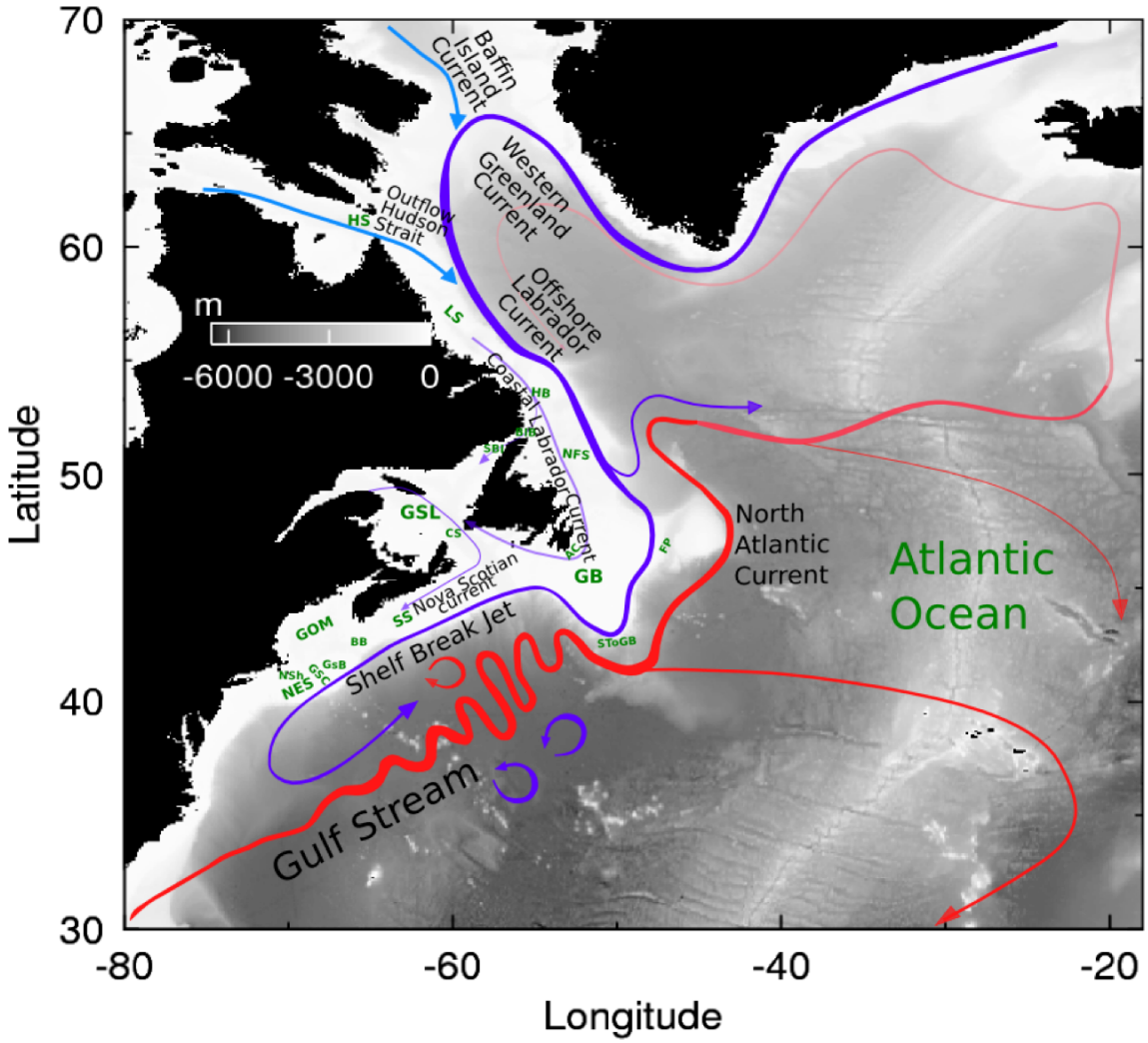

Figure 1.1. Main topographic features and schematic of surface circulation over the eastern Canadian shelf including the Labrador, Newfoundland and Scotian Shelves, the Gulf of St. Lawrence and the Gulf of Maine. Blue colors indicate relatively cold and fresh waters and red colors indicate relatively warm and salty waters. Abbreviations are given for Hudson Strait (HS), Strait of Belle Isle (SBI), Belle Isle Bank (BIB), Cabot Strait (CS), Grand Banks (GB), Georges Banks (GsB), Nantucket Shoals (NSh), Browns Bank (BB), Hamilton Bank (HB), Avalon Channel (AC), Flemish Pass (FP), Southern Tip of the Grand Banks (SToGB), Great South Channel (GSC), Scotian Shelf (SS), Gulf of St. Lawrence (GSL), Gulf of Maine (GOM), Labrador Shelf (LS), Newfoundland Shelf (NFS), and New England Shelf (NES).

1.1 Main Circulation Features over the Eastern Canadian Shelf (ECS)

The topography of the ECS (Fig. 1.1) is highly irregular with the coastline interrupted by several large gulfs, embayments, submarine banks and basins (Smith and Schwing, 1991; Loder et al., 1998). Numerous channels crossing the continental slope over the ECS allow for cross shelf advection of waters onto and off the shelf. The Labrador Shelf is relatively straight and rugged and extends from Hudson Strait to the south of Hamilton Bank. The Newfoundland Shelf is situated off the coast of Newfoundland from Belle Isle Bank to Cabot Strait and Laurentian Channel, including the Grand Banks and Flemish Cap. The Gulf of St. Lawrence is a semi-enclosed sea connected to the North Atlantic Ocean through Cabot Strait and to the Labrador and Newfoundland Shelves through the Strait of Belle Isle. To the west of Laurentian Channel lies the Scotian Shelf, which is connected to the Gulf of St. Lawrence to the northeast and to the Gulf of Maine to the southwest. The Gulf of Maine is also a semi-enclosed sea bounded by Georges Bank, Nantucket Shoals and Browns Bank at its seaward end and connects with the adjacent waters primarily through three main channels (Lynch et al., 1996). The general mean circulation over the ECS has been subject to many field and modelling studies in the past. A comprehensive review of the mean circulation over the region can be found in Smith and Schwing (1991) and Loder et al. (1998). Only a brief description of the major time-mean circulation features over the region is presented here.

The ECS lies in the western boundary confluence zone of the North Atlantic subpolar gyre and the North Atlantic subtropical gyre (Loder et al., 1998). The coastal and shelf circulation on the ECS is predominantly influenced by the Northern Atlantic subpolar gyre and its equatorward flowing western boundary current: the Labrador Current (Fig. 1.1). The ECS and adjacent waters are also affected by the Gulf Stream and its northern extension: the North Atlantic Current, both of which are western boundary currents of the North Atlantic subtropical gyre and lie offshore of the ECS (Fig. 1.1).

The combination of the Western Greenland Current, the Baffin Island Current and the outflow from Hudson Strait forms the “traditional” Labrador Current (Loder et al., 1998)

over the northern Labrador Shelf (Fig. 1.1). At the Hamilton Bank section of the southern Labrador Shelf the Labrador Current has three branches: an inshore branch near the coast; an offshore branch over the shelf break; and a deep branch beyond the shelf break (Lazier and Wright, 1993). The deep branch is part of the North Atlantic subpolar gyre and carries an annual mean transport of about 30 Sv (Thompson et al., 1986; Lazier and Wright, 1993; Loder et al., 1998), where 1 Sv = 1×10^6 m^3 s^{-1}. The inshore and offshore branches of the Labrador Current on the Labrador Shelf have annual mean transports of about 0.8 and 6.7 Sv, respectively (Loder et al., 1998).

A small fraction of the inner branch of the Labrador Current enters the Gulf of St. Lawrence through the Strait of Belle Isle (Loder et al., 1998). The rest of the inner branch and the other two branches of the Labrador Current flow onto the Newfoundland Shelf (Fig. 1.1). Over the northern Newfoundland Shelf, the Labrador Current has three branches: a coastal branch (about 0.39 Sv) flowing through Avalon Channel to coastal waters of Southern Newfoundland; a middle branch (about 5.8 Sv) following the shelf break through Flemish Pass; and an eastern branch (about 1.3 Sv) passing around the seaward flank of Flemish Cap (Petrie and Anderson, 1983; Sheng and Thompson, 1996; Colbourne et al., 1997; Loder et al., 1998). Some of the eastern branch of the Labrador Current moves into the deep ocean to join the North Atlantic Current, and the rest joins the middle branch to the south of the Flemish Pass (Loder et al., 1998). Upon reaching the Tail of the Grand Banks, some of the Labrador Current turns offshore into the Newfoundland Basin, and the rest (about 3.2 Sv) of the Current flows around the Tail and continues to flow equatorward along the shelf break of the southwestern Grand Banks (Loder et al., 1998).

Most of the Labrador Current that flows around the Tail of the Grand Banks reaches the eastern Scotian Shelf by crossing the Laurentian Channel, with a small amount of the Current entering the Gulf of St. Lawrence through the eastern side of Cabot Strait (Loder et al., 1998). The low-salinity water over the western Gulf of St. Lawrence emanates from the Gulf through the western side of Cabot Strait and moves onto the eastern Scotian Shelf where it mixes with the more saline slope water flowing onto the Shelf

(Hachey et al., 1954). This low-salinity water associated with the freshwater discharge from the St. Lawrence River is mostly confined to an inshore area of the Scotian Shelf, and moves southwestward as the Nova Scotian Current. Over the western Scotian Shelf, the low-salinity Nova Scotian Current (about 0.35 Sv, Drinkwater et al., 1979) enters the Gulf of Maine at Cape Sable.

In the deeper waters south of the Scotian Shelf break, Slope Water is found, which has two distinct zones in the vertical: the near-surface Warm Slope Water and the sub-surface Labrador Slope Water. The former is a mixture of coastal water and Gulf Stream water that flows primarily eastward, while the latter is a mixture of Labrador Current and North Atlantic Central waters that flows mostly southwestward (McLellan, 1957; Gatien, 1976). The offshore branch of the Labrador Current reduces its transport while flowing along the shelf break off Nova Scotia and later as its waters enter the Gulf of Maine through the Northeast Channel (Hannah et al., 2001; Han, 2007).

The near-surface Nova Scotian Current water in the Gulf of Maine, together with the sub-surface Slope Water that enters the Gulf of Maine through the Northeast Channel, forms the cyclonic Gulf of Maine gyre (Bigelow, 1927; Brown and Beardsley, 1978). Some of these waters leave the Gulf of Maine via the Great South Channel and flow onto the New England Shelf, whereas others flow northeasterly to Georges Bank (Bigelow, 1927; Smith et al., 1978; Brown and Irish, 1992; Xue et al., 2000). Previous studies have also demonstrated that the circulation over the Gulf of Maine, and particularly the anticyclonic circulation over Georges Bank, are significantly affected by tidal rectification (Loder, 1980).

There are still many unanswered questions about the circulation and associated variability over the ECS. For example, what drives the variability of the Labrador Current beyond the Tail of the Grand Banks? How is the circulation over the ECS affected by the Gulf Stream and the North Atlantic Current? How are the circulation and hydrographic variability dynamically linked among the different regions of the ECS? What are the main physical processes affecting the variability of circulation and hydrography over the

ECS? What are the effects of sea ice cover on the circulation over the ECS? What is the relative importance of sea ice dynamics and thermodynamics on the sea ice distributions over the ECS? These questions are important to understand the predictability of the ocean system in the ECS, which can have practical implications for studies of ecosystem dynamics or for other activities in the region such as transportation or exploitation of mineral resources. In this thesis, these scientific issues are addressed based on model results produced by a regional-scale, coupled ocean-ice model.

1.2 Objectives and Thesis Outline

The main goal is to improve our understanding of physical processes affecting subtidal (non-tidal frequencies) circulation and associated variability over the ECS. This is achieved by developing a nested-grid modelling system for the ECS, which couples a large-scale circulation model for the northwest Atlantic Ocean and a regional-scale shelf circulation model for the Gulf of St. Lawrence and the Scotian Shelf. The modelling system is based on the state-of-the-art ocean-ice system known as the Nucleus for the European Modelling of the Ocean (NEMO) (Madec, 2008). The modelling work also involves the assessment of different nesting techniques used in ocean models.

This thesis focuses on the subtidal circulation and associated variability over the ECS. The sea ice dynamics in the Gulf of St. Lawrence are also investigated. The main objectives of the thesis are the following:

(1) Investigate the main physical factors affecting interannual variability of circulation and hydrography over the ECS.
(2) Examine regional interconnections, and the variability, of circulation and hydrography in different frequency bands over the Gulf of St. Lawrence, the Scotian shelf, and the Gulf of Maine.
(3) Determine the importance of dynamic and thermodynamic processes in determining the sea ice distributions in the Gulf of St. Lawrence and adjacent waters.

(4) Assess the performance of different nesting techniques applied to a nested-grid circulation model of the ECS. The assessment focuses on the improvement of the large-scale and regional-scale circulation, reduction of numerical noise, and consistency between coarse-resolution and hugh-resolution model components.

The structure of this thesis is as follows. Chapter 2 presents an examination of the main factors affecting interannual variability over the eastern Canadian shelf. Chapter 3 examines the subtidal variability of the circulation and hydrography over the Gulf of St. Lawrence, Scotian Shelf and the Gulf of Maine in different frequency bands. Chapter 4 is a study of the importance of dynamics and thermodynamics on the sea ice distributions in the Gulf of St. Lawrence. Chapter 5 presents an assessment of conventional nesting techniques and an alternative nesting technique based on the semi-prognostic model. The main results of the thesis are summarized in Chapter 6.

Chapters 2-5 are based on four separate papers. Therefore, some similar background material can be found in these Chapters. In particular, text and figures describing general circulation features and geographical regions, as well as model setup and validation are similar in these chapters. Chapter 2 has been published in Atmosphere-Ocean under the title "Interannual variability of the circulation over the eastern Canadian shelf" (Urrego-Blanco and Sheng, 2012). Chapter 3 has been published in Ocean Dynamics under the title "Study on subtidal circulation and variability in the Gulf of St. Lawrence, Scotian Shelf, and Gulf of Maine using a nested-grid shelf circulation model" (Urrego-Blanco and Sheng, 2014). Chapter 4 has been submitted the Journal of Geophysical Research under the title of "Formation and distribution of sea ice in the Gulf of St. Lawrence: A process-oriented study using a coupled ocean-ice model". Chapter 5 has been submitted to Ocean Modelling under the title of "Assessing the performance of one-way and two-way nesting techniques using the shelf circulation modelling system for the eastern Canadian shelf". Copyright permission letters for Chapters 2 and 3 are provided in Appendix C.

CHAPTER 2

INTERANNUAL VARIABILITY OF THE CIRCULATION OVER THE EASTERN CANADIAN SHELF[1]

2.1 INTRODUCTION

The eastern Canadian shelf (ECS) comprises the coastal and continental shelf waters from the Labrador Sea in the north to the Gulf of Maine in the south (Fig. 2.1). Dynamically this region lies in the western boundary confluence zone of two large-scale gyre systems: the North Atlantic subpolar gyre and the North Atlantic subtropical gyre (Loder et al., 1998). The coastal and shelf circulation on the ECS is predominantly influenced by the North Atlantic subpolar gyre and its western boundary current that flows equatorward: the Labrador Current. The ECS and adjacent waters are also affected by the Gulf Stream and its northern extension, the North Atlantic Current, both of which are western boundary currents of the North Atlantic subtropical gyre and lie offshore of the ECS (Fig. 2.1a). Previous studies have demonstrated that the ECS is the most variable area of the North Atlantic and Pacific oceans (Thompson et al., 1988), with the largest seasonal variations in water temperature, about 16°C, occurring over the Scotian Shelf and the Middle Atlantic Bight. Significant efforts have been made in the past to determine the general circulation, hydrographic distributions and associated seasonal variability of the ECS (Smith and Schwing, 1991; Lynch et al., 1996; Sheng and Thompson, 1996; Colbourne et al., 1997; Loder et al., 1998; Xue et al., 2000; Sheng et al., 2001; Han and Loder, 2003; Han et al., 2008). Efforts have also been made to examine the interannual variability over this region (Thompson et al., 1988; Petrie et al.,

[1] Urrego-Blanco, J. and J., Sheng. 2012. Interannual variability of the circulation over the Eastern Canadian Shelf. *Atmosphere Ocean*. 50: 175–201.

1992; Petrie and Drinkwater, 1993; Han and Tang, 2001; Han, 2007). Many questions, however, remain unanswered regarding the general circulation and associated temporal and spatial variability over the region. The main objective of this chapter is to examine the main physical processes affecting the interannual variability of circulation and hydrography over the ECS.

This chapter is structured as follows. Section 2.2 reviews the general mean circulation and observational evidence of interannual variability over the ECS. Section 2.3 summarizes the coupled ocean–ice model and external forcing. The assessment of the model performance is presented in Section 2.4, and the main mechanisms affecting the interannual variability over the ECS are discussed in Section 2.5. A summary and conclusions are given in Section 2.6.

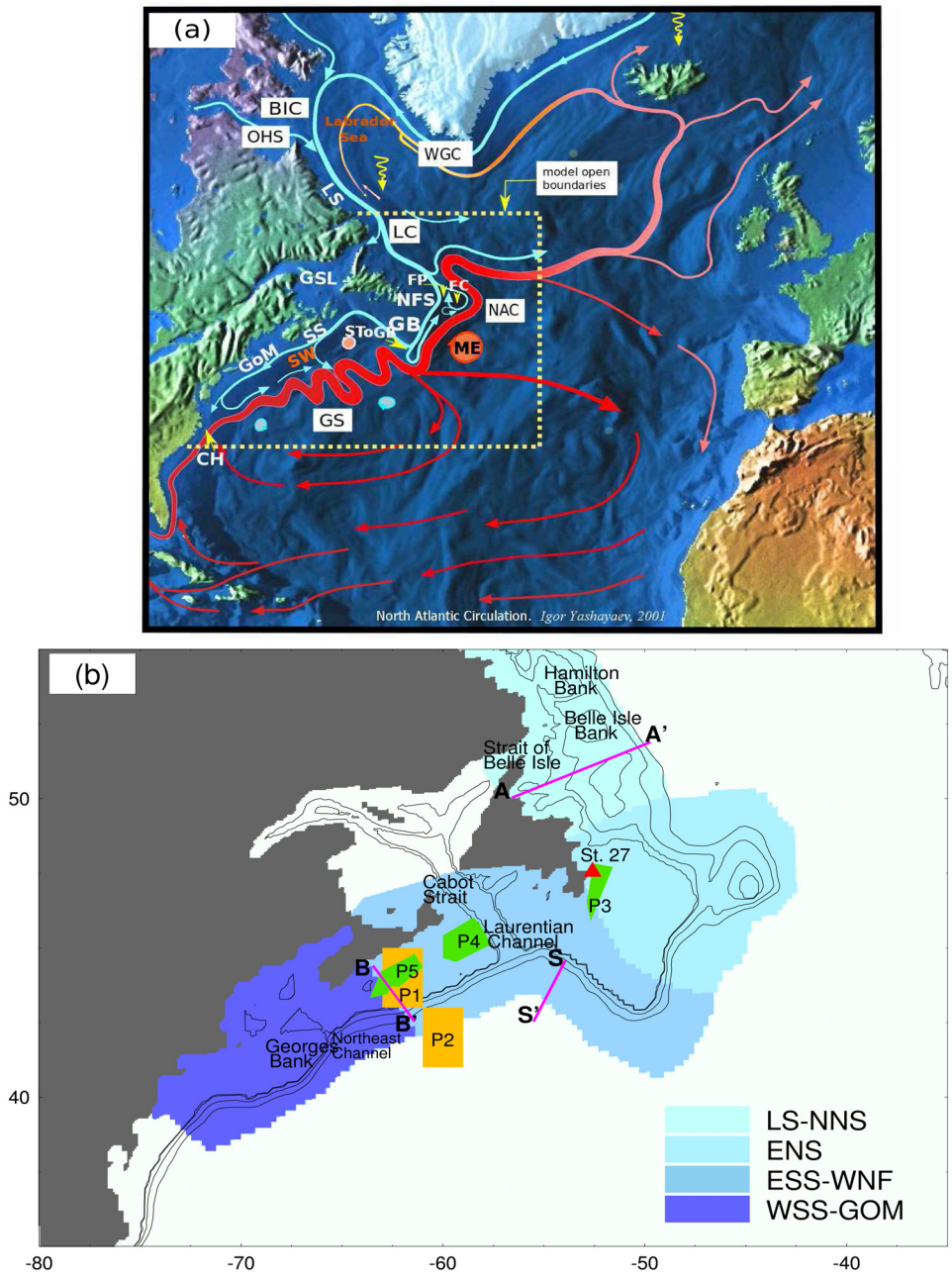

Figure 2.1. (a) Schematic of general upper-ocean circulation over the northwest Atlantic Ocean and the model domain marked by dashed lines (modified from the image created by Igor Yashayaev, reproduced by permission). (b) Topographic features over the eastern Canadian continental shelf. Model results over subregions with different colors are discussed in the thesis. Model results over areas marked by P1 and P5 and indicated sections are used for the model validation and the process study of interannual variability. Abbreviations are used for the Gulf Stream (GS), North Atlantic Current (NAC), Labrador Current (LC), Mann Eddy (ME), West Greenland Current (WGC), Baffin Island Current (BIC), Outflow from Hudson Strait (OHS), Labrador Shelf (LS), Newfoundland Shelf (NFS), Scotian Shelf (SS), Gulf of Maine (GOM), Gulf of St. Lawrence (GSL), Slope Water (SW), Grand Banks (GB), Flemish Cap (FC), Flemish Pass (FP), Southern Tip of the Grand Banks (SToGB), Cape Hatteras (CH).

2.2 INTERANNUAL VARIABILITY IN CIRCULATION AND HYDROGRAPHY

Circulation and hydrography over the ECS exhibit large interannual variability (Weare, 1977; Petrie et al., 1992; Petrie and Drinkwater, 1993; Colbourne et al., 1997), which could have a significant impact on ecosystem dynamics in the region. There was a massive mortality of "warm-water" tilefish, for example, occurring between April and August of 1882 over the Middle Atlantic Bight. Marsh et al. (1999) attributed this massive tilefish kill to a sudden cooling in the region as a consequence of an enhanced equatorward transport of cold water in the Labrador Current. Based on in situ hydrographic observations, Petrie and Drinkwater (1993) showed that a cooling trend occurred on the Scotian Shelf and in the Gulf of Maine from 1952 to 1967, followed by a rapid warming trend from 1968 to 1978 and then by a slow decline from the late 1970s to 1990 (Figs 2.2a and b). They also revealed that the observed cooling (warming) trends on the Scotian Shelf and in the Gulf of Maine were correlated with freshening (increasing) salinity trends (not shown). The interannual variability of hydrography on the Scotian Shelf and in the Gulf of Maine was found to occur over the entire water column but with the largest amplitudes occurring in the subsurface waters. Petrie and Drinkwater (1993) suggested that the variability of the westward transport of the Labrador Current was responsible for the interannual variability of the water properties from the Gulf of St. Lawrence to the Gulf of Maine.

It was found that water masses over the Newfoundland Shelf have cooling and warming trends significantly different from the observed trends over the Scotian Shelf and the Gulf of Maine. Based on hydrographic observations at Station 27 (Fig. 2.1b) in the Avalon Channel over the inner Newfoundland Shelf, Petrie et al. (1992) discovered that a warming period in the late 1960s was followed by a cooling period in the early 1970s and then a warming trend into the early 1980s for water masses at Station 27. Figures 2.2c and 2.2d show the monthly anomalies and five-year running mean anomalies of temperature after removing the annual cycle at Flemish Cap and Station 27, respectively, indicating that a warming period occurred from the mid-1950s to the mid-

1960s and significant cooling took place in 1966–71, 1982– 84 and 1987–92. The period with the most significant cooling events over the Newfoundland Shelf was 1966–71 which corresponds to the period of the "Great Salinity Anomaly" in the subpolar gyre (Dickson et al., 1988). Petrie et al. (1992) and Colbourne and Foote (2000) suggested that the advection of Labrador Current water onto the Newfoundland Shelf was the main cause of the interannual variability observed over the region. Petrie et al. (1992) also suggested that the large regional differences in the surface ice extent and advection over the Labrador and Newfoundland Shelves could explain why the interannual variability in sea surface temperature (SST) over these two Shelves is virtually uncorrelated.

Satellite-derived SST observations over the central Scotian Shelf and Slope areas (P1 and P2 marked in Fig. 2.1b) revealed that the SSTs had significant interannual variability with a cooling trend in 1999–2004 (Shadwick et al., 2010). The cooling during this period is of the order of 2°C over the central Scotian Shelf and slightly less in the Slope Water region. There was a sharp temperature decline of about 4°C in the winter of 2003 over the Slope Water region. A similar, but smaller, decline also occurred over the central Scotian Shelf.

The occurrence of the interannual temperature variability is by no means restricted to the sea surface of the ECS. Head and Sameoto (2007) demonstrated that the interannual variability also occurred in the depth-averaged temperature and salinity observations over the Newfoundland Shelf and the eastern and western Scotian Shelf. They showed that the depth-averaged temperatures over the western Scotian Shelf had marked cooling trends in 1995–98 and 2000–03 with a sharp warming tendency between these two periods. There was a significant warming period in 1997–2000 over the eastern Scotian Shelf that preceded a cooling trend in 2000– 03. The cooling trend of the depth-averaged temperature from 2000–03 over the Scotian Shelf is correlated with the sea surface cooling reported by Shadwick et al. (2010). Based on a correlation analysis of the annual anomalies of the depth-mean temperature observations with the North Atlantic Oscillation (NAO) index, Head and Sameoto (2007) revealed that a positive (negative) NAO index tends to lead to reduced (increased) temperatures on the Newfoundland Shelf

and to increased (reduced) temperatures on the central and western areas of the Scotian Shelf. In this study, the issue of determining the main physical processes affecting the interannual variability of circulation and hydrography over the ECS is addressed using model results produced by a regional-scale coupled ocean–ice model.

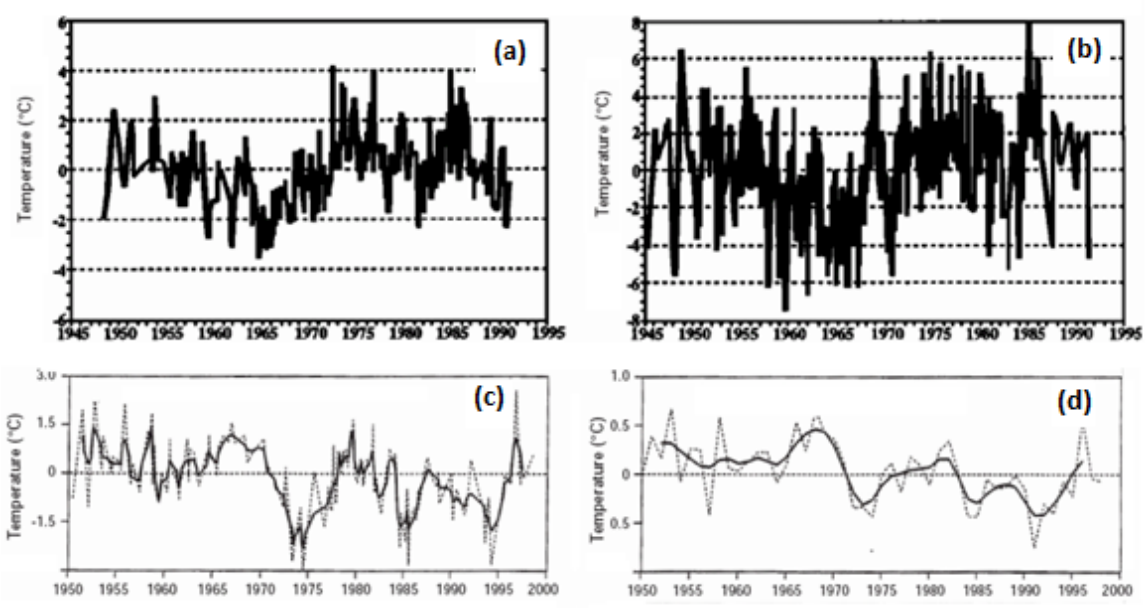

Figure 2.2. Time series of monthly temperature anomalies (annual cycle removed) from 1945 to 1992 at (a) Georges Basin at 100 m, (b) the Slope Water region at 100 m. Depth-mean monthly (dashed) and five-year running average (solid) anomalies of temperature at (c) Flemish Cap and (d) Station 27 (modified from Petrie and Drinkwater (1993) by permission of the American Geophysical Union and Colbourne and Foote (2000) by permission of the Northwest Atlantic Fisheries Organization).

2.3 Coupled Ocean–Ice Model

2.3.1 Model Setup and Forcing

The numerical model used in this study is based on version 2.3 of the Nucleus for European Modelling of the Ocean (NEMO) modelling system (Madec, 2008), which uses version 9 of the Océan PArallélisé System (NEMO-OPA9) as the ocean circulation component and version 2 of the Louvain-la-Neuve Ice Model (NEMO-LIM2) as the sea-

ice component. NEMO-OPA9 is a primitive-equation, finite difference ocean circulation model with a free sea surface and z-coordinate in the vertical (Madec, 2008). NEMO-LIM2 is a two-category (ice and open water) dynamic-thermodynamic sea-ice model (Timmermann et al., 2005).

The model domain covers the northwest Atlantic Ocean between 33°N and 55°N and between 80°W and 33°W (Fig. 2.1). The coupled ocean–ice model uses a horizontal curvilinear grid with a horizontal resolution of approximately 1/4° in longitude and approximately 1/4°cosϕ in latitude (ϕ). There are 46 z-levels in the vertical, with the vertical grid spacing increasing from 6 m in the uppermost z-level to 250 m at the lowermost z-level (Appendix A). The model bathymetry is taken from Earth Topography 2-arc-min (ETOPO2; Smith and Sandwell, 1997). The subgrid scale horizontal mixing for momentum and tracers is parameterized using a biharmonic friction with a Smagorinsky-like mixing coefficient which varies horizontally as a function of the grid size and is also flow dependent (Griffies and Hallberg, 2000). The vertical subgrid-scale mixing is parameterized using the turbulent closure scheme of Gaspar et al. (1990). The model time step is 2400 s. The coupled ocean–ice model is initialized from the climatological monthly mean hydrography of Geshelin et al. (1999). The model is spun up from a state of rest and integrated for 18 years from the beginning of 1987 to 2004. Only the model results for the last 17 years are used in this study.

The atmospheric forcing used to drive the coupled ocean– ice model is taken from the reanalysis fields, with a horizontal resolution of 2° in both longitude and latitude, produced by Large and Yeager (2004). The atmospheric reanalysis data used to calculate the air-sea fluxes include 6-hourly fields of zonal and meridional wind speeds, specific humidity and air temperature at 10 m above the sea surface; 12-hourly fields of short and longwave radiation; and monthly mean precipitation. All the atmospheric forcing fields are interpolated onto the model grid in time and space to obtain the momentum, heat and freshwater fluxes at the air–sea interface. The wind stress vector ($\vec{\tau}$) at the model sea surface is given by:

$$\vec{\tau} = f_i \vec{\tau}_{io} + (1 - f_i)\vec{\tau}_{ao} \tag{2.1}$$

where f_i is the fraction of the ocean surface covered by the sea ice, which is 1 if the ocean surface is fully covered by sea ice and 0 if there is no ice; $\vec{\tau}_{io}$ is the ice-ocean momentum flux; and $\vec{\tau}_{ao}$ is the air–ocean momentum flux without sea ice calculated from Large-Yeager's reanalyzed wind speeds using the formulation of Large and Pond (1981) with the transfer coefficient suggested by Large and Yeager (2004).

The net heat flux (Q) at the sea surface is computed based on (Gill, 1982):

$$Q = f_i Q_{io} + (1 - f_i)[Q_{sw} + Q_{lw} + Q_s + Q_l] \tag{2.2}$$

where Q_{io} represents the ice-ocean heat flux; Q_{sw} represents the incoming shortwave radiation into the ocean; Q_{lw} is the net longwave flux from the atmosphere to the ocean; Qs is the sensible heat flux due to conduction; and Q_l is the latent heat flux carried by the evaporated water. The net heat fluxes are defined to be positive when heat is being transferred from the atmosphere into the ocean. The formulation of Large and Yeager (2004) is used to calculate the sensible and latent heat fluxes Q_s and Q_l.

The net freshwater flux (F) at the sea surface is computed based on (Large and Yeager, 2004):

$$F = f_i F_{io} + (1 - f_i)[E - P + F_r] \tag{2.3}$$

where F_{io} is the freshwater flux between ice and water; E is the evaporative component of the freshwater flux; P is the precipitation over the ocean; and F_r is a term that restores the model sea surface salinity (S_m) to the climatological monthly mean sea surface salinity (S_c) defined as $F_r = \gamma_s^{-1}(1 - S_c/S_m)$, where γ_s is a restoring time scale to reduce model drift and is set to two months. In addition, freshwater runoff from major rivers in the region is specified to a monthly climatology compiled by Barnier et al. (2006).

The lateral boundary conditions specified in the model are as follows. At the model closed boundaries, a free slip condition is applied, with zero normal fluxes of momentum, temperature and salinity. At three lateral (northern, eastern and southern) open boundaries, the normal flow, temperature and salinity fields are adjusted based on the adaptive open boundary condition (e.g., Stevens, 1990; Marchesiello et al., 2001; Sheng and Tang, 2003). An explicit Orlanski radiation condition is first used to determine whether the open boundary is passive (outward propagation) or active (inward propagation). If the open boundary is passive, the model prognostic variables (i.e., model currents, temperature and salinity) are radiated outward to allow perturbations generated inside the model domain to propagate outward as freely as possible. If the open boundary is active, the model prognostic variables at each *z* level at the boundary are restored to the five-day time-mean currents, temperature and salinity extracted from the global ocean reanalysis data produced by Smith et al. (2010). A restoring time scale of 60 days is used for baroclinic currents, temperature and salinity at the three lateral open boundaries. An additional adjustment is made by restoring the depth-mean currents through the model open boundaries to the ocean reanalysis data with a restoring time scale of five days for the eastern and southern open boundaries and 40 minutes for the northern open boundary. The main reason for using a shorter restoring time scale at the northern open boundary is that this is the upstream border for shelf waves over the ECS. As a result, the northern open boundary condition significantly affects the circulation, hydrography and associated variability in the model domain, particularly over the Labrador and northern Newfoundland Shelves (for further discussion see Section 2.5). In particular, I found that a longer restoring time scale would result in a subpolar gyre in the model that is too strong in comparison with the general circulation feature of the subpolar gyre discussed in the literature.

2.3.2 The Spectral Nudging Method and Semi-prognostic Method

To reduce seasonal bias and drift in the model (which is due mainly due to a combination of unresolved physical processes such as turbulence, poor representation of

subgrid scale processes, and unaccurate model forcing), a combination of the spectral nudging method (Thompson et al., 2006) and the smoothed semi-prognostic method (Sheng et al., 2001; Greatbatch et al., 2004) is used. The spectral nudging method restores the model temperature and salinity in frequency-wavenumber bands that cover only information resolved by the hydrographic climatology (Thompson et al., 2007). In this study the spectral nudging method is used to restore the annual mean and the annual and semi-annual cycles of model temperature and salinity to the cycles determined from the monthly mean climatology produced by Geshelin et al. (1999). Outside these bands, the model temperature and salinity are not affected by the nudging and evolve prognostically. There are two key parameters in the application of this method: κ and γ. The first parameter (κ) specifies the band-pass width around the nudging frequencies where the nudging takes effect, and the second parameter (γ) determines the strength of the nudging such that large γ values imply weak nudging and vice versa. In this study κ is set to 3 years, which is similar to the values used previously; the value of γ is set to 200 days, which is a longer restoring time scale than the values used in other studies (Thompson et al., 2006, 2007; Wright et al., 2006).

Different from the spectral nudging method, the smoothed semi-prognostic method adds a correction to the horizontal pressure gradient terms in the model momentum equation based on the smoothed differences between observed (ρ_c) and modelled density (ρ_m). The correction is made through the hydrostatic equation:

$$\frac{\partial p}{\partial z} = -g\left[\rho_m + \beta\overline{(\rho_c - \rho_m)}\right] \tag{2.4}$$

where p is the pressure; z is the vertical coordinate, positive upward; g is the acceleration due to gravity; β is a coefficient ranging between 0 and 1; and the overbar represents a horizontal filter operator to eliminate small-scale features in the density difference term in the above equation. As a result, the smoothed semi-prognostic method applies only to large-scale features. If $\beta = 0$, the model is purely prognostic, and if $\beta = 1$, the model is diagnostic in large-scale circulation features. This study uses a simple moving average with five points (~125 km) in the eastward and northward directions with $\beta = 0.25$, which

is smaller than the typical value of 0.5 used in previous studies (Sheng et al., 2001; Eden et al., 2004; Zhao et al., 2006).

Both the spectral nudging and smoothed semi-prognostic methods can be considered simple data assimilation techniques. The main purpose of any data assimilation is to improve model skill by modifying model dynamics by assimilating observations into the model. Based on the model sensitivity study, I found that the combination of the spectral nudging method and the smoothed semi-prognostic method with coefficients that are smaller than usual for both methods is efficient in eliminating the seasonal model drift, while making the model more prognostic.

2.4 Model Validation

The performance of the NEMO coupled ocean–ice model in simulating the general circulation and interannual variability over the study region is assessed by comparing model results with previous observational and model results in the literature. Figure 2.3 presents the time-mean streamfunction of the depth-integrated flow simulated by the model over the 17-year period from 1988 to 2004. In comparison with previous numerical results published in the literature (e.g., Smith et al., 2000; Sheng et al., 2001; Wright et al., 2006; Han et al., 2008), the regional ocean circulation model reproduces the time-mean transports of the Labrador Current, the Gulf Stream, and the Northern Recirculation gyre over the slope water between the Scotian shelf and the Gulf Stream in the northwest Atlantic Ocean reasonably well. The maximum mean transport produced by the model is about 30 Sv for the Labrador Current, 80 Sv for the Gulf Stream and about 20 to 30 Sv for the recirculation over the slope water region, which are in good agreement with the results using different ocean circulation models with similar horizontal resolutions (Sheng et al., 2001; Wright et al., 2006). The model also reproduces reasonably well the depth-integrated flow near the separation of the Gulf Stream at Cape Hatteras and the pathway of the Gulf Stream roughly from 75°W, 35°N to 50°W, 41°N to the south of the Grand Banks of Newfoundland.

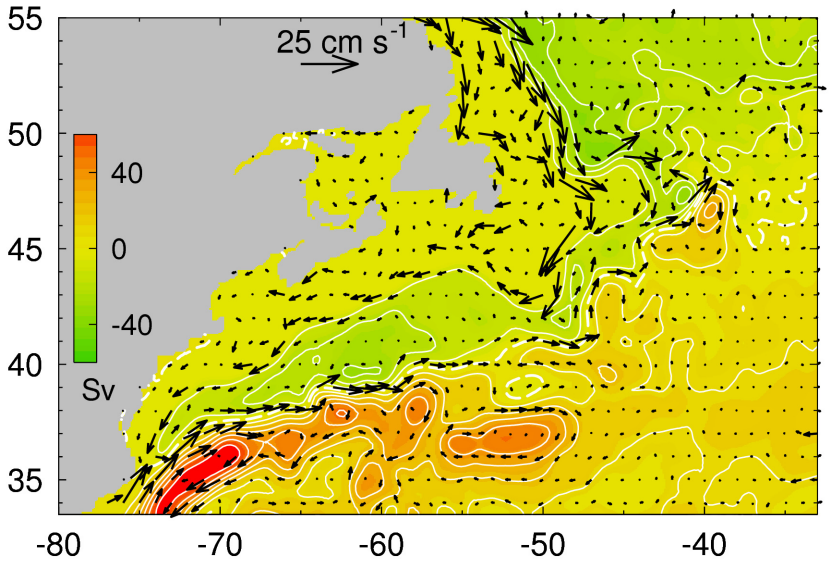

Figure 2.3. Time-mean streamfunction of the depth-integrated flow calculated from model currents in the 17-year period 1988–2004 with the arrows indicating the depth-averaged currents over the model domain. The contour interval is 10 Sv and the dashed line represents the 0 Sv contour.

Higginson et al. (2011) recently produced a time-mean sea surface topography (MSST) of the northwest Atlantic to study the mean circulation of the subpolar gyre from nine years of altimetry observations referenced with respect to a new regional geoid based on a blend of the Gravity Recovery and Climate Experiment (GRACE), terrestrial, and altimetry-derived gravity data. From a subset of the altimetry-derived MSST, the time-mean surface geostrophic currents were calculated based on the geostrophic balance (Higginson et al., 2011). It should be noted that the altimetry-derived MSST is not accurate near coastal regions because of errors associated with satellite altimeter measurements. The time-mean model surface geostrophic currents can be calculated from the time-mean model sea surface elevations. Figure 2.4a presents the comparison of the model-calculated and altimetry-derived surface geostrophic currents. The circulation model reproduces the altimetry-derived surface geostrophic currents very well, particularly the intense surface geostrophic currents associated with the Gulf Stream after its separation point at Cape Hatteras. The circulation model also performs reasonably well in simulating the strong poleward geostrophic currents associated with the North Atlantic Current in the deep waters to the east of the Grand Banks and over the northeast

corner as well as the equatorward geostrophic currents associated with the inshore and offshore branches of the Labrador Current over the Labrador Shelf. There are large differences between the simulated and altimetry-based surface geostrophic currents over the coastal and shelf waters of the ECS which might be attributed to some extent to errors associated with satellite altimeter measurements near the coast. The regional model also performs less well in simulating the anticyclonic circulation and the Mann Eddy to the east of the Grand Banks (Fig. 2.4a).

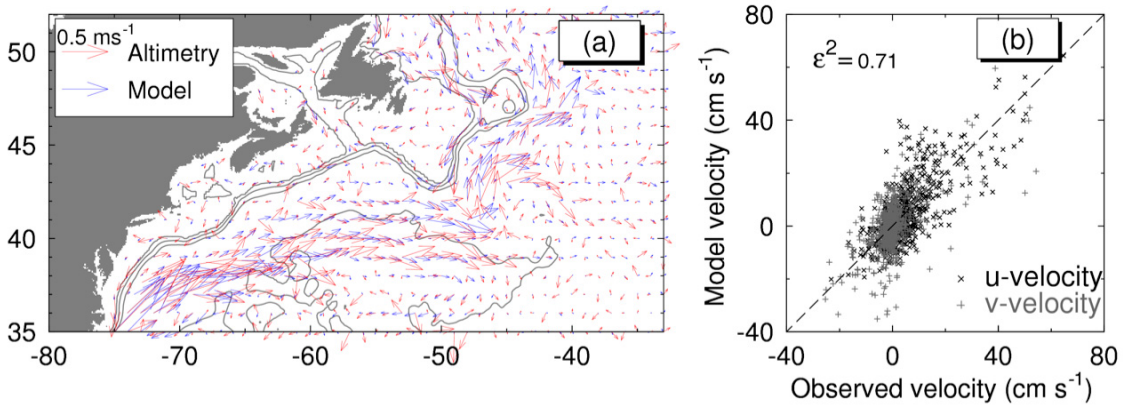

Figure 2.4. (a) Comparison of time-mean surface geostrophic currents in the five-year period 2000–04 calculated from the simulated (blue) and altimetry-derived (red) time-mean sea surface elevations (data from Higginson et al. (2011)). (b) Scatterplot of altimetry-derived and simulated time-mean surface geostrophic currents.

Figure 2.4b shows the scatterplot of eastward and northward components of altimetry-derived and simulated surface geostrophic currents. To quantify the fit between the altimetry-derived and simulated currents shown in Fig. 2.4a, the ε^2 value defined as follows is used (Schwab et al., 1989; Thompson et al., 2003):

$$\varepsilon^2 = \frac{\sum_{i=1}^{N}\left[\left(U_i^O - \bar{U}_i^O - U_i^M + \bar{U}_i^M\right)^2 + \left(V_i^O - \bar{V}_i^O - V_i^M + \bar{V}_i^M\right)^2\right]}{\sum_{i=1}^{N}\left(U_i^O - \bar{U}_i^O\right)^2 + \left(V_i^O - \bar{V}_i^O\right)^2} \qquad 2.5$$

where (U_i^O, V_i^O) and (U_i^M, V_i^M) represent, respectively, the time-mean eastward and northward components of the altimetry-derived and simulated surface geostrophic currents at the *i*th location of altimetry-derived currents, $(\bar{U}_i^O, \bar{V}_i^O)$ and $(\bar{U}_i^M, \bar{V}_i^M)$ the corresponding currents averaged over the total number of locations, and N is the total

number of locations. The index represents the ratio between the variance of the model errors and the variance of the observed variables. The skill of the model in simulating the observed currents is high for small values of ε^2 such that the model currents agree perfectly with the observations if ε^2=0. If ε^2 is larger than one, then a mean value is a more effective value predictor of the observed variability than the model results. The index is also a better metric than correlation because it also accounts for systematic deviations between observations and simulated model results. It can be demonstrated that if the simulated currents are biased by a factor δ from the observed currents, ε^2 equals $(1-\delta)^2$ (Thompson et al, 2003). The value of ε^2 is 0.71 for the results in Fig. 2.4b, indicating that the regional model has reasonable skill in simulating the time-mean surface geostrophic circulation derived from altimetry data.

The ocean circulation, particularly in the upper ocean, has strong ageostrophic currents (such as wind-driven currents, see Fig. 2.1a in Trossman et al. (2009)), in addition to the geostrophic currents discussed above. To assess the model performance in simulating the general circulation over the ECS, the time-mean sub-surface (15 m) currents derived from satellite-tracked drifting buoys drogued at 15 m depth between 1980 and 2005 (Niiler, 2001) are compared to the time-mean subsurface currents calculated from model currents at 15 m in the period between 1988 and 2004. Figure 2.5a demonstrates that the model reproduces well the drifter-derived time-mean sub-surface currents associated with the Gulf Stream and the North Atlantic Current in the deep waters off the ECS. Over the Labrador Shelf, the model generates relatively strong inshore and offshore branches of the Labrador Current with maximum speeds of about 20 and 30 cms^{-1}, respectively. The model also simulates well the bifurcation of the inshore Labrador Current before reaching Belle Isle Bank, with one branch flowing into the Gulf of St. Lawrence through the Strait of Belle Isle and the other branch flowing southward to the inshore waters of the Newfoundland Shelf. Over Flemish Pass and Flemish Cap and the eastern flank of the Grand Banks, the simulated time-mean sub-surface currents have the typical circulation features discussed in Section 2, featuring a southeastward throughflow over Flemish Pass, an anticyclonic gyre over Flemish Cap and an intense southwestward flow over the eastern flank of the Grand Banks. Figure 2.5b shows the scatterplot of eastward and

northward components of drifter-derived and simulated time-mean sub-surface currents at 15 m depth. By using Eq. (2.5) with (U_i^O, V_i^O) and (U_i^M, V_i^M) as the eastward and northward components of the drifter-derived and simulated time-mean sub-surface (15 m) currents, respectively, I obtain a value of ε^2 of approximately 0.39. This indicates again that the model has reasonable skill in simulating the time-mean sub-surface (15 m) circulation derived from the trajectories of drifters.

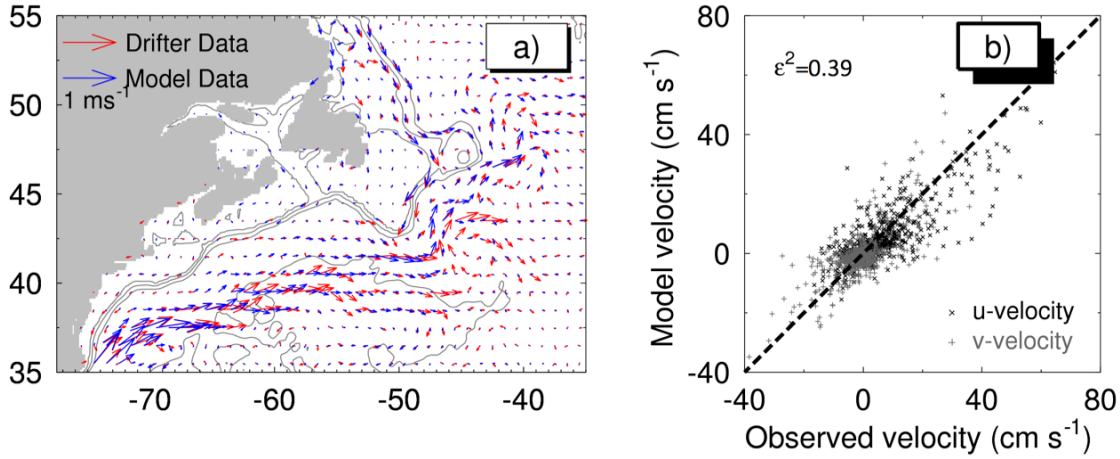

Figure 2.5. (a) Comparison of time-mean currents at 15 m inferred from sub-surface drifter movements (data from Niiler (2001)) and computed from 3-D model results (blue) and (b) scatterplot of drifter-derived and simulated time-mean horizontal currents over the northwest Atlantic.

Based on the measurements made with Conductivity-Temperature-Depth (CTD) sensors and acoustic transport floats as well as measured dissolved oxygen and chlorofluorocarbons along a transect across the southwestern Newfoundland Slope (S–S′ in Fig. 2.1b) between 1983 and 1995, Pickart and Smethie (1998) calculated the time-mean absolute geostrophic velocity normal to the transect (Fig. 2.6a). The vertical structure of the horizontal flow across the transect features equatorward currents associated with the upper Labrador Sea Water (ULSW; centred at about 800 m) originating from the western Labrador Sea, the classical Labrador Sea Water (CLSW; at about 1500 m) originating from the central Labrador Sea, and the Denmark Strait Overflow (DSO; at about 3500 m). Figure 2.6 also shows the poleward Slope Water Jet (SWJ) across the transect separating the Gulf Stream from the shelf break and from Labrador Sea Water in the top 500 m (Pickart and Smethie, 1998). The SWJ flows in the

upper ocean with an eastward velocity of the order of 3 cms^{-1} and extends to a depth of about 300 m in the northern side and from the surface to about 500 m in its offshore side (Fuglister and Worthington, 1951). Figure 2.6b presents the vertical distribution of time-mean horizontal currents normal to the same transect between 1988 and 2004 averaged from model results. The regional circulation model reproduces both the eastward SWJ and the westward Labrador Current in the upper and intermediate continental slope reasonably well, with simulated currents relatively stronger than the observations discussed by Pickart and Smethie (1998). The simulated Denmark Strait Overflow (DSO) is relatively weaker, and its position is further offshore than the observations (Fig. 2.6). A possible explanation for this discrepancy is that the circulation shown in Fig. 2.6a uses time-averaged observations collected over only three periods (in 1991, 1994, 1995) each of which spanned about one week. Therefore, caution should be taken in considering the pattern shown in Fig. 2.6a to be the true representation of the time-mean flow.

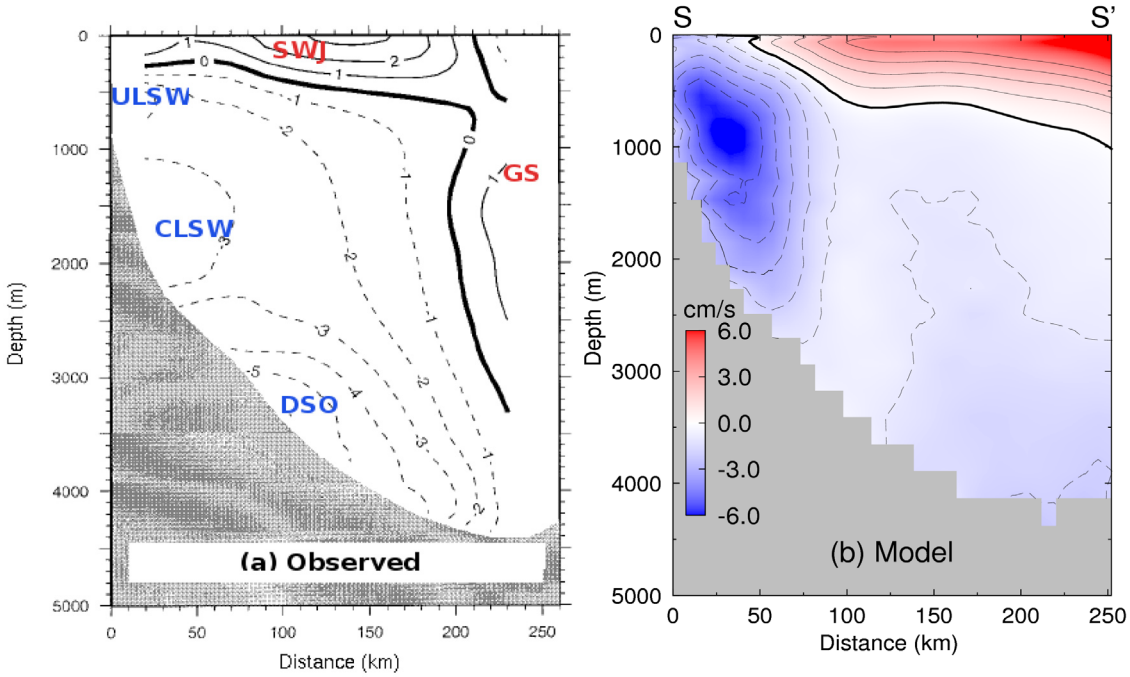

Figure 2.6. (a) Absolute geostrophic currents estimated from time-mean hydrographic observations at a transect off the southwestern Newfoundland Shelf at approximately 55°W (reprinted from Pickart and Smethie (1998) by permission of Elsevier). (b) Time-mean currents normal to the transect computed from model results between 1988 and 2004. Black contour lines indicate velocity contours spaced every 1 cms^{-1} with the thick black line indicating the zero velocity contour. Abbreviations are used for the Slope Water Jet (SWJ), Upper Labrador Sea Water (ULSW), Classical Labrador Sea Water (CLSW), Denmark Strait Overflow (DSO) and the Gulf Stream (GS).

I next examine the model performance in simulating the seasonal cycle of hydrography over the study region. Figure 2.7 presents the 17-year time-mean temperature and salinity at depths of 32 and 112 m calculated from model results between 1988 and 2004. The regional circulation model reproduces the general distributions of temperature and salinity over the northwest Atlantic discussed in the literature. The model also reproduces the relatively cold and fresh waters carried by the Labrador Current from the Labrador Shelf to the Tail of the Grand Banks and then to the shelf break of the Scotian Shelf and warm and salty waters carried by the Gulf Stream and the North Atlantic Current from tropical regions to the deep waters off the ECS. The model successfully simulates the relatively cold and fresh waters in the western Gulf of St. Lawrence, over the inner Scotian Shelf and inner Gulf of Maine, which are primarily driven by the equatorward coastal currents associated with freshwater discharge from the St. Lawrence River.

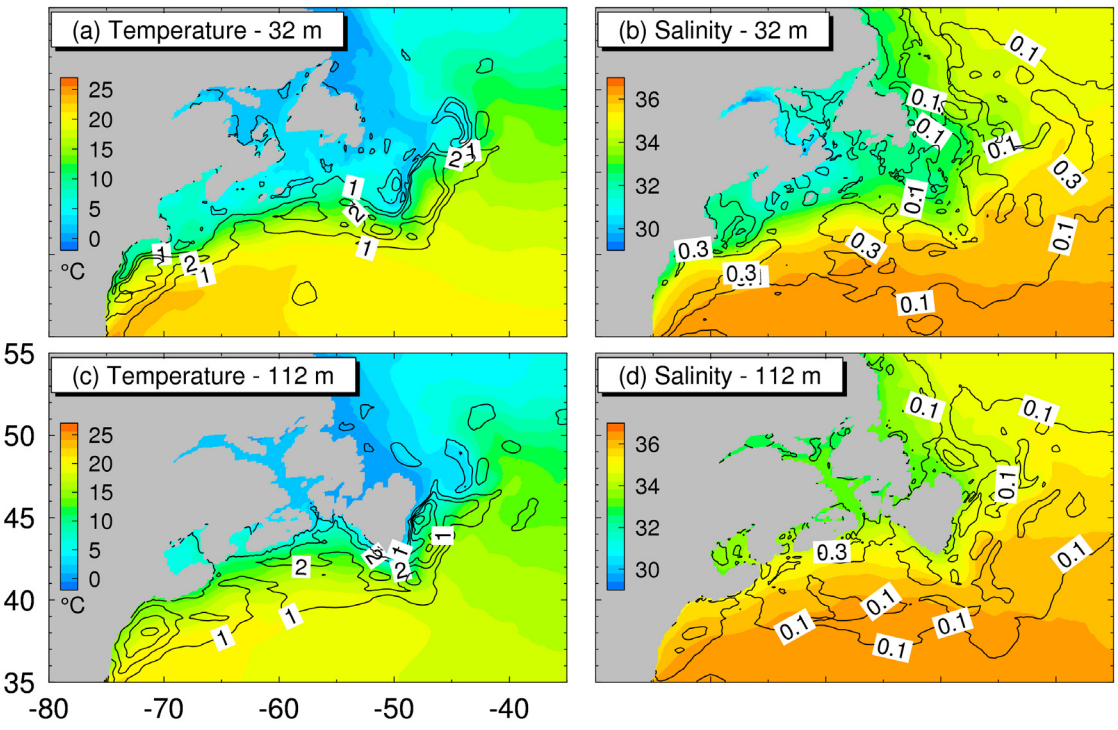

Figure 2.7. Color images showing time-mean temperature (a and c) and salinity (b and d) at depths of 32 and 112 m calculated from model results between 1988 and 2004. The black contours are the mean absolute differences between the climatological and simulated monthly mean temperature and salinity at the two depths.

To quantify the model skill in simulating the seasonal cycle of 3-D hydrography over the ECS, I calculated the average absolute difference (*AAD*) between the climatological and simulated monthly mean hydrography at each model grid point defined as:

$$AAD = \frac{1}{12}\sum_{i=1}^{12}\left|\hat{O}_i - \hat{M}_i\right| \tag{2.6}$$

where $\hat{O}_i$ and $\hat{M}_i$ are the climatological and simulated monthly mean temperatures (or salinity), respectively. The *AAD* is a simple metric to measure the model bias with the units of the model variable, which is useful to validate the model performance. The climatological monthly mean values are taken from the 3-D gridded fields constructed by Geshelin et al. (1999). The simulated time-mean monthly mean values are calculated from model results between 1988 and 2004. The *AAD*s are relatively small over the northwest Atlantic, except for the continental slope region and adjacent waters of the ECS (Fig. 2.7), indicating the efficiency of the spectral nudging method and the smoothed semi-prognostic method in suppressing the seasonal bias and drift in the model. The *AAD* values for temperature at 32 m and 112 m are less than 1°C over coastal and shelf waters of the ECS but are relatively large over the continental slope region and also the area to the north of Cape Hatteras near the separation point of the Gulf Stream. The *AAD* values for salinity at these two depths are less than 0.1 (practical salinity scale used) in the deep ocean but slightly higher over the continental slope and shelf regions of the ECS with the largest *AAD* being about 0.3. The *AAD* values for salinity are similar in magnitude in the upper and sub-surface waters of the northwest Atlantic, except for the area to the north of the separation point of the Gulf Stream, where the *AAD* values are larger in the upper ocean. It should be noted that a simple optimal interpolation scheme was used in constructing the monthly mean climatology of hydrography from sparse hydrographic observations (Geshelin et al., 1999). Therefore, large *AAD* values over the continental slope region of the ECS are partially associated with relatively larger errors in the gridded monthly mean climatology over the slope region than in other regions.

To demonstrate the model performance in simulating interannual variability of hydrography over the ECS, the monthly mean SST anomalies calculated from the model

results are compared with the SST anomalies estimated from satellite remote sensing data (Shadwick et al., 2010) between 1999 and 2005 over the Scotian Shelf and Slope (Fig. 2.8). The cooling trend from 1999 to 2005 at the ocean surface as seen from satellite observations is well reproduced by the model over the Scotian Shelf (Fig. 2.8a) and associated Slope region (Fig. 2.8b). It should be noted that the cooling trend during this period is actually part of the interannual variations in the SST as shown in the model results. Figure 2.8 also demonstrates that the model simulates the SST over the shelf waters better than over the slope waters because of complicated dynamics over the latter region (further discussion is provided in Section 2.5).

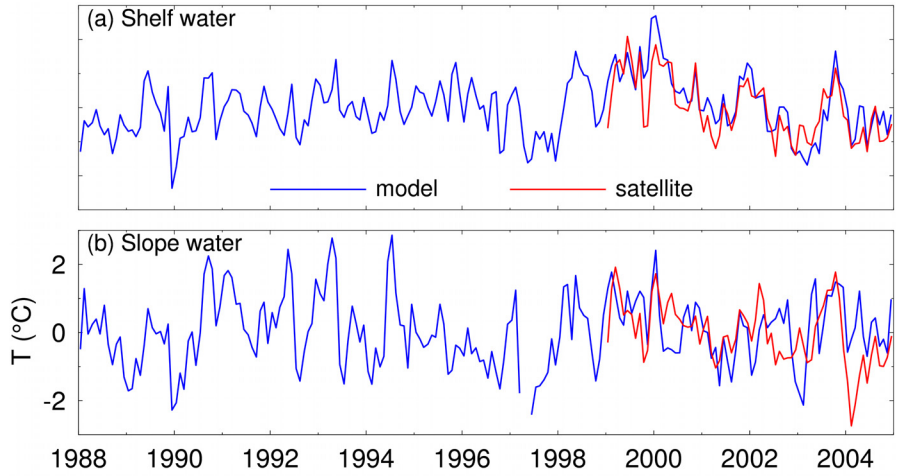

Figure 2.8. Monthly mean anomalies of sea surface temperature derived from satellite remote sensing data (Shadwick et al., 2010) and calculated from model results for (a) an area over the central Scotian Shelf centred at 44°N and 64°W (P1 in Fig. 2.1) and (b) an area over the Slope Water region centred at 42°N and 60°W (P2 in Fig. 2.1).

Figure 2.9 presents the annual-mean and depth-averaged observed anomalies of temperature and salinity over the Newfoundland and Scotian Shelves (Head and Sameoto, 2007) compared with the depth-averaged annual mean simulated anomalies calculated from the 3-D model results for the period 1988–2004. The observed temperature anomalies over the Newfoundland and Scotian Shelves are reasonably well reproduced by the model. In comparison, the observed annual mean salinity anomalies at P3 on the Newfoundland Shelf are less well reproduced by the model. I speculate that less realistic specification of the freshwater flux at the sea surface and unsolved processes

for the sea-ice dynamics in the model are responsible for the model deficiency in simulating the observed salinity anomalies over the Newfoundland Shelf.

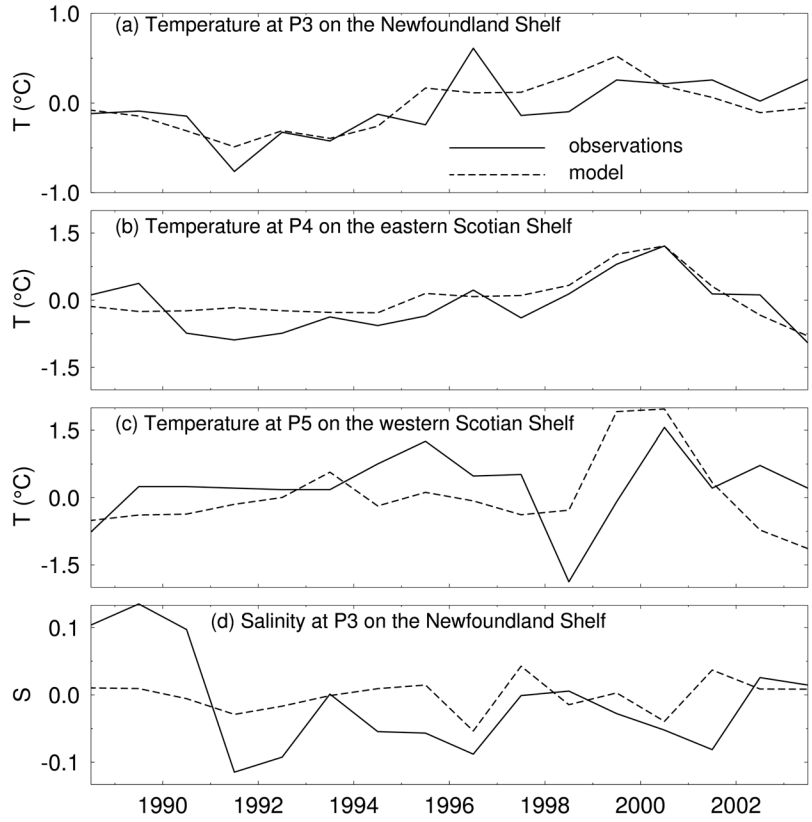

Figure 2.9. Comparison of annual mean anomalies of observed hydrography over the Newfoundland and Scotian Shelves (data from Head and Sameoto (2007)) with annual mean anomalies from model results for (a) temperature at P3 over the Newfoundland Shelf; (b) temperature at P4 over the eastern Scotian Shelf; (c) temperature at P5 over the central and western Scotian Shelf and (d) salinity at P3 at the Newfoundland Shelf.

2.5 INTERANNUAL VARIABILITY OVER THE EASTERN CANADIAN SHELF

2.5.1 Numerical Experiments with Different Model Forcing

There are three main mechanisms that affect the interannual variability of the circulation and hydrography in the model: (a) interannual variability in the atmospheric forcing, including surface wind stress and net sea surface heat and freshwater fluxes; (b)

interannual variability in the flow and hydrography specified at the model open boundaries; and (c) model internal dynamics, mostly the model non-linear dynamics.

Model results in four different numerical experiments are discussed in this section to examine the main physical processes affecting the interannual variability of circulation and hydrography over the ECS. The four experiments use the same NEMO coupled ocean–ice model with the same model setup, except for different model forcing as follows:

Exp-Control: The model in this experiment (control run) is driven by the suite of external forcing presented in Section 2.3. Some model results in this experiment were presented in Section 2.4.

Exp-ConstAll: The model in this experiment is driven by the time-mean atmospheric forcing taken from 18-year time-mean fields of surface winds, sea surface air temperature, specific humidity of the air, short and longwave radiation, and precipitation calculated from Large-Yeager's atmospheric reanalysis data. The model is also driven by the time-mean boundary forcing at the three model open boundaries taken from the ocean reanalysis data produced by Smith et al. (2010). In this run, model interannual variability results from the non-linear (internal) dynamics in the model (assuming that long-term model drift is small).

Exp-ConstOBC: The model in this experiment is driven by the same external forcing as in Exp-Control, except for the 18-year time-mean boundary forcing at the three model open boundaries. Interannual variability in the experiment comes from the non-linear (internal) dynamics in the model as well as from the interannual variability in the atmospheric forcing fluxes.

Exp-ConstFluxes: The model in this experiment is driven by five-day mean temperature, salinity and currents at the lateral open boundaries taken from the global ocean reanalysis data, which are the same data used in Exp-Control. The model in this experiment is

different from Exp- Control in that it is forced by the 18-year time-mean wind speed, air temperature, specific humidity of the air, short and longwave radiation, and precipitation. Interannual variability produced by the model in the experiment comes from the non-linear (internal) dynamics in the model and the interannual variability through the model lateral open boundaries.

Except where otherwise stated, the monthly mean results of the model temperature, salinity and horizontal currents in the 17-year period 1988–2004 in each experiment were used for the analysis of interannual variability over the ECS in this section. I followed Petrie and Drinkwater (1993) and subtracted the 17-year monthly averages of currents and hydrography from the monthly mean model results at each model grid point to generate the monthly mean anomalies. Figure 2.10 presents the monthly mean anomalies of temperature and salinity in the control run (Exp-Control) averaged vertically between 100 and 300 m at seven locations along the shelf break of the ECS. It should be noted that the monthly mean anomalies of temperature and salinity at the northern open boundary (Figs 2.10a (inset a-0) and 2.10b (inset b-0)) were taken from the ocean reanalysis data of Smith et al. (2010).

The monthly mean model temperature and salinity anomalies at intermediate depths of 100–300 m over the shelf break of the ECS in the control run have significant low-frequency (time scales longer than one year) variations, which are consistent with previous observations made in the region (Petrie et al., 1992; Petrie and Drinkwater, 1993; Colbourne and Foote, 2000). The maximum monthly mean anomalies of sub-surface (100–300 m) temperature and salinity in the control run are about 1°C and 0.2, respectively, over the shelf breaks of the Labrador and northern Newfoundland Shelves; and about 2°C and 0.5, respectively, over the shelf breaks of the southwestern Newfoundland and Scotian Shelves. Figure 2.10 also demonstrates that the sub-surface temperature and salinity anomalies at the shelf breaks of the Labrador and northern Newfoundland Shelves are coherent with the anomalies at the northern open boundary, much more than the anomalies at the shelf breaks of the western Newfoundland and Scotian Shelves.

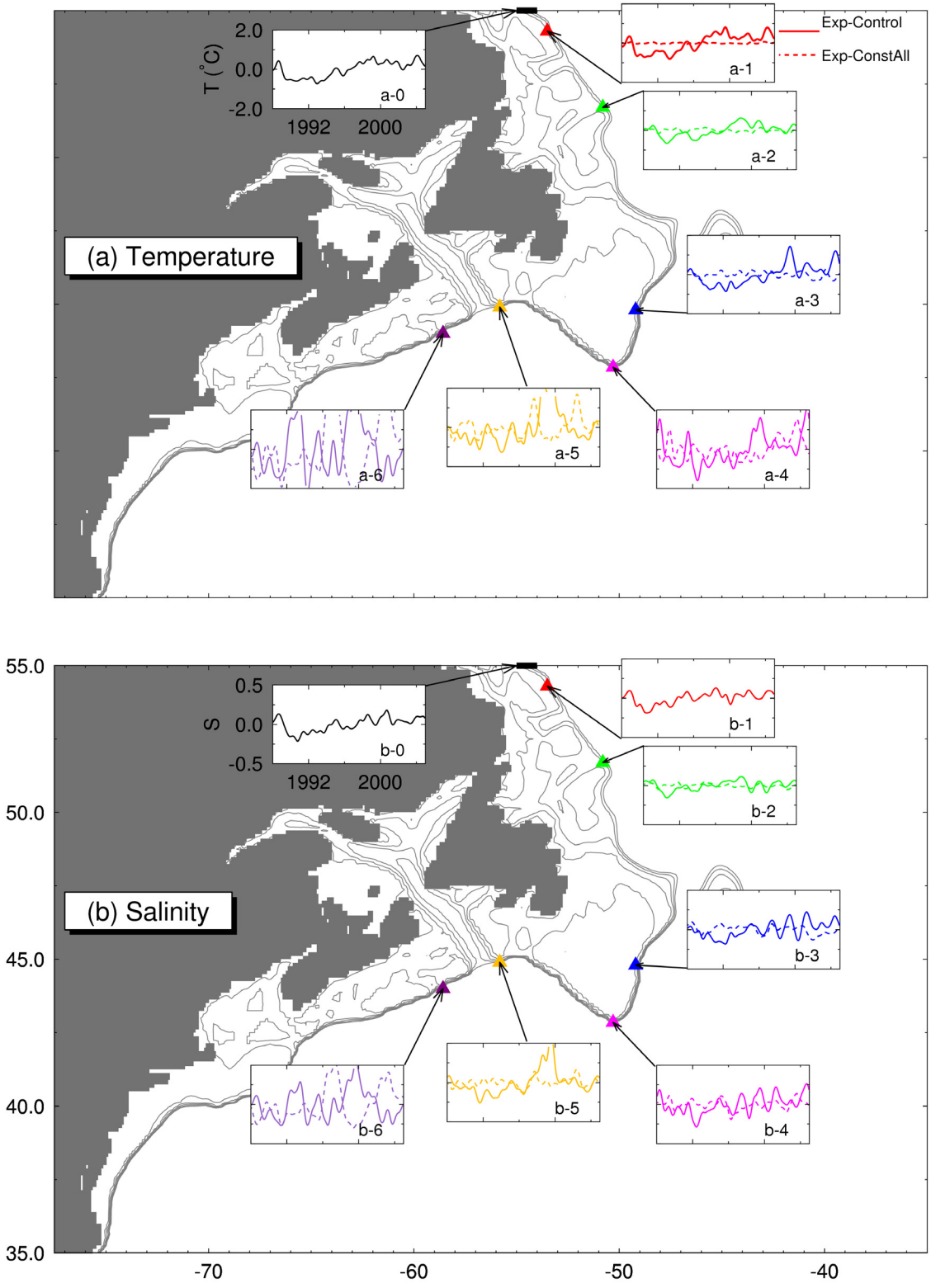

Figure 2.10. Monthly mean anomalies of sub-surface (100–300 m) model (a) temperature and (b) salinity at seven locations (marked by solid triangles) along the shelf break of the eastern Canadian Shelf in Exp-Control (solid) and Exp-ConstAll (dashed).

Correlation analysis is used to calculate the correlation coefficients and time lags between the anomalies specified at the northern open boundary and the anomalies produced by the model in Exp-Control at different positions along the shelf break of the ECS shown in Fig. 2.10. The monthly mean anomalies of sub-surface hydrography at the shelf breaks of the ECS are correlated with the anomalies at the northern open boundary with correlation coefficients decreasing from a maximum of 0.9 over the Labrador Shelf to less than 0.4 over the eastern Scotian Shelf (Figs 2.11a and 2.11b). The time lags increase from about one month over the Labrador Shelf to about five months over the Scotian Shelf, indicating the equatorward propagation of the anomalies associated with the Labrador Current. It should be noted that the correlations are small (less than 0.3) between sub-surface hydrographic anomalies at the shelf breaks of the central and western Scotian Shelf and the Gulf of Maine and anomalies specified at the northern open boundary, indicating that the interannual variability over these regions is significantly affected by physical processes other than the Labrador Current.

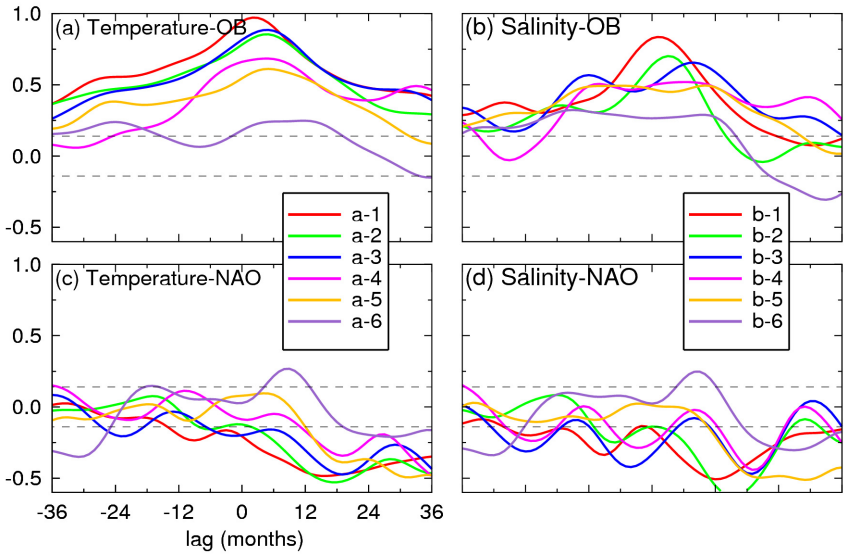

Figure 2.11. Correlation coefficients between the monthly mean (a) temperature and (b) salinity anomalies at six different positions along the shelf breaks of the eastern Canadian shelf and the anomalies at the northern open boundary (OB); (c) and (d); as in (a) and (b) but for the correlation coefficients between the temperature and salinity anomalies with the winter North Atlantic Oscillation index (NAO). Different line colors represent the different locations shown in Fig. 2.10.

A similar correlation analysis was made for the temperature and salinity anomalies presented in Fig. 2.10 with the winter NAO index (Figs 2.11c and 2.11d). The correlations are about 0.4 and statistically significant over the Labrador Shelf and the eastern Newfoundland Shelf, indicating that cooler and fresher conditions lag (by about one year) positive NAO phases, which is consistent with the findings of Petrie (2007). Over the southern Newfoundland Shelf and the Scotian Shelf the correlations are smaller and often below the significance level.

The other important processes that could affect the interannual variability over the Slope Water off the Scotian Shelf include the interannual variability in the wind forcing and heat and freshwater fluxes at the sea surface and anomalies produced by the non-linear dynamics in the model. To identify which processes play a dominant role, the monthly mean anomalies of sub-surface temperature and salinity in the control run (Exp-Control) are compared with the Exp- ConstAll case (Fig. 2.10). In comparison with the model results in Exp-Control, the monthly mean anomalies of sub-surface temperatures and salinity in Exp-ConstAll are relatively small at the shelf breaks of the Labrador and northern Newfoundland Shelves and have similar large variations but with different phases at the shelf break of the Scotian Shelf. Figure 2.10 also demonstrates that at the shelf breaks of the southern Newfoundland Shelf in the ConstAll case, the sub-surface temperature anomalies are relatively large and the sub-surface salinity anomalies are relatively small. It should be noted that the external model forcing in Exp-ConstAll does not have any interannual variability. As mentioned before, the monthly anomalies in model results in Exp-ConstAll are caused solely by the non-linear dynamics in the model.

2.5.2 The Complex Empirical Orthogonal Function Analysis

The Complex Empirical Orthogonal Function (CEOF) analysis is used to identify the advective processes affecting the interannual variability over the ECS in the model. The CEOF analysis is a multivariate statistical technique for extracting the dominant spatial patterns of variability from data series (Horel, 1984; Terradas et al., 2004). In comparison with the conventional Empirical Orthogonal Function (EOF) method for determining

statistically the spatial patterns coherent only at zero lag (Hannachi et al., 2007); the CEOF analysis has the advantage of isolating propagating and standing patterns. The first step in a CEOF analysis is to construct a complex field $\Psi(\vec{x},t)$ from the scalar field of monthly mean temperature (or salinity) anomalies $T(\vec{x},t)$:

$$\Psi(\vec{x},t) = T(\vec{x},t) + iH(\vec{x},t) \tag{2.7}$$

where $\vec{x}$ represents the position vector, t is time, $i = \sqrt{-1}$ and $H(\vec{x},t)$ represents the Hilbert transformation of $T(\vec{x},t)$. Hilbert transformation means that the amplitude of each Fourier spectral component of $T(\vec{x},t)$ is unchanged while its phase is advanced by π/2 (Horel, 1984). Since Ψ is complex, the eigenfunctions $E_n(\vec{x})$ and mode coefficients $A_n(t)$ (with n=1, 2, 3…N) resulting from the EOF analysis of $\Psi(\vec{x},t)$ are also complex. The complex field Ψ can be expressed in terms of $E_n(\vec{x})$ and $A_n(t)$:

$$\Psi(\vec{x},t) = \sum_{n=1}^{N} A_n(t)E_n(\vec{x}) = \sum_{n=1}^{N} R_n(t)e^{i\phi_n(t)}S_n(\vec{x})e^{i\theta_n(\vec{x})} \tag{2.8}$$

where $R_n(t)$ is the temporal amplitude function of $A_n(t)$; $\phi_n(t)$ is the temporal phase function defined as $\phi_n(t) = \arctan[\mathrm{Im}(A_n)/\mathrm{Re}(A_n)]$; $S_n(\vec{x})$ is the spatial amplitude function of $E_n(\vec{x})$; and $\theta_n(\vec{x})$ is the spatial phase function defined as $\theta_n(\vec{x}) = \arctan[\mathrm{Im}(E_n)/\mathrm{Re}(E_n)]$. Physically, the temporal amplitude function (R_n) describes the temporal variability in the magnitude associated with the nth eigenfunction, and the temporal phase function (ϕ_n) describes the temporal variation of the phase of the nth eigenfunction associated with periodicities in $T(\vec{x},t)$. The spatial amplitude function (S_n) describes the spatial distribution of variability associated with each eigenfunction, and the spatial phase function (θ_n) describes the relative phase function among various spatial locations. For a standing wave pattern, S_n has the structure of nodes and antinodes, and θ_n has a jump of π between the two neighboring antinodes. For propagating waves, the spatial phase function θ_n changes with space (Terradas et al., 2004). Furthermore, the time derivative of ϕ_n is a measure of the "instantaneous" frequency ($\mathrm{d}\phi_n/\mathrm{d}t$), while the

spatial derivative of θ_n provides a measure of the "local" wavenumber calculated using $\partial\theta_n/\partial x$, $\partial\theta_n/\partial y$.

Because of large regional differences in circulation and interannual variability over the ECS (Petrie et al., 1992; Petrie and Drinkwater, 1993), the CEOF analysis is performed separately for the monthly mean anomalies of model temperatures and salinity over four subregions (Fig. 2.1b): (1) the Labrador Shelf, the northern Newfoundland Shelf and adjacent waters (LS-NNFS); (2) the eastern Newfoundland Shelf and adjacent waters (ENFS); (3) the western Newfoundland Shelf, eastern Scotian Shelf and adjacent waters (WNFS-ESS); and (4) the western Scotian Shelf, Gulf of Maine and adjacent waters (WSS-GOM). In each subregion, the CEOF analysis is performed separately for the monthly mean anomalies of the temperature and salinity in three different vertical layers: (a) the upper layer 0–102 m, (b) an intermediate layer 102–350 m, and (c) a deep layer 350–1215 m. Because the model resolution used in this study is not spatially uniform, the monthly mean model temperature and salinity anomalies at each grid are weighted by the ratio of the grid volume to the maximum grid-point volume over the subregion before performing the CEOF analysis. After the analysis, the spatial amplitude function $S_n(\vec{x})$ is deweighted by the same ratio to ensure the resulting fields have meaningful units.

2.5.3 Monthly Mean Anomalies over the Eastern Canadian Shelf

2.5.3.1 The Labrador and northern Newfoundland Shelves

Table 2.1 lists percentages of the total variance explained by the first three CEOFs for the monthly mean temperature and salinity anomalies in three layers over this subregion in the control run. The first CEOF explains about 52%, 62% and 86% of the total variance in the temperature anomalies in the three layers, respectively. The second CEOF explains only about 14%, 11% and 7% of the total variance in the three layers, respectively. The third CEOF explains only between 2-9% of the total variance in the three layers. For the monthly mean salinity anomalies in the three layers, the first three CEOFs also explain similar percentages of the total variance. This suggests that the first

CEOF plays a very important role in the temperature and salinity anomalies over this subregion.

Table 2.1. Percentages of the total variance explained by the first three CEOFs extracted from the monthly mean temperature and salinity anomalies in the three layers over the Labrador Shelf and northern Newfoundland Shelf in the control run.

	Percentage of variance					
	Temperature			Salinity		
Layer	mode 1	mode 2	mode 3	mode 1	mode 2	mode 3
Upper (0-102 m)	51.5	14.1	7.3	50.9	10.2	8.9
Intermediate (102-350 m)	62.3	11.3	8.2	47.5	13.8	7.8
Lower (350-1215 m)	85.7	6.8	2.8	88.8	4.7	2.0

Figure 2.12 presents horizontal distributions of the spatial amplitude (S_1) and phase vectors (θ_1) of the first CEOF, with the time series of the associated temporal amplitude (R_1) and temporal phase change ($\Delta\phi_1$) for the monthly mean temperature anomalies at 160 m over the LS-NNS subregion in the control run. The spatial amplitude S_1 over this subregion is nearly spatially uniform with relatively larger values over Hamilton Bank and at the shelf break than other areas (Fig. 2.12a). The clockwise rotation of the phase vectors from the northern to the southern part of the subregion indicates the direction of propagation of the patterns. The spatial phase vectors θ_1 have phase differences of less than 40 degrees over this subregion, indicating long wavelengths (and faster phase speeds) of the waves. Distributions of S_1 and θ_1 shown in Fig. 2.12a indicate that the first CEOF in the control run represents the southeastward propagation of interannual variability of temperature anomalies from the Labrador Shelf to the northern Newfoundland Shelf with wavelengths of the order of 3000 km. The temporal amplitude R_1 over this subregion (Fig. 2.12c) has significant low-frequency variations, with the time-mean period (P) of the variability being about 4.7 years (estimated from the time change of the temporal phase $\Delta\phi$ in Fig. 2.12e, as $P = 2\pi\Delta t/\Delta\phi$, with $\Delta t = 1/12$ yr) which means phase speeds of the order of 2 cms^{-1}.

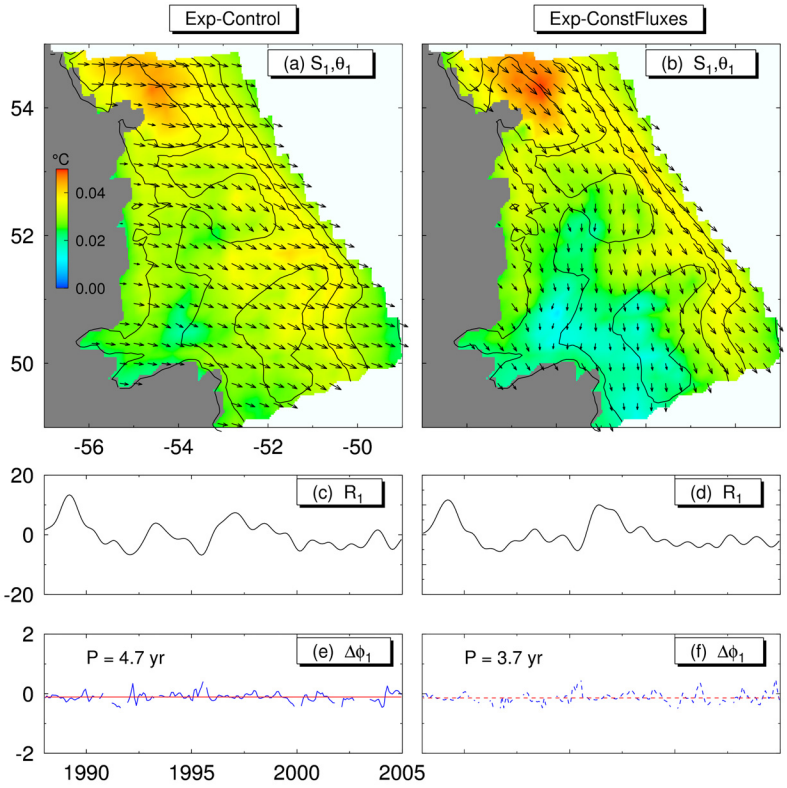

Figure 2.12. Distributions of spatial amplitude (S_1; colour image) and phase (θ_1; arrows), temporal amplitude (R_1) and temporal phase change ($\Delta\phi_1$) of the first CEOF for the monthly mean temperature anomalies at 160 m over the Labrador and northern Newfoundland Shelves in Exp-Control (left panels) and Exp-ConstFluxes (right panels). The red line in the bottom panels represents the averaged temporal phase change.

As shown in Fig. 2.10, the model temperature and salinity anomalies in Exp-ConstAll are small over the LS-NNS subregion, indicating that the non-linear dynamics play a minor role in the interannual variability over the LS-NNS subregion in the model. Therefore, only the anomalies in the sea surface forcing and boundary forcing in the model could be responsible for the CEOF shown in Fig. 2.12a. Figure 2.12 demonstrates that the spatial amplitude and phase functions of the first CEOFs in Exp-Control and Exp-ConstFluxes have very similar large-scale features, with similar temporal amplitude time series. The model external forcing, except for the model open boundary condition, is time-invariant in Exp-ConstFluxes, as mentioned earlier. This suggests that the interannual variability over this subregion in the control run is driven mostly by the variability at high latitudes that enter this subregion through the northern open boundary of the model. Figure 2.13 shows the vertical distribution of the spatial amplitude of the

first CEOF (S_1) for model temperature and salinity anomalies in the control run along transect AA′ at White Bay (Fig. 2.1b). The temporal amplitude R_1 in each layer is normalized by its standard deviation and the spatial amplitude S_1 is multiplied by its standard deviation in order to compare the vertical distributions of S_1 in different layers. The spatial amplitude S_1 has similar vertical distributions for temperature and salinity anomalies at transect AA′, featuring relatively larger values in the top 200 m and smaller values in the lower layer of the transect, with a maximum at about 40 m over the shelf break of the transect. Colbourne et al. (1997) revealed an intense southward jet in the top 100 m at Seal Island close to transect AA′. This suggests that the southward advection of the interannual variability carried by the offshore branch of the Labrador Current is responsible for the maximum interannual variability in the monthly mean temperature and salinity in the upper layer of the transect shown in Fig. 2.13.

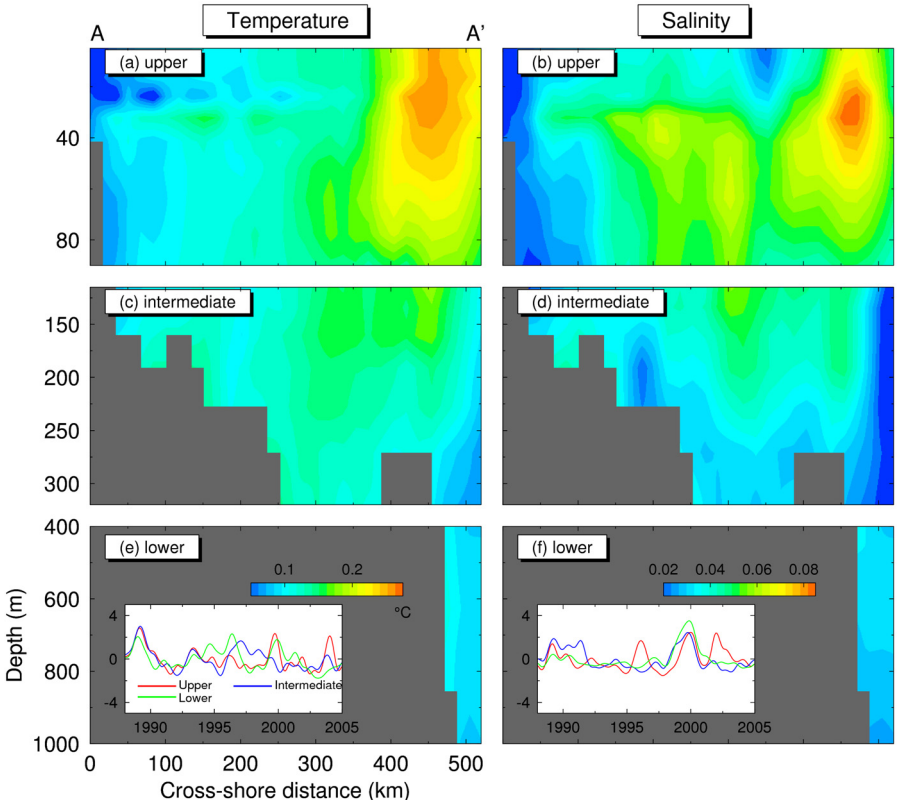

Figure 2.13. Vertical distributions of spatial amplitude functions (S_1) of the first CEOF for the temperature (left panels) and salinity (right panels) anomalies in the upper (upper panels), intermediate (middle panels) and lower (lower panels) layers along section AA′ at White Bay on the northern Newfoundland Shelf.

2.5.3.2 The eastern Newfoundland Shelf and adjacent waters

The CEOFs extracted from the monthly mean temperature and salinity anomalies over this subregion (ENFS) are significantly different from the CEOFs over the LS-NNS subregion. The first CEOF explains only about 27%, 31% and 44% of the total variance in the monthly mean salinity anomalies in the three vertical layers and percentages for the temperature anomalies over the ENFS subregion are similar (Table 2.2), which are about 1.5 to 2 times smaller than the percentages of the total variance explained by the first CEOF over the LS-NNS subregion. The spatial amplitude of the first CEOF over this subregion in the control run (S_1) has large values in the deep waters to the east of the Grand Banks and relatively small values over other areas (Fig. 2.14a). For the deep water areas where the spatial amplitude is large, the spatial phase of the first mode (θ_1) in the control run features a clockwise rotation (of about 30°) of the phase vectors from south to north, indicating that the first CEOF in the control run shown in Fig. 2.14 represents poleward moving waves with wavelengths of the order of 3000 km and a time-mean period of about 3.3 years for the temperature anomalies and 2.4 years for the salinity anomalies. In the three cases of Exp-Control, Exp-ConstAll and Exp-ConstFluxes, the spatial amplitude functions (S_1) have similar large-scale horizontal structures (Figs 2.14a–c) and the temporal amplitude functions R_1 have magnitudes of the same order (Figs 2.14d–f), indicating that the large interannual variability in the deep waters to the east of the Grand Banks is mainly associated with the non-linear dynamics of the Labrador Current and the North Atlantic Current.

Table 2.2. Percentages of the total variance explained by the first three CEOFs extracted from the monthly mean temperature and salinity anomalies in the three layers over the eastern Newfoundland Shelf in the control run.

	Percentage of variance					
	Temperature			Salinity		
Layer	mode 1	mode 2	mode 3	mode 1	mode 2	mode 3
Upper (0-102 m)	29.9	13.2	8.4	26.8	16.5	11.9
Intermediate (102-350 m)	35.7	14.5	8.5	31.1	15.2	10.7
Lower (350-1215 m)	45.2	15.0	8.7	43.6	19.3	11.4

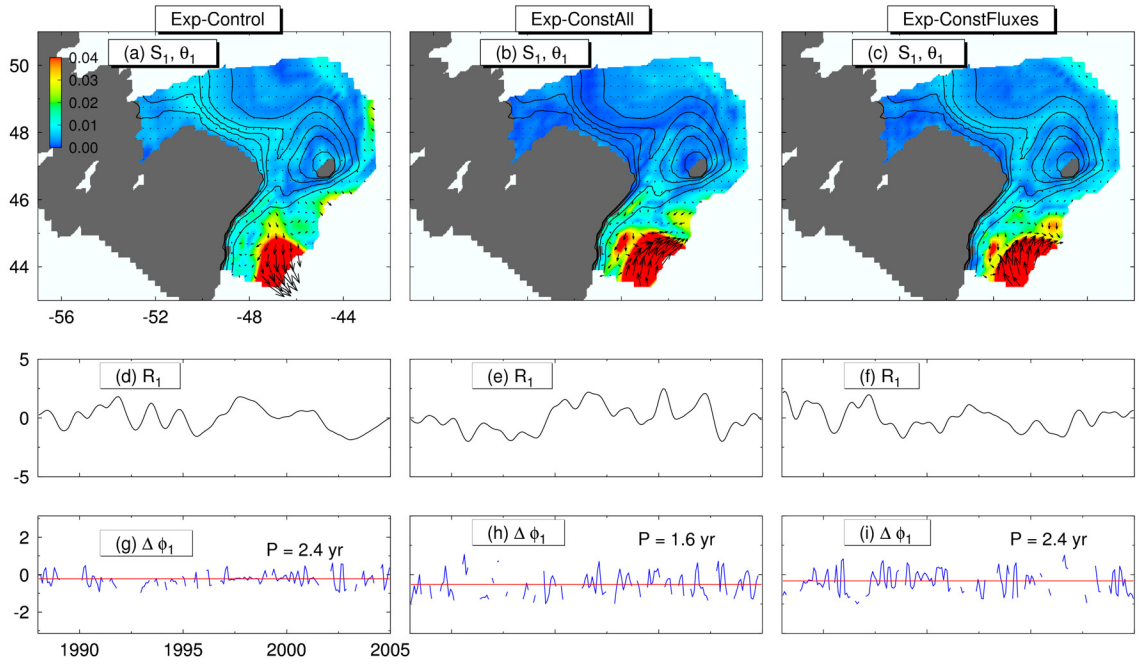

Figure 2.14. Distributions of spatial amplitude (S_1; colour image) and phase (θ_1; arrows), temporal amplitude (R_1) and temporal phase change ($\Delta\phi_1$) functions of the first CEOF for the monthly mean salinity anomalies at 160 m over the eastern Newfoundland Shelf and adjacent waters in Exp-Control (left panels), Exp-ConstAll (centre panels) and Exp-ConstFluxes (right panels). The red line in the bottom panels represents the averaged temporal phase change.

The second and third CEOFs shown in Fig. 2.15 feature large spatial amplitudes in the deep waters to the east of the Grand Banks which are similar to the first CEOF, except that the second and third CEOFs have moderate amplitudes with moderate spatial phase differences along the shelf break from the Northern Newfoundland Shelf to the eastern Grand Banks through Flemish Pass. The second and third CEOFs represent equatorward propagating waves of interannual variability along the shelf break from the northern Newfoundland Shelf to the eastern flank of the Grand Banks through Flemish Pass, in addition to the standing waves in the deep waters to the east of the Grand Banks.

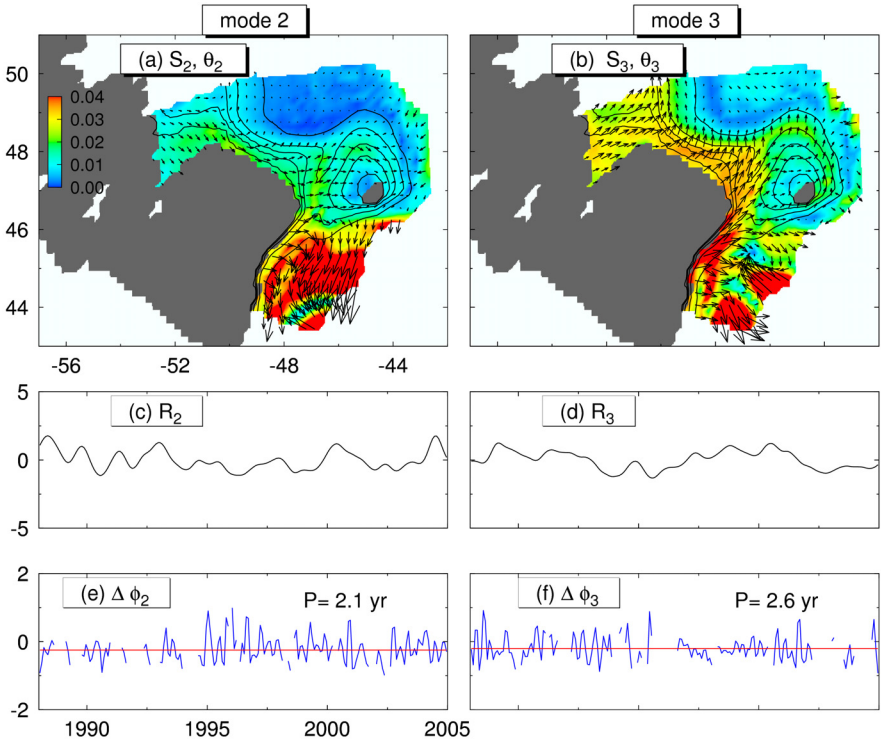

Figure 2.15. Distributions of spatial amplitude (S_I; colour image) and phase (θ_I; arrows), functions of the second (left panels) and third (right panels) CEOFs for the monthly mean temperature anomalies at 160 m over the eastern Newfoundland Shelf and adjacent waters in Exp-Control

Figure 2.16 presents the time evolution of the anomalies of the sub-surface (160 m) temperatures and currents taken from five-day mean model results with seasonal cycles removed from the five-day model mean temperature and currents (seasonal cycles were linearly interpolated from the 17-year monthly-mean temperature and currents). The anomalies shown in Fig.2.16 have significant temporal and spatial variations. In the deep waters between the shelf break of the eastern Grand Banks and the western edge of the North Atlantic Current, there are many positive and negative temperature anomalies which move very slowly, either northward or southward, depending on the competing influences of the Labrador Current and the North Atlantic Current. I focus on the positive temperature anomaly labeled "A1" in Fig. 2.16 as an example. This temperature anomaly is centred at about 47°W and 45°N in late March 1998 (Fig. 2.16a). Anomaly A1 undergoes stretching and transforming at its original position in April and May (Figs 2.16b and 2.16c) and then separates into two parts in early August (Fig. 2.16d). The

eastern part of anomaly A1 moves northward with the North Atlantic Current, and the western part is entrained by the Labrador Current and moves equatorward to the Tail of the Grand Banks and then to the southwestern flank of the Grand Banks in mid-December 1998 (Fig. 2.16f). During this period, a positive temperature anomaly labeled "A2" has very different movements. In late March 1998, anomaly A2 is centred at about 49°W and 41°N surrounded by three negative anomalies in the deep waters to the south of the Tail of the Grand Banks. Anomaly A2 undergoes significant stretching in April and May with its northwestern part advected equatorward by the Labrador Current along the shelf break of the southwestern Newfoundland Shelf (Figs 2.16b and 2.16c). The main part of anomaly A2 remains at its original position in early August and then moves westward onto the Slope Water region off the Scotian Shelf in December 1998 (Fig. 2.16e). It should be noted that as the northern part of anomaly A2 moves equatorward along the shelf break of the WNFS-ESS subregion, some of the northern parts enter the southern Gulf of St. Lawrence through Laurentian Channel (Fig. 2.16e). The northern part of anomaly A2 also affects the water properties in Emerald Basin by changing the monthly temperature fields from negative (Figs 2.16a–2.16d) to positive anomalies (Figs 2.16e–2.16f) once it reaches the central Scotian Shelf.

2.5.3.3 The western Newfoundland and eastern Scotian Shelves

The first three CEOFs over this subregion explain similar percentages of the total variance in the temperature and salinity anomalies in the three layers as those over the ENFS subregion (Tables 2.2 and 2.3). The spatial amplitude function of the first CEOF (S_1) over the WNFS-ESS subregion is different than over the ENFS subregion and features large values in the deep waters to the south of the Tail of Grand Banks and over the shelf breaks of both the western Newfoundland Shelf and the eastern Scotian Shelf (Fig. 2.17). The spatial phase of the first CEOF (θ_1) features large spatial gradients over the areas with large values of S_1, with a clockwise rotation of the phase vectors of about 40° between the Tail of the Grand Banks and Laurentian Channel giving wavelengths of the order of 5000 km. This suggests that the first CEOF over this subregion represents an equatorward propagation of the interannual variability from the deep waters to the

southeast of the Tail of the Grand Banks to the shelf breaks of both the western Newfoundland and eastern Scotian Shelves at 160 m. The first CEOF also indicates that some of the temperature anomalies at 160 m propagate into the Gulf of St. Lawrence through the Laurentian Channel (Fig. 2.17a). The first CEOF for the salinity anomalies at 160 m (not shown) has large-scale features similar to the CEOF for the temperature anomalies at the same depth. The time-mean period of the first CEOF is about 2.1 and 2.2 years, respectively, for the temperature and salinity anomalies in the intermediate layer over the WNFS-ESS subregion, with wavelengths of the order of 5000 km and phase speeds of about 7 cms^{-1}.

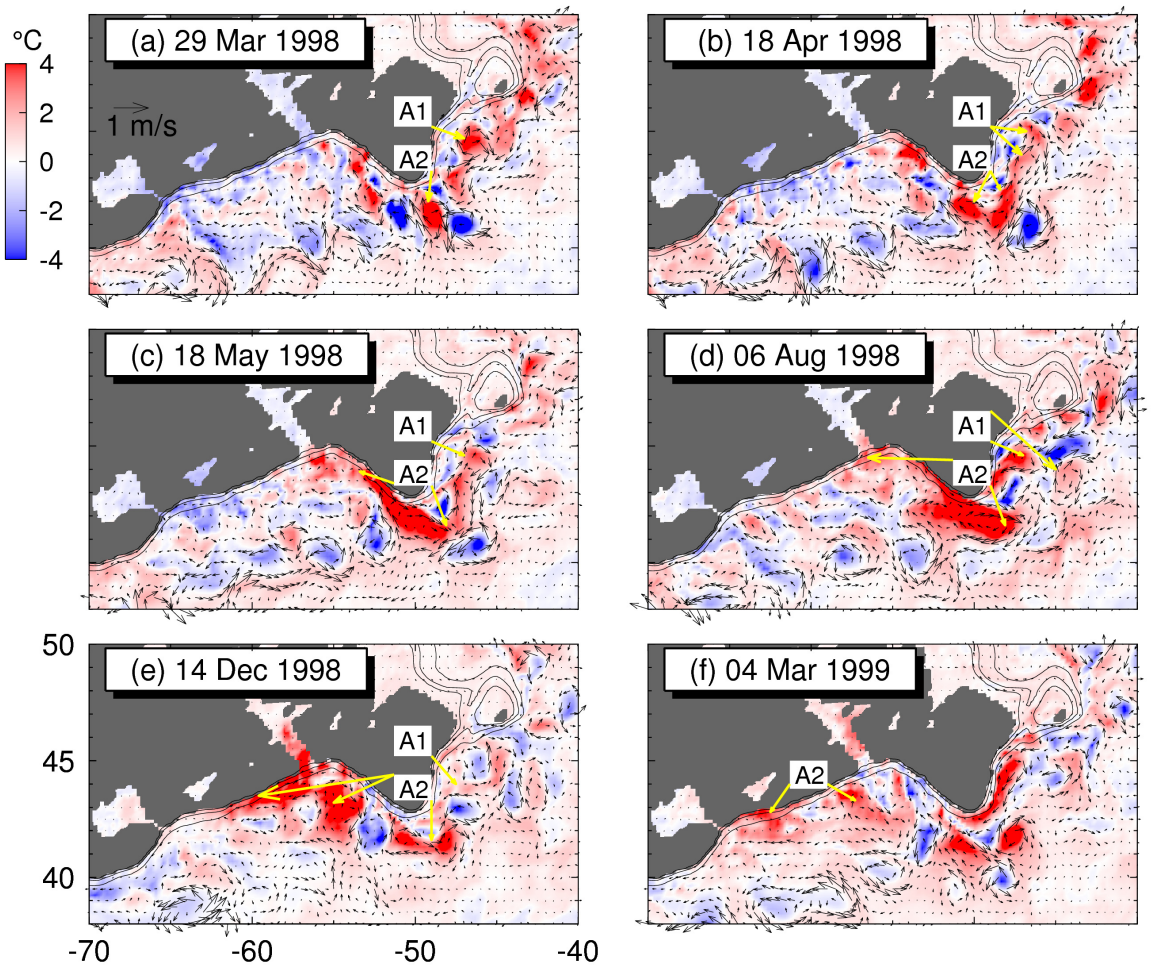

Figure 2.16. Temperature anomalies at 160 m over the Scotian Shelf and Newfoundland Shelf region at six different times in 1998–99: (a) 29 March 1998; (b) 18 April 1998; (c) 18 May 1998; (d) 6 August 1998; (e) 14 December 1998; and (f) 4 March 1999. A long-term monthly mean cycle has been removed from the five-day anomalies.

Table 2.3. Percentages of the total variance explained by the first three CEOFs extracted from the monthly mean temperature and salinity anomalies in the three layers over the subregion of the western Newfoundland Shelf, eastern Scotian Shelf and adjacent waters in the control run.

	Percentage of variance					
	Temperature			Salinity		
Layer	mode 1	mode 2	mode 3	mode 1	mode 2	mode 3
Upper (0-102 m)	28.3	12.7	10.0	19.4	13.2	10.1
Intermediate (102-350 m)	36.4	11.8	9.4	30.2	13.2	9.7
Lower (350-1215 m)	38.5	11.9	9.9	36.8	11.1	9.4

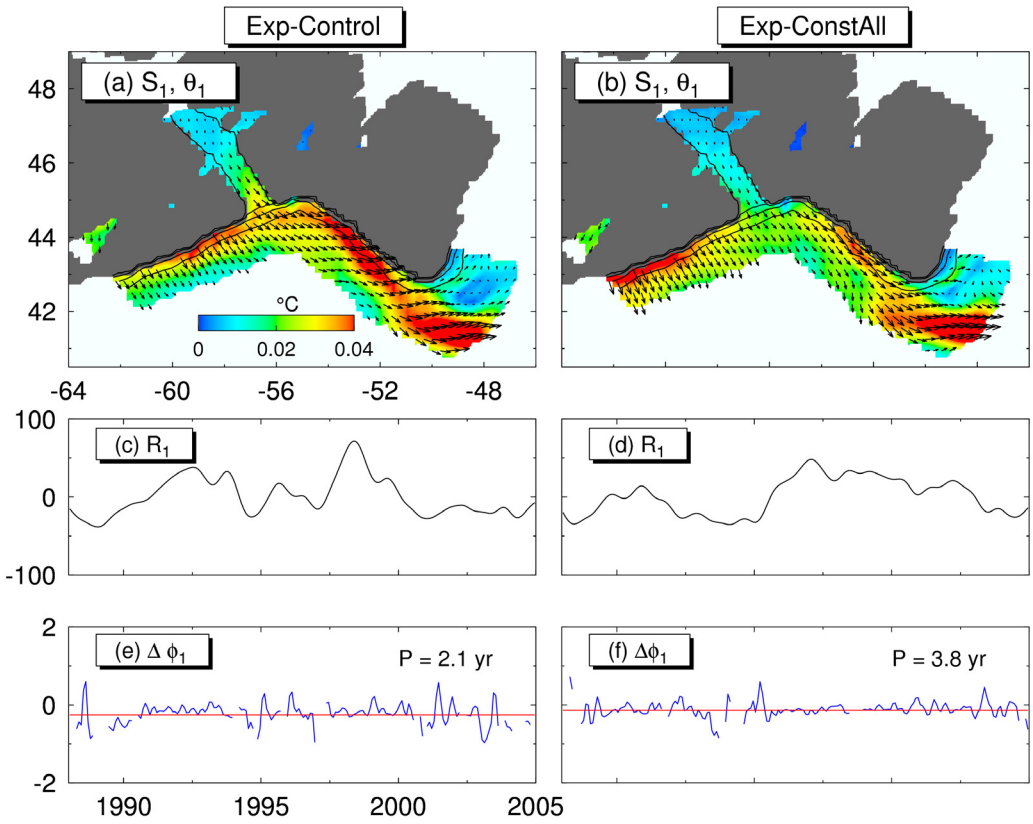

Figure 2.17. Distributions of spatial amplitude (S_1; colour image) and phase (θ_1; arrows), temporal amplitude (R_1) and temporal phase change ($\Delta\phi_1$) functions of the first CEOF for the monthly mean temperature anomalies at 160 m over the subregion of the western Newfoundland Shelf, eastern Scotian Shelf and adjacent waters in Exp- Control (left panels) and Exp-

ConstFluxes (right panels). The red line in the bottom panels represents the averaged temporal phase change.

The spatial amplitude and phase functions of the first CEOF in Exp-ConstAll (Fig. 2.17b) have similar horizontal features to those in the control run (Fig. 2.17a), which suggests that the interannual variability of sub-surface temperatures and salinity over the shelf break and the Slope Water region of this subregion in the control run can mostly be explained by the equatorward propagation of anomalies generated by the non-linear dynamics occurring to the south of the Tail of the Grand Banks.

The equatorward propagation is consistent with the evolution of the five-day temperature anomalies shown in Fig. 2.16, which demonstrates that the Gulf Stream carries temperature anomalies eastward (poleward) in the deep waters to the south of the Slope Water off the Scotian Shelf. Before reaching the deep waters to the south of the Tail of the Grand Banks, some anomalies (positive or negative) carried by the Gulf Stream turn northward and are entrained in the Labrador Current, and then propagate equatorward along the shelf break of the western Newfoundland Shelf and along the shelf break of the eastern Scotian Shelf.

The vertical distributions of the spatial amplitude functions of the first CEOF for temperature and salinity anomalies along transect BB′ (Halifax Line) feature large values in the subsurface waters between 20 and 300 m over the shelf break of the Scotian Shelf and between 60 and 100 m in Emerald Basin (Fig. 2.18). The temporal amplitude functions have similar temporal variability and are coherent for the different layers and also between temperature and salinity (insets in Figs 2.18e and 2.18f). The time-mean periods of the first CEOF range between 2.0 and 2.8 years in the three layers over this subregion.

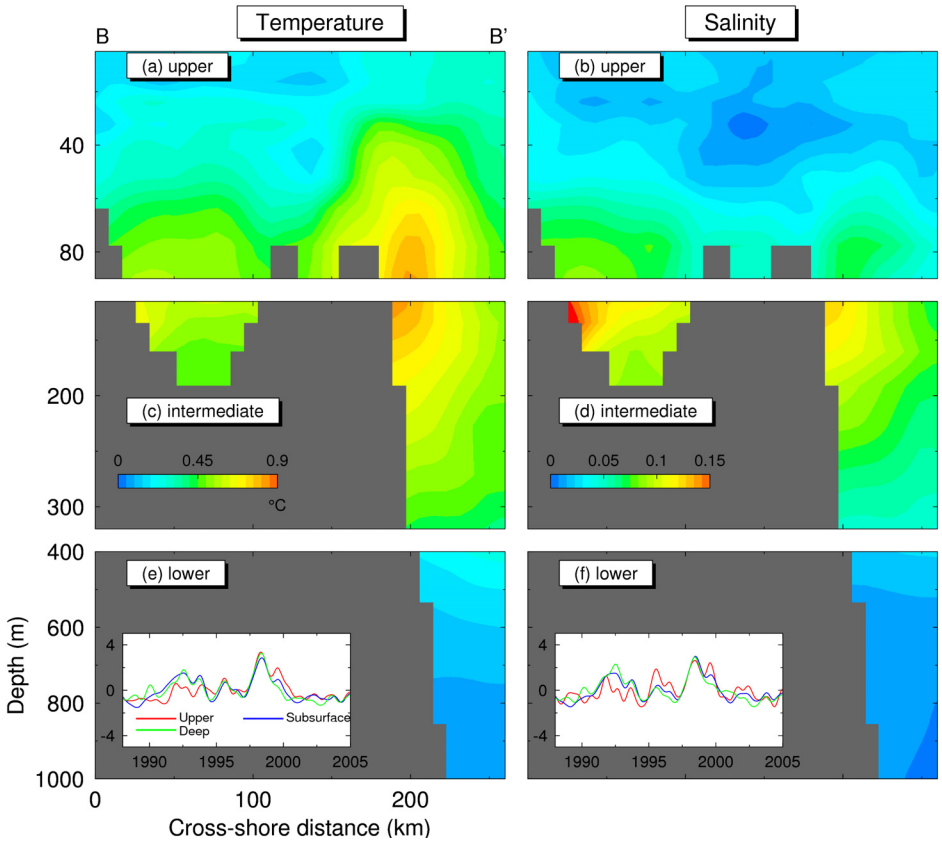

Figure 2.18. Vertical distributions of spatial amplitude functions (S_I) of the first CEOF for the temperature (left) and salinity (right) anomalies in the (a and b) upper, (c and d) intermediate and (e and f) lower layers along section BB′ (Halifax Line) on the Scotian Shelf.

2.5.3.4 The western Scotian shelf and Gulf of Maine

The percentages of the total variance explained by the first three CEOFs over this subregion range from 54% to 80% in the three vertical layers (Table 2.4). Figure 2.19 presents the spatial and temporal amplitude and phase functions of the first three CEOFs. In contrast to the WNFS-ESS subregion, the first CEOF over this subregion represents onshore (northwestward) propagations of the interannual variability from deep waters to the shelf region as indicated by the spatial phase vectors which rotate clockwise in the onshore direction (Fig. 2.19a). The first CEOF has large spatial amplitudes off Georges Bank, where anomalies from the Gulf Stream impinge on the shelf (see also Figs 2.16a and 2.16b). The second and third CEOFs differ from the first CEOF in that they represent

alongshelf advections of anomalies (Figs 2.19b and 2.19c). The time-mean periods are about 2.3–2.6 years for the first three CEOFs.

Table 2.4. Percentages of the total variance explained by the first three CEOFs extracted from the monthly mean temperature and salinity anomalies in the three layers over the subregion of the western Scotian Shelf, the Gulf of Maine and adjacent waters in the control run.

	Percentage of variance					
	Temperature			Salinity		
Layer	mode 1	mode 2	mode 3	mode 1	mode 2	mode 3
Upper (0-102 m)	41.8	18.5	7.5	39.7	17.3	7.2
Intermediate (102-350 m)	55.2	20.1	5.1	45.2	18.4	11.9
Lower (350-1215 m)	51.5	17.5	10.6	36.8	11.1	6.4

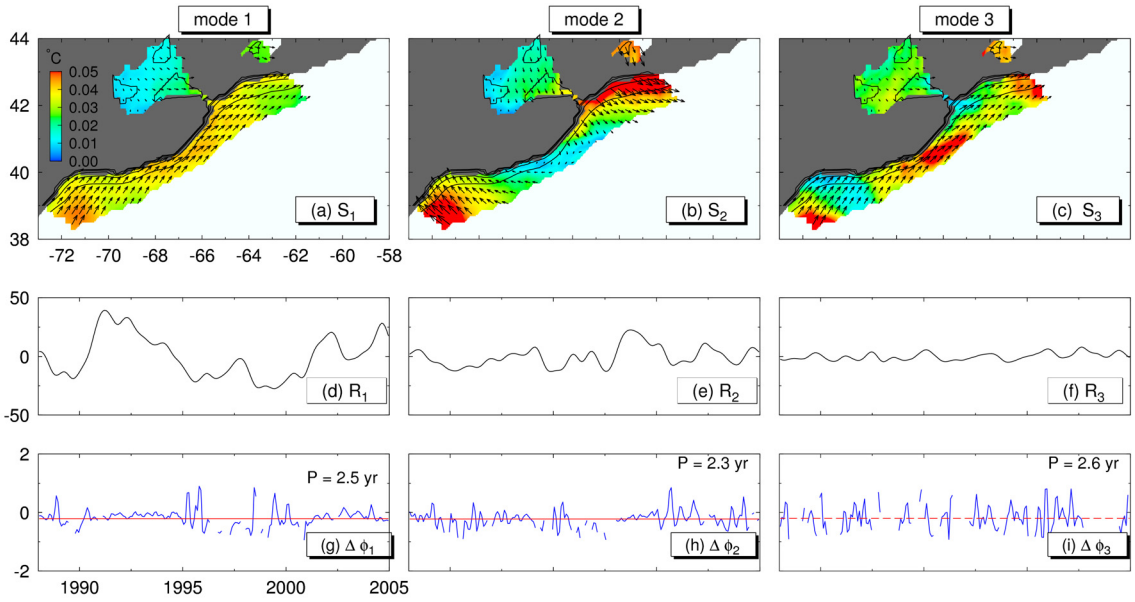

Figure 2.19. Distributions of spatial amplitude (S_1; colour image) and phase (θ_1; arrows), temporal amplitude (R_1) and temporal phase change ($\Delta\phi_1$) functions of the first (left panels), second (centre panels) and third (right panels) CEOFs for the monthly mean temperature anomalies at 160 m over the western Scotian Shelf and Gulf of Maine region. The red line in the bottom panels represents the averaged temporal phase change.

2.5.4 Influence of the Gulf Stream on the Interannual Variability over the Scotian Shelf and Slope

As discussed earlier, the non-linear dynamics of the flow play a very important role in driving interannual variability over the eastern Scotian Shelf and the southern Newfoundland Shelf. It was also shown that eddies and anomalies generated by the Gulf Stream or by its interaction with the Labrador Current affect the interannual variability in these regions. To establish the role of the Gulf Stream in the simulated interannual variability, I estimated the Gulf Stream position (GSP) index, along with the shelf-slope front (SSF) index based on model results in Exp-Control.

The GSP index is the (relative) north–south position of the 15°C isotherm at 200 m depth around the Gulf Stream region (Joyce et al., 2000). It should be noted that several different methods have been suggested for calculating the GSP index. For instance, Drinkwater et al. (1994) determined the GSP and the SSF indices based on the positions where the largest SST gradients are encountered in meridional sections crossing the Gulf Stream. Taylor (1996) used a principal component analysis to determine the GSP index. A comparison of the annual-mean GSP and SSF indices from model results (Drinkwater et al., 1994; Joyce et al., 2000) with the indices estimated from remote sensing data for the period 1992–2003 (Han, 2007) is presented in Fig. 2.20a. Satellite-derived estimates of the GSP index reveal that its range of variability is of the order of 0.8°, with the northernmost positions occurring around 1993 followed by a retreat to its southernmost position by 1996 and then a northward excursion until 2002. The variability displayed by the SSF index is qualitatively similar to that of the GSP index. Also, the model estimated indices match the observed trends of the GSP index having maximum northern excursions around 1992 and 2000 and a maximum southern excursion in 1996–1997.

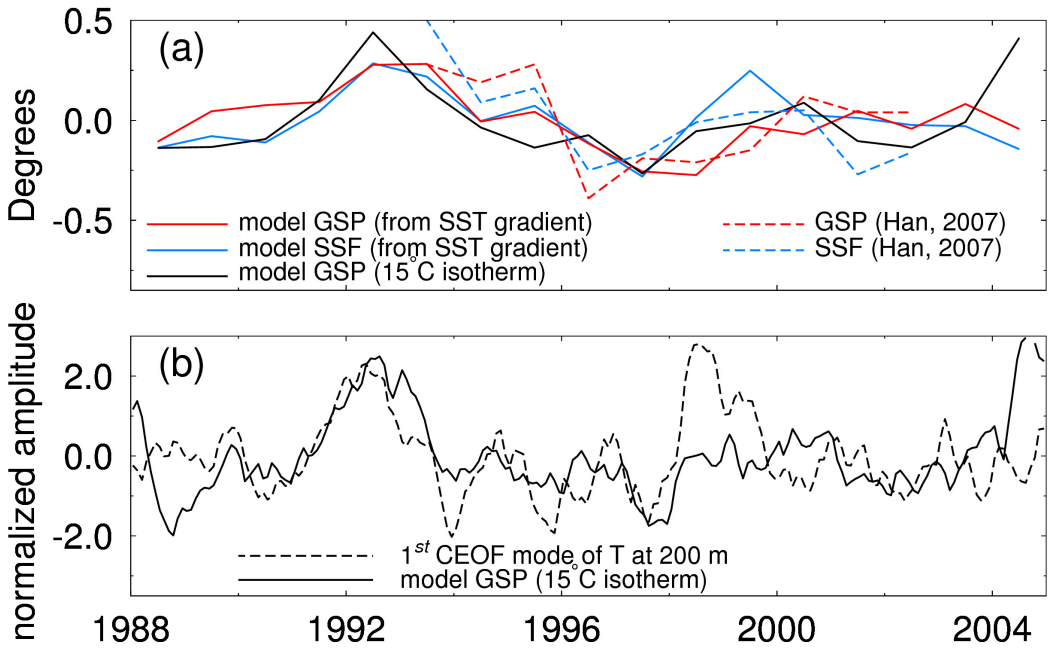

Figure 2.20. (a) Simulated annual-mean Gulf Stream (GSP) and shelf-slope front (SSF) position anomalies for the period 1988–2004 based on the methodologies used by Drinkwater et al. (1994) (SST gradients) and by Joyce et al. (2000) (15°C isotherm). Also shown are the GSP and SSF anomalies estimated from remote sensing data (data from Han (2007)) for the period 1992–2003; (b) standardized monthly time series of the first CEOF of temperature over the eastern Scotian Shelf at 200 m and the simulated GSP anomaly estimated from the position of the 15°C isotherm at 200 m depth.

When the Gulf Stream reached its northernmost positions (positive GSP index), the simulated interannual temperature over the Scotian Shelf and Slope region was warmer than during southern shifts of the Gulf Stream. Similarly, during positive GSP index periods the current anomalies along the shelf break and upper slope are in the northeast direction, indicating a reduced equatorward transport by the offshore branch of the Labrador Current. Therefore, there is evidence of connections between the meridional shifts of the Gulf Stream and the interannual variability of currents and hydrography over the Scotian Shelf and Slope Water region. Figure 2.20b shows the normalized time series of the GSP index and the first CEOF coefficients of interannual temperature anomalies at 200 m over the eastern Scotian Shelf. The interannual variabilities are remarkably similar for the two time series. A correlation analysis between the GSP index and the mode coefficients of the first CEOF reveals a maximum correlation of 0.4, which is statistically significant at the 95% confidence level. It should be noted that more study is needed to

examine how the Gulf Stream variability affects the interannual variability over the Slope Water region and the shelf break of the Scotian Shelf.

2.6 Summary and Conclusion

Circulation and hydrography over the eastern Canadian continental shelf (ECS) exhibit large seasonal and interannual variability (Petrie et al., 1992). I conducted a numerical investigation based on the NEMO coupled ocean–ice model (Madec, 2008) was conducted in this study to examine the main physical processes affecting the interannual variability over the ECS and adjacent waters using a regional ocean circulation model. The model uses a combination of the spectral nudging method and the smoothed semi-prognostic method with smaller-than-usual coefficients for both methods to reduce model seasonal bias and errors. By comparing model results with observations and previous numerical results in the literature, I demonstrated that the regional circulation model reproduces reasonably well the time-means and seasonal cycles in the 3-D circulation and hydrography over the ECS and adjacent waters. The model also has reasonable skill in simulating interannual variability over the ECS. This coupled ocean-ice model presented in this thesis is therefore ready-made to be used in future studies of ecosystem dynamics, and fisheries in the study region. It should also be noted that the horizontal resolution of our model is the same as that used by Smith et al. (2010) in the global ocean reanalysis from which the open boundary conditions are taken. Nevertheless, our model is fully prognostic in frequencies other than the seasonal cycle, which allows our model to be more suitable to conduct process studies in a wider range of frequency bands.

Four numerical experiments were conducted using the same model setup and parameters but with different combinations of model external forcing to investigate the role of monthly-mean anomalies in the surface forcing, boundary forcing and model internal dynamics, in the interannual variability of the 3-D circulation and hydrographic distributions. The model was integrated for 18 years, from 1987 to 2004, and model results for the last 17 years were presented in this chapter. A Complex Empirical

Orthogonal Function (CEOF) analysis was used to identify the propagating and standing patterns of interannual variability from the 3-D model results. The CEOF analysis was applied separately to model results over four different subregions of the ECS, mainly because of large regional differences in the 3-D circulation over these subregions.

It was demonstrated that the interannual variability in the model temperature and salinity over the Labrador Shelf and the northern Newfoundland Shelf in the control run was significantly affected by the interannual variability that propagates onto this subregion through the northern open boundary of the model. The interannual variability over the eastern Newfoundland Shelf and adjacent deep waters was also affected by the equatorward advection of the Labrador Current on the shelf and at the shelf edge. Over these two regions, significant correlations between the NAO index and the temperature and salinity anomalies were found with fresher and cooler conditions lagging intense winters (positive NAO index) in the northern hemisphere. Additionally, the variability over the eastern Newfoundland Shelf and adjacent deep waters is affected by the anomalies generated by the non-linear interaction between the equatorward Labrador Current and the poleward North Atlantic Current over the deep water region between the shelf edge of the eastern Grand Banks and the western edge of the North Atlantic Current. Once the anomalies were generated over this region, they moved slowly either poleward (northward) or equatorward (southward), depending on the competing influence of the Labrador Current and the North Atlantic Current. Similar processes also occurred for anomalies generated by the Gulf Stream in the deep waters to the south of the Tail of the Grand Banks.

The interannual variability over the western Newfoundland Shelf, Scotian Shelf, and adjacent waters, particularly at the shelf edge of the subregion, is affected by the variability that is advected into this subregion by the equatorward Labrador Current. The correlation between the monthly mean hydrographic anomalies over this subregion and those at the northern open boundary (including Labrador Current anomalies transport), however, is rather low. It was found that the interannual variability in this region has larger amplitudes in the subsurface waters, which is in agreement with Petrie and

Drinkwater (1993). The analysis of model results demonstrates that the variability in this subregion, particularly over the Slope Waters off the Scotian Shelf is significantly affected by the anomalies generated by the Gulf Stream, which are entrained into the continental slope of the southern Newfoundland Shelf and advected into this subregion by the Labrador Current. The Gulf Stream and its north–south excursions seem to play a role in the interannual variability of the hydrographic properties, and perhaps transport variability, of the Labrador Current along the shelf-break region south and west of the Grand Banks.

There are two important advective processes that affect the interannual variability of the circulation and hydrography over the western Scotian Shelf and the Gulf of Maine subregion. The first is the onshore propagation of the interannual variability, produced by the Gulf Stream, from deep waters to this subregion in the upper water column of less than 300 m. The second is the equatorward propagation of the interannual variability along the shelf break from the Scotian Shelf to this subregion. This particular interannual variability is originated over the deep waters close to the Tail of the Grand Banks.

CHAPTER 3

STUDY ON SUBTIDAL CIRCULATION AND VARIABILITY IN THE GULF OF ST. LAWRENCE, SCOTIAN SHELF, AND GULF OF MAINE USING A NESTED-GRID SHELF CIRCULATION MODEL[1]

3.1 INTRODUCTION

The study region of this chapter comprises the Gulf of St. Lawrence, the Scotian Shelf and the Gulf of Maine (GSL-SS-GOM), which is an interconnected estuarine-shelf system (Fig. 3.1). Circulation and associated variability over this region are affected by irregular bathymetry, highly varying tidal, oceanic and atmospheric forcing and large river discharge (Koutitonsky and Bugden, 1991; Hannah et al., 2001). The shelf waters in the upper water column in the region are relatively fresh and influenced significantly by the net sea surface heat/freshwater fluxes and river discharge. The vertical distribution of temperature in winter features cold waters extending from the surface to intermediate depths in the region (GSL-SS-GOM) due to cooling at the surface and winter convection events. Seasonal heating of the upper waters (~0-30 m) during summer months turns this two-layer structure into a three-layer structure in the vertical, with a cold-intermediate layer lying between two relatively warm layers (Banks, 1966; Drinkwater and Gilbert, 2004; Smith et al., 2006).

[1] Urrego-Blanco, J. and J. Sheng. 2014a. Study on subtidal circulation and variability in the Gulf of St. Lawrence, Scotian Shelf and Gulf of Maine using a nested-grid shelf circulation model. *Ocean Dyn*. doi: 10.1007/s10236-013-0688-z.

Previous studies demonstrated that the general circulation in the upper layer of the GSL is cyclonic (Han et al., 1999). The other notable circulation features in the GSL include the Gaspé Current flowing around the Gaspé peninsula (Koutitonsky and Bugden, 1991; Sheng, 2001); the Anticosti gyre to the west of Anticosti Island; and a coastal jet that enters the GSL through the Strait of Belle Isle and runs westwards along Québec's northern shore (Fig. 3.1b). Over the eastern part of Cabot Strait a flow consisting of part of the inshore Labrador Current and part of the offshore Labrador Current enters the GSL (El-Sabh, 1976; Koutitonsky and Bugden, 1991). Over the western side of the Strait there is a two-layer circulation structure in the vertical with a seaward flow in the upper 50-100 m and a landward flow into the GSL in the lower layer. The low-salinity estuarine waters emanate from the GSL flow southwestward to form the Nova Scotian Current. Over the Scotian Shelf, the main circulation features include the Nova Scotian Current flowing along the coast and a shelf break jet flowing southwestward (Fig. 3.1b). The Nova Scotian Current enters the GOM and flows around coastal waters off Cape Sable, to form a cyclonic coastal circulation in the Bay of Fundy (Xue et al., 2000). Another source of shelf waters into the GOM is a northwestward inflow along the eastern side of the Northeast Channel. This inflow was found to peak in spring with a tendency for cross-channel flows or crossovers towards Georges Bank in winter (Smith et al., 2003). Previous studies also indicated that the circulation in the GOM and the Bay of Fundy is influenced significantly by near-resonant tides (Garrett, 1972) and by mixing and tidal rectification on Georges Bank (Loder and Greenberg, 1986).

Several studies have been conducted in the past to improve our understanding of the circulation and associated variability in the study region using available oceanographic observations (El-Sabh, 1976; Drinkwater et al, 1979; Smith and Schwing, 1991; Koutitonsky and Bugden, 1991; Sheng and Thompson, 1996; Loder et al., 1998) and numerical ocean circulation models (Han et al., 1999; Hannah et al., 2001). Sheng (2001) studied the dynamics of the Gaspé Current and circulation in the northwest GSL. Ohashi et al (2009) used a nested-grid baroclinic circulation model to study the variability of near-bottom currents on the Scotian Shelf. Saucier et al. (2003) used a numerical model of the GSL to study the seasonal hydrography and ice cover in the region. Many

important issues however remain to be addressed, such as regional connections for the circulation and hydrography between sub-regions of the GSL-SS-GOM, and the nature of the variability in different frequency bands. This chapter will address some of these issues based on the simulated subtidal circulation and hydrographic distributions over the region. The main objectives of this chapter are: 1) to assess the performance of a shelf circulation model developed recently for the GSL-SS-GOM; and 2) to examine main physical processes (such as atmospheric forcing, river runoff, and influences from deeper waters) affecting subtidal circulation and associated variability in this region using the validated shelf circulation model.

The structure of this chapter is as follows. The nested-grid shelf circulation model for the GSL-SS-GOM is presented in Section 3.2 and the model performance is assessed in Section 3.3. In Section 3.4 main physical processes affecting circulation variability in the region are discussed based on model results. Summary and conclusions are presented in Section 3.5.

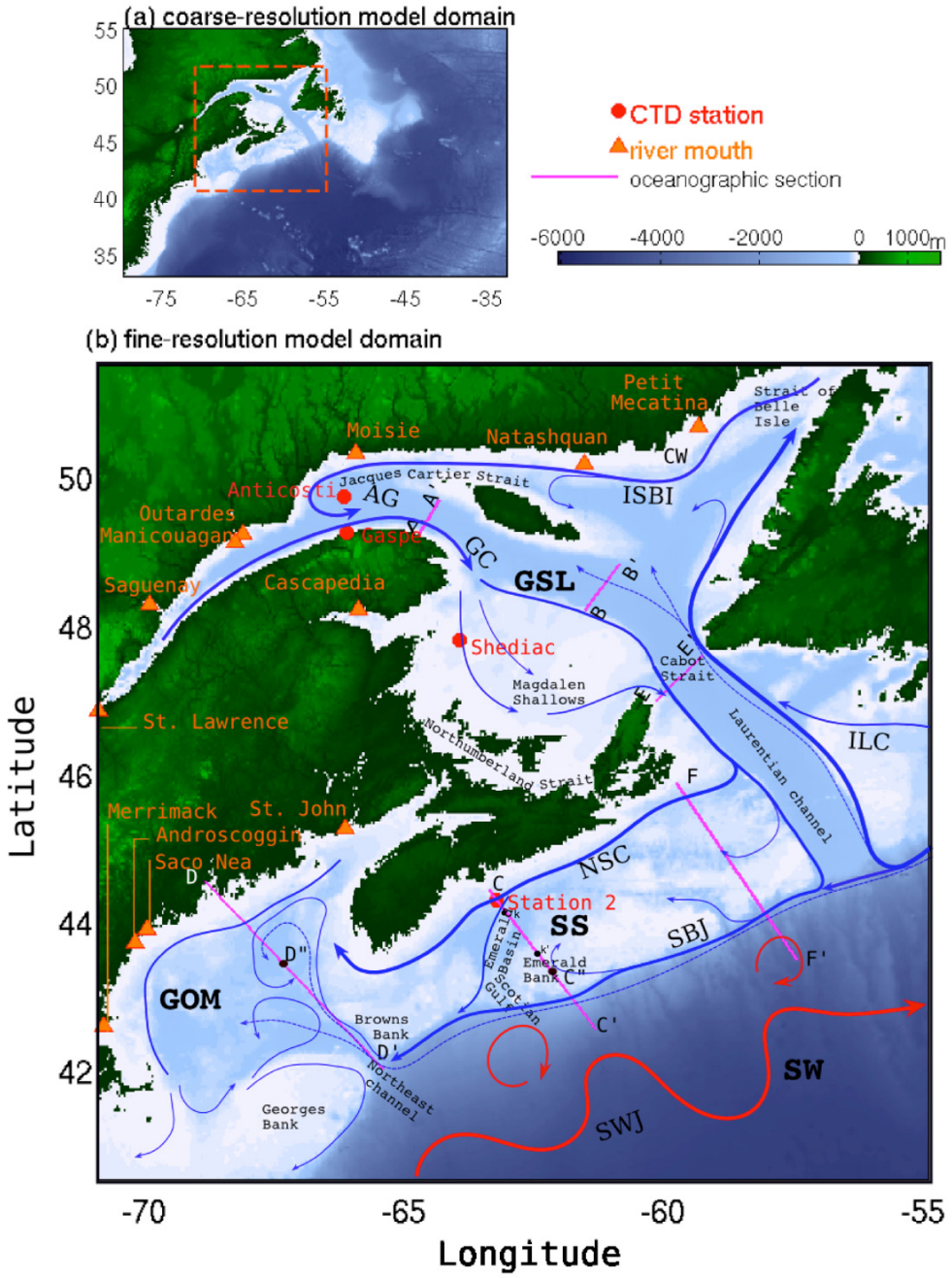

Figure 3.1. (a) The domain and bathymetry of the coarse-resolution parent model of the Northwest Atlantic, with the child model domain marked by *dashed lines*. (b) Schematic of the general circulation and bathymetry of the child model for the Gulf of St. Lawrence, Scotian Shelf, and Gulf of Maine. Major rivers in the study region, hydrographical stations used for validation of model results, and transects used in the analysis of model results are marked in **b**. Abbreviations are used for the Gulf of St. Lawrence (GSL), Scotian Shelf (SS), Gulf of Maine (GOM), Slope Water (SW), inflow through the Strait of Belle Isle (ISBI), Anticosti Gyre (AG), Gaspé Current (GC), inner branch of the Labrador Current (ILC), shelf break jet (SBJ), Nova Scotian Current (NSC), and Slope Water Jet of the Gulf Stream (SWJ)

3.2 Model Setup and Forcing

The nested-grid shelf circulation model used in this study is based on the NEMO (Nucleus for European Modelling of the Ocean) modelling system (Madec, 2008), which consists of the primitive equation Océan PAralléllisé (OPA 9) ocean circulation model and the dynamic-thermodynamic Louvain-Le-Neuve2 (LIM2) sea-ice model (Timmermann et al., 2005). The nested-grid model includes a coarse-resolution parent model (PM) covering the northwest Atlantic Ocean between 34°N and 55°N and between 33°W and 80°W, and a fine-resolution child model (CM) covering the GSL-SS-GOM between 41°N and 52°N and between 55°W and 72°W. The PM uses a 1/4° resolution and 40-minute time step. The CM has a horizontal resolution of 1/12° and uses a 10-minute time step. Both the PM and CM use horizontal curvilinear grids and bathymetries based on Earth Topography 2 (Smith and Sandwell, 1997). Both models have 46 z-levels with partial cells in the vertical with a vertical resolution increasing from 3 m in the upper layer to about 250 m in the lowest layer. The CM is embedded inside the PM using a two-way nesting technique to exchange information between the two models (Fig. 3.2). In the basic configuration (Control Run) the initial conditions are the state of rest, with the initial model temperature and salinity to be the monthly-mean hydrography of Geshelin et al. (1999). The nested-grid model uses the spectral nudging (Thompson et al., 2007) and semi-prognostic methods (Sheng et al., 2001) to reduce seasonal bias and drift in the model. The sea surface salinity in the model is also restored to the climatological monthly-mean surface salinity. The subgrid-scale horizontal mixing of tracers and momentum, as well as the subgrid-scale vertical mixing use the same parametrizations as described in Chapter 2 and also in Urrego-Blanco and Sheng (2012).

The nested-grid model in the Control Run is forced by wind stress and net heat/freshwater fluxes at the sea surface which are calculated from 6-hourly wind speeds, specific humidity and air temperature, 12-hourly short and long wave radiation, and monthly-mean precipitation extracted from the 2° resolution atmospheric reanalysis data

produced by Large and Yeager (2004). The formulation used to calculate the momentum, heat and freshwater fluxes at the sea surface, and at the ice-ocean interface are the same as in Chapter 2 and also in Urrego-Blanco and Sheng (2012).

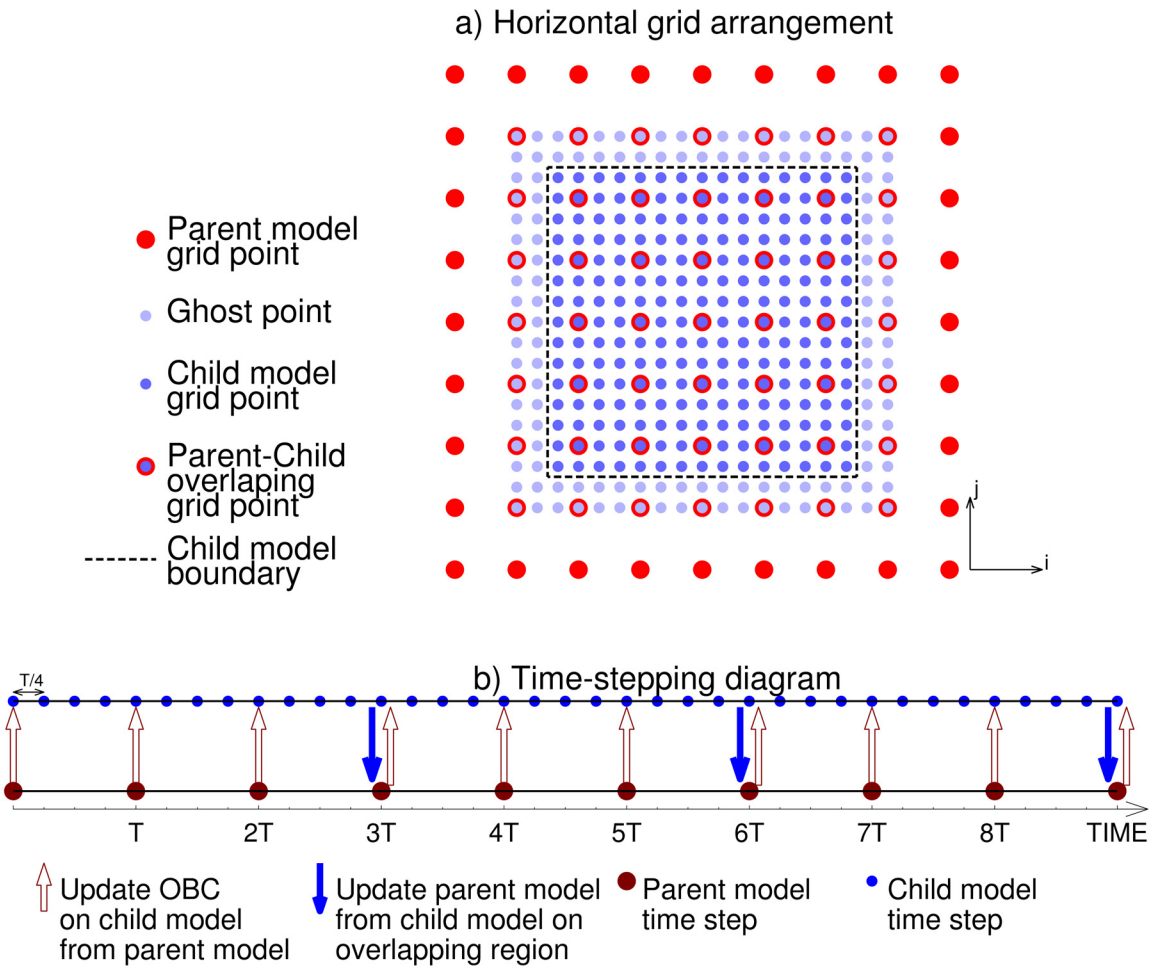

Figure 3.2. Schematics of the two-way nesting technique used in this study. (a) Horizontal arrangement of the nested-grid model and (b) time-stepping diagram showing the two-way information exchange between the parent and child model grids. The ghost points around the CM boundary are used for easy implementation of the CM boundary conditions.

The nested-grid model is also forced by freshwater discharge from 12 major rivers in the GSL-SS-GOM region (Table 3.1), using the observed monthly-mean time series of freshwater discharge extracted from the global monthly streamflow dataset of Dai et al. (2009). The monthly-mean discharge of each river is specified in terms of precipitation over a specific influence area in the model. The influence area is determined based on a

radius of influence, which is proportional to the monthly river discharge (see the Appendix B for details).

Table 3.1. Main rivers and annual mean discharges into the Gulf of St. Lawrence, Scotian Shelf, and Gulf of Maine system during the period 1987–2005 (Dai et al. 2009).

River	Annual mean discharge (10^3 m^3 s^{-1})
St. Lawrence (including Ottawa and St. Maurice)	9.08
Saguenay	1.47
Manicouagan	1.01
Outardes	0.38
Moisie	0.41
Natashquan	0.35
Petit Mecatina	0.49
Cascapedia	0.06
St. John	0.98
Saco Nea	0.03
Androscoggin	0.03
Merrimack	0.02

The open boundary conditions in the PM are taken from the 5-day mean ocean reanalysis data of Smith et al. (2010) using the adaptive open boundary condition as described in Chapter 2. The lateral open boundary conditions for the CM are taken from the interpolation of the prognostic variables (such as currents, temperature, salinity, and sea ice concentrations and velocities) of the PM using the two-way nesting technique to be discussed below (Debreu et al., 2008).

It should be noted that there is no an explicit implementation of tidal forcing in the model configuration available for this study. Tides are, however, important over the lower St. Lawrence Estuary, the Bay of Fundy, and Georges Banks. The combined use of

the spectral nudging and semiprognostic methods, as well as the flow-dependent parameterization of lateral mixing account indirectly for the effect of tidal rectification on the density distributions in the study region. Therefore, the present model configuration is suited to simulate the subtidal circulation in the GSL-SS-GOM.

In the configuration used in this study, the PM is integrated for two consecutive time steps. The prognostic variables of the PM are linearly interpolated in time and space to obtain lateral open boundaries of the CM at four CM time steps between the consecutive PM time steps (Fig. 3.2). The CM uses these interpolated variables as lateral open boundaries and is integrated for four child model time steps. A new integration of the PM takes place and a new interpolation cycle of its prognostic variables starts both in space and time to obtain new open boundaries for the CM. At every three PM time steps, the prognostic variables of the PM are updated using the interpolated variables of the CM over the overlapping region between the two models. In this way, the PM takes information from the CM and benefits from the finer-resolution results produced by the CM.

The nested-grid model is integrated for 18 years from 1987 to 2005, and the last 17-year model results are used in this study. Analysis and comparison of model results in three numerical experiments are used to identify the main processes affecting the circulation and variability in the region. The three numerical experiments are:

Experiment Control Run: The model configuration, the atmospheric forcing and open boundary conditions described above are used in this experiment.

Experiment ConstFluxes: In this experiment the atmospheric forcing, including wind speeds, temperature and specific humidity of the air above the sea surface, long and shortwave radiation, and precipitation are set to be time invariant and equal to the time-means of the fields averaged over 18-years between 1987-2005. As a result, the temporal variability generated by the model can only be caused by the internal dynamics and the

variability of the flow through the model open boundaries, assuming the systematic model drift is small.

Experiment NoBI: In this experiment the bathymetry at the Strait of Belle Isle is modified to block the flow between Labrador Shelf and the GSL. The circulation and hydrography inside the GSL produced by the CM in this experiment are not affected directly by the inflow associated with the coastal Labrador Current through the Strait of Belle Isle.

3.3 MODEL VALIDATION

The performance of the nested-grid model in the Control Run is assessed in this section with an emphasis on the accuracy of the CM in simulating circulation and associated variability over the GSL-SS-GOM region. The performance of the PM was previously assessed in Chapter 2 where I demonstrated that the PM has good skill in simulating the seasonal cycle and interannual variability of temperature and salinity and the time-mean and seasonal circulation over the eastern Canadian shelf (ECS). The simulated time-mean circulation produced by the PM features the general southwestward flow over the Scotian Shelf and a relatively weak cyclonic circulation over the GOM. The PM, however, performs less well in simulating the coastal circulation such as the Gaspé Current and the Nova Scotian Current as well as the flows through the Strait of Belle Isle and Cabot Strait, due mainly to the relatively coarse horizontal resolution used in the PM. The time-mean surface geostrophic currents produced by the PM (red arrows in Fig. 3.3b) feature a northeastward flow in the Slope Water region and a southeastward flow along the shelf break of the Scotian Shelf, which are in reasonably good agreement with the altimetric and drifter-derived estimates as discussed in Chapter 2. As mentioned in Chapter 2, the altimetry-derived geostrophic circulation should be used with caution due to errors associated with the accuracy of satellite measurements in coastal regions.

Urrego-Blanco and Sheng (2012) quantified the fit between the simulated currents and the altimetry-derived surface currents shown in Fig. 3.3 using ε^2 defined in Eq (2.5). The ε^2 value between the observed geostrophic estimates and the model calculated surface geostrophic currents shown in Fig. 3.3 is about 0.71, indicating that the PM has certain skill in reproducing the time-mean surface geostrophic circulation over the study region.

The top panels in Fig. 3.4 present the time-mean normal velocities produced by the PM at the transects of Anticosti, Cabot and Halifax Line (see Fig. 3.1). At the Anticosti transect (Fig. 3.4a), the observed main features of the Gaspé Current are not well resolved by the PM. Instead the PM generates a weak eastward flow in the top 30 m of the water column along the entire transect. At Cabot Strait the northward inflow on the eastern side in the PM is very weak and the jet flows detached from the coast (Fig. 3.4b). At the Halifax Line, the observed features of the Nova Scotian Current are not very well resolved by the PM (Fig. 3.4c). The rest of this section focuses on the performance of the CM. Unless otherwise specified, only results produced by the CM in the Control Run are used in the assessment.

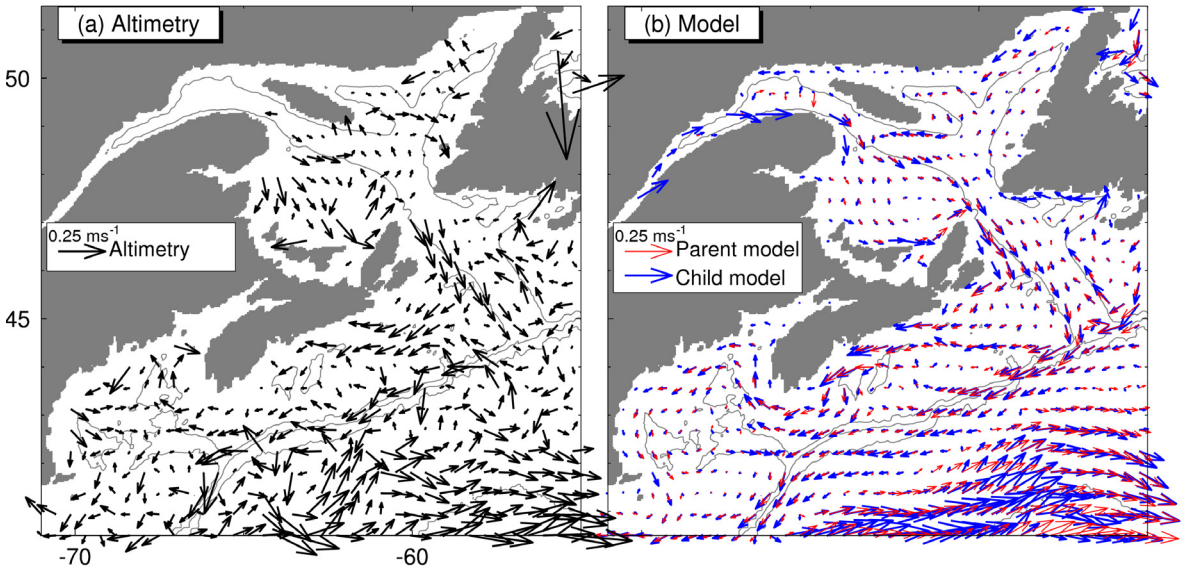

Figure 3.3. Comparison of (a) the altimetry-derived (*black arrows*) and (b) the simulated time-mean surface geostrophic currents in the 5-year period of 2000–2004 calculated from the time-mean sea surface elevations produced by the parent (*red*) and child (*blue*) models in the Control Run experiment.

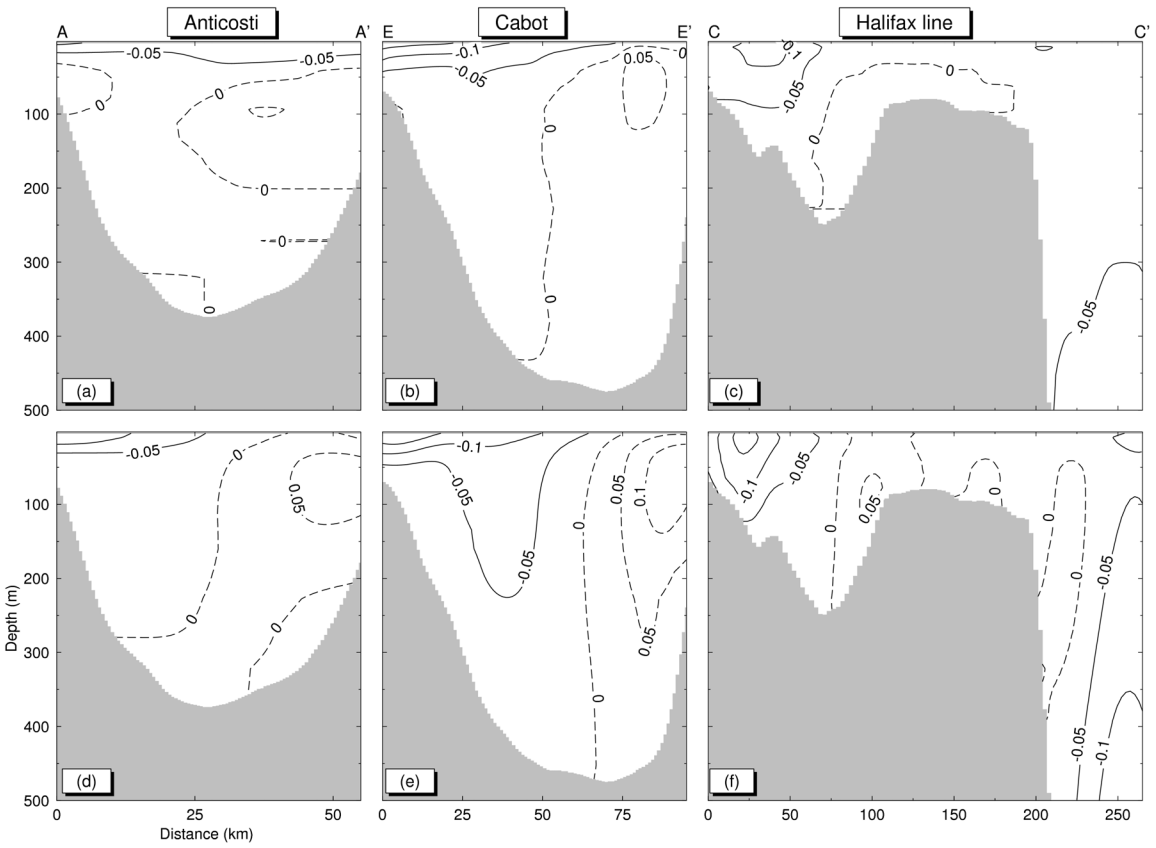

Figure 3.4. Vertical structures of simulated time-mean normal velocities in the 5-year period of 2000–2004 produced by the parent (*upper panels*) and child (*lower panels*) models in the Control Run at the transects of Anticosti (*left*), Cabot (*middle*), and Halifax Line (*right*).

3.3.1 Model performance in simulating time-mean circulation and hydrography

I first assess the performance of the CM in simulating the time-mean circulation over the GSL-SS-GOM during the 5-year period 2000-2005. The time-mean surface geostrophic circulation over the GSL produced by the CM (Fig. 3.3b) features a westward flow along Québec's north shore; a cyclonic circulation over the northwestern GSL to the west of Anticosti Island; and a recirculation of the flow southeast of Anticosti Island. The CM also generates a narrow inflow over eastern Cabot Strait and a relatively broad outflow over western Cabot Strait. The CM also generates a southwestward flow along the Scotian Shelf and a cyclonic circulation in the GOM. All of these time-mean

circulation features produced by the CM are in good agreement with the altimetry-derived surface geostrophic currents (Fig. 3.4a). The ε^2 value is about 0.81, indicating that the CM has good skill in simulating the time-mean surface geostrophic circulation in the GSL-SS-GOM. It should be noted that the ε^2 value for the CM is higher than the value for the PM. One of the most plausible reasons is that the estimates of altimetry-derived surface geostrophic currents are less accurate over coastal waters than deep waters of the GSL-SS-GOM (Higginson et al., 2011). The other plausible reason is that the CM with fine horizontal resolution resolves the currents more accurately than those inferred from altimetric measurements. Therefore any slight shift in the location of the currents can affect the values of the ε^2 metric.

In comparison with the results produced by the PM, the CM better reproduces the vertical structures of time-mean normal currents at transects of Anticosti, Cabot and Halifax Line (Fig. 3.4). At the Anticosti transect the simulated Gaspé Current runs southeastward with large time-mean velocities in the top 30 m over the western part of the transect. Over the eastern side of the transect, close to Anticosti Island the CM generates a relatively weaker time-mean flow that runs northward in the entire water column. The time-mean flow at Cabot Strait is also more realistically reproduced by the CM than the PM based on comparisons of model results with observations discussed in the literature. The time-mean outflow in the CM is more concentrated on the southwestern side of the Strait with the maximum time-mean currents near 0.20 ms^{-1} in the upper 10 m. The inflow into the GSL on the northeastern side of Cabot Strait produced by the CM features a coastal jet with the maximum velocities of about 0.13 ms^{-1} centered at about 70 m depth (Fig. 3.4e). The structure of the Nova Scotian Current simulated by the CM has a time-mean maximum velocity of 0.18 ms^{-1} in the top 20 m at about 20 km from the shore.

The total volume transports are estimated from the monthly-mean currents produced by the CM at the Strait of Belle Isle, Cabot Strait and Halifax Line. At the Strait of Belle Isle the annual mean westward transport in the CM is about 0.18 Sv, with maximum and minimum monthly-mean transports of about 0.39 Sv in January and 0.03 Sv in July,

respectively. From hydrographic measurements, Petrie et al. (1988) estimated the westward transport through the Strait to be about 0.13 Sv for July-October and 0.3 Sv for January-May. Other numerical studies estimated the transport to be about 0.42 Sv in winter and 0.15 Sv in spring (Saucier et al., 2003). All of these previous estimates are of the same order of magnitude with the transport through the Strait produced by the CM. At western Cabot Strait the annual mean southward transport produced by the CM is about 0.91 Sv with the maximum monthly-mean transport of about 1.67 Sv in January and minimum of about 0.39 Sv in July. By comparison, the annual mean northward transport at eastern Cabot Strait is about 0.72 Sv, with the maximum monthly-mean of about 1.24 Sv in January and minimum of about 0.32 Sv in August. The simulated transports at Cabot Strait are in rough agreement with the annual mean of 0.50 Sv estimated by El-Sabh (1977). Over the inner Scotian Shelf, Loder et al. (2003) estimated the westward transport of the Nova Scotian Current shoreward of the isobath 244 m to be about 0.75 Sv. The simulated annual mean transport of the Nova Scotian Current in the CM is about 0.66 Sv with the maximum monthly-mean transport of 0.98 Sv in January and minimum of 0.45 Sv in September, which are also in rough agreement with measurements made by Anderson and Smith (1989), who estimated the transport of the Current to be about 1.2 Sv in December 1985 and 0.66 Sv in March 1986.

Figure 3.5a, b show the time-mean distributions of salinity produced by the CM. The simulated time-mean salinity during the 17-year period 1988-2005 is characterized by relatively low salinity in the GSL-SS-GOM and high salinity in the deep ocean, which agree very well with the observed climatologies (Geshelin et. al., 1999) and previous numerical results (Saucier et. al.,2009). Over the GSL the simulated time-mean near surface salinities have values of less than 31 over the western side and between 31 and 32 over the eastern side. Over the SS and the GOM the time-mean salinities are about 32 near the surface and slightly higher in sub-surface waters (Fig. 3.5b). Over Emerald Basin and in the deep basins in the GOM the simulated salinity is influenced by relatively saltier waters of oceanic origin which are transported to these shelf areas through the deep channels in the Scotian Shelf and the Northeast Channel, respectively.

The simulated time-mean water temperatures are generally below 12°C in the GSL-SS-GOM and relatively warmer in the deep ocean (Figs. 3.5c, d). The near-surface temperature in the study region is generally warmer than the sub-surface temperature in the CM, which is consistent with the presence of a cold intermediate layer in the region. Over the GSL, the time-mean near-surface temperature produced by the CM is relatively uniform with slightly colder conditions along the coastal waters off Quebéc's northern shore. Over the eastern SS and inner parts of the central SS the simulated time-mean near-surface temperature is about 7°C which is relatively low in comparison with temperatures over the central Scotian Shelf and the GOM where temperatures are about 9°C. The simulated time-mean temperature in the subsurface waters are also warmer in the GOM and in Emerald Basin (~5°C) than over the eastern and inner Scotian Shelf (~2.5°C), due to the influence of deep oceanic waters that flow onto the shelf regions through deep channels. The contour lines in Fig. 3.5 show the absolute difference between the time-mean observed climatological and simulated temperature and salinity. Over the shelf, the absolute differences are about 0.25 for salinity and about 0.5-1°C for temperature. In deep waters, the differences are slightly higer, with values up to 0.5 for salinity and 2°C for temperature. In general, the distributions of the time-mean near-surface and sub-surface temperature and salinity produced by the CM are in good agreement with observed climatologies (Geshelin et. al., 1999).

3.3.2 Model performance in simulating seasonal-mean currents

I next assess the performance of the CM in simulating the seasonal-mean circulation using available current-meter observations. Since current-meter observations are sparse in time and space, I compare the simulated and observed seasonal-mean currents only in two vertical layers: the upper layer at 5-30 m and the lower layer at 30-100 m. The vertically averaged seasonal-mean currents in these two layers were calculated from the 17-year results produced by the CM. The observed seasonal-mean currents were estimated from current-meter observations archived by the Department of Fisheries and Oceans of Canada (DFO) (Gregory, 2004). Only moored current-meter observations with continuous record lengths longer than 14 days during the period 1960-2004 were used in

this study. The observations were interpolated onto a horizontal grid with a resolution of 1/4°, and vertically averaged over the 0-30 m and 30-100 m layers.

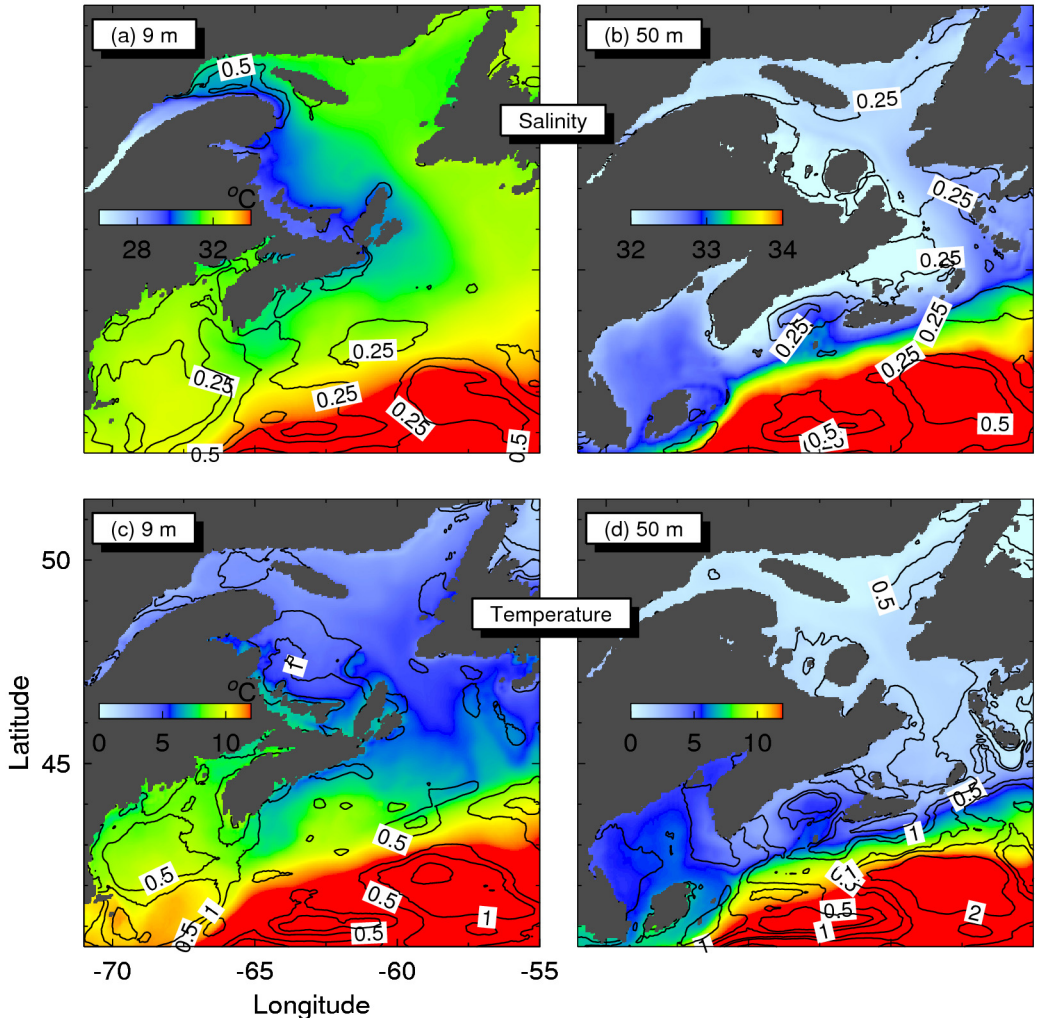

Figure 3.5. Time-mean near-surface (9 m) and subsurface (50 m) salinity (*upper panels*) and temperature (*lower panels*) calculated from results in the Control Run produced by the CM in the period of 1988–2005. Black contours and associated numbers are the absolute differences between climatological and simulated time-mean salinity and temperatures.

Figures 3.6 and 3.7 show the simulated (red and blue vectors) and observed (black vectors) seasonal-mean circulation in the 5-30 m and 30-100 m layers over the GSL-SS-GOM, respectively. The CM reproduces the main circulation features in the GSL such as the Gaspé Current; a southeastward flow along Magdalen Shallows and the inflow from

the Labrador Shelf through the Strait of Belle Isle. The inner model also reproduces the cyclonic circulation of the Anticosti gyre; and the inflow through eastern Cabot Strait into the GSL. Over the SS, the CM reproduces the Nova Scotian Current and the shelf break jet of the Scotian Shelf, and a cyclonic circulation in the inner GOM and an anticyclonic flow over Georges Bank. The circulation over Georges Bank is affected by tidal rectification, which is not explicitly included in the model. The use of spectral nudging, however, ensures the correct distribution of water masses (section 3.3.3) and the associated seasonal circulation in the region.

I also use the ε^2 value to quantify the fit between the simulated and observed seasonal-mean currents (insets of Figs. 3.6 and 3.7) by setting U and V in Eq. (3.1) to be the seasonal-mean currents. The ε^2 values are between 0.57-0.93 in winter (Dec-Feb) and 0.58-0.67 in fall (Sep-Nov), indicating that the CM performs well in simulating the winter-fall circulation. The ε^2 values are between 1.36 and 2.07 in spring (Mar-May), and between 0.70 and 1.57 in summer (Jun-Aug), indicating relatively larger differences between observations and model results. In general, the largest discrepancies between the seasonal-mean simulated and observed currents occur over areas along the shelf break and on Georges Bank. Over these regions, the time-mean observed currents could be affected by tidal rectification and the complex mesoscale dynamics in the region, both of which are not resolved by the current model setup. The other possible explanation is that the CM resolution is still not fine enough to resolve the strong currents over these regions.

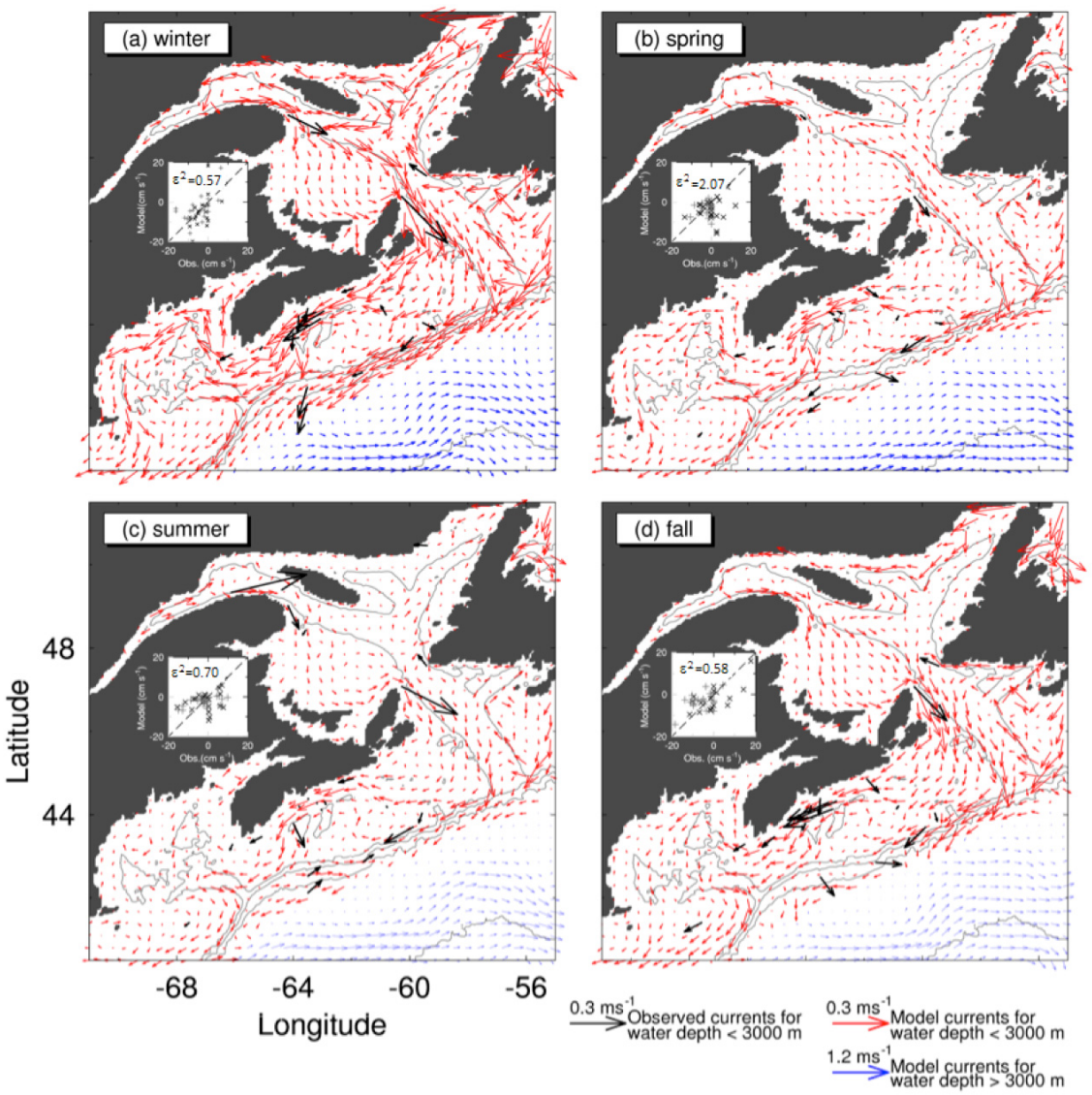

Figure 3.6. Comparison of simulated and observed seasonal-mean currents in the upper layer (0–30 m) of the GSL-SS-GOM region. *Red arrows* indicate velocity vectors over regions with water depths shallower than 3,000 m, and *blue arrows* indicate velocity vectors over regions deeper than 3,000 m. Note the different scales used in deep and shallow regions. *Thick black arrows* show velocity vectors from moored observations from the Department of Fisheries and Oceans Canada (Gregory 2004).

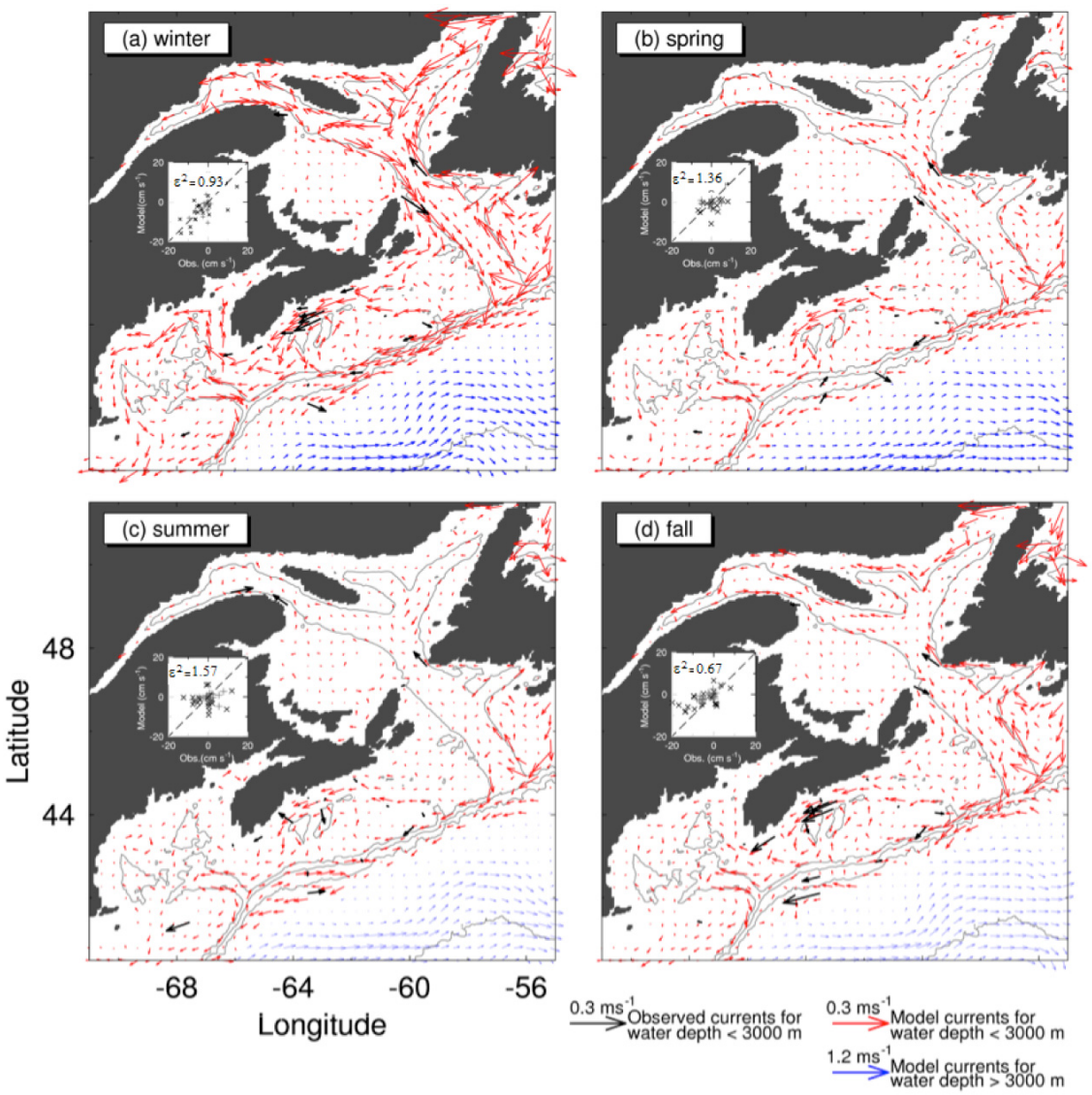

Figure 3.7. Comparison of simulated and observed seasonal-mean currents in the lower layer (30–100 m) of the GSL-SS-GOM region. *Red arrows* indicate velocity vectors over regions with water depths shallower than 3,000 m, and *blue arrows* indicate velocity vectors over regions deeper than 3,000 m. Note the different scales used in deep and shallow regions. *Thick black arrows* show velocity vectors from moored observations from the Department of Fisheries and Oceans Canada (Gregory, 2004).

Figures 3.6 and 3.7 also demonstrate that there are large seasonal variations in circulation over the GSL-SS-GOM. The seasonal-mean circulation in the region is relatively strong in winter and weak in summer. In the upper layer (Fig. 3.6), the ε^2 value is about 0.57, indicating that the CM has satisfactory skill in reproducing the observed winter-mean currents (Fig. 3.6a) in the region. The currents simulated by the

CM in spring ($\varepsilon^2 \sim 2$) compare well with the observations over the western side of Cabot Strait and along the main pathway of the shelf break jet. In spring, the simulated and observed Nova Scotian Current agree less well with the observations in comparison with other seasons. In summer, the currents produced by the CM have the same directions as the current-meter observations but are weaker, particularly for the Gaspé Current, the flow through Cabot Strait and the flow over the northwestern Scotian Shelf. The ε^2 value in summer is about 0.70. The agreement between the currents derived from observations and the CM results is also very good in fall ($\varepsilon^2 \sim 0.58$), particularly for the flow on both sides of Cabot Strait and the Nova Scotian Current over the inner Scotian Shelf.

In the lower layer between 30 and 100 m, the winter-mean currents ($\varepsilon^2 \sim 0.9$) produced by the CM agree well with current-meter estimates at Cabot Strait and over the inner Scotian Shelf (Nova Scotian Current). In spring, the simulated subsurface flows at both sides of Cabot Strait decrease, and the agreement between the simulated currents and the current-meter observations is reasonable ($\varepsilon^2 \sim 1.36$). In summer months the simulated subsurface currents agree less well with the observations ($\varepsilon^2 \sim 1.57$). By comparison, the agreement between the CM results and observations is satisfactory in fall ($\varepsilon^2 \sim 0.58$).

3.3.3 Model performance in simulating monthly-mean hydrography

The use of the spectral nudging and semi-prognostic methods reduces model bias in the annual cycles of the simulated temperature and salinity distributions (Urrego-Blanco and Sheng, 2012). In this section the average absolute difference (AAD) defined in Eq. (2.6) is used to quantify the fit of the monthly-mean child model results to the climatological monthly-mean fields of temperature and salinity.

The distributions of the *AAD*s are shown by contour lines in Fig. 3.8. The *AAD*s are about 0.25 or smaller for salinity at 9 and 50 m over the most of the CM domain, except over the Slope Water region where the *AAD* values are about 0.5 (Fig. 3.8a and b) and in

the lower St. Lawrence Estuary where the *AAD* values are about 1 at 9 m. The area-averaged *AAD* for salinity over the CM domain (Table 3.2) is about 0.26-0.31 in the top 100 m, and less than 0.2 in deeper layers.

The *AAD* values for temperature at 9 m (Fig. 3.8c) are about 1°C in the GSL and over the eastern Scotian Shelf and the Slope Water region, and slightly higher in the GOM (1-2°C). In the sub-surface waters (Fig. 3.8d) the *AAD* values for temperature are smaller than in the upper water column over the GSL-SS-GOM with values about 0.5°C in the GSL and over the eastern Scotian Shelf. The area-averaged *AAD* for temperature is about 1°C in the top 100 m (Table 3.2) with the largest value of 1.3°C at 16 m and less than 1°C below 100 m.

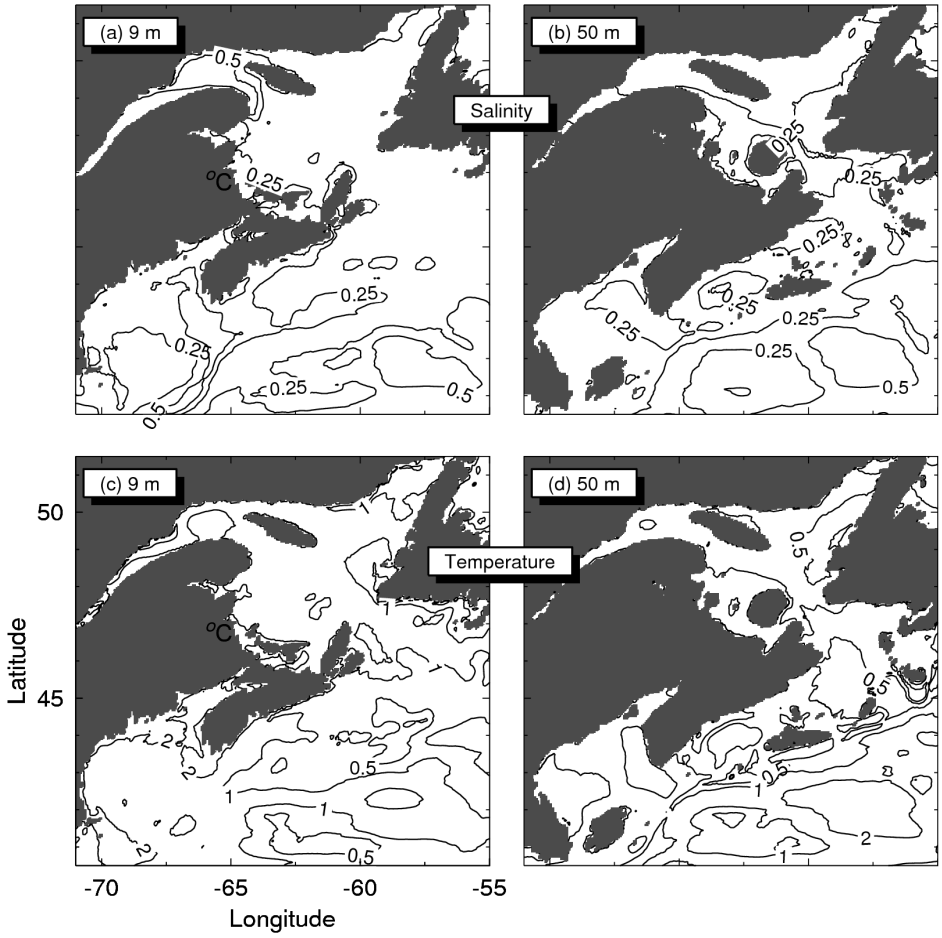

Figure 3.8. Average absolute differences between climatological and simulated monthly mean near surface (left panels) and subsurface (right panels) salinity and temperatures.

Table 3.2. Values of the domain-mean average absolute error (*AAD*) at different depths.

Depth (m)	*T* (°C)	*S*
3	0.99	0.31
9	1.06	0.30
16	1.27	0.30
32	0.88	0.26
50	1.00	0.26
112	0.97	0.23
191	0.89	0.17
322	0.74	0.14
534	0.81	0.12
989	0.25	0.02
1470	0.07	0.01

In-situ measurements of temperature and salinity have been made at selected mooring locations in the region by the Department of Fisheries and Oceans of Canada since 1999 as part of the Atlantic Zone Monitoring Programme (Fisheries and Oceans Canada, 2012). Figure 3.9 presents the T-S diagrams from monthly CTD observations (left panels) and model results (right panels) at four stations marked in Fig. 3.1 for 1999-2005. At these four stations water masses simulated by the model (Figs. 3.9b, d, f, h) have similar compositions as the water masses in the T-S diagrams from observations .(Figs. 3.9a, c, e, g). I quantify the agreement between observed and simulated T-S diagrams by using ε^2 in Eq. 2.5 and replacing U and V with monthly-mean temperature and salinity, respectively. The ε^2 ranges between 0.2-0.3 for the T-S diagrams at Station 2, Shediac and Gaspé and is about 0.45 for the T-S diagrams at the Anticosti station. This good agreement is partly due to the use of spectral nudging, which is necessary to reduce annual biases in temperature and salinity distributions, and indicates that the CM properly simulates the water mass distributions in the GS-SS-GOM region.

Figure 3.10 presents time-depth distributions of monthly-mean temperatures produced by the CM (right panels) and those taken from CTD observations in the upper water columns at four stations during 1999-2005. The CM reproduces the seasonal evolution of temperature stratifications at Station 2 over the inner Scotian Shelf due to the use of spectral nudging. At this location both the model results and CTD observations demonstrate that the temperature is relatively uniform in the top 40 m in winter months due to winter convection. The thermal stratification is gradually re-established in spring and reaches the maximum in late summer due to surface heating. The temperature stratification in the vertical is reduced in early fall and almost completely eliminated in late fall and winter due to surface cooling.

The CM also reproduces the general features of the vertical distribution and seasonal changes of observed temperatures at three stations in the GSL (Shediac, Gaspé, and Anticosti in Fig. 3.1). The CM also reproduces reasonably well the winter convection events and weak thermal stratification in winter due to strong mixing at these three locations. By comparison, the CM performs less well in simulating the thermal structure in summer months. The model results are more diffusive in comparison with the observations at the three positions, particularly at Gaspé and Anticosti.

The CM also reproduces the observed monthly-mean salinity at three stations in the GSL (Shediac, Gaspé, and Anticosti in Fig. 3.1), but less well at Station 2 (Fig. 3.11). The observed seasonal cycle of salinity in the upper 20 m at Gaspé and Shediac is well reproduced by the CM, with the lowest salinities occurring at Gaspé in May and at Shediac in June. In the lower water column, the CM reproduces well the seasonal variations of salinity at Shediac and Gaspé. At Station 2 the CM has deficiencies in reproducing the seasonal cycle of salinity in the lower water column. At Anticosti the simulated seasonal cycle of salinity is very weak and consistent with the CTD observations.

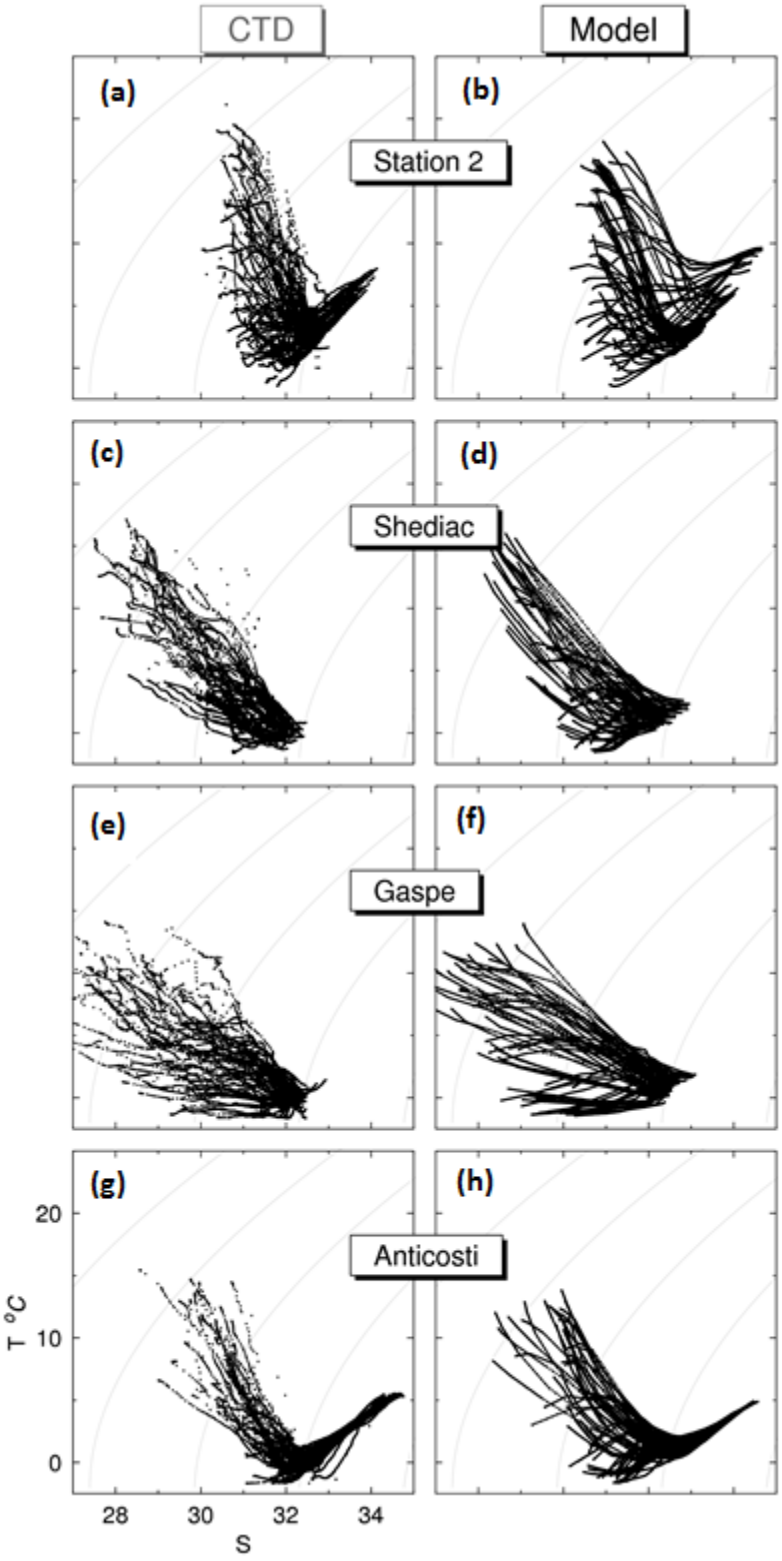

Figure 3.9. *T* -*S* diagrams of water masses at the stations of the AZMP indicated in Fig. 3.1, based on the monthly mean observations of temperature and salinity during the period of 1999–2005.

3.3.4 Model performance in simulating interannual variability

Figures 3.10 and 3.11 demonstrate that the observed and simulated hydrography has significant interannual variability over the GSL-SS-GOM. Both CTD measurements and models results shown in Fig. 3.10 feature relatively cold temperatures in the top 50 m of the water column during the winters of 2001, 2003 and 2004, due mainly to strong winter convection events during these years. By comparison, the water temperatures during the winters of 1999 and 2000 are relatively warm, due mainly to mild winters and therefore weaker winter convection in these years. It should be noted that some events of interannual variability produced by the CM, such as the warmer and saltier conditions in the sub-surface waters (~50-100 m) during 2000 and 2001 are not consistent with the observed time-depth distributions.

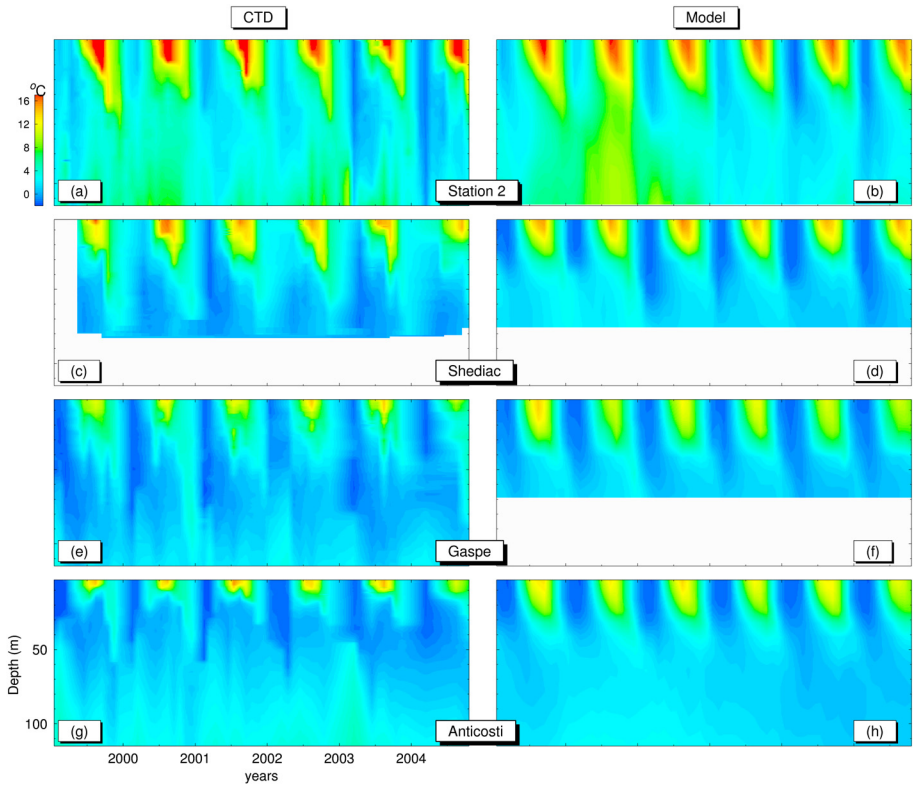

Figure 3.10. Time-depth distributions of monthly mean temperatures at four stations (marked in Fig. 3.1) taken from CTD measurements (*left panels*) and from model results (*right panels*) in the Control Run for the period of 1999–2005. White areas in the middle panels represent that either temperature observations are not available, or model topography is shallower than the observed water depth.

In Chapter 2 I demonstrated that an observed cooling trend in SST over the Scotian Shelf and Slope region was well reproduced by the PM of the nested-grid model. The annual mean and depth-averaged anomalies of temperature and salinity produced by the PM were shown to be in reasonable agreement with observations (Head and Sameoto, 2007) over the Newfoundland and Scotian Shelves. In addition, the PM also has reasonable skill in simulating the interannual variability of the north-south excursions of the Gulf Stream.

Galbraith et al. (2009) examined the interannual variability of hydrography in the GSL by calculating the annual mean anomalies of observed hydrography at three layers (centered at 150 m, 200 m, and 300 m) in the gulf (Fig. 3.12). I calculated the annual mean anomalies of hydrography from the results produced by the CM in the same way as in Galbraith et al. (2009). Both the model results and observations demonstrate that the interannual variability is correlated in the three layers, but with maximum amplitudes in layers centered at 150 m and 200 m. These maximum interannual variability is about 2°C and 0.5 for temperature and salinity, respectively. Figure 3.12 demonstrates that the interannual temperature and salinity anomalies are coherent for the intermediate waters of the GSL. The observed time series in the GSL (Fig. 3.12) demonstrate that relatively high temperature and salinity occur in 1988-1989 and 2000-2004, and relatively cold and fresh conditions occur around the mid 1990's. The CM reproduces some of these anomalies, particularly in the early 1990s and 2000, with correlation coefficients of about 0.50-0.55 for temperature and about 0.30-0.37 for salinity. It is important to note that even though the CM (also the PM) uses the spectral nudging and semi-prognostic methods to eliminate the model drift, the model is capable of reproducing reasonably well the interannual variability of hydrography in the region.

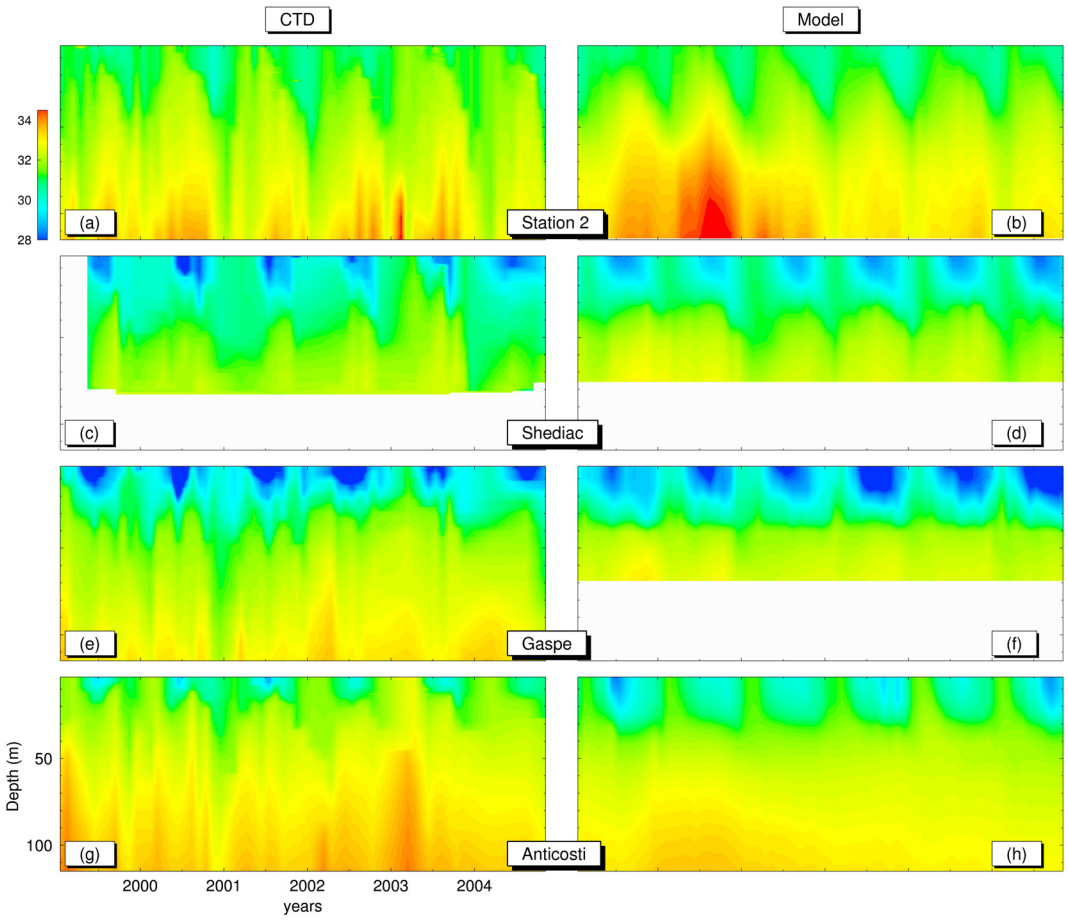

Figure 3.11. Time-depth distributions of monthly mean salinities at four stations (marked in Fig. 3.1) taken from CTD measurements (*left panels*) and from model results (*right panels*) in the Control Run for the period of 1999–2005. White areas in the middle panels represent that either salinity observations are not available, or model topography is shallower than the observed water depth.

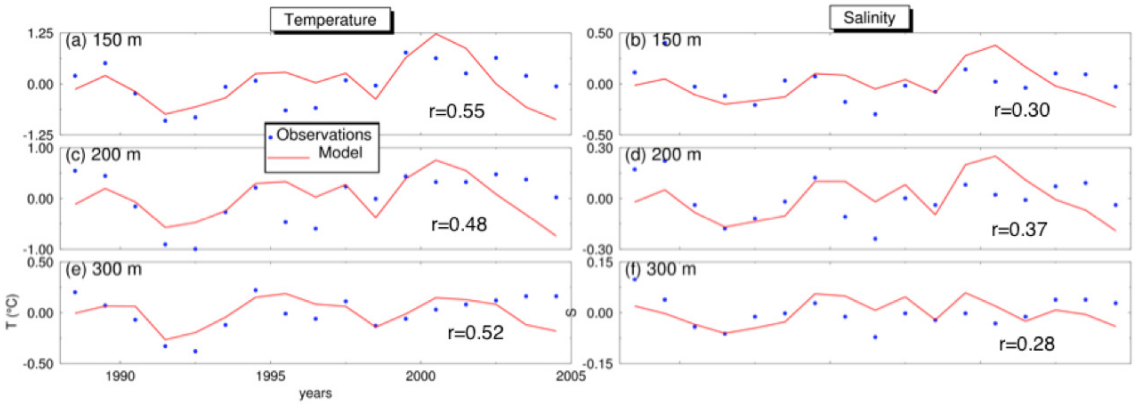

Figure 3.12. Comparison of the observed (*blue dots*) and simulated (*red lines*) annual mean anomalies of temperature (*left panels*) and salinity (*right panels*) averaged over the Gulf of St. Lawrence in three layers centered at 150, 200, and 300 m, respectively.

3.3.5 Model performance in simulating intraseasonal variability of temperature and salinity

I next assess the performance of the CM in simulating intraseasonal variability by comparing simulated SST fields (Figs. 3.13b, d) with remote sensing observations (Figs.3.13a, c). The comparison is made for the 5-day mean SST fields on February 7 of 2003 and June 7 of 2003. These two days were selected to examine synoptic conditions at specific times in winter and summer, respectively. Figure 3.13a and b demonstrates that the ocean surface in winter 2003 has cold temperatures ranging from –1°C to 5°C over the GSL-SS-GOM (Figs. 3.13a, b), with relatively warmer conditions over the western GOM. Over the Slope Water region a frontal thermal structure occurs in the simulated SST and the remote sensing data. In the deep ocean both the simulated and observed SST varies spatially between 10°C and 15°C with slightly higher SST in the model results. Over the Slope Water region the CM also generates small-scale features associated with the thermal front and the meandering of the Slope Water Jet, which do not necessarily agree with the observations due to the lack of data assimilation in the model and the complex mesoscale dynamics in that region.

Figure 3.13c, d shows relatively cold conditions (~4°C) over the central and eastern GSL, and warm conditions over the coastal waters of the western GSL (~10°C) in summer 2003. During this time, both observations and model results also demonstrate relatively cold waters (~5-6°C) over the eastern Scotian Shelf and warmer over the central and western Shelf (~7-10°C). Over the GOM the simulated SST is between ~8-11°C, which is comparable to the observed SST. Over the Slope Water region the simulated SST ranges between 15-20°C, with several warm-core eddy rings. Figure 3.13 demonstrates that, by comparing model results with observations, the CM produces good estimates of the large-scale distributions of SST on synoptic time scales. The small-scales are less well reproduced by the model particularly over the Gulf of Maine in summer.

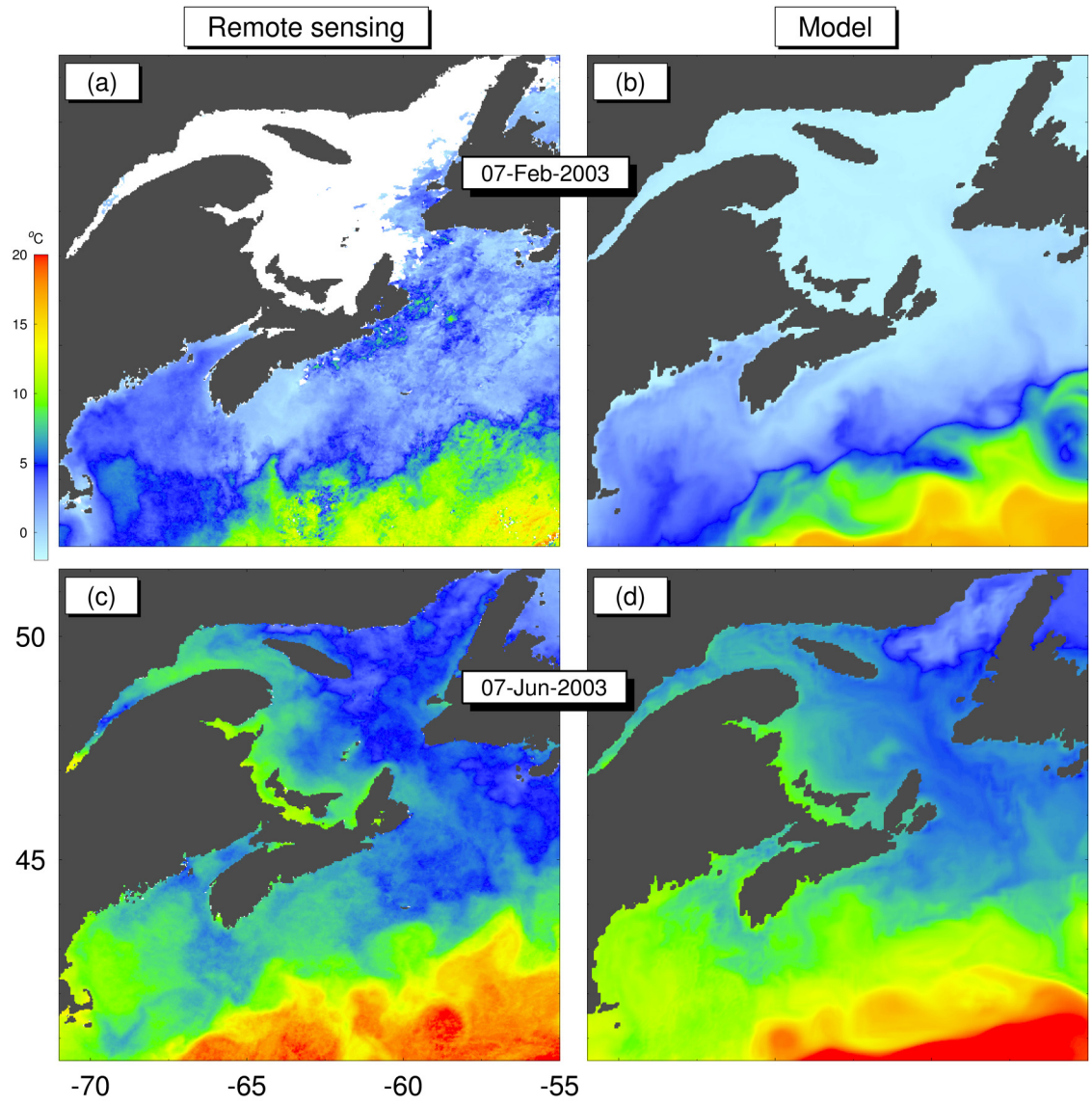

Figure 3.13. Comparison of the 5-day mean SST derived from remote sensing data (*left panels*) and model results (*right panels*) in the Control Run. *Upper* and *lower panels* correspond to periods centered on February 7 of 2003 and June 7 of 2003, respectively. The remote sensing data are not available in the Gulf of St. Lawrence in February 7 due to the ice cover in the Gulf of St. Lawrence.

I next present a comparison of the simulated and observed hydrography at a transect along the Halifax line (Fig 3.1) in December 1997. The observed hydrography was collected by the Bedford Institute of Oceanography using a moving vessel profile (Drinkwater et al., 1998). The observed salinity (Fig. 3.14b) features relatively low salinities (<31) in the upper 50 m of the water column and a rapid increase to values

above 33 from 50-70 m over Emerald Basin and the offshore locations in the transect. The salinity in the deep waters of Emerald Basin features values of about 35 indicating the influence of oceanic waters in the deepest parts of the shelf. The increase in salinity over the coastal side of the transect is more gradual, with the salinity contours tilting downwards towards the coast. The simulated salinity at the Halifax line in December 1997 (Fig. 3.14a) is similar to the observations, featuring fresher conditions in the upper water column, a sharp halocline at subsurface waters over Emerald Basin and offshore waters, and tilting of the contours over coastal waters. The simulated salinity in the deep waters of Emerald Basin is also high (~34.5), matching relatively well the observed values of salinity of about 35.

The observed temperature at the Halifax Line on December 1997 shown in Fig. 3.14d (Drinkwater et al., 1998), features a mixed layer (4-5°C) in the upper 70 m of the water column. The observed temperature increases from 70 m down to the bottom, reaching temperatures of about 9°C in deep waters over Emerald Basin, and about 7-8°C in the deep waters on the onshore side of the transect (right hand side in the figure). The simulated temperature distribution on December 1997 (Fig. 3.14c) is qualitatively similar to the observed distribution. The simulated thermocline in Fig. 3.14c, is however, located between 40-50 m in the upper water column, and the simulated temperatures are slightly lower than the observed temperatures by about 1°C which is satisfactory considering that observations are not assimilated in the model. A finer horizontal model resolution, better spatial and temporal resolutions of model forcing, and tidal forcing are needed for the model to perform better in simulating the observed intraseasonal variability.

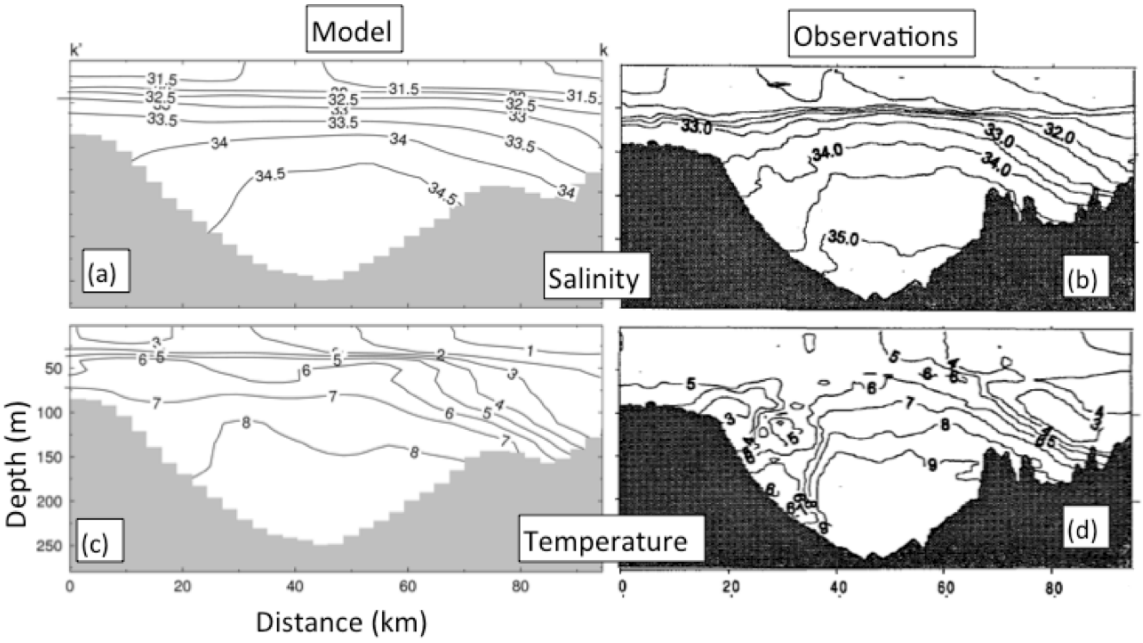

Figure 3.14. Comparison of the observed hydrography (Drinkwater et al., 1998) (*right panels*) and simulated (*left panels*) hydrography in the Control Run in December 1997 at a transect of the Halifax Line (Fig. 3.1). *Upper* and *lower panels* correspond to salinity and temperature, respectively. The coast of Nova Scotia is located on the right hand side and offshore waters to the left hand side.

3.4 Main Physical Processes Affecting Variability in the GSL-SS-GOM

In this section the model results in three experiments are separated into four frequency bands and a principal component and correlation analyses are used to identify main physical process in each frequency band.

3.4.1 Separation in frequency bands

Time series of a model variable ϕ can be expressed in terms of components in four different frequency bands:

$$\phi = \bar{\phi} + \hat{\phi} + \tilde{\phi} + \phi' \qquad (3.1)$$

where ϕ represents a time series of a original model variable (such as temperature, salinity, or currents), $\bar{\phi}$ represents the time-mean over 17 years between 1988 and 2005,

$\hat{\phi}$ is the interannual (periods greater than 12 months), $\tilde{\phi}$ is the annual cycle, and ϕ' is the intraseasonal (periods less than 12 months, excluding tidal frequencies) components of the time evolution of the model variables.

Due to the limitation of computer resources, ϕ is the 5-day mean output of 3D model temperature, salinity and currents in 17 years between 1988 and 2005 over the study region. After computing the time-mean value over the 17-year period ($\bar{\phi}$), for every variable at each model grid point a long-term trend (which is small and can be ignored due to the elimination of the model drift by using the combination of the semi-prognostic and spectral nudging methods) is removed from the original time series of model results. The seasonal cycle is obtained by first applying a 6-point (or 30-day) running average to the time series to remove frequencies higher than 30 days and then averaging the band-passed time series over the 17 years. The resulting average is the annual cycle ($\tilde{\phi}$), which repeats over the 17-year simulation period. The interannual component ($\hat{\phi}$) is obtained by removing the annual cycle ($\tilde{\phi}$) from the original time series and low-pass filtering the resulting time series with a 1-year running average. The intraseasonal component (ϕ') is obtained by subtracting the time-mean ($\bar{\phi}$), the annual cycle ($\tilde{\phi}$), and the interannual component ($\hat{\phi}$) from the original time series (ϕ).

A principal component (or empirical orthogonal function) analysis of the model results in the intraseasonal, seasonal, and interannual frequency bands was conducted for the temperature, salinity and currents. The anomalies of the space-time fields are expressed as:

$$\Psi(\vec{x},t) = \sum_{n=1}^{N} R_n(t) S_n(\vec{x}) \tag{3.2}$$

where t is time and $\vec{x}$ is the space vector, N is the number of modes contained in the field, $S_n(\vec{x})$ is the empirical orthogonal function (EOF) of the covariance matrix of the anomaly field $\Psi(\vec{x},t)$, and $R_n(t)$ is the mode coefficient for the nth EOF.

3.4.2 Time-mean circulation

The time-mean circulation of the 17-year period produced by the CM in the Control Run is similar with the distribution presented in Fig. 3.3b. In this section I focus only on the role of the net sea surface fluxes and the flow through the Strait of Belle Isle on the mean circulation over the GSL-SS-GOM. Figures 3.15a-c and 3.16a-c present vertically-averaged time-mean currents produced by the CM in the upper layer (less than 30 m) and intermediate layer (30-100 m) in three experiments: Control Run, ConstFluxes, and NoBI. In addition, Figs. 3.15d, e and 3.16d, e present the differences in the time-mean circulation between the Control Run and the other two experiments.

Comparison of model results in Control Run and ConstFluxes (Figs. 3.15a, b, d and 3.16a, b, d) in the GSL demonstrates that the southeastward flow over the Magdalen Shallows, and the outflow through western Cabot Strait produced by the CM is weaker if the model is forced only by the time invariant atmospheric forcing in comparison with the Control Run. The portion of the outflow from the GSL at Cabot Strait that runs onto the coastal region of Nova Scotia is larger in the Control Run than in ConstFluxes. In the latter experiment the Nova Scotian Current is mainly fed by the cross-shelf flow from the offshore Labrador Current that flows onto the inner Scotian Shelf through Banquereau Bank and Sable Island Bank (Fig. 3.15a, b and 3.16a, b). This suggests that the temporal variability in the atmospheric forcing plays a noticeable role in affecting the outflow at the western side of Cabot Strait as it flows downstream onto the Scotian Shelf. The most plausible explanation for the differences in the time-mean circulation between these two experiments over the GSL and Cabot Strait area is that temporal variability in atmospheric forcing enhances the tilt of the isopycnal surfaces, which increases the seaward flow in the upper layer and the landward flow in the subsurface layer.

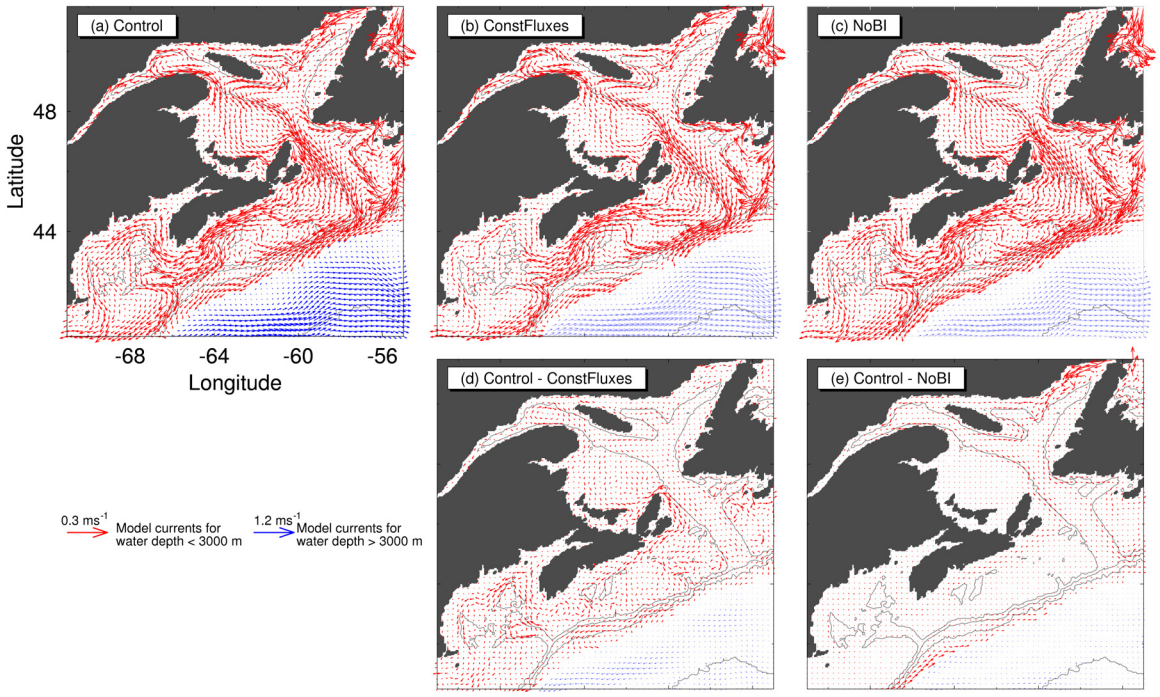

Figure 3.15. *Upper panels* show the vertically averaged time-mean currents over the CM domain in the 0–30 m layer calculated from model results in experiments (a) Control run, (b) ConstFluxes, and (c) NoBI. The *lower panels* show the difference of the vertically averaged time-mean currents (d**)** between the Control Run and ConstFluxes experiments and (e) between the Control Run and NoBI experiments.

In comparison with the Control Run, the cyclonic circulation in the GOM is significantly weaker in ConstFluxes (Fig. 3.15a, b, d and 3.16a, b, d), suggesting that the temporal variability in the atmospheric forcing also plays an important role in the time-mean circulation in the GOM. This can also be seen in Fig. 3.17a, b which shows the time-mean normal velocities across transect DD" in the GOM in the Control Run and ConstFluxes, respectively. By comparison, the circulation in the GOM in experiment NoBI is very similar to that in the Control Run (not shown), indicating that the inflow through the Strait of Belle Isle does not affect the circulation in the GOM. The southwestward jet over the inner shelf of the western GOM is stronger and broader in the Control Run than in ConstFluxes. The most plausible physical explanation for the time-mean circulation differences over the Scotian Shelf is that the baroclinic pressure gradient is increased by the temporal variability in the atmospheric forcing, which leads the Nova Scotian Current and shelf break jet to be stronger. Based on the conservation of momentum, this will increase the circulation over the Gulf of Maine.

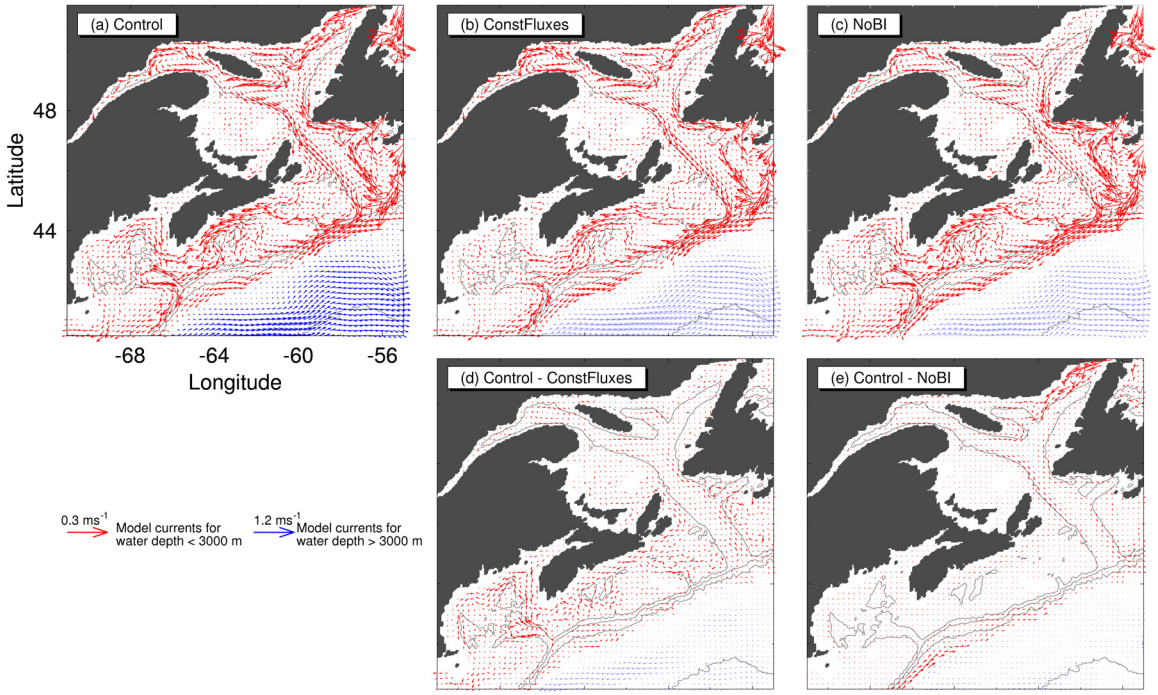

Figure 3.16. *Upper panels* show the vertically averaged time-mean currents over the CM domain in the 30–100 m layer calculated from model results in experiments (a) Control run, (b) ConstFluxes, and (c) NoBI. The *lower panels* show the difference of the vertically averaged time-mean currents (d**)** between the Control Run and ConstFluxes experiments and (e) between the Control Run and NoBI experiments.

Figures 3.15a, c, e and 16a, c, e show that the flow over the northeastern GSL, particularly along Québec's northern shore, is significantly reduced in NoBI in comparison with the Control Run. This indicates that the circulation over the northeastern GSL is significantly affected by the inflow through the Strait of Belle Isle. In the top 30 m the cyclonic circulation in the northwest GSL is also relatively weaker in NoBI than in the Control Run. The circulation at Cabot Strait is also influenced by the flow at the Strait of Belle Isle. The inflow of the coastal Labrador Current into the GSL which flows along the southwestern Newfoundland coast is relatively stronger in NoBI than in the Control Run (Fig. 3.15a, c, e).

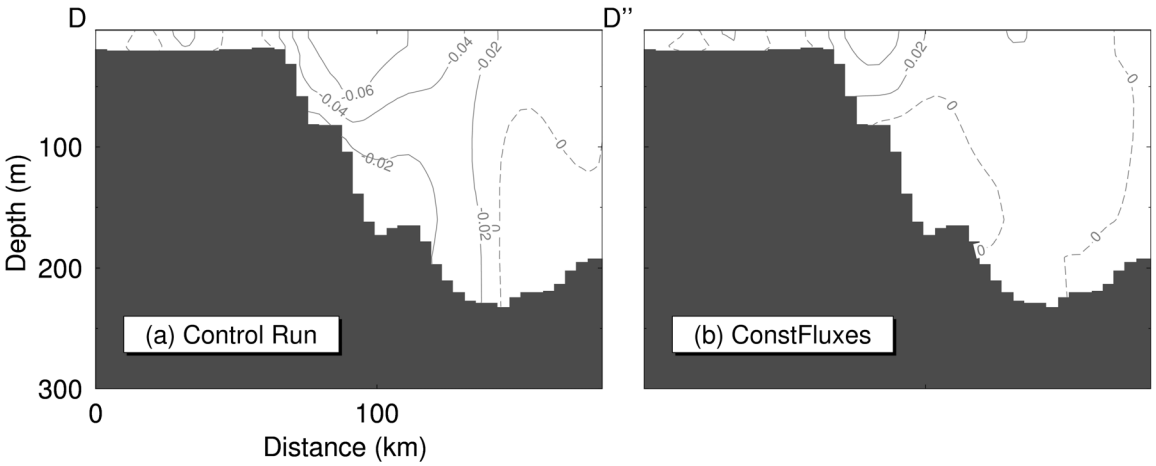

Figure 3.17. Time-mean currents normal to transect DD" in the GOM calculated from model results in (a) the Control Run and (b) ConstFluxes.

In experiment ConstFluxes, the time-mean wind stress at the ocean surface might be underestimated based on the conversion of the time-mean wind velocity rather than the time-mean of the time-dependent wind stress converted from instantaneous wind velocity. To examine the extent to which the undersestimation is important, I have conducted a sensitivity experiment (ConstFluxes*) in which the time-mean stress is computed in terms of the mean wind velocity and the standard deviation of the wind velocity according to (Wright and Thompson, 1982):

$$\vec{\tau}_{ao} = \rho C_{ao}(a) a \vec{W} \tag{3.3a}$$

$$a = \left[\left| \vec{W} \right|^2 + \left(2\sigma_W \right)^2 \right]^{1/2} \tag{3.3b}$$

where $\vec{\tau}_{ao}$ is the stress at the air-ocean interface, $C_{ao}(a)$ is a drag coefficient between the atmosphere and the ocean estimated at a, $\vec{W}$ is the time-mean wind velocity vector, and σ_W the standard deviation of the fluctuating wind speed field. It should be noted that in this sensitivity experiment, the drag coefficient in Eq. 3.3a has been computed at $a = \left| \vec{W} \right|$, but the coeffient a uses the expression given in 3.3b which accounts for the effective wind speed for the purpose of determining the mean stress.

Figure 3.18 presents the difference of the vertically-averaged (0-30 m) time-mean currents between ConstFluxes* and ConstFluxes experiments in 1988. The time-mean

currents in ConstFluxes* are slightly larger than in ConstFluxes, indicating that the influence of the variability of the wind field on the mean wind stress also has some effect on the time-mean ocean currents. The differences of the vertically-averaged currents between ConstFluxes* and ConstFluxes (Fig. 3.18), are however, relatively smaller than in the Control Run and ConstFluxes (Fig. 3.16d), indicating that the vertically-averaged currents in ConstFluxes are slightly smaller than in ConstFluxes*.

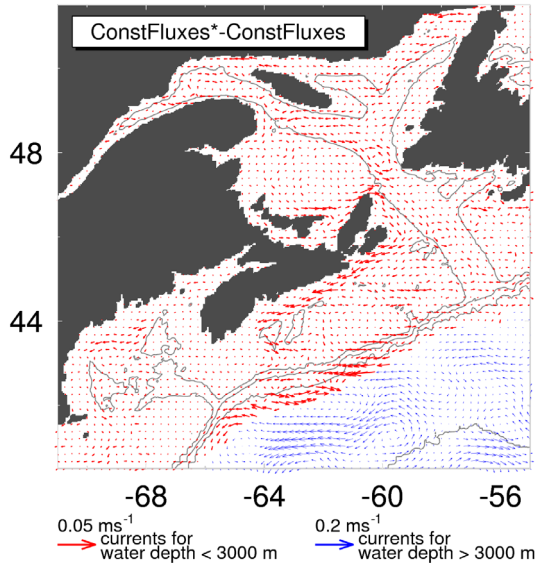

Figure 3.18. Differences of the vertically averaged time-mean currents over the CM domain in the 0–30 m layer between ConstFluxes* and ConstFluxes experiments.

3.4.3 Seasonal variability

An EOF analysis of model results demonstrates that seasonal variations of temperature in the GSL-SS-GOM are strongly affected by the large-scale seasonal heating and cooling at the sea surface. The timing of these seasonal cooling and warming events is spatially coherent over the study region. Furthermore, the seasonal variability in simulated temperature is largely explained by the first mode (>90%) and is confined to the top 60-70 m of the water column (not shown).

In contrast, the seasonal variations of simulated salinity are not spatially coherent over the GSL-SS-GOM region (Drinkwater et al., 1979; Smith and Schwing, 1991). To

quantify the advective processes that affect the seasonal salinity distributions, the EOF analysis is conducted for seasonal cycles of salinity at transects AA', EE' and CC'. Figure 3.19 presents the first EOFs and associated mode coefficients at these three transects.

At AA' the first mode explains 91% of the seasonal variability and is large in the top 30 m of the water column (Fig. 3.19a). At Cabot Strait (EE') the first mode explains 81% and is large in the top 50 m over the western side of the strait due to the influence of the estuarine plume. Over the eastern side of EE' the first mode is relatively small and shallow (Fig. 3.19b). The lowest salinity of the seasonal cycle occurs around July in the Anticosti transect (AA') and mid-October at Cabot Strait (EE') as indicated by the first mode (Fig. 3.19d). The propagation time of the lowest salinity between the two transects is about 4 months estimated based on the phase lag of the mode coefficients shown in Fig. 3.19d. The highest salinity of the seasonal cycle, on the other hand, are coherent within the GSL as the mode coefficients peak at the end of February at Anticosti, Cabot Strait (Fig. 3.19d) and cGSL transects. This could be due partially to time-varying currents, and partially to gulf-wide processes such as sea-ice formation, or enhanced mixing of near surface waters with more saline deep waters in winter months in the GSL.

Along the Halifax Line (CC'), the first mode explains 66% of the seasonal variability of salinity and is large in the sub-surface waters at depths between 30 m to about 60 m, which are affected mainly by the Nova Scotian Current on the near-shore side of the transect and by the southwestward jet at the shelf break (Fig. 3.19c). The lowest salinity of the seasonal cycle at the Halifax Line occurs in mid-January. The estimated advection time from Cabot Strait to the Halifax Line is about two and a half months, which is in good agreement with the advection time of the maximum transport between these two transects estimated by Smith and Schwing (1991) and by Drinkwater et al. (1979).

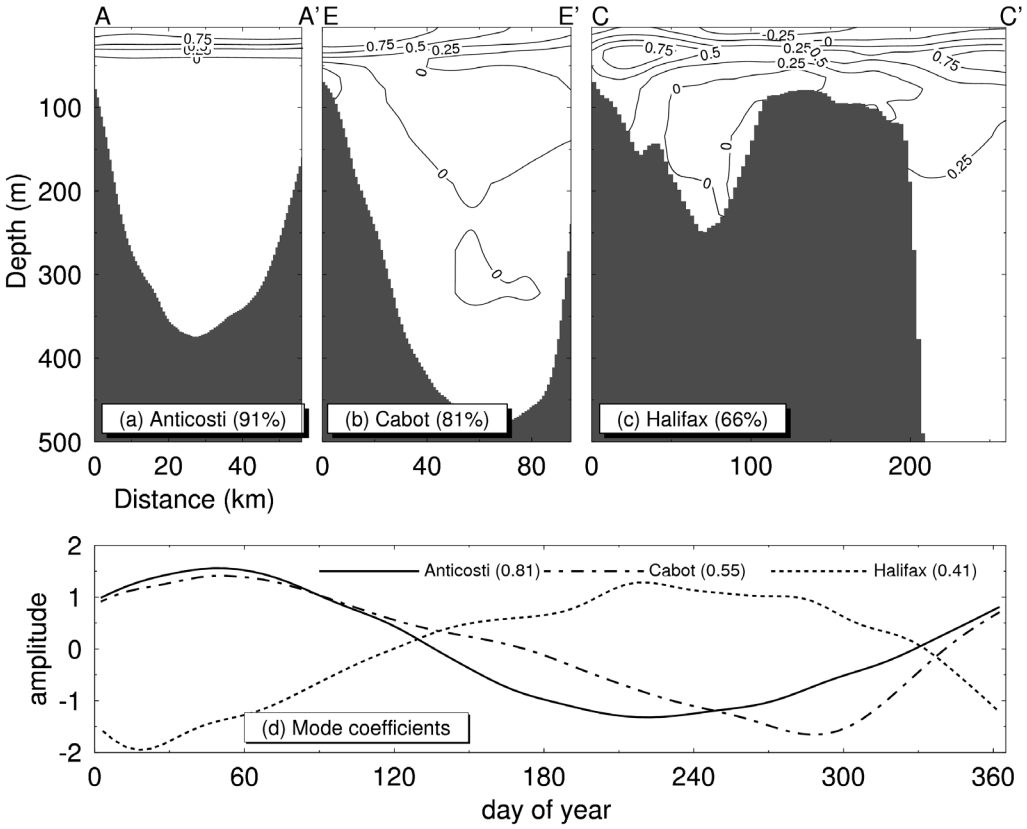

Figure 3.19. *Upper panels* show distributions of the first EOFs of the seasonal salinity variations at transects (a) AA', (b) EE', and (c) CC'. The *lower panel* shows time series of the normalized mode coefficients along the three transects. The standard deviation of the mode coefficients is given in parentheses.

Figure 3.20a, b shows vertical distributions of the first mode of seasonal variability in the model currents normal to the Halifax Line and Cabot Strait, respectively. On the western side of Cabot Strait the first mode is important over the whole water column, with large amplitude in the top 80 m near the coast. On the eastern side of the Strait the first mode has large amplitudes in the top 200 m of the water column. Along the Halifax Line the first mode has large amplitudes (i.e. large seasonal variability) over the pathway of the Nova Scotian Current and over the region of the shelf break jet. A correlation analysis of the first modes of seasonal variations in salinity and normal currents at the Halifax Line indicates that the lowest salinity of the seasonal cycle is coherent with the enhanced westward transports by the Nova Scotian Current and the shelfbreak jet. The first mode coefficients of salinity and normal velocity in the Halifax Line (Fig. 3.20c) are strongly correlated at zero lag. By comparison, at Cabot Strait these two modes are not in

phase (Fig. 3.20d). The lowest seasonal salinity at Cabot Strait occurs in mid-October, about 3 months before the maximum outflow transport through Cabot Strait takes place.

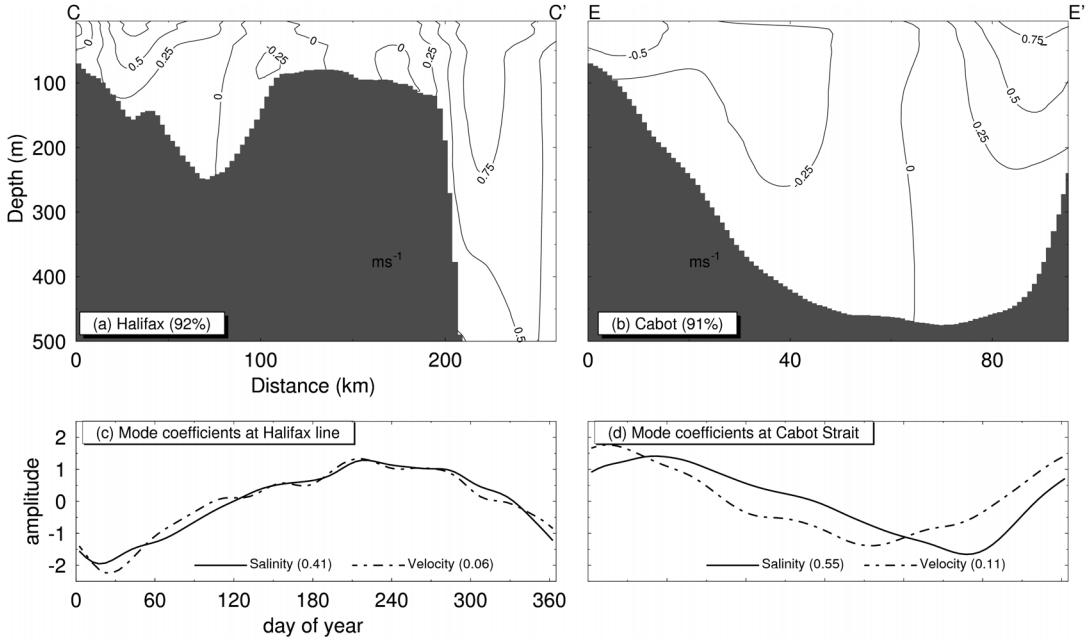

Figure 3.20. *Upper panels* show distributions of the first EOFs of the seasonal variations in normal currents at transects (a) CC' and (b) EE'. *Lower panels* show time series of the normalized mode coefficients of the first mode of seasonal variation in currents (*dashed*) and salinity (*continuous*) at (c) cc' and (d) EE'. The standard deviation of the mode coefficients is given in parentheses.

3.4.4 Interannual variability

The EOF analysis of the interannual variability in the GSL indicates that most of the interannual variability in the model temperature and salinity occurs in the water column between 50 and 300 m (Fig. 3.21). The interannual variability in temperature affects the cold intermediate layer (CIL) in the GSL, with the core of the CIL located at about 100 m depth. The first mode of the interannual variability has similar vertical and horizontal structures for temperature and salinity over the GSL (Fig. 3.21a-d), with large amplitudes occurring mainly in the 100-200 m layer at transects BB' in the cGSL and EE' at Cabot Strait. The time-dependent coefficients associated with these modes in Fig. 3.21a-d are statistically correlated at zero lag. The total variance of the interannual variability that is explained by the first mode is about ~80% at the cGSL and about ~70% at Cabot Strait.

Figure 3.21 also demonstrates that warmer and saltier anomalies occur in the subsurface waters of the GSL in the late 1980's, mid 1990's and the early 2000's. Relatively colder and fresher anomalies occur in the early 1990's and mid 2000's, which is consistent with the results of Drinkwater and Gilbert (2004).

Figure 3.21 also indicates that interannual fresh (saltier) and cold (warm) anomalies are coherent in intermediate waters below 50 m over the GSL. Drinkwater and Gilbert (2004) attributed the interannual variability in hydrography in the region to the local atmospheric variability and the variability of the flow through the Strait of Belle Isle. To confirm their finding, I compare the EOFs of model temperature in the cGSL between Control Run and ConstFluxes (Fig. 3.22). In comparison with the Control Run (Fig. 3.22a), the amplitude of the first EOF in ConstFluxes is relatively smaller in the deep water and relatively larger in the top 50 m. The amplitude of the first mode coefficient is significantly smaller in ConstFluxes compared to the Control Run (Fig. 3.22c), indicating that the atmospheric interannual variability is indeed an important factor affecting the interannual variability of the intermediate water column in the GSL. A comparison of model results in Exp-Control and Exp-NoBI also indicates that the interannual variability of the inflow through the Strait of Belle Isle plays a minor role in affecting the interannual variability of circulation in the region outside the northeast GSL.

To further examine the horizontal distribution of the interannual variability in the GSL, the horizontal distribution of the first EOF made at 160 m over the GSL and the Laurentian Channel is shown in Fig. 3.23. The horizontal structure of the first modes is similar in both the Control Run and ConstFluxes (Fig. 3.23). In both cases the highest mode amplitudes occur over the offshore waters in the Laurentian Channel and along the coastal waters of the southwestern Newfoundland Shelf. The first mode coefficients in Fig. 3.23c are highly correlated to the mode coefficients in Fig. 3.22c indicating the same mechanism of variability. Figure 3.23c also demonstrates that the variability of the first mode coefficients in ConstFluxes is smaller than in the Control Run. Both the horizontal pattern and mode coefficients of the first mode of interannual variability are very similar in the Control Run and experiment NoBI (not shown). The interannual variability of

hydrography in the GSL must be driven by a combination of interannual atmospheric forcing and interannual variability of the circulation in the Laurentian Channel and the southwestern Newfoundland Shelf. The latter excites variabilities in the GSL through Cabot Strait which are linked to interannual variability that is generated by non-linear dynamics in the Newfoundland Shelf as pointed out by Urrego-Blanco and Sheng (2012).

The first mode of interannual variability in temperature at the Halifax Line (Fig. 3.24) explains about 81% of the total variance and is not linked to interannual variability in the GSL. The first mode has large amplitude over the shelf break with the largest values at about 100 m. Urrego-Blanco and Sheng (2012) argued that the first mode of the interannual temperature variability over the Scotian Shelf is related to interannual variability advected southwestward by the shelf break jet. At the Halifax Line the first mode of interannual variability in temperature is correlated positively with the first mode of interannual variability in salinity (0.98) and negatively with the first mode of interannual variability of the currents (–0.85). This indicates that cold and low salinity interannual variability is coherent with the enhanced equatorward transport associated with the shelf break jet.

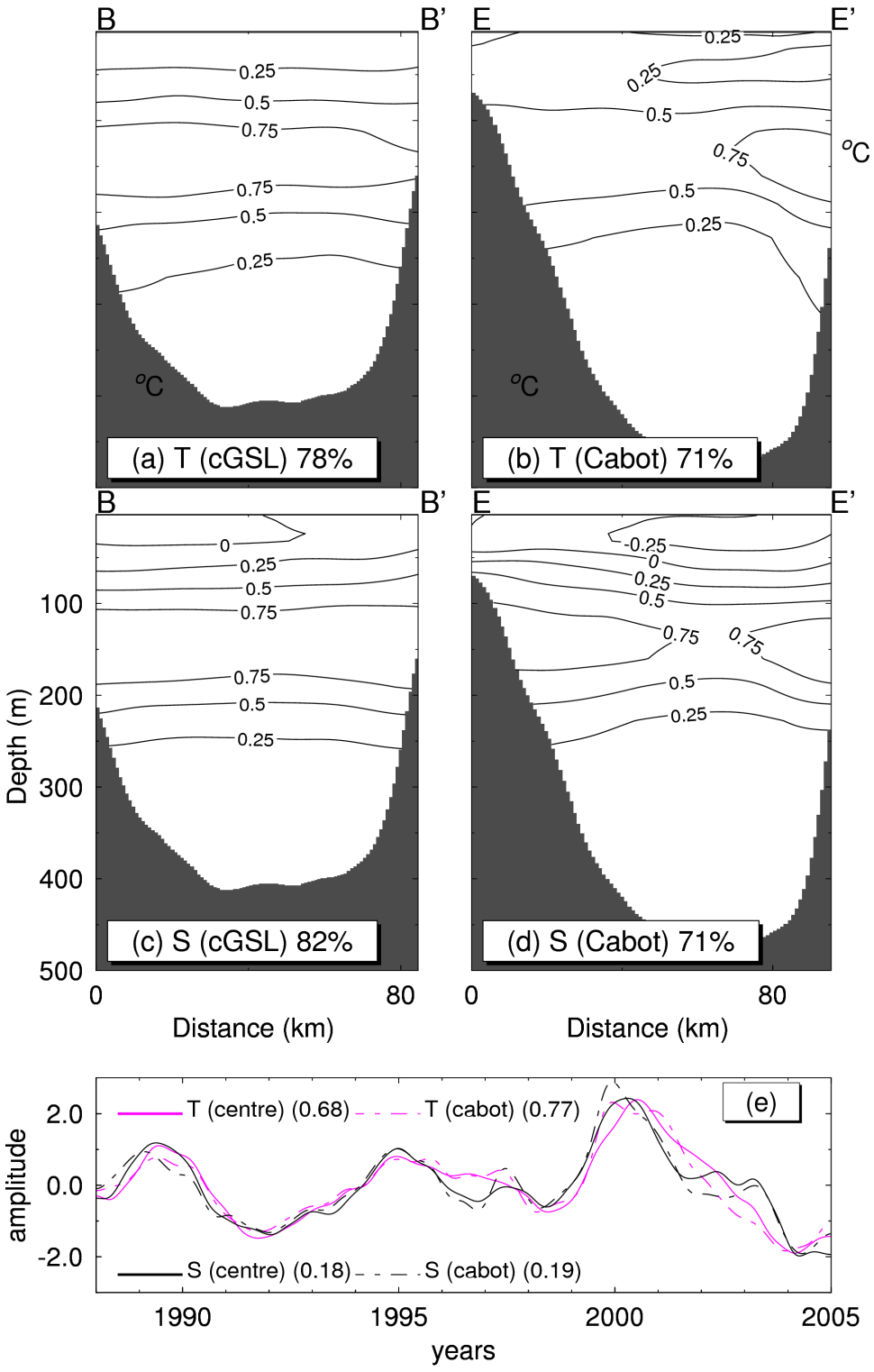

Figure 3.21. The first EOFs of the interannual variation of the temperature (*upper*) and salinity (*middle*) along transects BB' over the cGSL (*right*) and EE' over Cabot Strait (*left*). The *lower panel* shows time series of the normalized mode coefficients along the two transects. The standard deviation of the mode coefficients is given in parentheses.

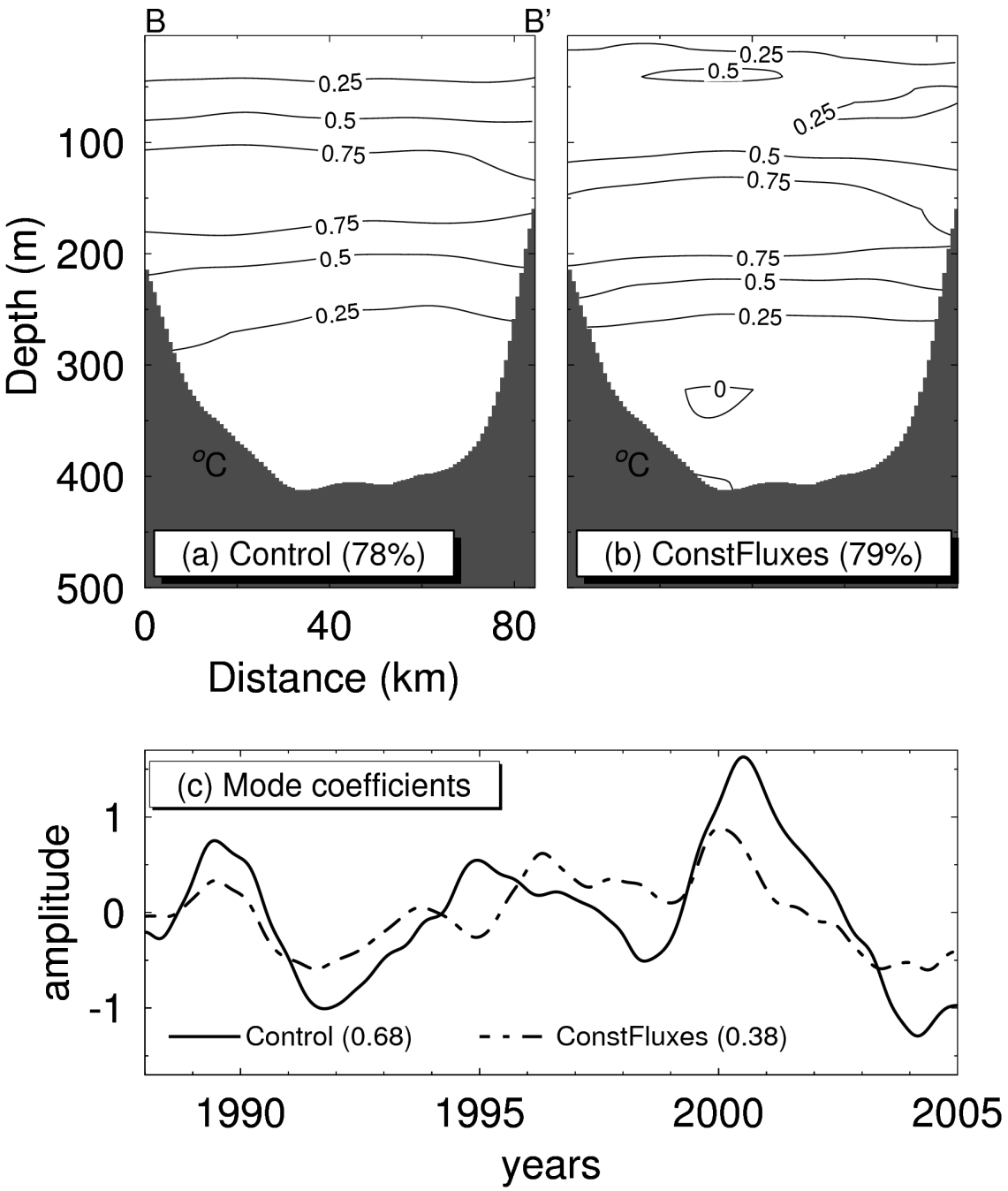

Figure 3.22. *Upper panels* show the first EOFs of the interannual variation of temperature along transect BB' over the cGSL using model results in experiments (a) Control Run and (b) ConstFluxes. The *lower panel* shows time series of the mode coefficients in the experiments with the *numbers in parentheses* indicating the standard deviation of each mode.

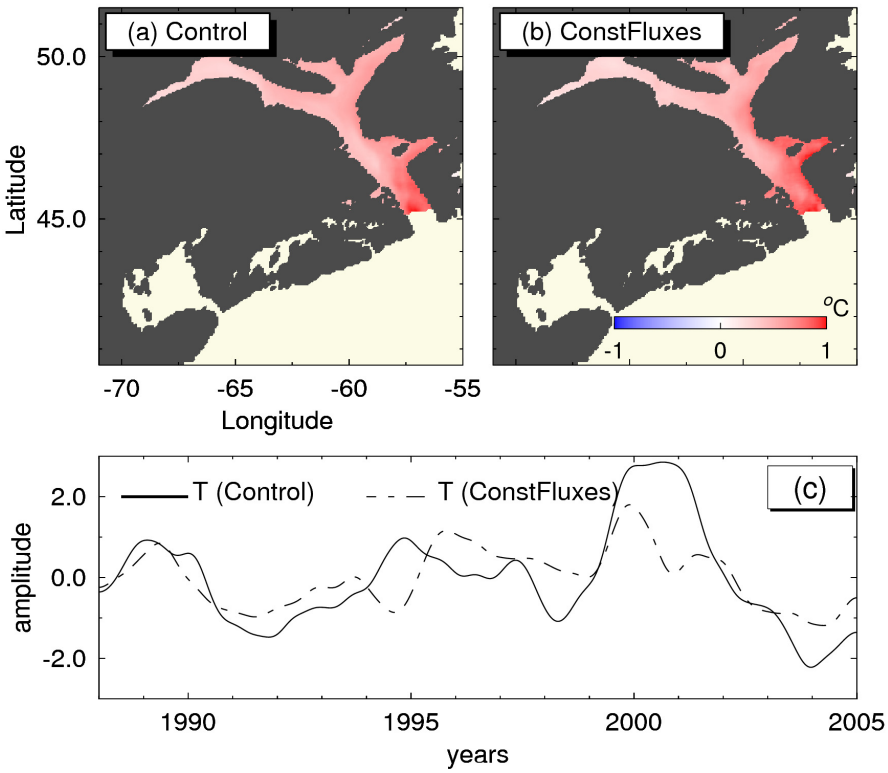

Figure 3.23. *Upper panels* show distributions of the first EOFs of interannual variability in temperature at 160 m calculated from model results in (a**)** the Control Run and (b**)** ConstFluxes. The *lower panel* shows the time series of the corresponding mode coefficients along with the mode coefficients (*black line*) of the first EOF at the transect BB' in the cGSL in the Control Run.

3.4.5 Intraseasonal variability

The 3D currents produced by the CM in the Control Run also have significant intraseasonal variability over the GSL-SS-GOM. The first mode of intraseasonal variability in the normal currents at the transects in the cGSL (BB') and Cabot Strait (EE') explains about 47% and 41% of the total variance, respectively (Fig. 3.25). The coefficients of the first mode at Cabot Strait have larger intraseasonal variability with a standard deviation of 0.12, in comparison with the intraseasonal variability over the cGSL with a standard deviation of 0.03. These two modes have a correlation of 0.82 at zero lag (Fig. 3.25c). Over the cGSL, the first mode is characterized by a strong (weaker) southeastward flow along the western side of transect BB' and a weaker (stronger) northwestward flow on the eastern side (Fig.3.25a). The dipole structure of this mode

indicates the strengthening and weakening of the recirculation to the south of the Anticosti Island.

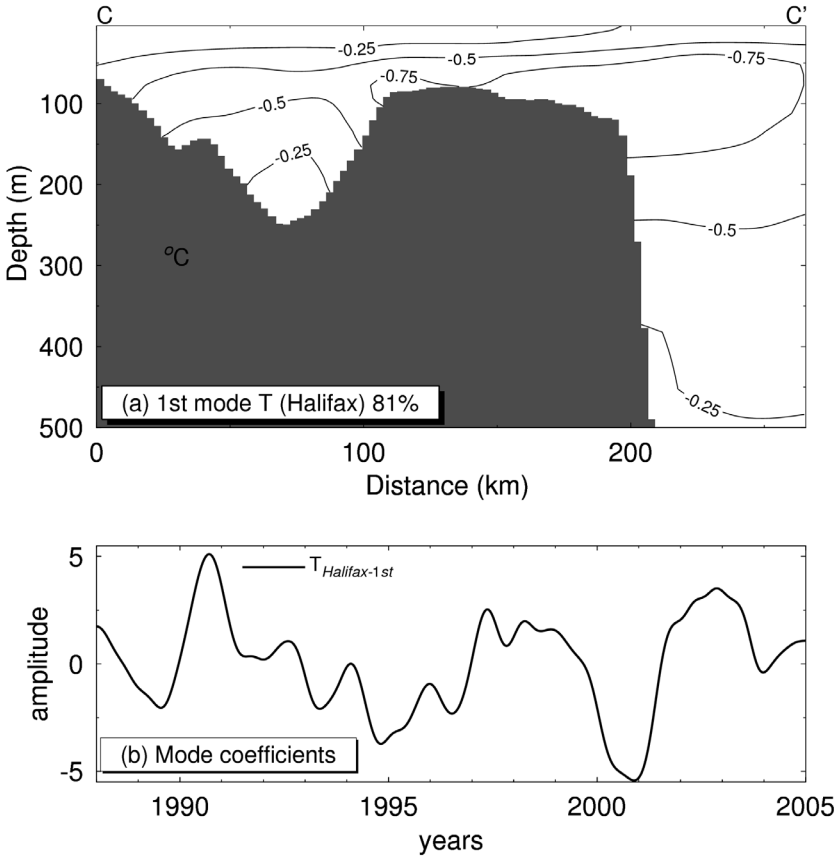

Figure 3.24. *Upper panel* shows distributions of the first EOF of the interannual variability of temperature along the Halifax Line (transect CC'). The *lower panel* shows the time series of the mode coefficients.

Along transect EE' in Cabot Strait, the first mode of intraseasonal variability in the normal currents has large amplitudes on both sides of the transect in the upper water column and small amplitudes in the deep waters of the transect (Fig. 3.25b). The large amplitudes of this first mode are significantly reduced in the upper water column if the time-mean atmospheric forcing is applied to the model (not shown). The first mode in the upper layer indicates that when the outflow from the GSL strengthens in the western side of Cabot Strait, the inflow into the GSL weakens on the eastern side of the transect. This mechanism represents the strength of the net seaward flow in the upper layer of the GSL. In the lower water column over Cabot Strait, the first mode of intraseasonal variations of normal currents features amplitudes of the opposite sign than in the upper water column,

indicating that over this part of the water column the intraseasonal anomalies have an opposite direction. This mode represents intraseasonal variations in the strength of the estuarine circulation over Cabot Strait, which is also coherent with the strength of the deep recirculation south of Anticosti Island (Fig. 3.25a) discussed above.

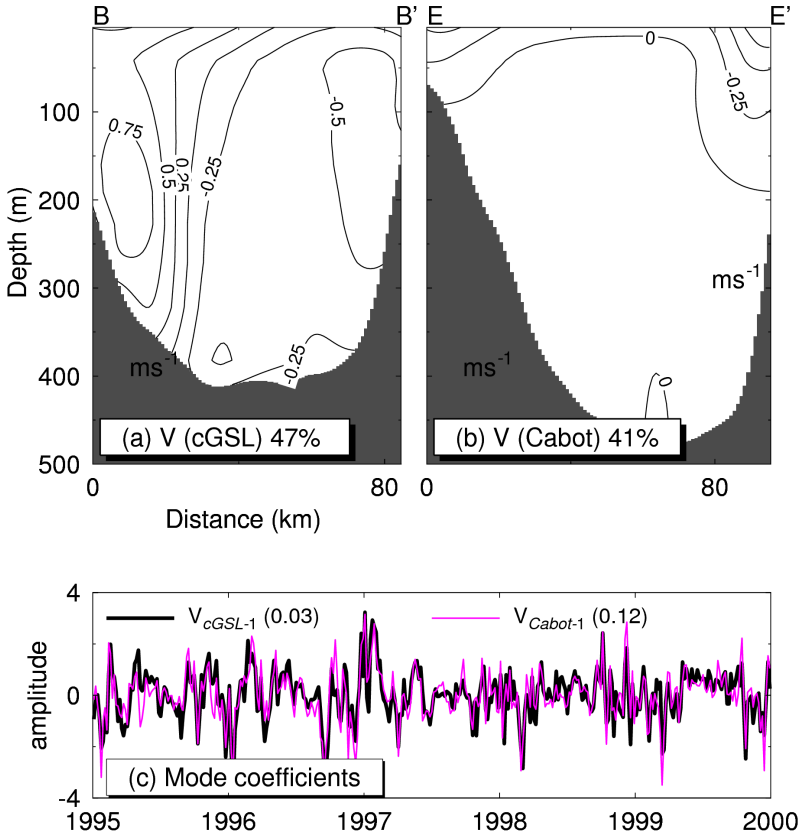

Figure 3.25. *Upper panels* show distributions of the first EOFs of intraseasonal variability in normal currents calculated from model results in the Control Run at transects (a) BB' at the cGSL and (b) EE' over Cabot Strait. The *lower panel* shows the time series of the normalized mode coefficients with the standard deviation indicated in parentheses.

The intraseasonal variability in the currents over the Scotian Shelf is not correlated to the intraseasonal variability in the GSL. The first two modes of intraseasonal variability of currents in the Scotian Shelf in the Control Run account for 72% of the total variance. The intraseasonal variability in the currents, temperature and salinity is larger over the Slope Water region than in nearshore waters, and is mainly caused by the non-linearity and the mesoscale variability of the flow (not shown). In the inner parts of the Scotian Shelf, the intraseasonal variability of the Nova Scotian Current is large in the Control Run and significantly smaller in ConstFluxes, indicating that temporal variability of the

wind forcing is responsible for the large intraseasonal variability of the Nova Scotian Current. Temporal variability of the wind affects vertical mixing in the water column either by changes in wind speed or by affecting coastal upwelling and horizontal currents due to variability in wind directions. Further studies are needed to quantify the importance of these mechanisms in driving the intraseasonal variability of the circulation over the inner Scotian Shelf.

3.5 Summary and Conclusion

A nested-grid shelf circulation model was used to examine circulation and hydrographic variability in four different frequency bands (time-mean, intraseasonal, seasonal, and interannual) over the Gulf of St. Lawrence (GSL), the Scotian Shelf (SS) and the Gulf of Maine (GOM). The nested-grid model has two components: a child model and a parent model. Both the child and parent models are based on the NEMO modelling system (Madec, 2008). The parent model was discussed previously by Urrego-Blanco and Sheng (2012). In this study I focused on the performance of the child model. I demonstrated that the child model performs reasonably well in simulating the time-mean general circulation and hydrography and associated variability in the study region.

Variability in the currents, temperature and salinity produced by the child model was examined by separating the 5-day mean model output in 17 years into the time-mean, seasonal, intraseasonal and interannual components. An empirical orthogonal function (EOF) analysis was conducted for model variables in each frequency band. Comparison of model results in different numerical experiments indicates that the time-mean circulation in the northern GSL, along Quebec's northern shore is mainly affected by the inflow through the Strait of Belle Isle. The temporal atmospheric variability also affects the time-mean southeastward flow over the Magdalen Shallows and is responsible for a broader and stronger outflow at the western side of Cabot Strait, which in turn affects the transport of the Nova Scotian Current, particularly over the northeastern Scotian Shelf. Model results also suggested that time-mean circulation in the GOM, particularly the

gulf-wide cyclonic circulation, is affected by the time-mean and temporal variability of the atmospheric forcing.

It was found that different physical processes are responsible for the seasonal variability of temperature and salinity in the study region. Seasonal variations in temperature are spatially coherent over the GSL-SS-GOM in response to surface heating in the upper water column in summer and cooling in the winter months, accompanied by convection and formation of a cold intermediate layer in late fall and winter. Seasonal variations of salinity, on the other hand, are mostly affected by river runoff and the equatorward advection of the fresh salinity signals by the coastal currents in the region including the Gaspé and the Nova Scotian currents. Over the GSL the high seasonal anomalies of salinity are coherent which could be caused by wind mixing of the surface layer with more saline deep waters in winter months.

My results also demonstrate that the interannual variability of simulated temperature and salinity in the GSL is affected by the variability in the atmospheric forcing and anomalies originated in the open ocean in the southern Newfoundland Shelf. This mechanism was found to account for more than 70% of the total interannual variability in the GSL and to be strongest in intermediate waters at depths between 50 m and 250 m. Over the Scotian Shelf, the interannual variability is affected more by anomalies generated by non-linear dynamics over the southern Newfoundland and northeastern Scotian Shelves (Urrego-Blanco and Sheng, 2012) which are advected by the equatorward shelf break jet. The EOF analysis of interannual variabilities from model results revealed cross-correlations between 0.85 and 0.98 between the first modes for temperature, salinity and normal velocity at the Halifax Line, indicating that stronger westward transport of the shelf break jet leads to cooler and fresher conditions along the transect.

The first mode of intraseasonal variability of currents in the GSL explained around 45% of the variance, with a correlation of about 0.8 between different sections in the GSL. This mode is related to the strength of the estuarine circulation over the western and

northwestern GSL. The largest intraseasonal current variability in the GSL occurs in Cabot Strait and is affected by the temporal variability of atmospheric forcing. The intraseasonal variability of currents at Cabot Strait in the model is not connected to intraseasonal fluctuations over the Scotian Shelf. The advection of intraseasonal anomalies between transects located along the Scotian Shelf plays only a minor role. The main mechanism affecting the intraseasonal variability of the Nova Scotian Current was found to be the temporal variability in the atmospheric forcing.

CHAPTER 4

FORMATION AND DISTRIBUTION OF SEA ICE IN THE GULF OF ST LAWRENCE: A PROCESS-ORIENTED STUDY USING A COUPLED OCEAN-ICE MODEL[1]

4.1 INTRODUCTION

The Gulf of St. Lawrence (GSL) is a semi-enclosed sea located in the eastern Canadian shelf, and is the habitat of ecologically and economically important marine species (Dufour and Ouellet, 2007). The GSL is also the main waterway route in Canada, connecting the Great Lakes region to the Atlantic Ocean. The GSL is connected to the Labrador Shelf through the Strait of Belle Isle and to the Newfoundland and Scotian Shelves through Cabot Strait (Fig. 4.1). The GSL is affected by large riverine input, oceanic and atmospheric forcing, and sea ice. The presence of sea ice not only has practical implications for various economical activities taking place in the GSL, but also affects hydrodynamics and ecosystem dynamics in the GSL. For instance, sea ice in the Gulf acts to insulate the ocean from the atmosphere, modifying the air-ocean fluxes and vertical convection. The presence of sea ice in the GSL also modifies the characteristics of the wind-driven circulation in the region since wind stress is not applied directly to the Gulf's surface but to the top of the sea ice. The salt rejection into the ocean during sea ice formation and the freshwater flux during sea melting affect salinity distributions in the upper layers of the GSL, which in turn modify deep convection and the buoyancy-driven circulation in the region.

[1] Urrego-Blanco, J. and J. Sheng. 2014b. Formation and distribution of sea ice in the Gulf of St. Lawrence: A process-oriented study using a coupled ocean-ice model. *Submitted to J. Geophys. Res*.

Sea ice has significant seasonal variability in the GSL. On average, sea ice begins to form in the upper St. Lawrence Estuary in early December and starts spreading seaward (Canadian Ice Service, 2011). Sea ice also appears early in shallow areas such as Baie des Chaleurs, Northumberland Strait and along the northern GSL. The appearance of sea ice progresses eastwards in the GSL, partially covering the central GSL and reaching the western Cabot Strait by the end of January. In February, sea ice thickens and covers most of the GSL except for waters off western Newfoundland. Sea ice is also exported from the GSL through western Cabot Strait. By mid-March the sea ice in the GSL reaches its maximum stage of development and then starts to melt.

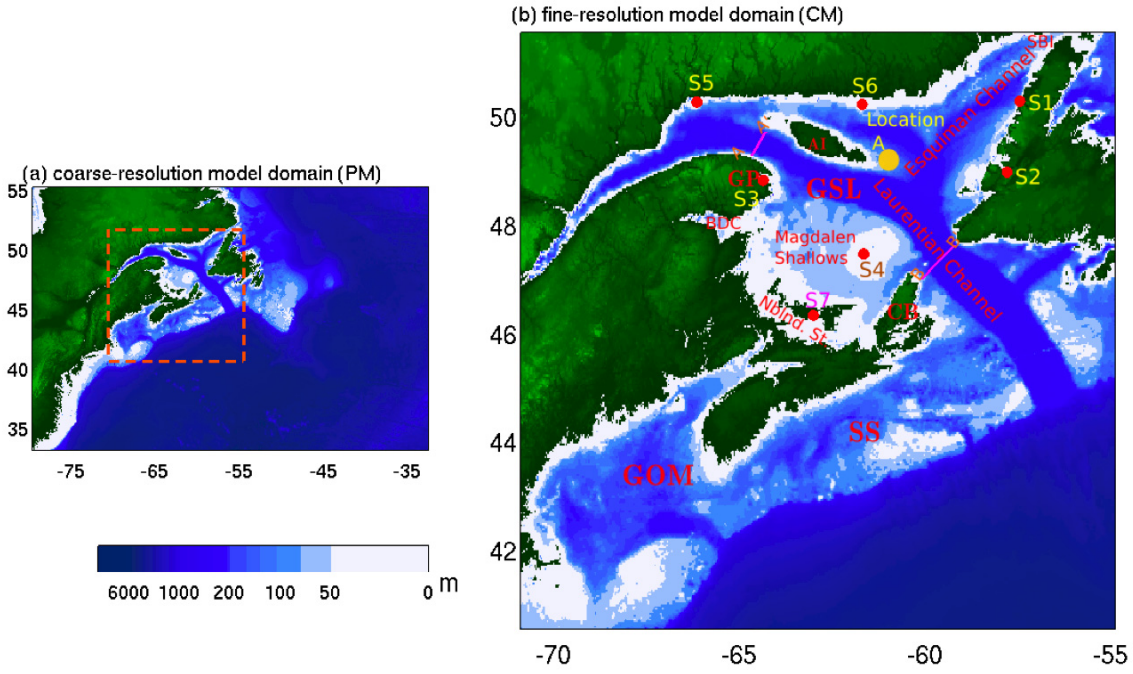

Figure 4.1. (a) Domain and bathymetry of the coarse-resolution parent model of the nested-grid model. Dashed lines in (a) mark the fine-resolution child model domain. (b) Domain and bathymetry of the child model. Abbreviations are used for the Gulf of St. Lawrence (GSL); Scotian Shelf (SS); Gulf of Maine (GOM); Strait of Belle Isle (SBI); Gaspé Peninsula (GP); Anticosti Island (AI); Baie des Chaleurs (BDC); and Northumberland Strait (Nblnd St). Meteorological stations are marked by red dots at Daniels Harbor (S1); Corner Brook (S2); Gaspé (S3); Magdalen Islands (S4); Sept Isles (S5); Natashquan (S6); and Charlottetown (S7).

Sea ice in the GSL has been subject to several studies in the past. Drinkwater et al. (1999) characterized the production and regional distributions of sea ice based on observations. Saucier et al. (2003) used a numerical model to reconstruct previous

observations of sea ice in the GSL and suggested that the growth rate of sea ice is sensitive to heat loss and stratification in fall and early winter. They also made some estimates of ice production in the GSL. Smith et al. (2013) recently developed a forecast sea ice system for the GSL. There are, however, many important scientific issues to be addressed regarding the dynamics and the thermodynamics of sea ice in the GSL. For instance, what are the roles of thermodynamic or dynamic processes in the sea ice distributions and variability in the GSL? what is the effect of sea ice on the circulation in the GSL, and how sensitive is sea ice in the Gulf to stability conditions in the lower atmosphere?

The main objective of this chapter is to examine the role of the thermodynamics and dynamics on the sea ice distribution in the GSL, based on results produced by a coupled ocean-ice model developed recently for the eastern Canadian shelf (Chapter 3). The structure of this chapter is as follows. A brief description of the coupled ocean-ice model and the model forcing is made in section 4.2. The performance of the coupled model in simulating sea ice and circulation in the GSL is evaluated in section 4.3. A process study of dynamics and thermodynamics of sea ice is presented in section 4.4. Summary and conclusions are presented in section 4.5.

4.2 Model Setup and Forcing

The coupled ocean-ice model used in this study was developed by Urrego-Blanco and Sheng (2014a) based on the Nucleus for European Modelling of the Ocean modelling system (NEMO). The ocean circulation component of the system uses version 9 of the Ocean PArallélisé ocean circulation model (OPA9). The sea-ice component uses the Louvain-la-Neuve Sea Ice Model (LIM2). The coupled model also uses a two-level nested-grid setup, with a fine-resolution child model (CM) nested inside a coarse-resolution parent model (PM). The PM covers the region of 34°N-55°N and 33°W-80°W with a nominal horizontal resolution of 1/4°. The CM domain covers the region of 41°N-52°N and 55°W-72°W with a nominal horizontal resolution of 1/12° (Fig. 4.1). The PM time step is 1800 s and the CM time step is 600 s. Both the PM and CM are coupled

using a two-way nesting technique in which the PM provides lateral open boundary conditions to the CM, and the CM results are used to adjust the PM fields over the region where the CM and PM overlap. A reader is referred to Urrego-Blanco et al. (2014) for more information about the nested-grid model setup. Unless otherwise stated, only the model results produced by the fine-resolution CM are used in this study.

4.2.1 Sea ice component

The sea ice component of the coupled ocean-ice system, LIM2, is a two-category (thick ice and open water) sea ice model that includes thermodynamics and dynamics of sea ice (Fichefet and Morales-Maqueda, 1997; Goosse and Fichefet, 1999). The thermodynamic component of LIM2 is a three-layer thermodynamic model suggested by Semtner (1976), which consists of two layers of ice of equal thickness and one layer of snow which can accumulate if the surface temperature falls below the freezing point (Semtner, 1976; Fichefet and Morales-Maqueda, 1997). The vertical profile of temperature within the ice is determined by solving the one-dimensional heat diffusion equation, with the thermal conductivity to be parameterized as a function of ice thickness. The thermodynamic component uses a parameterization to allow the incoming shortwave radiation to be stored in brine pockets within the ice pack, and a parameterization of the surface albedo as a function of ice thickness and cloudiness (Shine and Henderson-Sellers, 1985). The thermodynamic component also accounts for creation of new ice in the open water and at the ice bottom, creation of snow-ice at the top of the ice pack, and melting at the upper and lower interfaces of the ice pack.

The dynamic component of LIM2 treats the ice pack as a two-dimensional compressible fluid driven by winds and ocean currents based on the conservation of linear momentum defined as:

$$m\frac{\partial \vec{u}}{\partial t} = A(\vec{\tau}_{ai} + \vec{\tau}_{io}) - mf\vec{k} \times \vec{u} - mg\nabla\eta + \nabla \cdot \vec{\sigma} \tag{4.1}$$

where m is ice mass per unit area, $\vec{u}$ is the ice velocity vector, $\vec{\sigma}$ is the internal stress tensor, A is the ice concentration, $\vec{\tau}_{ai}$ and $\vec{\tau}_{io}$ are the air-ice and ice-ocean momentum

fluxes, respectively, f is the Coriolis parameter, $\vec{k}$ is a unit vector pointing upwards, g is the gravity acceleration, and η is the sea surface elevation. The internal ice stress is dependent on the ice strength and the strain rate through a viscous-plastic constitutive law. The latter describes the nature of the ice interaction (Hibler, 1979). The ice strength is assumed to be a simple function of ice thickness and concentration. The advection term ($\vec{u} \cdot \nabla \vec{u}$) is neglected in Eq. (4.1) since this term is small in comparison with the local acceleration term $\left(\frac{\partial \vec{u}}{\partial t}\right)$ (Thorndike, 1986). Changes in volume and area of ice resulting from the sea ice dynamic and thermodynamic sources and sinks are accounted for through the conservation of ice volume and area according to:

$$\frac{\partial \chi}{\partial t} = -\nabla \cdot (\vec{u}\chi) + T_{\chi} \tag{4.2}$$

where χ is the model variable (ice concentration, or ice volume per unit area) being conserved and T_{χ} is the rate of change of χ due to themodynamics.

4.2.2 Ocean circulation component

The ocean circulation component of the coupled ocean-ice model is OPA9, which is a primitive equation, second-order, *z*-coordinate numerical model and uses a linear formulation of the free surface (Roullet and Madec, 2000). The circulation model uses 46 *z*-levels in the vertical and bathymetries based on the 2-minute gridded global relief data (Smith and Sandwell, 1997). The circulation component uses a sub-grid scale parameterization of horizontal mixing based on a biharmonic friction, with a Smagorinsky-like formulation of mixing coefficients for momentum and tracers (Griffies and Hallberg, 2000). The vertical sub-grid scale vertical mixing is based on a parameterization using the turbulent closure scheme of Gaspar et al. (1990). The circulation component also uses spectral nudging (Thompson et al. 2006) and semi-prognostic methods (Sheng et al. 2001) to reduce seasonal bias and drift in the model. The sea surface salinity in the model is restored to the climatological monthly mean surface salinity.

4.2.3 Coupling between the ocean and sea ice components

The ocean circulation component is coupled (as described in Chapters 2 and 3) to the sea ice component by the exchange of heat, freshwater and momentum at the ice-ocean interface. At the ocean surface, the net heat flux (Q) is computed based on:

$$Q = f_i Q_{io} + (1 - f_i)\left[Q_{sw} + Q_{lw} + Q_s + Q_l\right] \tag{4.3}$$

where f_i is the fraction of each model grid cell covered by sea ice and Q_{io} is the ice-ocean heat flux. The last four terms on the right hand side of Eq. (4.3) represent the air-ocean heat fluxes. Q_{sw} and Q_{lw} are the shortwave and longwave radiations into the ocean respectively, and Q_s and Q_l are the sensible and latent heat fluxes respectively. In Eq. (4.3) Q_{io} also represents the balance between the shortwave radiation reaching the bottom of the ice cover (Q_{swio}) and the sensible heat flux from the ice to the ocean (Q_{sio}) defined as:

$$Q_{swio} = i_o (1 - \alpha) Q_{sw} e^{\left[-1.5(h_i - 0.1)\right]} \tag{4.4}$$

$$Q_{sio} = \rho_0 C_w C_{io} u_{io}^{*} \left(T_f - T_0\right) \tag{4.5}$$

where i_o is the fraction of the net shortwave radiation penetrating the snow-ice layer, α is the albedo of the snow-ice, and h_i is the mean sea ice thickness. In Eq. (4.5) ρ_o is a reference density of seawater, C_w the specific heat of seawater, C_{io} an exchange coefficient equal to 0.006, u_{io}^{*} the friction velocity between the ice and the ocean surface, T_f the freezing point of seawater assumed to be a quadratic function of sea surface salinity, and T_0 the temperature of the surface layer of the ocean.

The sea ice and the ocean circulation components are also coupled through the exchange of freshwater at their interface. For the circulation component, the net freshwater flux (F) is given by:

$$F = f_i F_{io} + (1 - f_i)\left[E - P\right] + R \tag{4.6}$$

where F_{io} is the ice-ocean freshwater flux, E is the evaporation of seawater, P is the

precipitation over the ocean, and R is the continental runoff specified as a water flux near river mouths. In Eq. (4.6), F_{io} includes the effect of snow and ice melting, and salt rejection during ice formation:

$$F_{io} = S_m\left(\frac{\partial m_s}{\partial t}\right) + \left(S_m - S_i\right)\left(\frac{\partial m_i}{\partial t}\right) + \left(S_m - S_i\right)\left(\frac{\partial m_s}{\partial t} + \frac{\partial m_i}{\partial t}\right) + S_i\left(\frac{\partial m_s}{\partial t}\right) \tag{4.7}$$

where S_m and S_i are a reference seawater salinity and the sea ice salinity, respectively, and m_s and m_i are the masses of snow and ice per unit area, respectively. The stress $\vec{\tau}$ at the ocean surface is specified as:

$$\vec{\tau} = f_i\vec{\tau}_{io} + (1 - f_i)\vec{\tau}_{ao} \tag{4.8}$$

where $\vec{\tau}_{ao}$ is the air-ocean momentum flux estimated based on the formulation of Large and Pond (1981) using transfer coefficients suggested by Large and Yeager, (2004), and $\vec{\tau}_{io}$ is the ice-ocean momentum transfer defined as a quadratic function of the difference between the ice velocity ($\vec{u}_i$) and surface ocean velocity ($\vec{u}_o$):

$$\vec{\tau}_{io} = \rho_o C_{Dio}|\vec{u}_i - \vec{u}_o|\left(\vec{u}_i - \vec{u}_o\right) \tag{4.9}$$

where C_{Dio} is the drag coefficient between ice and ocean set to 1.6×10^{-3}.

4.2.4 Model forcing

As mentioned in section 4.2.3, the fluxes of momentum, heat and freshwater at the surface of the ice-ocean system are specified based on Eqs. (4.3-4.9) using the atmospheric reanalysis fields with a horizontal resolution of 2° produced by Large and Yeager (2004). The atmospheric fields used here consist of 6-hourly wind speed, air temperature and specific humidity at 10 m above the sea surface, 12-hourly short and long wave radiation and monthly precipitation. The air-sea fluxes are estimated based on the bulk formulae with the drag coefficient, and transfer coefficients for evaporation and sensible heat estimated in terms of height, atmospheric stability, wind speeds, and clear-sky conditions suggested by Large and Yeager (2004).

To evaluate the accuracy of the atmospheric reanalysis data over the study region, the air temperatures (T_R) and wind speeds (W_R) from the reanalysis fields were interpolated onto seven stations in the GSL (marked in Fig. 4.1b) and compared with observations (T_O, W_O) obtained from the National Climate Data and Information Archive of Environment Canada. Figure 4.2 presents scatterplots of the observed and reanalyzed data of the daily mean maximum and minimum winter air temperatures and wind speeds at Natashquan (Fig. 4.1) for the period 1988-2004. To quantify the error in the atmospheric reanalysis, the absolute difference between the observations and the reanalysis is calculated for the maximum and minimum temperatures and wind speeds, and then averaged over the entire daily record in 1988-2004 to obtain the average absolute difference (AAD) based on:

$$AAD = \frac{1}{D}\sum_{d=1}^{D}\left|O_d - R_d\right| \tag{4.10}$$

where O_d and R_d are the daily minimum and maximum temperatures and wind speeds obtained from observed and reanalyzed fields respectively, and D is the number of daily records in the period 1988-2004.

The data points in Fig. 4.2 are scattered around the line of perfect agreement for the daily minimum (AAD_{TMIN}=2.9°C) and daily maximum (AAD_{TMAX}=1.9°C) air temperatures at Natashquan, indicating that there are no obvious systematic biases and trends at this location. Table 4.1 lists the AAD values at seven stations in the GSL. The AAD value is relatively small at the Magdalen Islands (AAD_{TMIN}=1.7°C and AAD_{TMAX}=1.3°C) and large at Sept Iles (AAD_{TMIN}=3.1°C and AAD_{TMAX}=2.9°C). It is important to note that sea ice formation is sensitive to the estimates of the net heat fluxes at the air-ocean interface. The latter are calculated using the air temperature fields extracted from the atmospheric reanalysis data. Therefore, large errors in the air temperatures could lead to large errors in the sea ice formation in the model.

For the analyzed wind speeds, the data points are scattered more above than below the line of perfect agreement, indicating a tendency of the reanalysis fields of wind speeds to

overestimate the observed minimum and maximum wind speeds at Natashquan (Fig. 4.2c, d). At this station, the absolute errors in the reanalyzed wind speed data are about 1.3 ms^{-1} and 1.6 ms^{-1} for the minimum and maximum wind speeds, respectively. The AAD values of wind speeds at other stations in the GSL listed in Table 4.1 also feature relatively small values of about 1-3 ms^{-1} and 1.5-4 ms^{-1} for the daily minimum and maximum wind speeds, respectively.

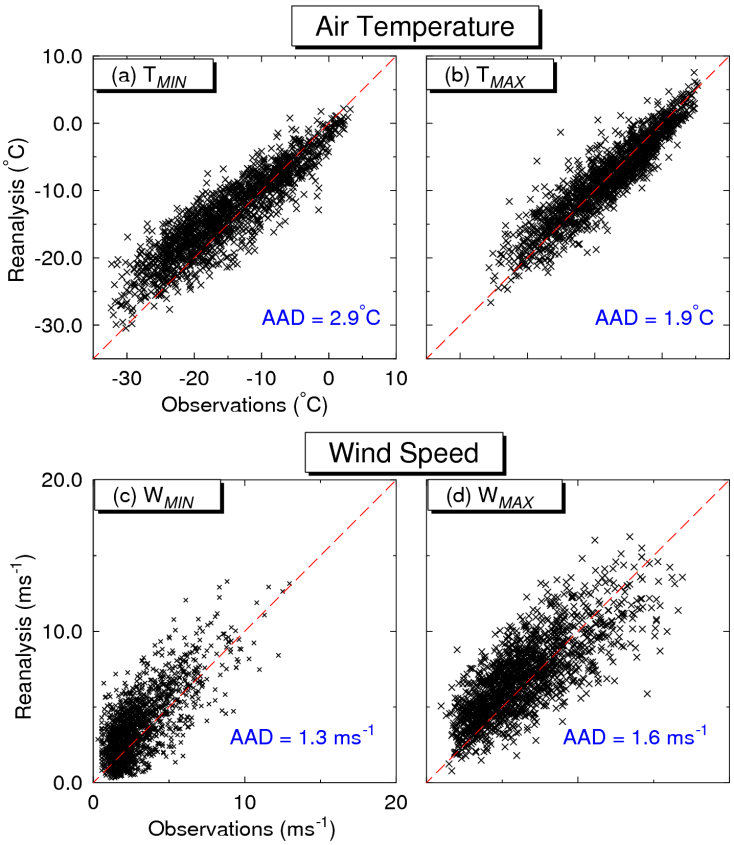

Figure 4.2. Scatterplots of daily minimum (a, c) and maximum (b, d) air temperatures (upper panels) and wind speeds (lower panels) at Natashquan (S6 marked in Fig. 4.1b) estimated from the atmospheric reanalysis of Large and Yeager (2004) and from observations archived in the National Climate Data and Information Archive of Environment Canada.

Table 4.1. Average absolute differences between the observed and reanalyzed daily minimum and maximum air temperatures (AAD_T) and wind speeds (AAD_W) at seven stations in the Gulf of St. Lawrence marked in Fig. 4.1.

Station	AAD_T (°C)		AAD_W (ms^{-1})	
	min	max	min	Max
Sept Isles	3.1	2.9	0.9	1.5
Charlottetown	2.3	1.7	2.3	3.7
Natashquan	2.9	1.9	1.3	1.6
Gaspé	2.4	1.9	2.3	3.4
Corner Brook	1.9	1.6	3.0	4.1
Daniels Harbor	2.4	2.0	1.7	2.1
Magdalene Islands	1.7	1.3	1.9	2.5

To further examine the accuracy of the atmospheric reanalysis data, the reanalyzed air temperatures (T) and wind speeds (W) at each station are decomposed into components in four frequency bands. The four frequency bands are the time-mean ($\overline{T},\overline{W}$), the annual cycle ($\tilde{T},\tilde{W}$), the high frequency with periods less than 12 months (T',W'), and the interannual ($\hat{T},\hat{W}$) component with periods greater than 12 months. Figure 4.3 shows the original time series and their components in three frequency bands of the reanalyzed and observed air temperatures at Charlottetown. The reanalyzed air temperatures compare well with the observations at this station. In particular, the amplitudes of the seasonal cycle of about 30°C in the reanalyzed air temperature data are in close agreement with the observations (Fig. 4.3b). The seasonal cycle of the reanalyzed air temperatures, however, lags behind the observed seasonal cycle by about two weeks. The high-frequency variability in the reanalyzed air temperatures at Charlottetown is also in relatively good agreement with the counterparts of observations (Fig. 4.3c). The errors in the high frequency temperature variations are generally small in the reanalysis data, with errors of more than 5°C in a few events. The low frequency variations in the reanalysis of air temperature at Charlottetown are generally within ±0.5°C of the counterparts of observations, except for relatively large errors of about 1.5°C in 1999 (Fig. 4.3d).

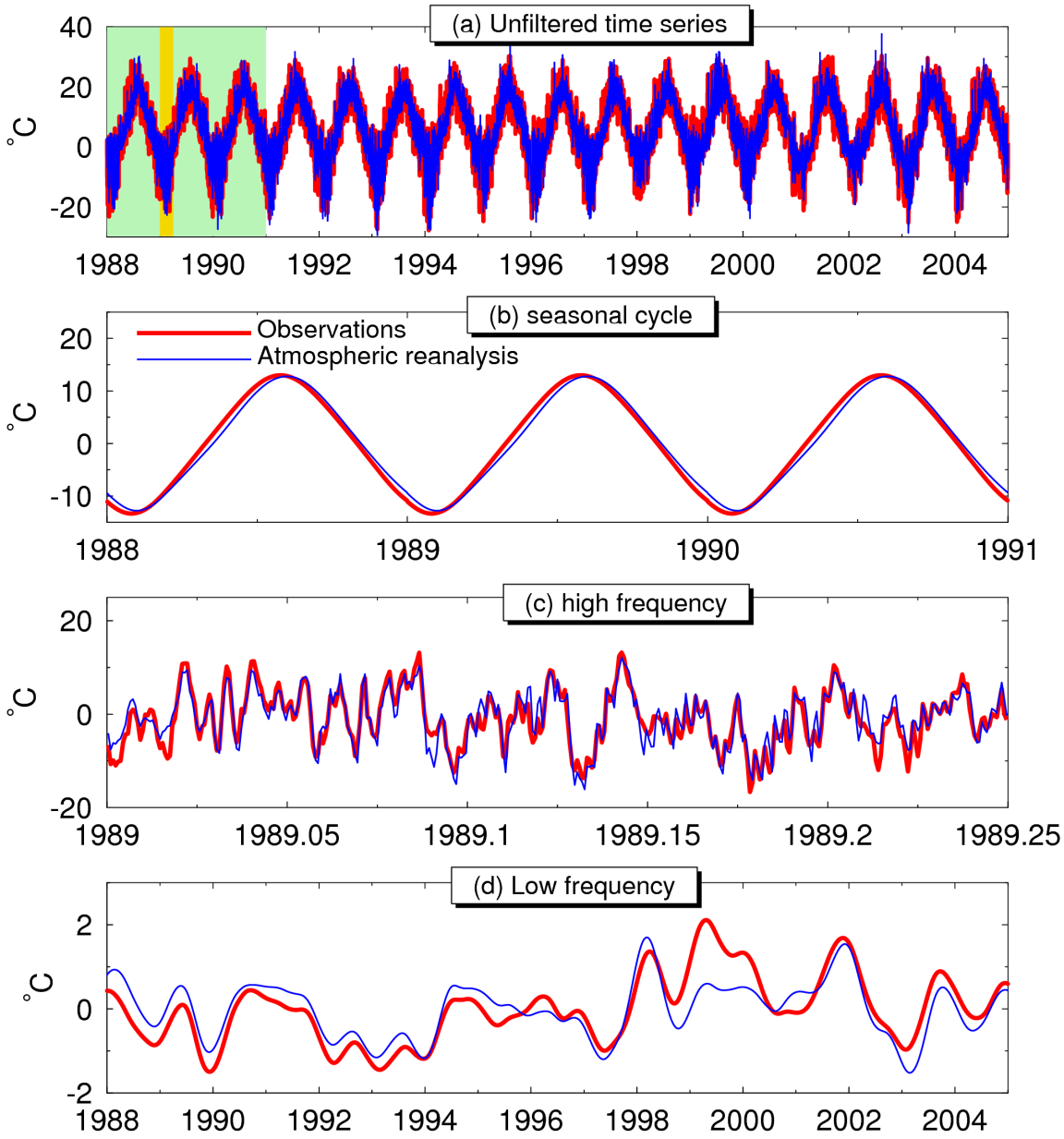

Figure 4.3. Time series of 6-hourly air temperatures at 10 m above the sea surface observed at Charlottetown (red) (Fig. 4.1) and from the atmospheric reanalysis fields (blue) of Large and Yeager (2004). From top to bottom panels show (a) the original time series, (b) the seasonal cycle, (c) the high frequency, and (d) the low frequency component. The time window shaded in green in (a) is shown in the time series in (b) and the time window shaded in yellow is shown in panel (c).

To examine the distribution of the errors in the reanalysis data ($\varepsilon_T = T_O - T_R$ and $\varepsilon_W = W_O - W_R$) at seven stations in the GSL, their probability density functions (PDF) are calculated using the kernel density estimation technique (Parzen, 1962). This technique

provides an estimate of the PDF of a random variable from a sample data set. The estimate of the PDF for the reanalysis error (ε) is obtained based on:

$$\hat{f}(\varepsilon) = \frac{1}{nh}\sum_{j=1}^{n} K\left(\frac{\varepsilon - \varepsilon_j}{h}\right) \tag{4.11}$$

where $\hat{f}(\varepsilon)$ is an estimate of the PDF of ε, K is a weighting function taken to be a normal distribution in this study, h is the bandwidth controlling the smoothness of the estimated PDF, and n the number of elements in the data set which in this study is the number of 6-hourly reanalysis errors during 1988-2004. The peak of the distributions ($\hat{f}(\varepsilon)$) represents bias, and the shape of the distribution represents the temporal (or spatial) variation of the error. For instance, if the peak is located at a positive value, there is negative bias. A wide distribution represents large temporal (or spatial) variations in the error, and a narrow distribution represents uniformly distributed errors.

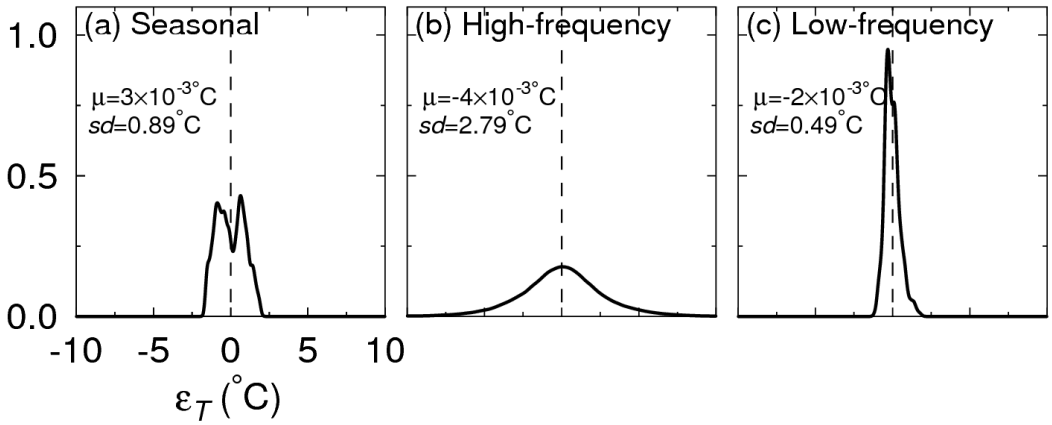

Figure 4.4. Probability density functions of reanalysis errors in frequency bands of (a) seasonal cycle, (b) high frequency, and (c) low frequency components for the air temperatures at seven stations in the GSL (marked by red dots in Fig. 4.1b).

Figures 4.4 and 4.5 present the PDFs of reanalysis errors at seven stations in the GSL for air temperatures and wind speeds on the three frequency bands of the seasonal cycle, high frequency and low frequency components, respectively. The errors in the seasonal cycle of the reanalyzed air temperatures ($\tilde{\varepsilon}_T$) feature a relatively narrow bimodal PDF distribution with one mode centered at about –1°C and the other centered at about 0.8°C (Fig. 4.4a). This bimodal distribution is consistent with the time shifting between the

seasonal cycles shown in Fig. 4.3b. The mean (μ) and standard deviation (sd) of $\tilde{\varepsilon}_T$ are about 3×10^{-3}°C and 0.9°C respectively, indicating that the seasonal cycle of the reanalyzed air temperatures are in good agreement with the counterparts of the observations. The PDF of the errors in the high frequency component of the reanalyzed air temperatures (ε'_T) has a Gaussian-type distribution with a mean value close to zero (μ=0.004°C), and is relatively broad with sd=2.8°C, indicating that the temporal variability of the air temperature errors is large in the high frequency band (Fig. 4.4b). The low frequency component of the reanalyzed air temperature has the smallest errors as indicated by its narrow PDF distribution having a standard deviation of about 0.5°C (Fig. 4.4c). The PDF of the errors in the seasonal cycle of the reanalyzed wind speeds ($\tilde{\varepsilon}_W$) is characterized by a relatively narrow distribution with a standard deviation of about 0.55 ms^{-1} (Fig. 4.5a) and a mode of about 0.5 ms^{-1}. The PDF of the errors in the high frequency component of the wind speeds (ε'_W) have a small mean value of about 4×10^{-6} ms^{-1} and a large temporal variability with a standard deviation of 1.99 ms^{-1} (Fig. 4.5b). The smallest reanalysis errors in wind speeds occur at low frequencies ($\hat{\varepsilon}_W$) as indicated by the PDFs, which have a mean error very close to zero and a narrow distribution with a standard deviation of about 0.26 ms^{-1} (Fig. 4.5c).

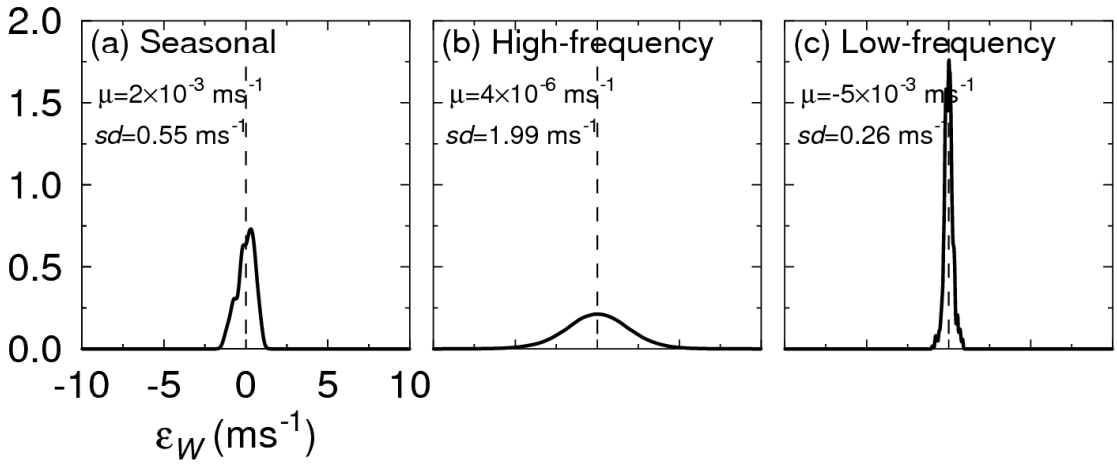

Figure 4.5. Probability density functions of reanalysis errors in frequency bands of (a) seasonal cycle, (b) high frequency, and (c) low frequency components for the wind speeds at seven stations in the GSL (marked by red dots in Fig. 4.1).

4.3 Validation of Model Performance in Simulating Circulation and Sea Ice in the GSL

The coupled ocean-ice model is initialized from the January mean hydrography of Geshelin et al. (1999) and integrated from 1987 to 2004. The model results in the last 17 years (1988-2004) are used in the study. In this study the assessment of the model performance in simulating circulation and hydrography focuses on surface fields. The reader is referred to Chapters 2 and 3 for more discussion on the validation of the ocean circulation component.

Figure 4.6 presents the seasonal mean sea surface temperatures (SSTs) in fall and winter in the GSL calculated from satellite remote sensing data (Reynolds et al., 2007) and model results during 1988-2004. It should be noted that the satellite remote sensing SSTs over ice-covered areas in Fig. 4.6c are based on a quadratic relationship of SSTs with ice concentrations (Rayner et al., 2003). The satellite data demonstrate that the SSTs in fall in the GSL are characterized by relatively cold waters over the St. Lawrence Estuary and the central and northeastern GSL. The warmest surface conditions during fall occur in shallow waters around Prince Edward Island. In winter, SSTs drop significantly over the entire Gulf, with surface temperatures of about 0°C over the central and western GSL and about 1°C near Cabot Strait and the southern Magdalene Shallows.

The simulated seasonal mean SSTs (Fig. 4.6b,d) are in good agreement with the remote sensing estimates (Fig. 4.6a,c), particularly in fall when both model results and observations feature surface waters around 8°C over the central and northern GSL, and relatively warmer waters over the Magdalene Shallows. It should be noted that the simulated SSTs are, however, relatively warmer than the observations over Northumberland Strait by about 1°C. In winter, the simulated SSTs are also in general agreement with the remote sensing data, which is partially due to the use of spectral

nudging to reduce temperature biases. It should be noted, however, that model results are slightly colder than the observations by about 1°C.

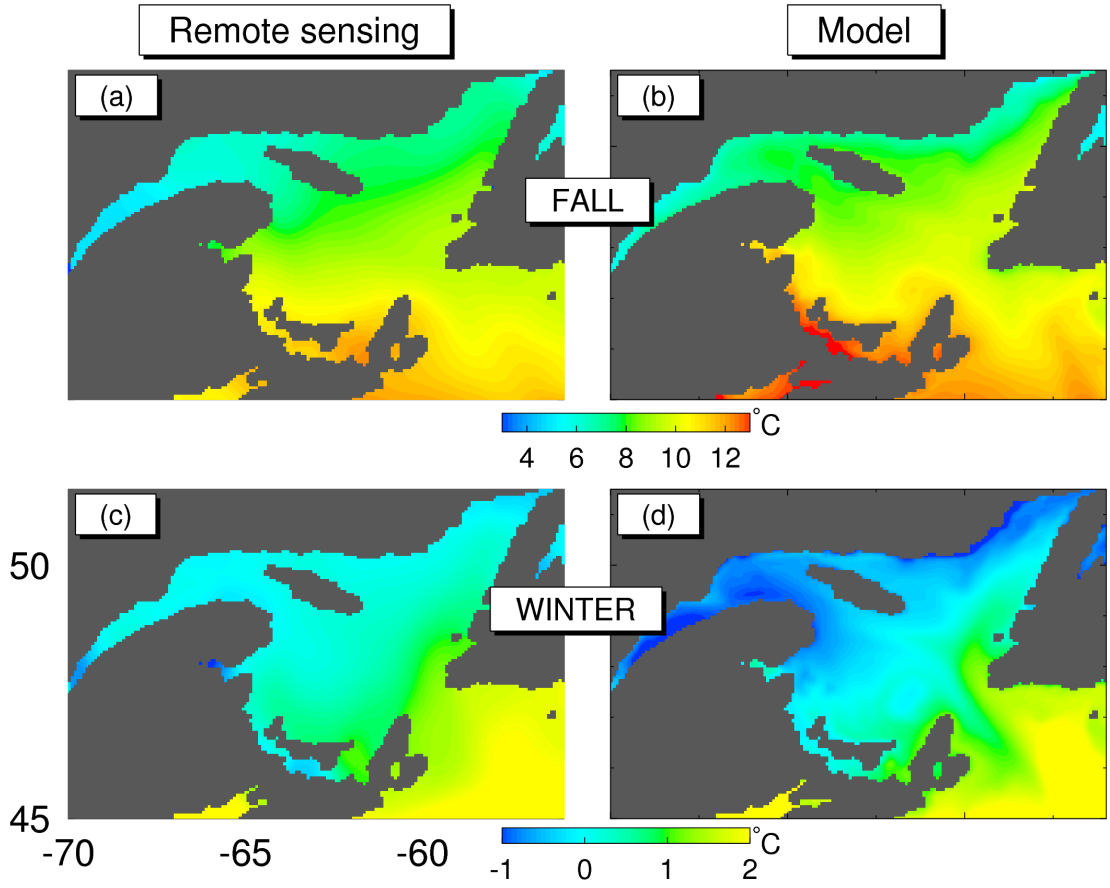

Figure 4.6. Distributions of seasonal mean sea surface temperatures (SSTs) in the Gulf of St. Lawrence and adjacent waters calculated from (a, c) satellite remote sensing data (NOAA) and (b, d) model results in the 17-year period 1988-2004.

Figure 4.7 presents the probability density functions of spatial model errors in simulating the seasonal mean SSTs in the GSL in four seasons. The spatial model errors in the seasonal mean SSTs are defined as (SST_{OBS}-SST_M), where SST_{OBS} are the observed SSTs and SST_M the model simulated SSTs at every model grid point. Model errors in fall are mainly negative (μ= –0.65°C), indicating that model estimates of SSTs, on average, are slightly warmer than the remote sensing data (Fig. 4.7d). By contrast, the model errors are slightly positive in winter (μ=0.38°C), spring (μ=0.28°C), and summer (μ=0.88°C), indicating, on average, cooler surface conditions produced by the model than

observations in these three seasons (Fig. 4.7a-c). The PDFs with similar widths in Fig. 4.7a,b,d indicate that model errors in the SSTs have similar spatial variability in winter (*sd*=0.40°C), spring (*sd*=0.57°C), and fall (*sd*=0.55°C). By comparison, the relatively broad distribution of the PDF in Fig. 4.7c indicates that the model errors in SSTs have large spatial variability (*sd*=0.84°C) in summer.

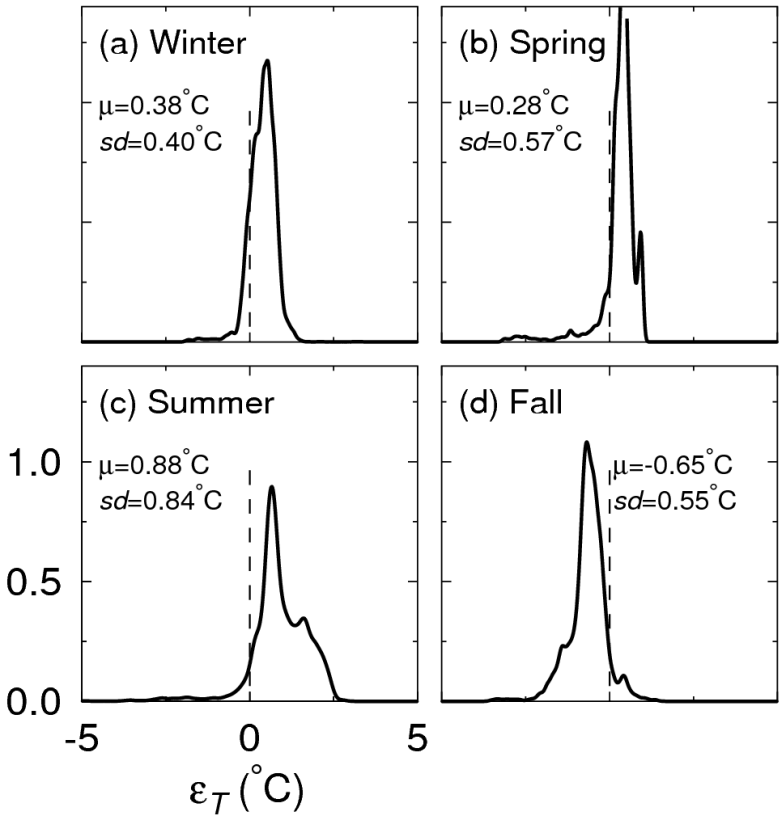

Figure 4.7. Probability density functions of model errors in simulating sea surface temperatures in the Gulf of St. Lawrence in (a) winter, (b) spring, (c) summer, and (d) fall in the 17-year period 1988-2004.

Next, the performance of the coupled ocean-ice model in simulating sea ice is evaluated by comparing model results with the observational estimates provided by the Canadian Ice Service (2013). Observational data used here include ship and aircraft observations and radarsat imagery. Observational datasets of sea ice typically consist of ice state variables such as ice concentrations and stages of ice development. The stage of ice development is used as a proxy to estimate the sea ice thickness. In this study the monthly-mean sea ice thickness in the GSL is estimated based on the equivalences

between ice age and thickness listed in Table 4.2 according to the coding convention for sea ice known as the *egg code* (Karvonen et al., 2012).

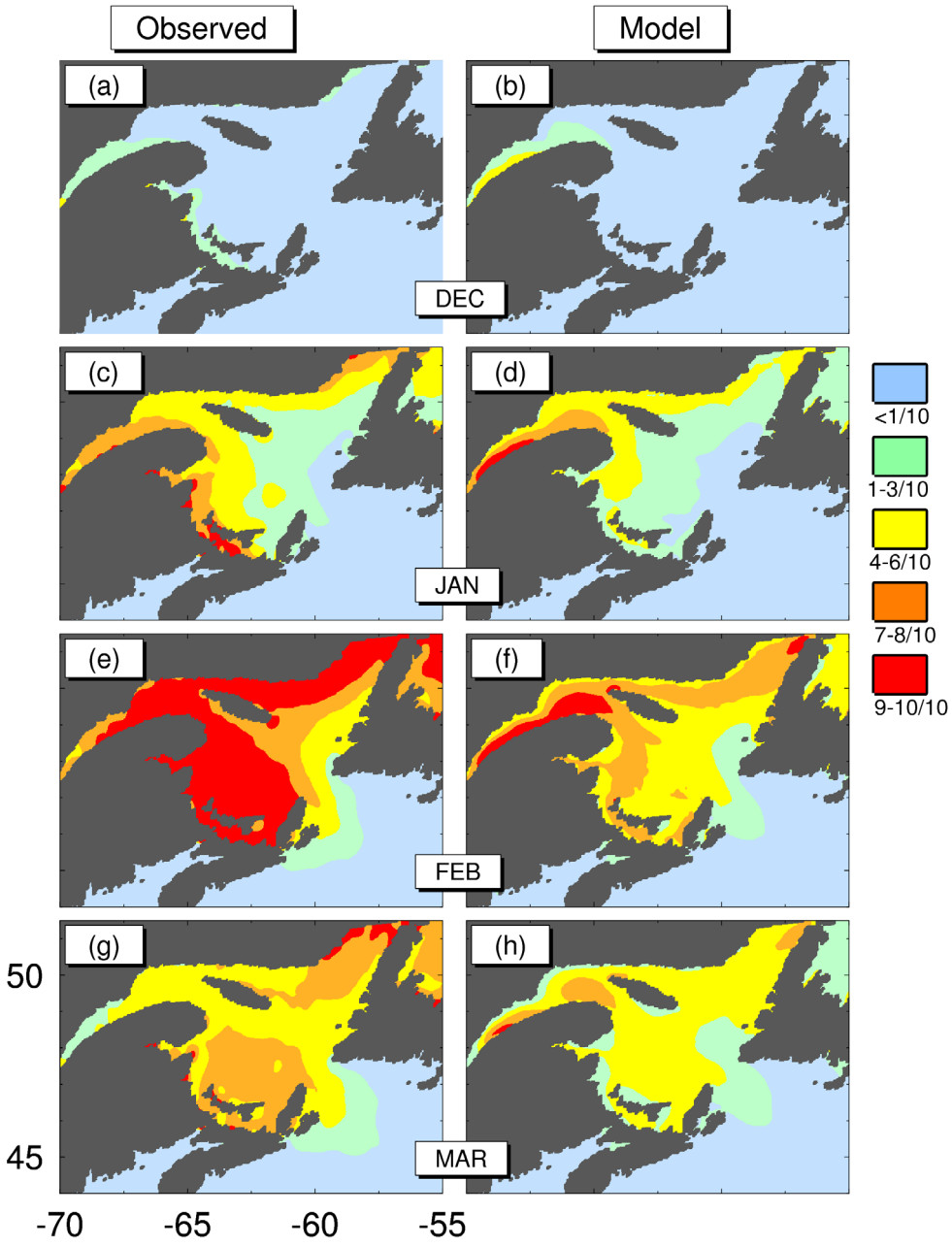

Figure 4.8. Monthly-mean observed (left panels) and simulated (right panels) sea ice concentrations in winter months calculated from observational estimates (Canadian Ice Service) and model results during the 17-year period 1988-2004.

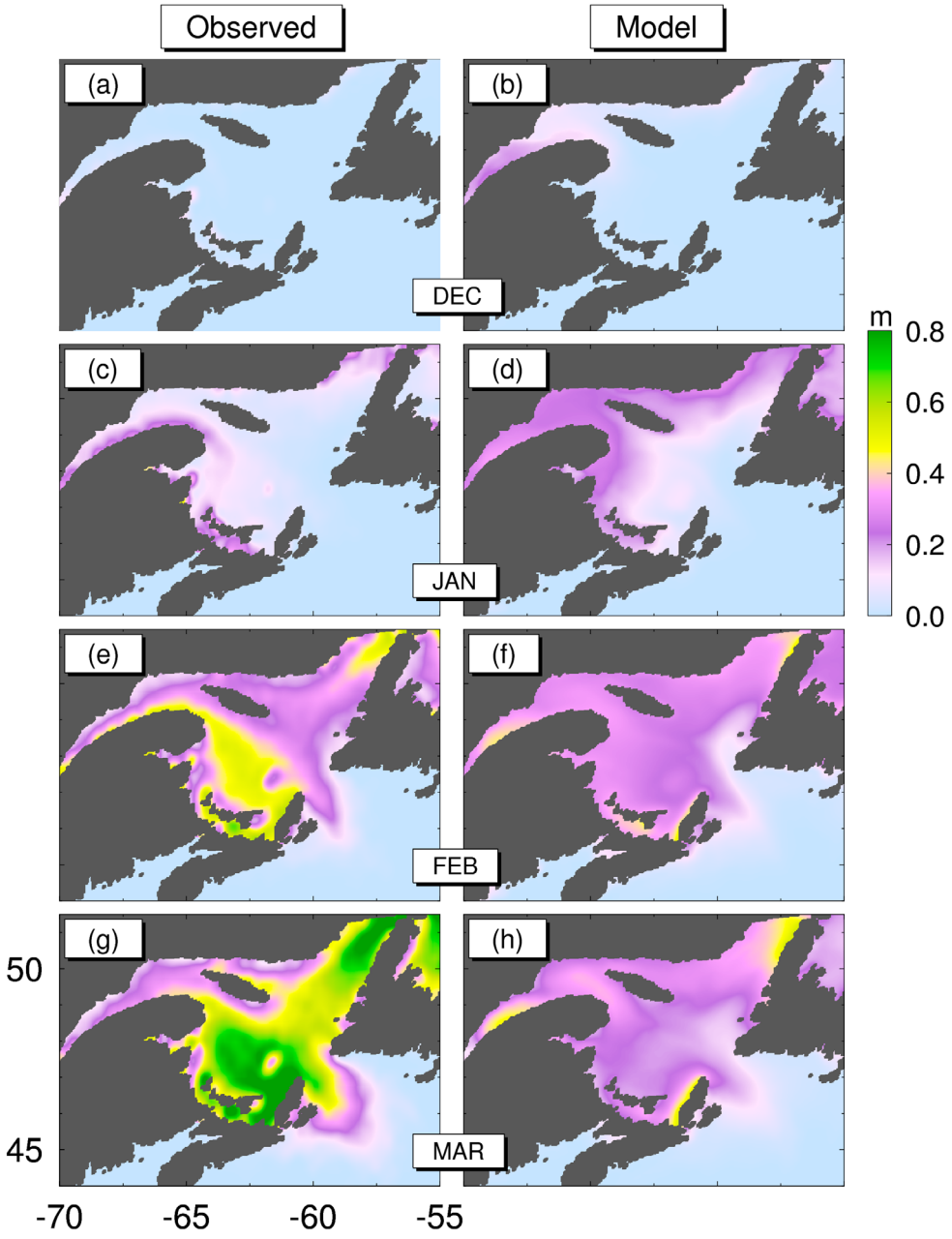

Figure 4.9. Monthly-mean observed (left panels) and simulated (right panels) sea ice thickness in winter months calculated from observational estimates (Canadian Ice Service) and model results during the 17-year period 1988-2004. The observed thickness was estimated from the equivalences between ice type and thickness shown in Table 4.2.

Table 4.2. Equivalences between ice age and thickness according to the coding convention known as *egg code*, used to obtain observational estimates of sea ice thickness from remote sensing data (Karkoven et al., 2012).

Egg code	Stage of development	Thickness (cm)
1	New ice	7.5
2	Nilas	7.5
3	Young ice	15
4	Gray Ice	15
5	Gray-white ice	30
6	First-year ice	50
7	Thin first-year ice	60
1.	Medium first-year	120
4.	Thick first-year ice	140

Figures 4.8 and 4.9 present observed and simulated monthly-mean sea ice concentrations and thickness for the winter months in 1988-2004. The monthly-mean observed ice fields reveal that very thin ice appears first in December in the St. Lawrence Estuary and along coastal waters to the south of the Baie des Chaleurs and over Northumberland Strait. The monthly-mean observed sea ice concentrations in these regions range between 10-30% in December (Figs. 4.8a and 4.9a). In January, the observed sea ice thickens over the western GSL and along Québec's northern shore has ice concentrations above 40%. In this month the maximum ice concentrations and thickness occur over Northumberland Strait which are about 90% and 30 cm, respectively (Fig. 4.8c and 4.9c). Also in January, thin ice with relatively low concentrations appears over the central GSL. In February, sea ice is present over most of the GSL, with observed concentrations near 100% over the western Gulf and between 40-80% over the eastern Gulf. Some areas over the eastern Scotian Shelf near Cape Breton have observed sea ice concentrations between 10-60% (Fig. 4.8e). During February, the observed ice thickness is greater than 50 cm over the Magdalen Shallows, Northumberland Strait and near the Strait of Belle Isle (Fig. 4.9e). In March, the observed sea ice starts to melt but relatively

dense ice packs still occur over the Magdalen Shallows, along the western coast of Cape Breton, and over the northeastern GSL (Fig. 4.8g). The maximum thickness of about 80 cm appears in the Esquiman Channel and the Magdalen Shallows (Fig. 4.9g).

The simulated monthly-mean sea ice concentrations (Figs. 4.8b,d,f,h) have typical seasonal variations and horizontal distributions similar to the observations discussed above. In particular, simulated sea ice also starts to appear in December in the upper St. Lawrence Estuary, reaches maximum concentrations in February, and starts to melt in March. The coupled model also generates high ice concentrations in January over the coastal waters along Québec's northern shore and around Prince Edward Island, which are in good agreement with observations. The coupled ocean-ice model also reproduces well the presence of sea ice over the Scotian Shelf and the Laurentian Channel outside the GSL during February and March. The simulated sea ice in the GSL also displays a progressive thickening from December to March (Figs. 4.9b, d, f, h), which is qualitatively similar to the general patterns of ice thickening revealed by the observations. Furthermore, the areas with the maximum ice thickness produced by the coupled model include the Magdalen Shallows, coastal waters off western Cape Breton, and the southeastern Esquiman Channel, which are similar to the areas of maximum observed sea ice.

It should be noted that, except for the use of the spectral nudging and semi-prognostic methods to eliminate seasonal bias, the coupled ocean-ice model is prognostic. As a result, the model performance is not always satisfactory, particularly for the sea ice simulation. In December, for example, the simulated concentrations and thickness over the St. Lawrence Estuary are slightly higher than observations and the model also does not reproduce the incipient formation of ice over Northumberland Strait. In January, the simulated ice coverage is lower than observations along Northumberland Strait. In this month, however, the simulated thickness is generally larger than the observations. In February, the model has some difficulty in reproducing the maximum observed concentrations and thickness, which also translates to relatively low amounts of simulated sea ice in March.

Figures 4.10 and 4.11 present scatterplots of monthly mean observed and simulated sea ice concentrations and thickness, with the ε^2 in Eq. (2.5) redefined as:

$$\varepsilon^2 = \frac{\sum_{i=1}^{N}\left(\phi_i^O - \overline{\phi}_i^O - \phi_i^M + \overline{\phi}_i^M\right)^2}{\sum_{i=1}^{N}\left(\phi_i^O - \overline{\phi}_i^O\right)^2} \qquad 4.12$$

where ϕ_i^O is an observed variable (concentration or thickness) and ϕ_i^M a simulated variable at model grid point. The overbar indicates the mean of the observed and simulated variables. Again, the agreement is perfect between observed and simulated variables if ε^2=0, and the model skill decreases as ε^2 increases. In December, ε^2 is about 0.98, indicating some disagreement between observed and simulated concentrations (Fig. 4.10a). By comparison, from January to March the agreement between the observed and simulated concentrations is better with ε^2 values between 0.15 and 0.30. In these months the model has a tendency to underestimate the observed ice concentrations (Fig. 4.10b-d). It should be noted that ε^2 is smaller in February than in January, but the scatterplots show less datapoints near the line of perfect agreement in Fig. 10c than in Fig. 10b. This is because the scatterplots show a point by point comparison without removing the means of the observed and simulated fields. The agreement between the simulated and observed ice thickness is less satisfactory than the concentrations. In December, the ε^2 value is about 8.8 and the simulated thickness is greater than the observations (Fig. 4.11a). In January, the thickness produced by the coupled model is in better agreement with the observations (ε^2=0.74) but the model still has a tendency to overestimate the ice thickness (Fig. 4.11b). In February and March the simulated thickness is generally less than the observations featuring ε^2 values of about 0.18 and 0.43, respectively (Fig. 4.11c, d).

It should also be noted that the accuracy of observational estimates might be biased towards higher values for navigation safety purposes (Saucier et al., 2003), which could partly explain differences between observed and simulated monthly-mean sea ice fields. It was found that the use of spectral nudging in the upper layer of the ocean could lead to

underestimation of sea ice because winter climatologies of sea surface temperature might be biased towards warmer values. As a result, we have used an even weaker nudging coefficient in the upper layer than in the subsurface layers of the ocean model. There are many other factors that could affect the performance of the coupled ocean-ice model such as the use of a relatively simple sea ice thickness distribution formulation with two categories (open water and thick ice) in the model. Other factors are the accuracy of atmospheric forcing, ocean surface conditions including net heat and freshwater fluxes, and the representations of feedbacks between the atmosphere and the ocean-ice system.

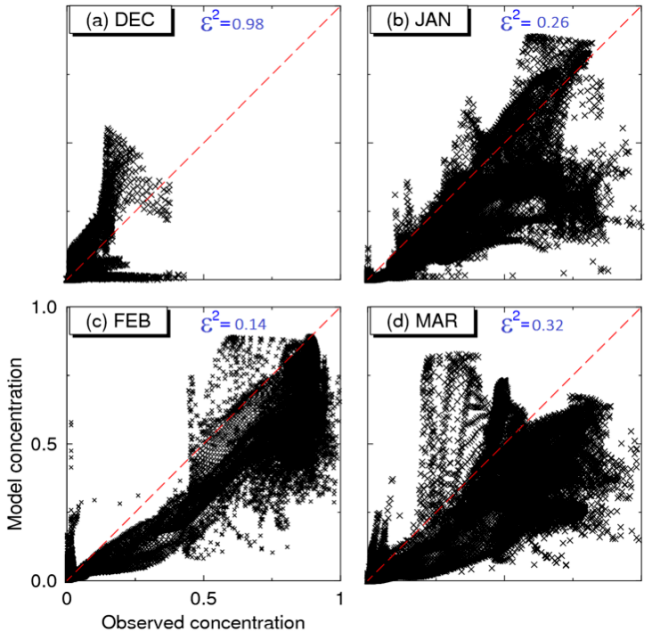

Figure 4.10. Scatterplots of monthly mean observed (Canadian Ice Service) and simulated sea ice concentrations in the 17-year period 1988-2004.

In recognition of model deficiency in simulating temporal and spatial distributions of sea ice, I next examine the model performance in simulating the domain-integrated sea ice over the whole GSL. Figure 4.12 presents time series of the observed and simulated domain-integrated sea ice area over the GSL and adjacent waters during 1988-2004. The temporal variability of the observed total ice coverage in the whole GSL is reasonably well reproduced by the model with the small extents in sea ice coverage in the early 2000s and the large extents in the early 1990s and 2003. It should be noted that the total sea ice area produced by the coupled ocean-ice model is lower than the total observed

area by about 20%. In 1990 and 1994, however, the observed total ice area in the GSL is well reproduced by the model. The time series shown in Fig. 4.12 demonstrate that the observed and simulated sea ice start to appear at the beginning of December. However, the simulated ice disappears by late March, which is about 2-3 weeks earlier than the observations. This model deficiency in producing early melting has been a common problem in simulating sea ice conditions over the northwest Atlantic (Zhang et al., 2004). Nevertheless, the newly developed coupled ocean-ice model is an useful tool to identify the role of dynamics and thermodynamics in the sea ice distributions in the GSL.

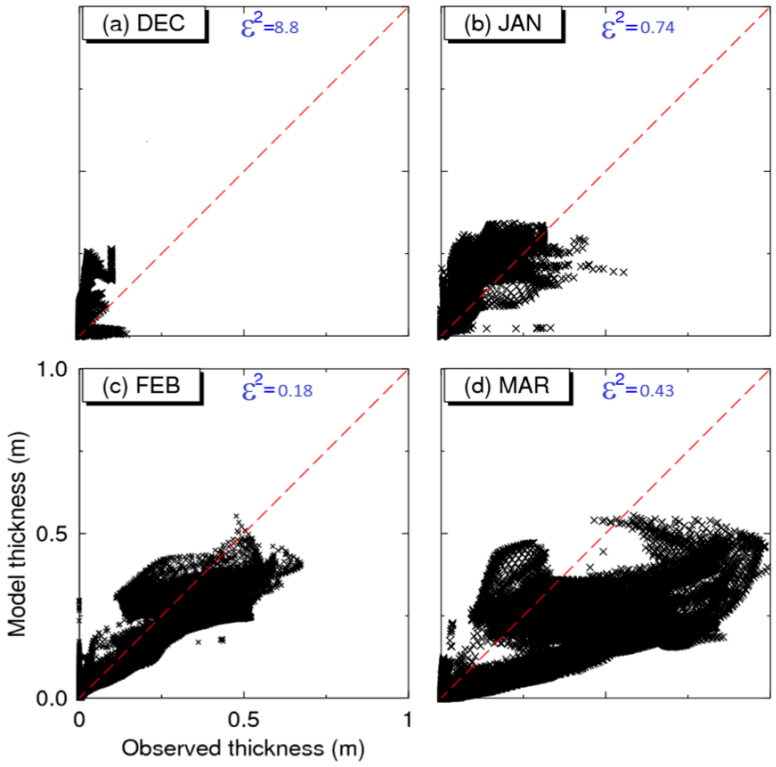

Figure 4.11. Scatterplots of monthly mean observed (Canadian Ice Service) and simulated sea ice thickness in the 17-year period 1988-2004.

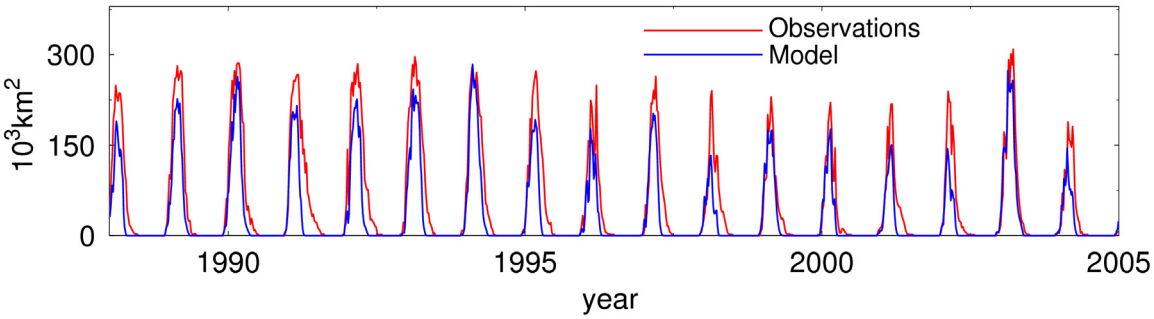

Figure 4.12. Integrated sea ice areas over the Gulf of St. Lawrence and adjacent waters from 1988-2005 calculated from observational estimates (red) and model results (blue).

4.4 Process Study of Sea Ice Formation and Distribution in the GSL

In this section the coupled ocean-ice model is used to examine the roles of thermodynamics and dynamics in the formation and distribution of sea ice, and the effect of sea ice on the circulation in the GSL. Model results in the following two numerical experiments are used for the process study.

Exp-Control: This is the control run described in Section 4.3. The thermodynamic and dynamic equations are used in the sea ice component of the modelling system.

Exp-NoDYN: In this experiment only the thermodynamic equations of the sea ice component is used. The model results in this experiment do not include the effect of sea ice dynamics. Together with the results in Exp-Control, the model results in this experiment can be used to examine the effect of sea ice dynamics on the ice production and the ocean circulation.

Discussion in this section is based on model results in the 4-year period 1988-1991 during which the typical sea ice coverage occurs in the GSL.

4.4.1 Effect of sea ice dynamics and thermodynamics

Sea ice conditions in the ocean are affected not only by thermodynamics, but also by dynamics of sea ice. Removal of sea ice by ocean currents or wind from areas where intense cooling takes place facilitates further ice growing over these areas. On the other hand, sea ice advected onto a certain area can slow down heat losses at the ocean surface and therefore reduce sea ice growth over this area.

Monthly-mean sea ice concentrations and thickness in Exp-Control and Exp-NoDYN (Figs. 4.13 and 4.14) are compared to determine the role of thermodynamics and dynamics of sea ice in the GSL. The large-scale sea ice concentrations simulated in both the experiments are very similar from January to March, indicating that thermodynamics play a significant role in the formation of sea ice in the GSL. In both experiments sea ice starts to appear in December and January over shallow areas along Québec's northern shore, the St. Lawrence Estuary and coastal waters over the western GSL, suggesting that it is the thermodynamics that triggers the first appearance of sea ice in the region.

There are, however, some significant differences in sea ice concentrations and thickness over several local areas between Exp-Control and Exp-NoDYN, indicating the important role of dynamics in affecting the spatial distribution of sea ice in the GSL. In January, the sea ice pack is thicker and has higher concentrations along Québec's northern shore and over shallow areas southeast of the Gaspé Peninsula in Exp-Control than in Exp-NoDYN (Figs. 4.13c,d and 4.14c,d). The main reason is that the sea ice produced over these areas is advected onto deeper waters in Exp-Control but not in Exp-NoDYN. The advection of sea ice opens leads where further production of sea ice is enhanced.

In February and March, the ice-covered areas in Exp-Control are smaller than in Exp-NoDYN along Québec's northeastern shore and over coastal waters between the Gaspé Peninsula and Northumberland Strait. In these two months, the sea ice concentrations and thickness in Exp-Control are larger than in Exp-NoDYN over the southeastern Esquiman

Channel, the central GSL, and waters off the western coast of Cape Breton, demonstrating that the sea ice dynamics are also important for the regional distributions of sea ice in the GSL. In February and March, sea ice appears over the eastern Scotian Shelf and the Laurentian Channel outside the GSL in Exp-Control. Sea ice is, however, much less important over the regions outside the GSL in Exp-NoDYN, indicating that export of sea ice from the GSL through Cabot Strait is important (Figs. 4.13e-h and 4.14e-h).

To further quantify the role of dynamics and thermodynamics, I examine the sea ice volume produced by the coupled model in the two experiments. Figure 4.15a shows that the total volume of sea ice over the GSL and adjacent waters is very similar in Exp-Control and Exp-NoDYN. The small differences between the two experiments indicate the minor role of dynamics in the production of the domain-integrated sea ice in the whole GSL. Figure 4.15b shows time series of sea ice volume over a grid cell to the southeast of Anticosti Island (location A in Fig. 4.1) between 1988-1991. Significant differences in the ice volume present at this location in Exp-Control and Exp-NoDYN, indicating that the local dynamics of sea ice are very important in the GSL. In the winters of 1988 and 1991 the ice volume at location A in Exp-Control is larger than Exp-NoDYN, suggesting a net import of sea ice into this location. By comparison, in 1990 the amount of ice at location A in Exp-NoDYN is larger than Exp-Control, indicating a net export of sea ice from this location into other areas in the GSL.

I next examine the sea ice production (units of volume per unit area) at every model grid point calculated from model results in Exp-Control. The production of sea ice includes lateral accretion, basal growth or melting, and snow ice formation due to the flooding of snow. The total ice growth (positive production) and melting (negative production) are calculated for every ice season and then used to calculate their time-means in the 4-year period 1988-1991. Figure 4.16 presents spatial distributions of the 4-year mean fields of sea ice growth and melting in the GSL. It should be noted that the time-means of sea ice growth and melting in Exp-Control do not, in general, compensate for each other at each model grid point due to the effect of sea ice dynamics. In Exp-

Control the areas where sea ice growth is important include coastal waters along Québec's northern shore and from the Gaspé Peninsula to Northumberland Strait and waters around Prince Edward Island. Sea ice melting is more important over the eastern side of the GSL, central GSL, the coastal waters off Cape Breton and along the Laurentian Channel between the Newfoundland and Scotian Shelves. It should be noted that the predominant areas of sea ice growth have smaller areal extent than the predominant areas of sea ice melting in the GSL.

The rate of change of ice volume at a model grid point is equal to the sum of the net volume change due to the local thermodynamic growth (or melting), and the flux divergence of sea ice volume (Eq. 4.2). Figure 4.17 presents the time-mean sea ice volume per unit area advected (flux divergence term in Eq. 4.2) during 1988-1991 calculated from model results in Exp-Control. Positive and negative values indicate local net sea ice import and export, respectively. The areas with the net export of sea ice produced by the model consist of coastal waters along Québec's northern shore from the upper St. Lawrence Estuary to the Strait of Belle Isle. The net sea ice export also occurs over coastal areas along the northeastern coast of Anticosti Island, coastal waters from the Gaspé Peninsula to Northumberland Strait, coastal waters around Prince Edward Island and the Magdalen Islands, and waters along the eastern coast of Cape Breton and over Bras d'Or Lake. The net import areas of sea ice include the deep waters along the Laurentian Channel from western Anticosti Island to the mouth of the Channel in the Atlantic Ocean and areas between Grand Banks and the eastern Scotian Shelves. Other net import areas include coastal waters off northwestern Cape Breton and the deepest parts of the Magdalen Shallows between the Magdalen Islands and Prince Edward Island.

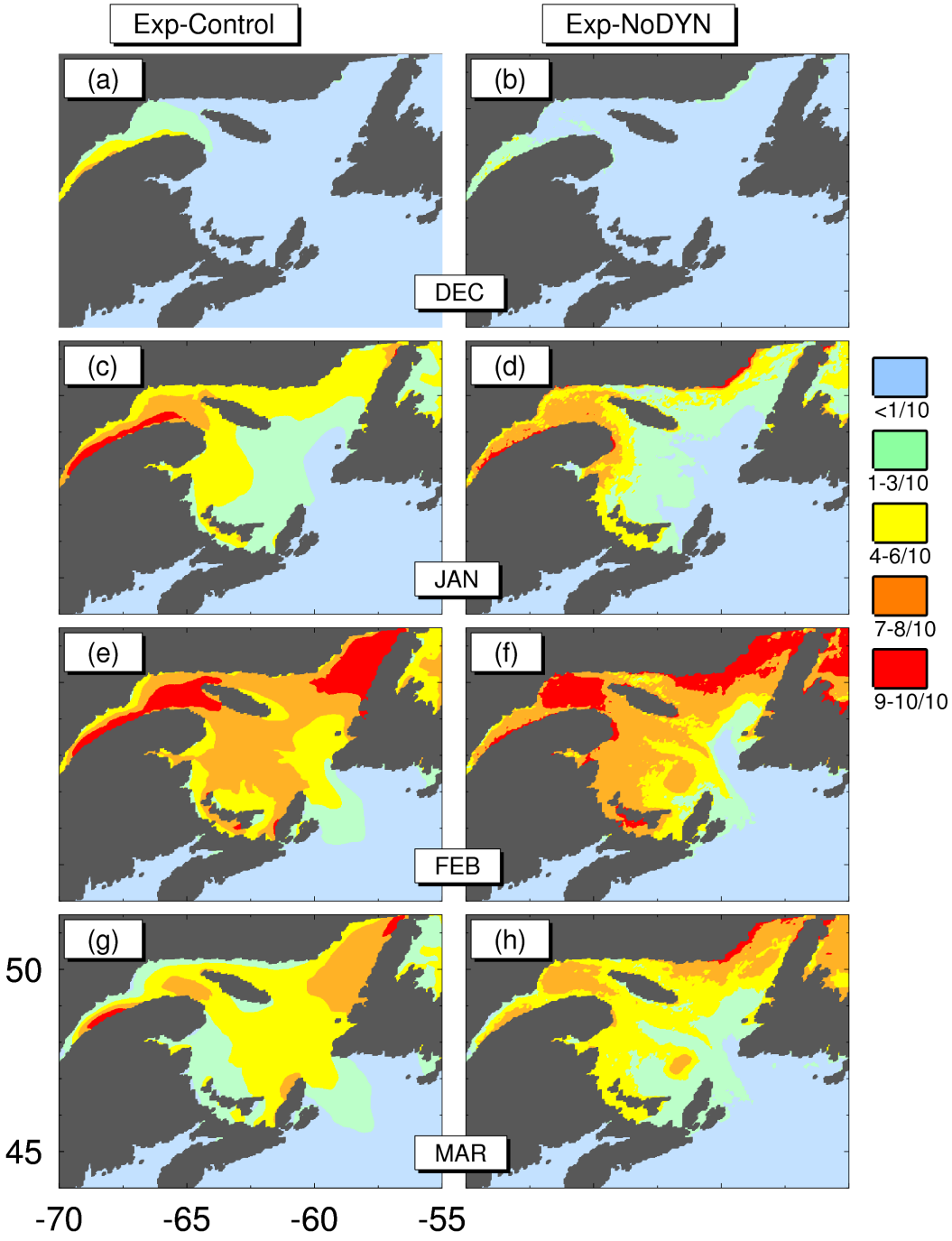

Figure 4.13. Monthly-mean sea ice concentrations calculated from model results in the 4-year period 1988-1991 in Exp-Control (left panels) and Exp-NoDYN (right panels).

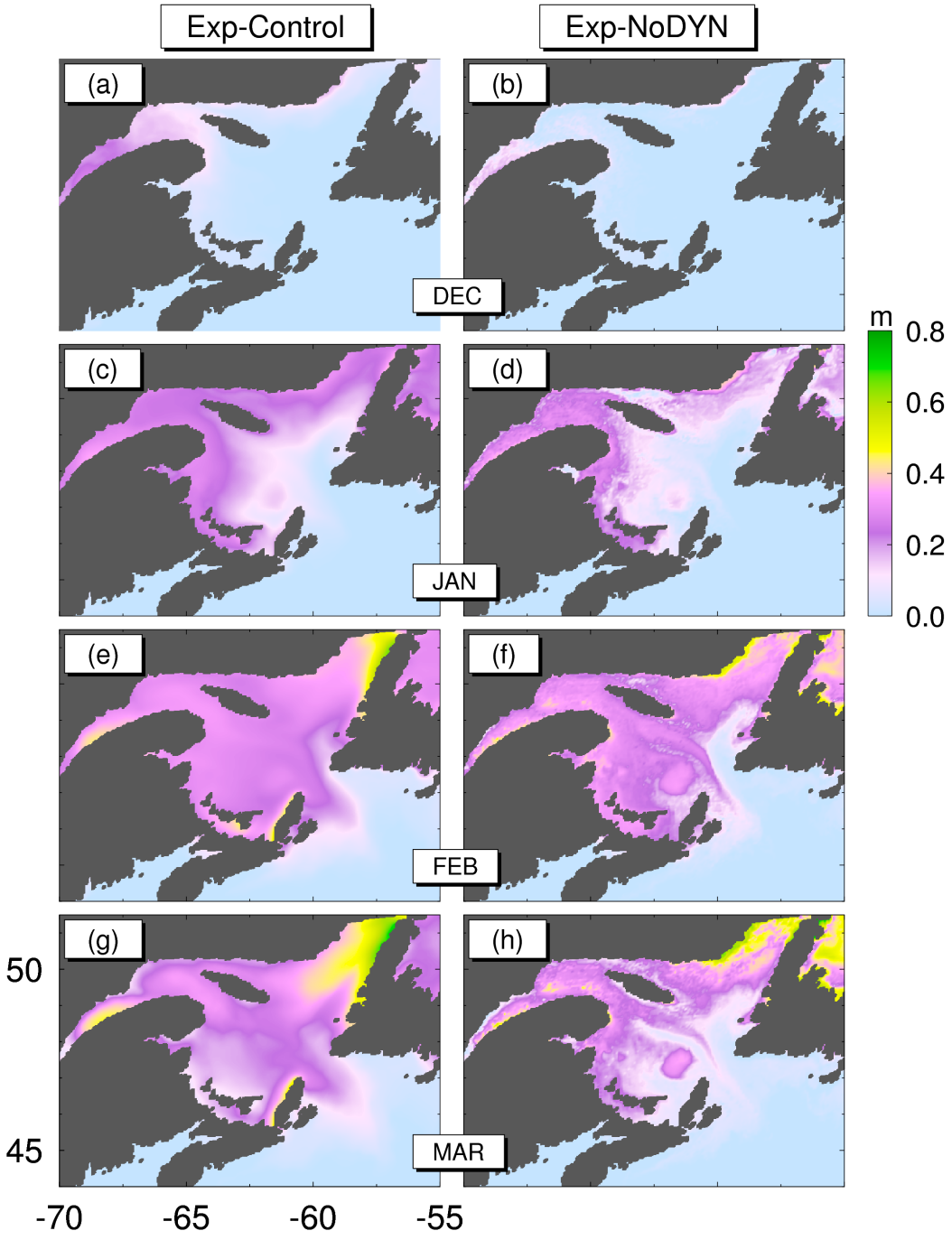

Figure 4.14. Monthly-mean sea ice thickness calculated from model results in the 4-year period 1988-1991 in Exp-Control (left panels) and Exp-NoDYN (right panels).

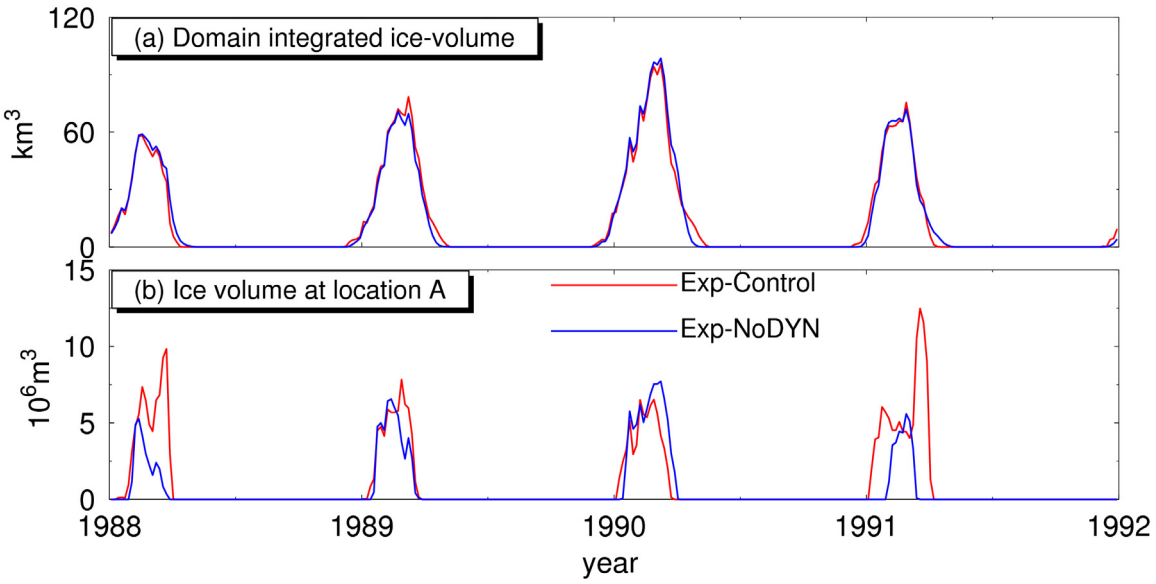

Figure 4.15. Time series of (a) domain-integrated ice volume over the Gulf of St. Lawrence and adjacent waters and (b) ice volume over a model grid cell to the southeast of Anticosti Island (location A) produced in Exp-Control (red) and Exp-NoDYN (blue) in the 4-year period 1988-1991.

The time-mean sea ice velocities shown in Fig. 4.17 can be used to examine sources, sinks and pathways of sea ice in the GSL and adjacent waters. The net export (import) areas are consistent with divergent (convergent) sea ice velocities (Fig. 4.17). Waters off western Newfoundland receive sea ice coming from the northern side of the Esquiman Channel, the northern side of Anticosti Island, and from the central GSL. Areas over the Magdalen Shallows, the central GSL, and the Laurentian Channel, receive sea ice advected by currents and winds from coastal waters in New Brunswick, and from the St. Lawrence. It should be noted that the sea ice imported onto the eastern Scotian Shelf is relatively small. A large fraction of the sea ice leaving the GSL through Cabot Strait is melted by relatively warmer waters in the Laurentian Channel.

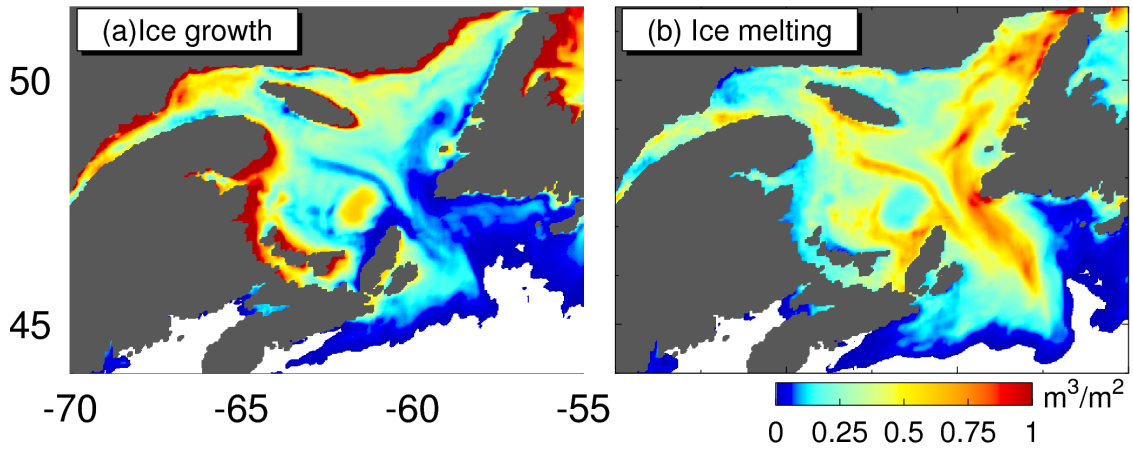

Figure 4.16. Winter-mean (a) production and (b) melting of sea ice over the Gulf of St. Lawrence and adjacent waters in Exp-Control during 1988-1991.

To further investigate the effect of sea ice dynamics on spatial patterns of sea ice growth and melting, the time-mean production of sea ice in Exp-NoDYN during 1988-1991 is presented in Fig. 4.18. Since there is no ice advection in this experiment, the time-mean total growth of sea ice at every model grid point is equal to the time-mean total melting during an ice season. Comparison of Figs. 4.16a and 4.18 demonstrates that the spatial patterns of sea ice production are significantly affected by the sea ice dynamics. In comparison with results in Exp-Control, the ice production in Exp-NoDYN is not as high over the shallow and coastal waters within the GSL. The amount of sea ice production in Exp-NoDYN is about 0.2-0.3 m^3m^{-2} over the western GSL and about 0.3-0.5 m^3m^{-2} over the northeastern Gulf. Waters around Cape Breton, the Magdalen Islands and the northern side of Anticosti Island have productions below 0.25 m^3m^{-2}. Waters over the eastern Cabot Strait have no ice growth or melting of sea ice in both Exp-Control and Exp-NoDYN, indicating that the production of sea ice is not affected by dynamics over this area. It should be noted, however, that the total volume of sea ice over that area is affected by advection of sea ice from other regions.

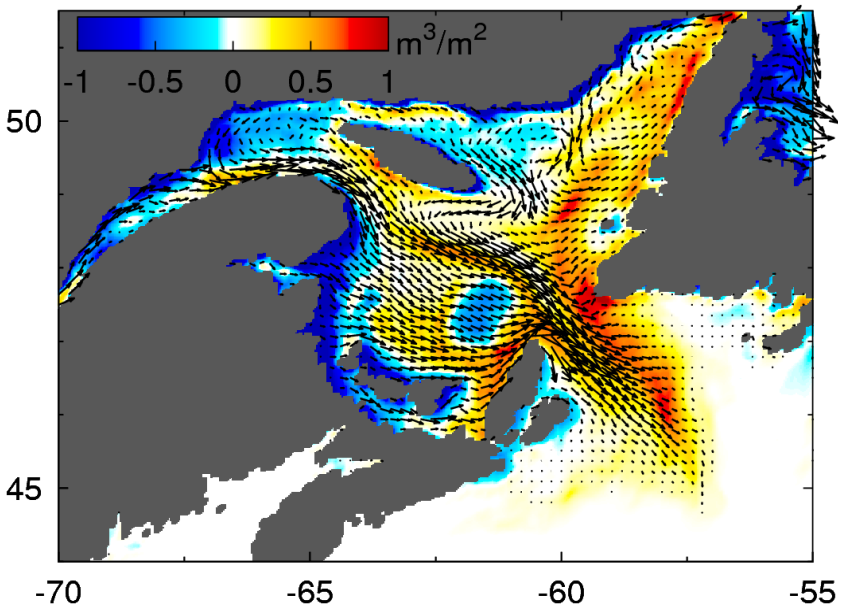

Figure 4.17. The time-mean volume of sea ice per square meter advected (image) and time-mean sea ice velocities (arrows) in winter during 1988-1991 in Exp-Control over the Gulf of St. Lawrence and adjacent waters. Areas with cold (warm) colors represent the net export (import) of sea ice in winter months in the 4-year period 1988-1991.

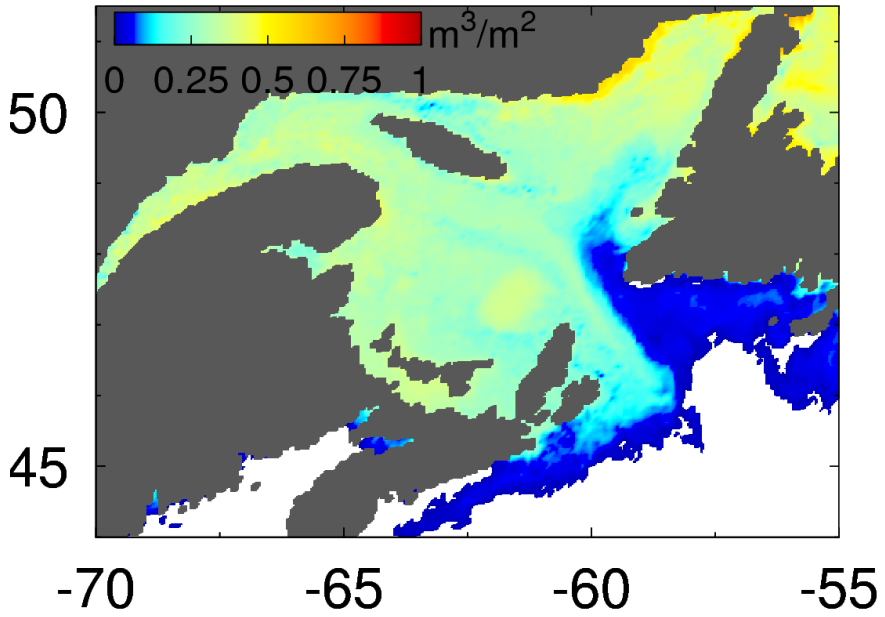

Figure 4.18. Winter-mean production and melting of sea ice over the Gulf of St. Lawrence and adjacent waters in Exp-NoDYN during 1988-1991. The winter-mean growth and melting of sea ice are the same at every model grid point in Exp-NoDYN.

4.4.2 An index for dynamics and thermodynamics of sea ice

A simple index is developed to identify the importance of thermodynamics and dynamics of sea ice based on the time change of ice volume at each model grid cell defined as:

$$\Delta V^{CR} = V_p^{CR} + V_a^{CR} \tag{4.13a}$$

$$\Delta V^{NoDYN} = V_p^{NoDYN} \tag{4.13b}$$

where ΔV^{CR} and ΔV^{NoDYN} are the time change of ice volume at each time step in Exp-Control and Exp-NoDYN, respectively; V_p^{CR} and V_p^{NoDYN} are the thermodynamic production of sea ice in Exp-Control and Exp-NoDYN, respectively; and V_a^{CR} is the volume of sea ice advected in Exp-Control. In Exp-Control, the thermodynamic production of sea ice (V_p^{CR}) could also be affected by advection of sea ice. Assuming that the thermodynamic production of sea ice that is not associated with ice dynamics is given by V_p^{NoDYN}, the sea ice production in Exp-Control which is associated with ice dynamics $V_p^{CR|DYN}$ can be approximated by:

$$V_p^{CR|DYN} \approx V_p^{CR} - V_p^{NoDYN} \tag{4.14}$$

where $V_p^{CR|DYN}$ is the production of sea ice associated with the dynamics in Exp-Control. Eq. (4.13a) is equivalent to:

$$\Delta V^{CR} \approx V_p^{NoDYN} + V_p^{CR|DYN} + V_a^{CR} \tag{4.15}$$

In Eq. (4.15), the first term on the right hand side is the thermodynamic production of sea ice which is not associated with sea ice dynamics, and the last two terms represent the time change of sea ice volume associated with sea ice dynamics. Using these relative contributions to the total time-change in ice volume in Exp-Control, I define an index *I* relating the thermodynamics and dynamics of sea ice:

$$I = \frac{\left|V_p^{NoDYN}\right|}{\left|V_p^{NoDYN}\right| + \left|V_p^{CR|DYN} + V_a^{CR}\right|} \tag{4.16}$$

where I=0 indicates that dynamics is the only important process for sea ice at a model grid point and I=1 indicates that sea ice is only affected by thermodynamics.

Figure 4.19 presents the regional distribution of the I-values for the GSL and adjacent waters averaged during the ice seasons in 1988-1991. Areas around eastern Cabot Strait, over the eastern Scotian Shelf and the Laurentian Channel outside the GSL have I-values very close to zero, indicating that the presence of sea ice is due mainly to advection. Inside the GSL, the index value ranges between 0.2 and 0.55, indicating that both dynamics and thermodynamics are important. The role of thermodynamics is, however, relatively more important over the northwestern Esquiman Channel, the western GSL, the St. Lawrence Estuary, and a narrow strip of areas along the Laurentian Channel in the central GSL. By comparison, areas around Anticosti Island, Cape Breton, the southeastern Esquiman Channel and parts of the central GSL are more affected by sea ice dynamics.

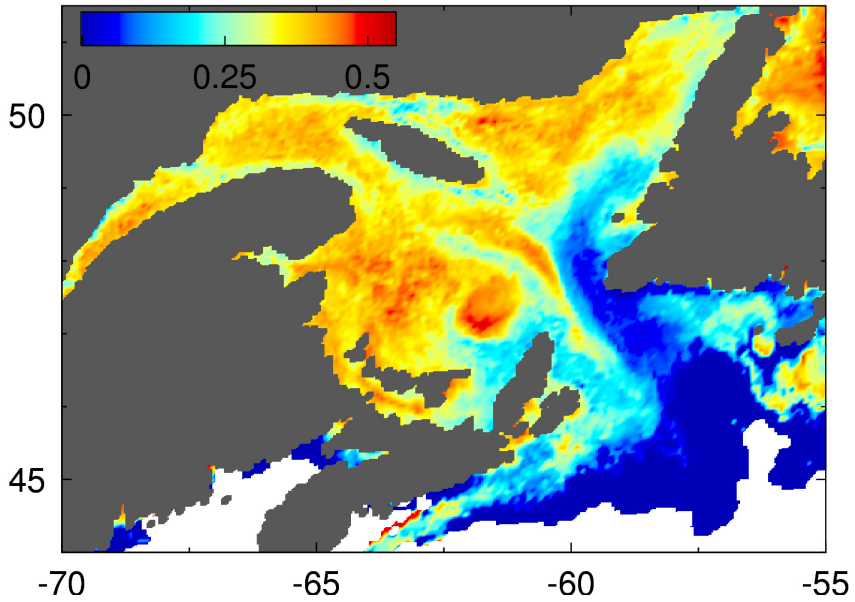

Figure 4.19. Time-mean index (I) calculated based on Eq. (4.16) from model results in Exp-Control and Exp-NoDYN during 1988-1991. White areas in the figure indicate that the I value is not defined due to ice free conditions over these areas during 1988-1991.

4.4.3 Effect of sea ice capping on the circulation in the GSL

The presence of sea ice affects the circulation and hydrography by impeding the direct transfer of wind stress to the ocean surface and reducing the heat exchange between the ocean and the atmosphere. In Exp-Control, the ocean surface experiences the wind stress from the atmosphere ($\vec{\tau}_{ao}$) over the ice free fraction of a grid cell, and the stress from the ice ($\vec{\tau}_{io}$) over the ice covered fraction. By contrast, in Exp-NoDYN $\vec{\tau}_{ao}$ is applied over the entire ocean surface on every model grid cell. Therefore, results in Exp-Control and Exp-NoDYN can be used to examine the sea ice capping effect on the circulation as follows.

Figure 4.20 presents the time-mean normal currents in February during the period 1988-1991 along a transect between the Gaspé Peninsula and Anticosti Island (A-A' in Fig. 4.1) in Exp-Control and Exp-NoDYN. February is the month with the largest sea ice coverage in this area. In this month, the southeastward currents in Exp-Control are significantly weaker than in Exp-NoDYN, indicating that the sea ice cover significantly affects the wind-driven circulation in the northwest GSL. The maximum speed of the Gaspé Current is about 0.12 ms^{-1} in Exp-Control which is about half of the maximum speed in Exp-NoDYN (0.2 ms^{-1}). In Exp-NoDYN, the equatorward currents on the western side of the transect also extend down to about 150 m which is significantly deeper than Exp-Control. Over the eastern side of the transect, the currents are also significantly stronger in Exp-NoDYN than in Exp-Control, indicating the importance of sea ice in modulating the currents in the entire section.

At Cabot Strait, sea ice concentrations are relatively lower than inside the GSL. At the Strait (B-B' in Fig. 4.1) the southeastward currents simulated in Exp-Control and Exp-NoDYN do not differ significantly from December to February, indicating a relatively small effect of ice capping on the circulation during most of the ice season over this area. In March, sea ice is advected from the interior of the GSL towards Cabot Strait, increasing the ice concentrations in the region. In this month, the southeastward currents

in the Strait are more than 50% weaker in Exp-Control than in Exp-NoDYN, indicating again the importance of sea ice on the strength of the estuarine circulation the end of the ice season (Fig. 4.21).

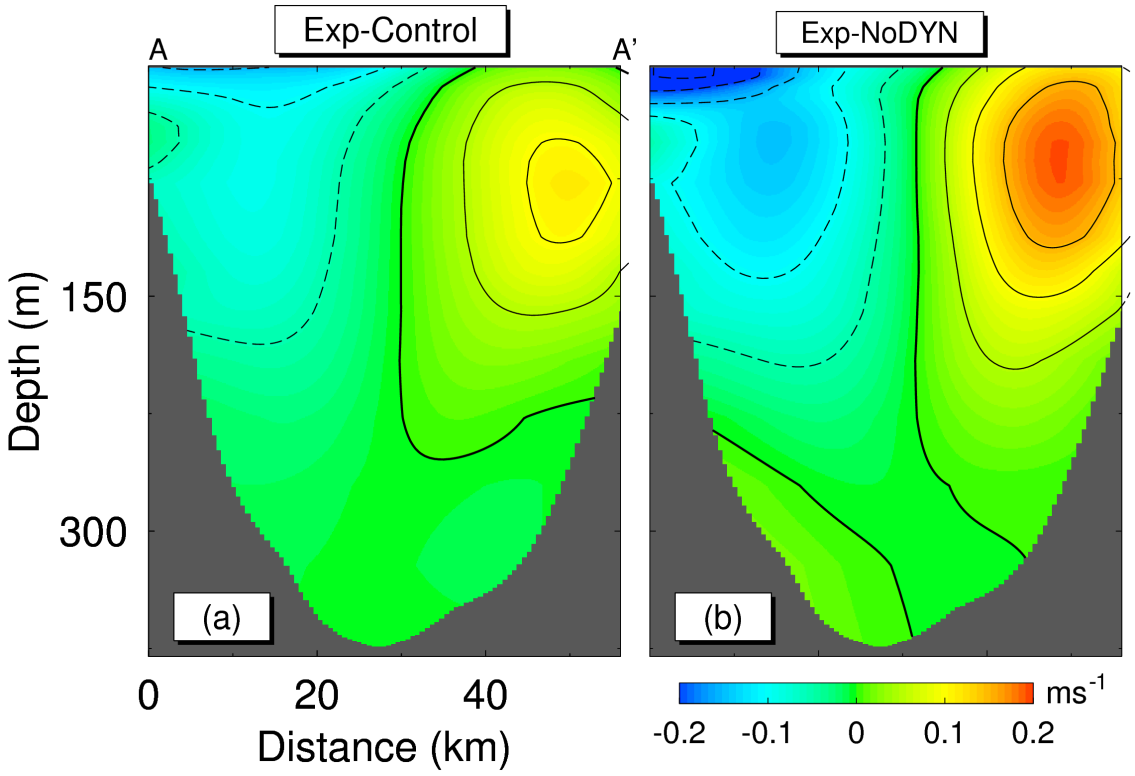

Figure 4.20. February-mean normal velocities during 1988-1991 at transect A-A' (Fig. 4.1) between the Gaspé Peninsula and Anticosti Island in (a) Exp-Control and (b) Exp-NoDYN. The thick black contour line indicates the zero normal velocity, and thin dashed and continuous contour lines indicate southeastward and northwestward flow, respectively. The velocity contours are drawn every 0.05 ms^{-1}.

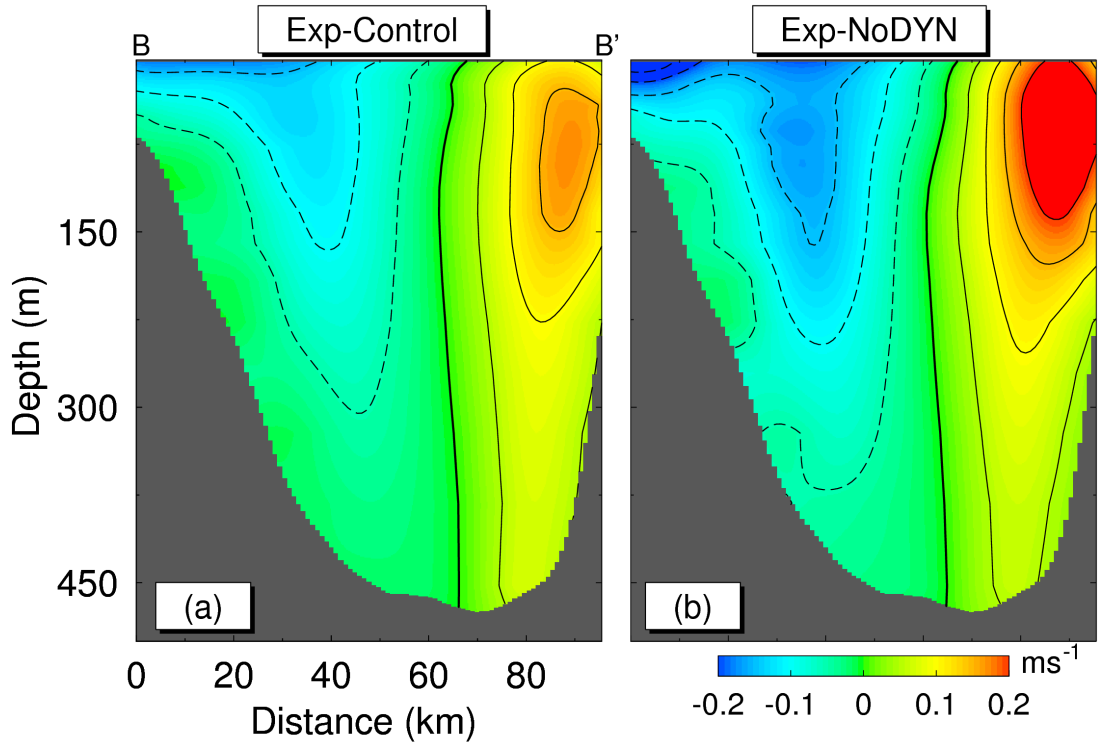

Figure 4.21. March-mean normal velocities during 1988-1991 at Cabot Strait (B-B' in Fig. 4.1) in (a) Exp-Control and (b) Exp-NoDYN. The thick black contour line indicates the zero normal velocity, and thin dashed and continuous contour lines indicate southeastward and northwestward flow, respectively. The velocity contours are drawn every 0.05 ms^{-1}.

4.4.4 Sensitivity of sea ice to atmospheric stability conditions in the GSL

The atmospheric stability condition affects the air-ocean heat fluxes which are important for the thermodynamic sea ice production. The atmospheric stability also determines the magnitude of the turbulent fluxes of momentum and heat, and is used in the parameterization of the turbulent exchange coefficients. In the present model configuration, a stability parameter is estimated based on the Monin-Obukhov length (Large and Yeager, 2004). The parameter is less than zero for unstable conditions, and greater than zero for stable conditions. The stability parameter is then used in conjuction with the turbulent length scales in the lower atmospheric boundary layer to determine turbulent exchange coefficients. Two additional experiments are conducted to examine the effect of the stability of the atmospheric boundary layer on the formation of sea ice in the model:

Exp-STAB: This experiment is the same as the control run experiment except that the air-sea turbulent fluxes are computed based on the assumption that the atmospheric boundary layer is always stable. In this experiment, the exchange coefficients between the air and the ocean are calculated from a parameterization for a positive stability parameter.

Exp-UNSTAB: This experiment is the same as the control run experiment except that the air-sea turbulent fluxes are computed based on the assumption that the atmospheric boundary layer is always unstable. In this experiment, the exchange coefficients between the air and the ocean are calculated from a parameterization for a negative stability parameter.

The sea ice concentrations in Exp-UNSTAB (Figs. 4.22a,c,e,g) are much higher than in Exp-STAB (Figs. 4.22b,d,f,h). Under unstable atmospheric conditions, the maximum ice concentrations greater than 90% occur over the lower St. Lawrence estuary, the northeastern GSL and coastal waters along the western coast of Cape Breton. By contrast, the maximum concentrations of about 60% in Exp-STAB occur in February, with significant loss of ice coverage in March. Sea ice thickness is also affected by the stability in the atmospheric boundary layer (Fig. 4.23). In particular, sea ice is much thicker in Exp-UNSTAB than in Exp-STAB. Large differences between the two experiments occur in February and March when the simulated sea ice thickness off the western Newfoundland and Cape Breton coasts are about 40 cm larger in Exp-UNSTAB than in Exp-STAB. The domain-integrated ice-covered area is significantly smaller in Exp-STAB than in Exp-UNSTAB (Fig. 4.24). The maximum sea ice coverage in Exp-STAB occurs in February and is about 60-70% of the coverage in Exp-UNSTAB.

The large amounts of sea ice produced by the model under unstable atmospheric conditions are due mainly to large exchange coefficients which are functions of the stability parameter and the turbulent lenght scales. More turbulence in the lower atmospheric boundary layer is expected to occur under unstable conditions than stable

conditions. Stronger turbulence implies larger vertical eddy fluxes, which should result in larger exchanges of heat and momentum between the air and ocean. In fall and winter, the heat loss from the ocean to the atmosphere is expected to be larger in Exp-UNSTAB than in Exp-STAB, which should explain the larger amounts of sea ice simulated in the former than in the latter experiment.

My model results suggest the strong sensitivity of sea ice to the atmospheric stability which affects the turbulent exchange between the ocean and the atmosphere, and the importance of reliable parameterizations of the turbulent exchange between the ocean and the atmosphere. My model results also suggest that significant shifts in the oceanographic and sea ice regimes could occur in the GSL if the atmospheric conditions change significantly in fall and winter due to future climate change.

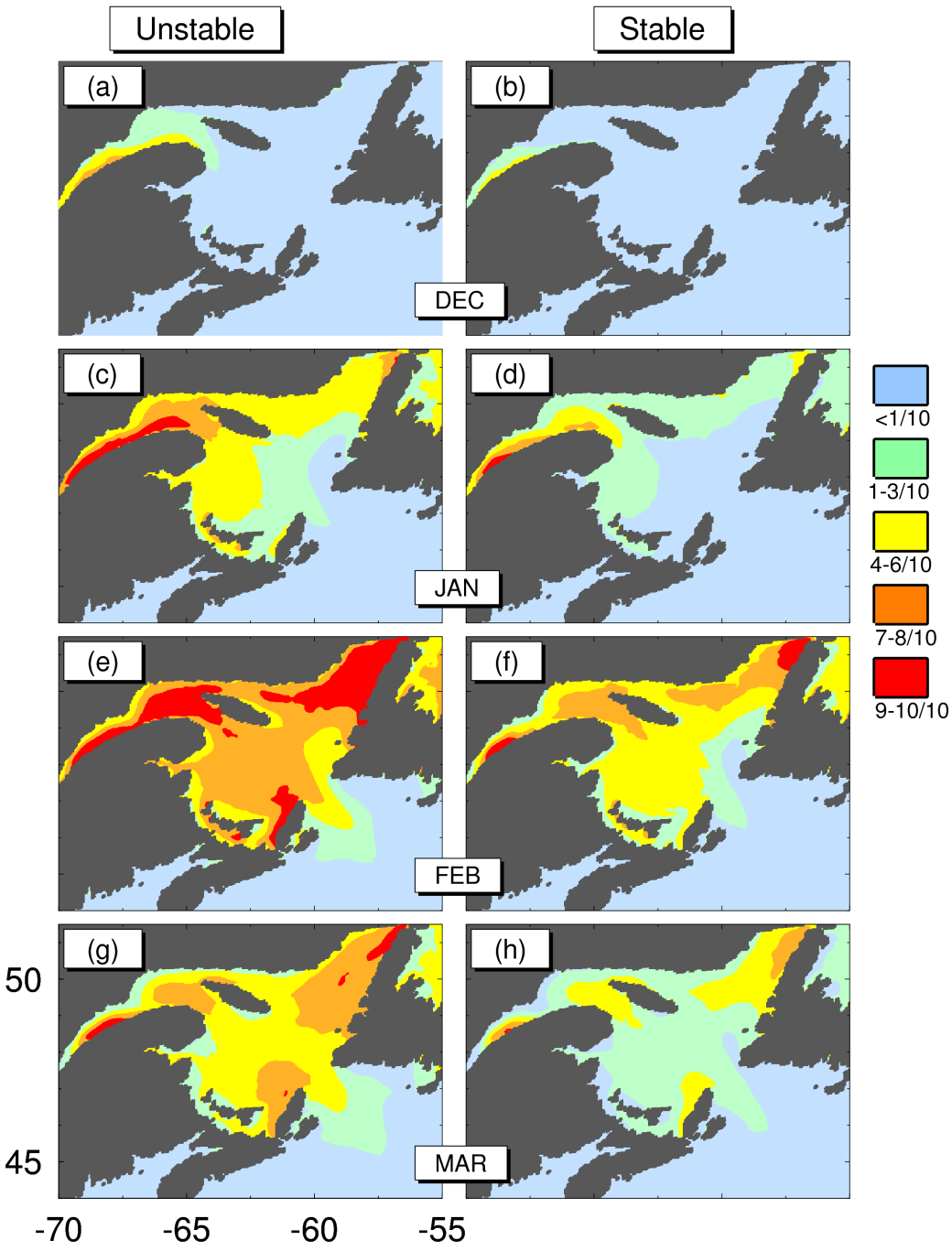

Figure 4.22. Monthly-mean sea ice concentrations calculated from model results in the 4-year period 1988-1991 in Exp-UNSTAB (left panels) and Exp-STAB (right panels).

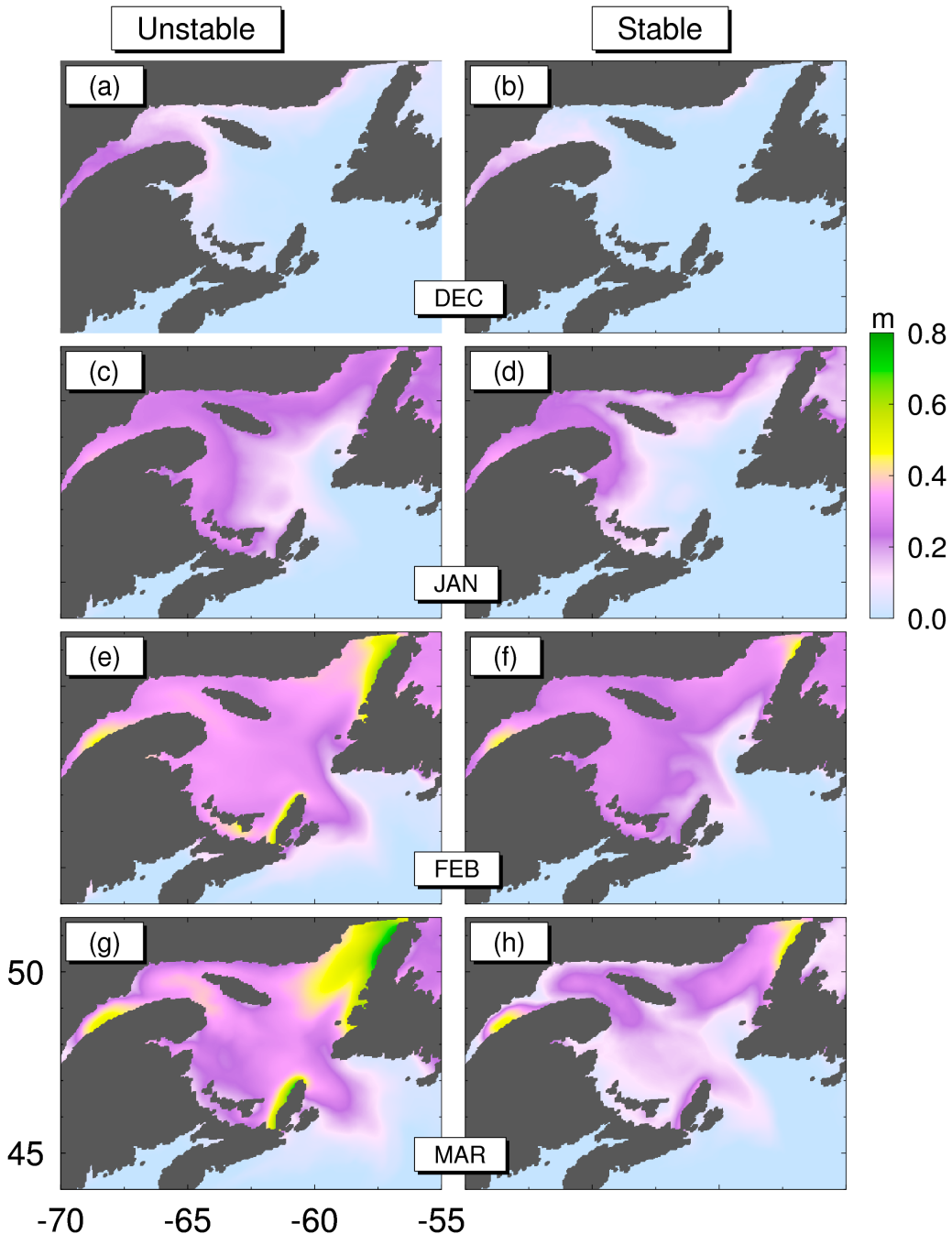

Figure 4.23. Monthly-mean sea ice thickness calculated from model results in the 4-year period 1988-1991 in Exp-UNSTAB (left panels) and Exp-STAB (right panels).

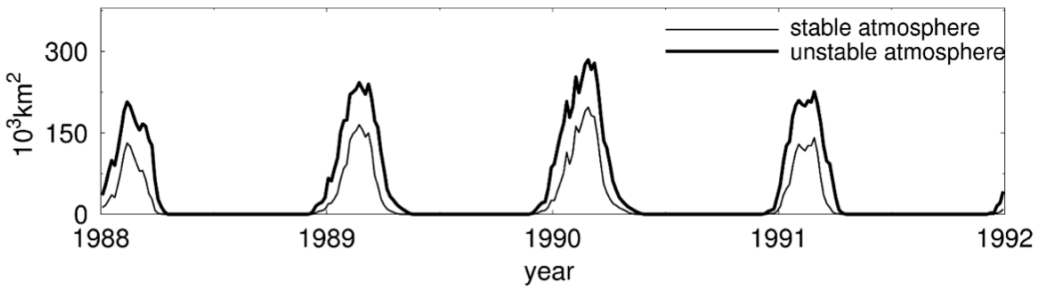

Figure 4.24. Time series of domain-integrated ice area over the Gulf of St. Lawrence and adjacent waters produced in Exp-UNSTAB (thick line) and Exp-STAB (thin line) in the 4-year period 1988-1991.

4.5 SUMMARY AND CONCLUSIONS

A nested-grid coupled ocean-ice model for the eastern Canadian shelf was used to study sea ice conditions in the Gulf of St. Lawrence (GSL) and adjacent waters. The coupled model has certain skill in simulating circulation and sea ice conditions in the GSL during 1988-2004. The coupled model, however, underestimates the amount of sea ice in the region, which could be caused by a number of factors and approximations, such as the lack of a multi-category ice thickness formulation in the model since sea ice of different thicknesses has different thermal properties, and thick ice grows and melts more slowly than thin ice. Other factors that could explain the underestimation of sea ice in the model include the relatively simple ice albedo parameterizations, the lack of a parameterization of melt ponds at the ice surface, or the poor representation of heat stored in brine pockets, and less accurate parameterization of the turbulent heat fluxes. A sensitivity study demonstrated that sea ice produced by the model under stable atmospheric conditions is significantly lower than the sea ice under unstable atmospheric conditions. There would also be a great benefit in coupling actively the ocean-ice system to the atmospheric boundary layer. This approach would allow the estimates of heat and momentum fluxes to account, for instance, for the effect of varying roughness at the interface of the ocean-ice-atmosphere system.

The coupled model was used to quantify the importance of the thermodynamics and dynamics in the formation and distributions of sea ice in the GSL. The model results suggest that the net sea ice growth occurs over coastal waters along Québec's northern

shore and between the Gaspé Peninsula and Northumberland Strait. By contrast, the net sea ice melting occurs over the central GSL, near Cabot Strait, and over the Laurentian Channel outside the GSL. The coupled model results also demonstrate that significant amounts of ice are first produced near coastal regions and then advected into the central and southern GSL where melting occurs. This enhances production of sea ice in coastal waters due to the continuous heat loss. Meanwhile, waters in the central and southern GSL are isolated from the atmosphere, slowing down heat losses in the ocean surface and inhibiting high ice formation rates. It was shown that the Gaspé Current and the equatorward flow over the Magdalene Shallows are responsible for the advection of sea ice onto the southern GSL and its export from the GSL onto the Grand Banks and eastern Scotian shelf. The presence of sea ice over coastal waters off western Newfoundland is caused mainly by advection of sea ice from the northern Esquiman Channel and southern Anticosti Island.

Model results also demonstrate that sea ice modulates the strength of the currents in the upper water column throughout the GSL. The presence of sea ice inhibits the direct momentum transfer between the atmosphere and ocean. As a result, the winter circulation is significantly weaker than otherwise would be in absence of the ice cap at the sea surface. This could indicate that significant changes in the physical environment of the GSL might be expected as seasonal ice cover is lost in a warmer climate.

CHAPTER 5

ASSESSING THE PERFORMANCE OF ONE-WAY AND TWO-WAY NESTING TECHNIQUES USING THE SHELF CIRCULATION MODELLING SYSTEM FOR THE EASTERN CANADIAN SHELF[1]

5.1 INTRODUCTION

Numerical ocean circulation models have increasingly been used in simulating three-dimensional (3D) circulation and hydrography over coastal and shelf waters and in deep oceans. The accuracy of any ocean circulation model is affected by its spatial and temporal resolution and grid arrangement. The latter may use either unstructured or structured grids. Unstructured grids can use grid cells with different shapes and sizes and are better suited to accurately represent coastline and bathymetry. Significant efforts have been made in developing models based on unstructured grids. Nevertheless, unstructured-grid models still have some limitations due to high computational cost, difficulties to accurately represent the geostrophic balance, and because changes in grid spacing can result in unphysical wave scattering. By comparison, ocean models based on structured grids are widely used in ocean and climate applications, which have an advantage of more than 10 times less computational cost than models based on unstructured grids (Danilov, 2008). Structured grids use regular cells which are also very convenient for the discretization of model equations and application of finite difference schemes. It has been shown that a grid refinement can be applied to locally increase the model resolution in

[1] Urrego-Blanco, J.; J. Sheng and F. Dupont. 2014. Assessing the performance of one-way and two-way nesting techniques using the shelf circulation modelling system for the eastern Canadian shelf. *Submitted to Ocean Modelling*.

structured grids over model regions where complexities associated with the flow require high accuracy. If the local refinement in the model is allowed to evolve with the flow, it is known as adaptive grid refinement (Hernstein et al., 2005). While this adaptive approach is attractive to obtain high accuracy in particular regions, stability requirements can increase significantly the computational cost. An alternative way to obtain high accuracy in ocean models is to embed a high-resolution child model (CM) within a certain area of a coarse-resolution parent model (PM). The result is a nested-grid modelling system that does not impose a constraint of small time steps over regions where relatively coarse horizontal resolution is acceptable. An additional advantage of embedding algorithms is that different numerical schemes and sub-grid scale mixing parameterizations can be applied to different components of the nested-grid system (Debreu and Blayo, 2008).

There are two basic nesting techniques widely used to exchange information between the PM and CM: one-way and two-way nesting. In one-way nesting (OWN) the only interaction between the CM and PM is the use of variables (such as currents, temperature and salinity) produced by the PM to specify lateral open boundaries of the CM, without any feedback from the CM to PM. By comparison, in two-way nesting (TWN) the CM results are fed back to the PM in addition to the use of PM results in specifying open boundary conditions of the CM. The interaction between the CM and PM in the TWN can take place either at the dynamic interface between them (Kurihara et al., 1979) or over their overlapping region (Oey and Chen, 1992). Sheng et al. (2005) also suggested an alternative nesting technique based on the semi-prognostic method (Eden et al., 2004; Greatbatch et al., 2004). The important scientific issues for nesting algorithms include conservation properties, consistency and noise control at the interface between PM and CM, as suggested by Debreu and Blayo (2008). More work is needed to examine the performance of different nesting techniques. The main objective of this chapter is to assess the performance of different nesting techniques using a nested-grid circulation modelling system developed recently for the eastern Canadian shelf (Urrego-Blanco and Sheng, 2014a). The performance assessment to be considered in this chapter focuses on the following four aspects: (a) to what extent the choice of two-way nesting over one-way

nesting leads to more consistent fields of the large-scale circulation and hydrography produced by the PM and CM, (b) whether the use of two-way nesting introduces numerical noise in the PM during the feedback step from the CM, (c) whether the large-scale flow in the PM is improved, and (d) whether the small-scale or regional circulation features are improved by the use of a high-resolution CM.

This chapter is arranged as follows. Section 5.2 discusses different nesting techniques used in this study. Section 5.3 presents a nested-grid circulation modelling system developed recently for the eastern Canadian shelf. Section 5.4 assesses the performance of one-way and two-way nesting techniques, including the two-way nesting technique based on the semi-prognostic method. Section 5.5 presents a summary and conclusions.

5.2 METHODOLOGY

For simplicity but without losing generality, I consider a nested-grid modelling system in which a fine-resolution CM is embedded inside a coarse-resolution PM with a grid refinement only in the horizontal direction (Fig. 5.1a). I also assume the ratio of the grid spacing between the PM and CM to be an odd number (which is set to 3 in our study) in order for the cell edges and faces of the PM to coincide with the edges and faces of the CM. Furthermore, I consider only the grid point for the pressure variable (or temperature or salinity) in the presentation of the methodology. Figure 5.1b shows the spatial arrangement of the child grid (blue dots) and the parent grid (red dots) and the dynamical boundary between the CM and the PM. The region inside the thick black line in Fig. 5.1b is the computational domain of the CM. There are two ghost cells around the CM boundary (light blue dots in Fig. 5.1b) for implementation of the open boundary conditions. The nested-grid system also allows temporal refinement, which is illustrated by the integration flow chart shown in Fig. 5.2. A time refinement factor of 3 is used in this study, which is the same as the spatial grid refinement.

The numerical algorithm used for nesting in this study is AGRIF (Adaptive Grid Refinement In FORTRAN), which is a package for adaptive mesh refinement within a

finite difference model written in Fortran 90 (Debreu and Blayo, 2002). In this study I use the horizontal and temporal refinement of AGRIF for fixed grids. AGRIF allows the interaction between the CM and PM to be either one-way or two-way, depending on the direction of information transferred between the PM and CM. A general description of these approaches is discussed as follows.

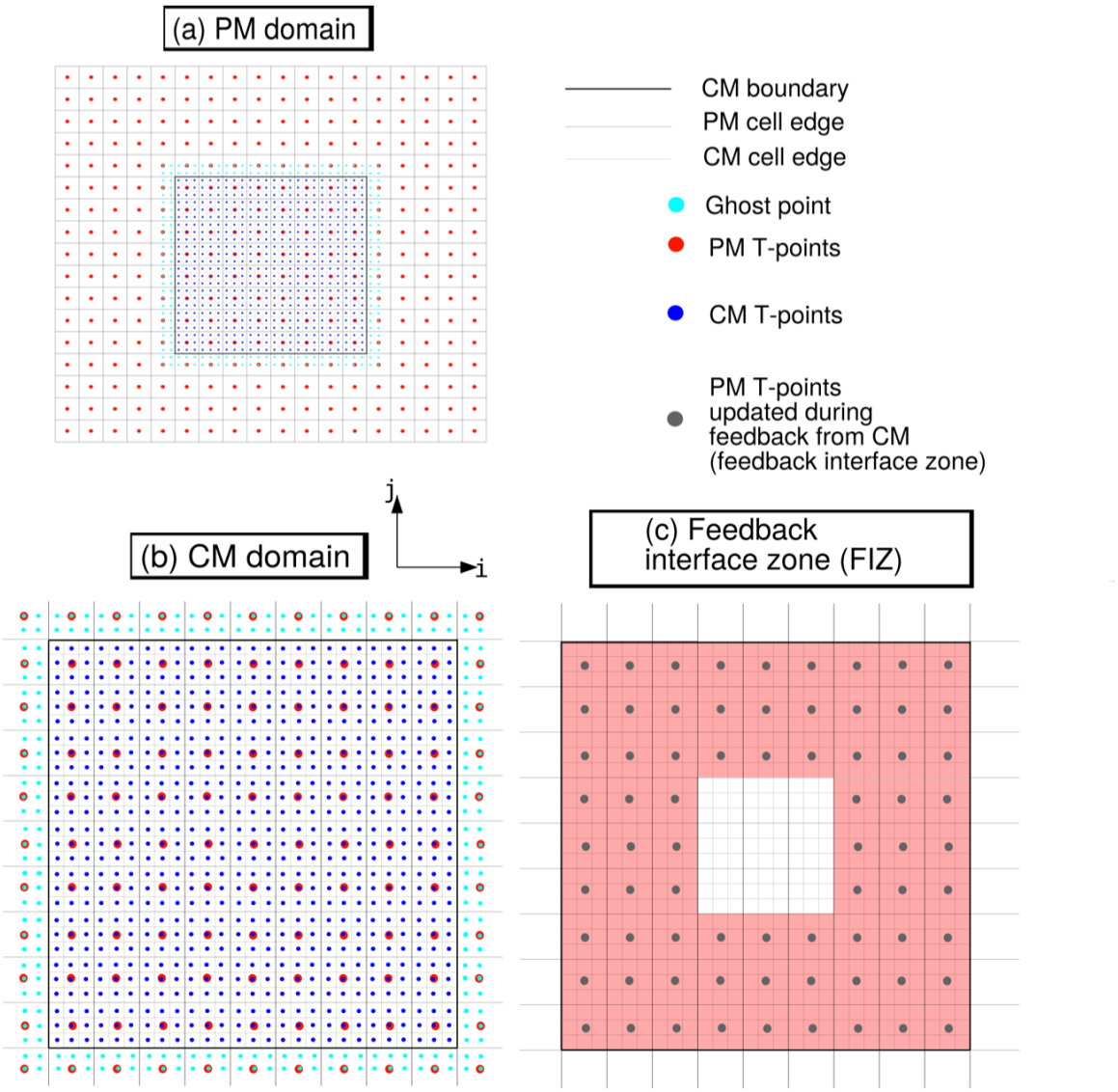

Figure 5.1. (a) Schematic of a fine-resolution child model (CM) nested inside a coarse-resolution parent model (PM) with a horizontal refinement factor of 3. (b) Grid point arrangements of the PM and CM over the CM domain. (c) The feedback interface zone (areas marked in red) close to open boundaries of the CM in two-way nesting.

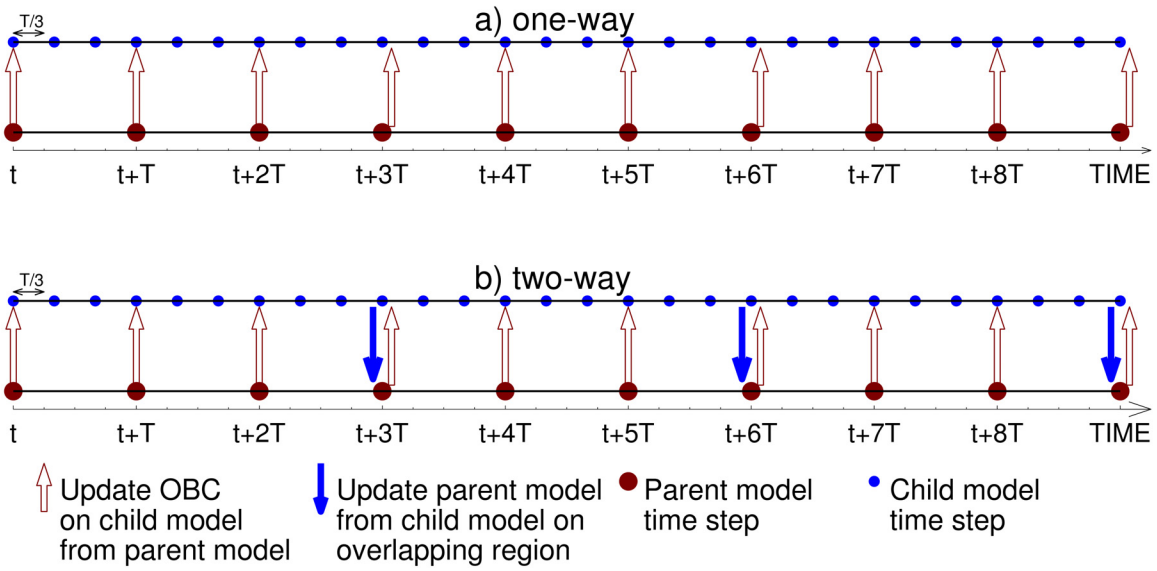

Figure 5.2. Time integration in (a) one-way and (b) two-way nesting with the temporal refinement factor of 3 and $T=\Delta t_{PM.}$

5.2.1 One-Way Nesting

For an OWN configuration, the open boundary conditions for the CM are specified using prognostic variables (temperature, salinity and currents) of the PM which are interpolated onto the CM grid between two consecutive time steps in the PM. A sponge layer with large viscosity near the CM boundary is applied to smooth inconsistencies between the PM and CM. The integration sequence for the time refinement factor of 3 (Fig. 5.2a) takes the following steps. Assuming all model variables at time t are known, the PM is integrated from time t to $t+\Delta t_{PM}$. The PM variables are linearly interpolated in time at intervals separated by $\Delta t_{PM}/3$ onto the corresponding CM time steps. Since interpolated variables at each CM time step are still on the PM grid, they are spatially interpolated onto the CM grid points over the feedback interface zone (FIZ). In this study, the pressure, temperature and salinity variables are linearly interpolated from the PM grid onto the CM grid and the velocity variables use a nearest-neighbor interpolation in space which guarantees the conservation of model variables during the interpolation step. Once the open boundary conditions for the CM are obtained, the CM is integrated $\Delta t_{PM}/\Delta t_{CM}$ times until the CM reaches $t+\Delta t_{PM}$. The PM is then advanced and the above procedure repeats. For OWN there is no feedback from the CM to PM and the CM can be run

offline in this case. As mentioned above, the disadvantage of the OWN approach is that the PM with a coarse resolution does not benefit from the finer resolution results produced by the CM and therefore inconsistencies in results produced by the PM and CM could occur, which will be discussed more in Section 5.4.

5.2.2 Two-Way Nesting

The first step in TWN is the specification of open boundary conditions for the CM in the same way as in OWN. The second step is the feedback of CM variables to the PM (Fig. 5.2b). The feedback from the CM to PM can take place over the whole domain of the CM, or over a feedback interface zone (FIZ) close to open boundaries of the CM (Fig. 5.1c). The FIZ consists of three and two PM grid points for tracers and currents, respectively. The feedback over the whole domain can take place at time intervals $N\Delta t_{PM}$ during the integration of the PM, where N is an integer equal or larger than 1. Over the FIZ, however, the feedback occurs every Δt_{PM} time steps. AGRIF provides three types of spatial interpolations for the feedback from the CM to PM: (a) the direct copy from the child to the parent grid (available when an odd horizontal refinement factor is used), (b) spatial averaging, and (c) a full weighting scheme. In this study only the spatial averaging is used, which means that for the space refinement factor of 3 a simple average of 9 CM grid cells around each PM grid cell is made. This filters out small-scale features in the CM which could introduce numerical noise in the PM (Debreu and Blayo, 2008) and therefore the information passed from the CM to PM has horizontal scales that are well resolved by the PM. This interpolation method, however, does not ensure conservation through the CM and PM interface and therefore a flux correction method (Debreu and Blayo, 2008) is applied to balance the misfit between the fluxes at the interface.

5.2.3 The Semi-Prognostic Method as a Two-Way Nesting Technique

In the conventional TWN technique discussed above, numerical noise could be generated in the PM since PM variables over the overlapping region are constrained by the CM results, and outside the overlapping region the PM variables are purely

prognostic and not constrained directly by the CM results. An alternative to the conventional TWN technique is the use of the semi-prognostic method (SPM) to transfer information from the CM to PM as suggested by Sheng et al. (2005). By using the SPM, the temperature and salinity fields in the PM are prognostic over its entire domain and numerical noise in the tracer fields due to the nesting will be eliminated. This makes the TWN technique based on the semi-prognostic method to be very attractive, especially in the study of tracer distributions in the ocean.

In the semi-prognostic method, the hydrostatic equation in the PM is modified based on:

$$\frac{\partial P_{PM}}{\partial z} = -g\rho_{PM} - g(1-\beta)\langle \hat{\rho}_{CM} - \rho_{PM} \rangle \tag{5.1}$$

where P_{PM} is the pressure in the PM, which is used to calculate the horizontal pressure gradient in the horizontal momentum equations of the PM, ρ_{PM} is the PM density, $\hat{\rho}_{CM}$ the CM density interpolated onto the PM grid, and the angle brackets represent a smoothing operator to choose the spatial scales of the feedback from CM to PM. In Eq. (5.1), β is a coefficient ranging between 0 and 1, which determines the strength of the feedback from CM to PM. In the case of β=1, the density of the CM does not affect the PM and the nesting becomes one-way. In the case of β=0, the density of the CM is used to replace the density in the PM. In this study I examine the application of the semi-prognostic method as an alternative to the conventional two-way nesting technique.

5.3 Nested-Grid Shelf Circulation Modelling System

The regional shelf circulation modelling system for the eastern Canadian shelf discussed in Chapeter 3 is used to assess the performance of different nesting techniques. The nested-grid modelling system is based on the coupled ocean-ice NEMO modelling system. The ocean component of the system is based on the primitive equation, second-order of accuracy, z-coordinate OPA9 model. The sea-ice component is based on the two-category dynamic-thermodynamic LIM2 model. The nested-grid modelling system

consists of a coarse-resolution PM with a nominal horizontal resolution of 1/4° covering 34°N and 55°N and 33°W and 80°W, and a fine-resolution CM with a nominal horizontal resolution of 1/12° covering between 41°N and 52°N and between 55°W and 72°W (Fig. 5.3). Both the PM and CM use the same 46 z-levels with partial cells in the vertical. The PM uses a time-step Δt_{PM}=30 min and the CM a time-step Δt_{CM}=10 min. The coupling between the PM and CM is made using AGRIF as described in Section 5.2. Both the PM and CM use horizontal curvilinear grids and bathymetries based on Earth Topography 2 (Smith and Sandwell, 1997). The initial conditions of the modelling system are the state of rest, with initial model temperature and salinity set to be the monthly-mean hydrography of Geshelin et al. (1999). The sea surface salinity is also restored to the climatological monthly-mean surface salinity. The subgrid-scale horizontal mixing of tracers and momentum uses a biharmonic friction with a smagorinsky-like mixing (Griffies and Hallberg, 2000) and the subgrid-scale vertical mixing is parameterized using the turbulent closure scheme of Gaspar et al. (1990). The nested-grid modelling system uses the spectral nudging (Thompson et al., 2007) and semi-prognostic methods (Sheng et al., 2001) to reduce seasonal bias and drift in the modelling system as described in Urrego-Blanco and Sheng (2012). It should be noted that these two methods adjust the model dynamics on seasonal or longer time scales and do not affect characteristics of nesting interactions considered in this study.

The nested-grid modelling system is integrated for 5 years from January 2000 to December 2004 and forced by wind stress and net heat/freshwater fluxes at the sea surface computed from the atmospheric reanalysis fields of Large and Yeager (2004). The reanalysis used here consists of 6-hourly fields of wind speed, specific humidity and air temperature at 10 m above sea level, 12-hourly fields of short and long wave radiation, and monthly precipitation. The modelling system is also forced by monthly-mean river runoff. The open boundary conditions in the PM are taken from the 5-day mean ocean reanalysis data of Smith et al. (2010). More details on the model forcing, lateral open boundary conditions and model validation can be found in Chapters 2 and 3.

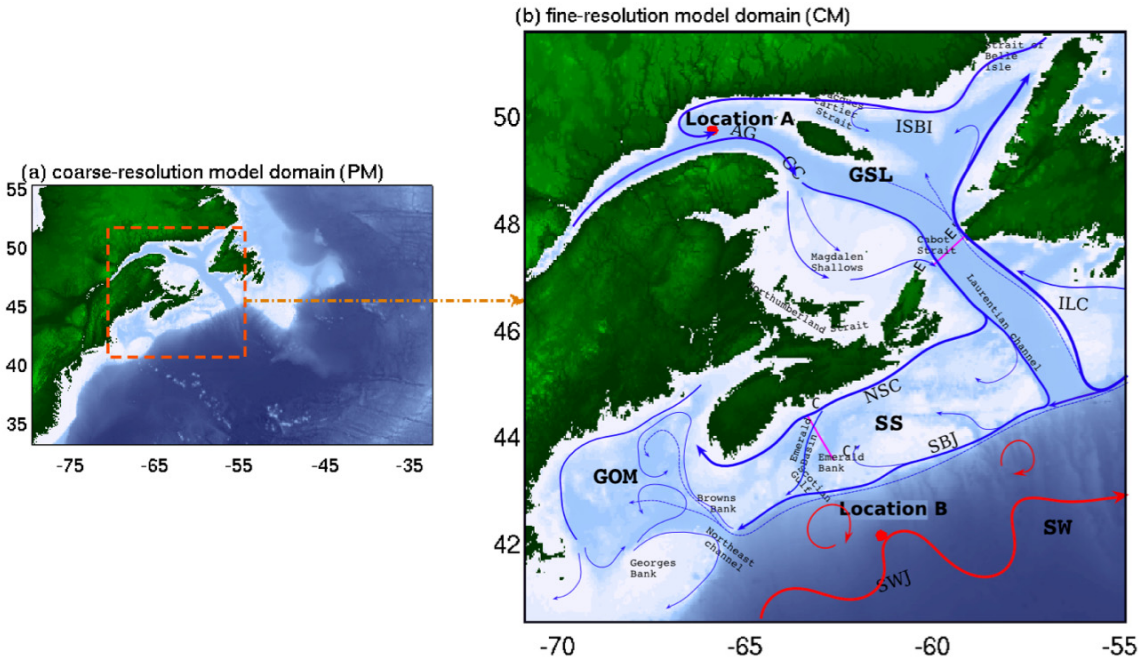

Figure 5.3. (a) Domain and major bathymetric features of the coarse-resolution parent model of the Northwest Atlantic, with the child model domain marked by dashed lines. (b) Domain and bathymetric features of the child model for the Gulf of St. Lawrence, Scotian Shelf and Gulf of Maine. Abbreviations used in (b) are: Anticosti Gyre (AG), Gaspé Current (GC), Nova Scotia Current (NSC), shelf break jet (SBJ), Slope Water Jet (SWJ), inflow from the strait of Belle Isle (ISBI), and inflow of the Labrador Current (ILC).

To examine the performance of different nesting techniques, model results in the following five numerical experiments are used:

Experiment TWN-CR: This is the control run in which the external forcing discussed above and the conventional two-way nesting are used. The feedback from the CM to PM takes place over the whole domain, with the exchange frequency of $3\Delta t_{PM}$, or 1.5 hours.

Experiment OWN: The model setup and forcing in this case are the same as in TWN-CR except that the interaction between the PM and CM is only one-way as discussed in section 2.1. Model results in this experiment are used to demonstrate the model inconsistencies between the CM and PM when no feedback occurs from CM to PM.

Experiment TWN-SP: In this experiment the semi-prognostic method is used as a two-way nesting technique. The model forcing and setup in this case are the same as in the control run except that the temperature, salinity, and currents in the CM do not feedback directly onto the PM over the whole CM domain. Instead, the CM density calculated from the CM temperature and salinity is used to update the hydrostatic equation of the PM based on Eq. (5.1) with $\beta = 0$. This experiment is used to demonstrate the advantage of the semi-prognostic method used as a two-way nesting technique in reducing numerical noise resulting from the feedback from CM to PM.

Experiment TWN-20D: This experiment is same as the control run except that the exchange frequency between the PM and CM is $960\Delta t_{PM}$, or 20 days. The model results in this experiment are used to examine how frequent the two-way coupling between the PM and CM should be in order to generate consistent subtidal circulation between the two model components.

Experiment TWN-BND: In this experiment two-way interaction between the PM and CM occurs only over their dynamical interface (FIZ zone). The exchange frequency is $3\Delta t_{PM}$, or 1.5 hours. Results in this case are used to examine the limitation of the two-way coupling occurring only over the FIZ.

5.4 RESULTS

In this section, the model results from the control run (TWN-CR) are first presented to demonstrate the performance of the nested-grid model with the default setup and model forcing. Comparisons of model results in different numerical experiments will then be used to assess the performance of different nesting techniques.

5.4.1 Model Results in the Control Run (TWN-CR)

Figures 5.4 and 5.5 present the 5-day mean temperature and currents on July 7, 2004 produced by the PM and CM at 9 m and 100 m, respectively. The near-surface circulation

produced by the PM (Fig. 5.4a) features the northeastward flow associated with the Gulf Stream and temperatures above 20°C in the deep waters of the Slope Water Region; the north and northeastward flow of the North Atlantic Current; and the equatorward flowing Labrador Current along the shelf break of the Labrador Shelf. All these large-scale circulation features produced by the PM are in good agreement with the general knowledge of circulation in this region (Loder et al., 1998). On July 7, 2004, near-surface temperatures of about 8°C are found over the Labrador Shelf, Gulf of St. Lawrence and eastern Scotian Shelf, and slightly warmer in the Gulf of Maine and the western Scotian Shelf (~12°C). In comparison with the PM results, the CM reproduces more realistically the southeastward flow from the lower St. Lawrence Estuary to Cabot Strait and the southwestward flowing Nova Scotia Current along the inner Scotian Shelf, due to the finer horizontal resolution used in the CM (Fig. 5.4b). A quantitative comparison of Fig. 5.4a and b indicates that large-scale circulation features in the PM and the CM are very similar, except that the model results in the CM have more small-scale features.

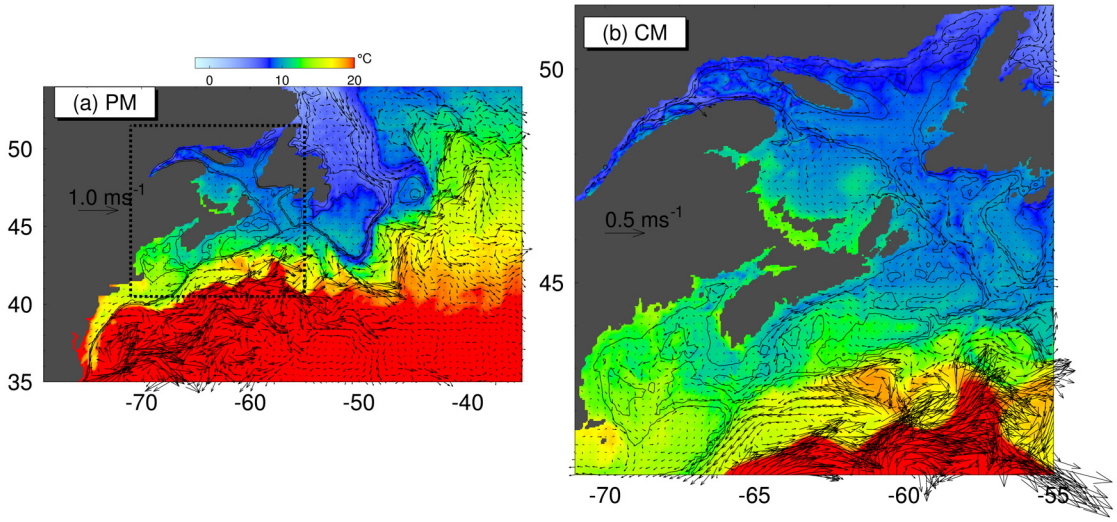

Figure 5.4. 5-day mean temperature and currents at 9 m on July 7, 2004 produced by (a) the PM and (b) the CM in TWN-CR. Velocity vectors are plotted at every 3rd model grid point.

The sub-surface circulation (100 m) over the eastern Canadian shelf produced by the nested-grid modelling system also features the Labrador Current, the Gulf Stream, and the North Atlantic Current (Fig. 5.5a). In deep waters, the sub-surface currents are weaker than the near-surface currents (Figs. 5.4b and 5.5b). Over the shelf region,

comparison of near-surface and sub-surface temperature shows a significant decrease in temperature, with warmer waters lying on top of cold waters, which is consistent with the observed vertical thermal structure of the waters in summer months over the region (Banks, 1966; Drinkwater and Gilbert, 2004).

The near-surface salinity distribution on July 7, 2004 produced by the PM is significantly fresher over the eastern Canadian shelf and saltier over deep waters over the northwest Atlantic Ocean (Fig. 5.6a). This is due mainly to the combined effect of equatorward propagation of low-salinity waters from high latitudes and fresh water discharge from rivers over coastal and shelf regions. A comparison of Fig. 5.6a and b indicates that the estuarine circulation associated with the river discharge over the western Gulf of St. Lawrence, the inner Scotian Shelf and coastal waters of the Gulf of Maine is better simulated by the CM than by the PM. For instance, instabilities in the Gaspé current and the freshwater plume of the St. John River are simulated by the CM, but not by the PM (Fig. 5.6).

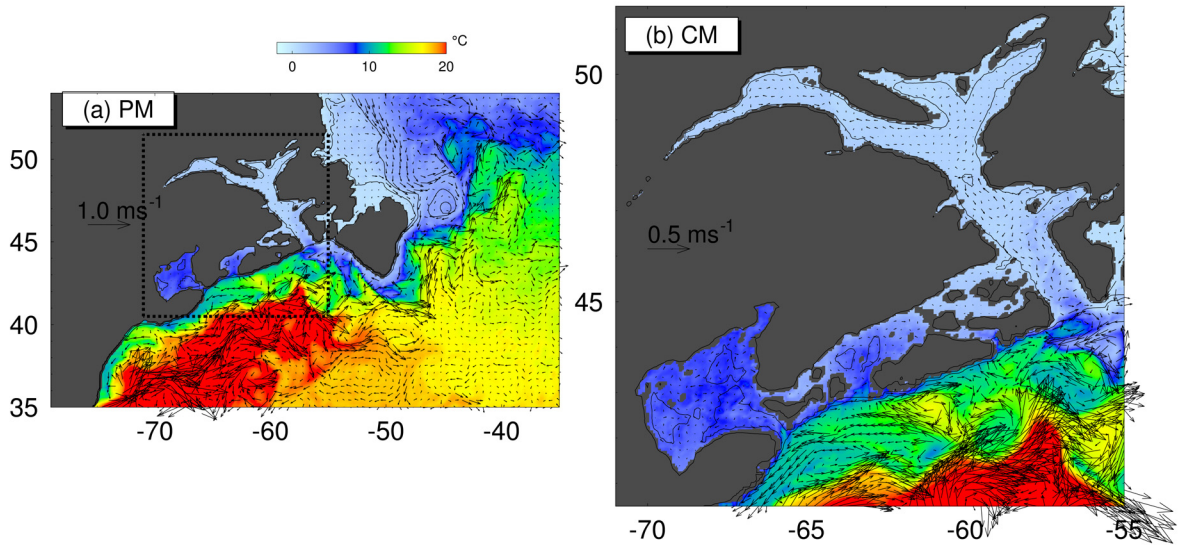

Figure 5.5. 5-day mean temperature and currents at 100 m on July 7, 2004 produced by (a) the PM and (b) the CM in TWN-CR. Velocity vectors are plotted at every 3rd model grid point.

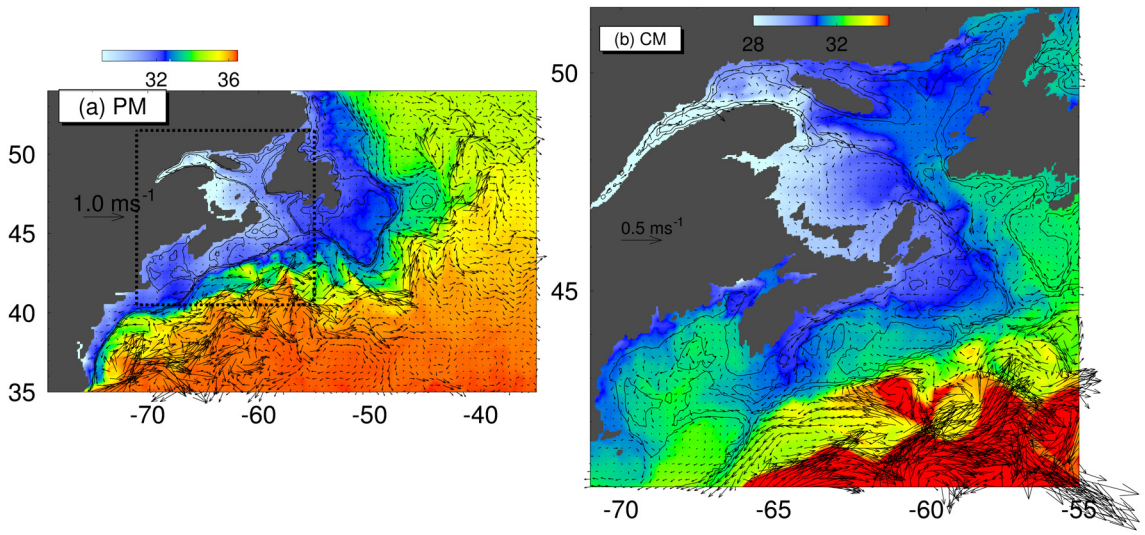

Figure 5.6. 5-day mean salinity and currents at 9 m on July 7, 2004 produced by (a) the PM and (b) the CM in TWN-CR. Velocity vectors are plotted at every 3rd model grid point.

5.4.2 Performance of One-Way and Two-Way Nesting Techniques

To further demonstrate the advantage of conventional TWN, I examine the consistency between the PM and CM results. The 5-day mean CM and PM results of salinity and currents in TWN-CR and OWN on July 17, 2004 are presented in Fig. 5.7. The near-surface salinity fields produced by the CM and PM are very similar in TWN-CR (Fig. 5.7a and b), with relatively high salinity over the Slope Water region and low salinity over the western Gulf of St. Lawrence and coastal waters of the Scotian Shelf. The TWN approach ensures the circulation produced by the PM and CM to be consistent. For instance, an anticyclonic eddy centered at about 62°W and 42°N occurs in both the CM and the PM on July 17. A salinity front in the central Gulf of St. Lawrence and the fresh water plume extending down to the western Scotian Shelf are also reproduced well by the CM and PM.

Figures 5.7c and d present 5-day mean near-surface circulation and salinity fields produced by the PM and CM in OWN. The use of the OWN technique could lead to significant differences in the circulation produced by the PM and CM. Over the lower St. Lawrence Estuary, for example, the near-surface salinity is much fresher in the PM than

in the CM. The influence of the freshwater plume over coastal waters of the Scotian Shelf is more intense in the CM than in the PM (Fig. 5.7c and d). The shelf break jet is significantly stronger in the CM than in the PM. There are also significant differences over the Slope Water region where meso-scale features appear at different positions in the CM and PM.

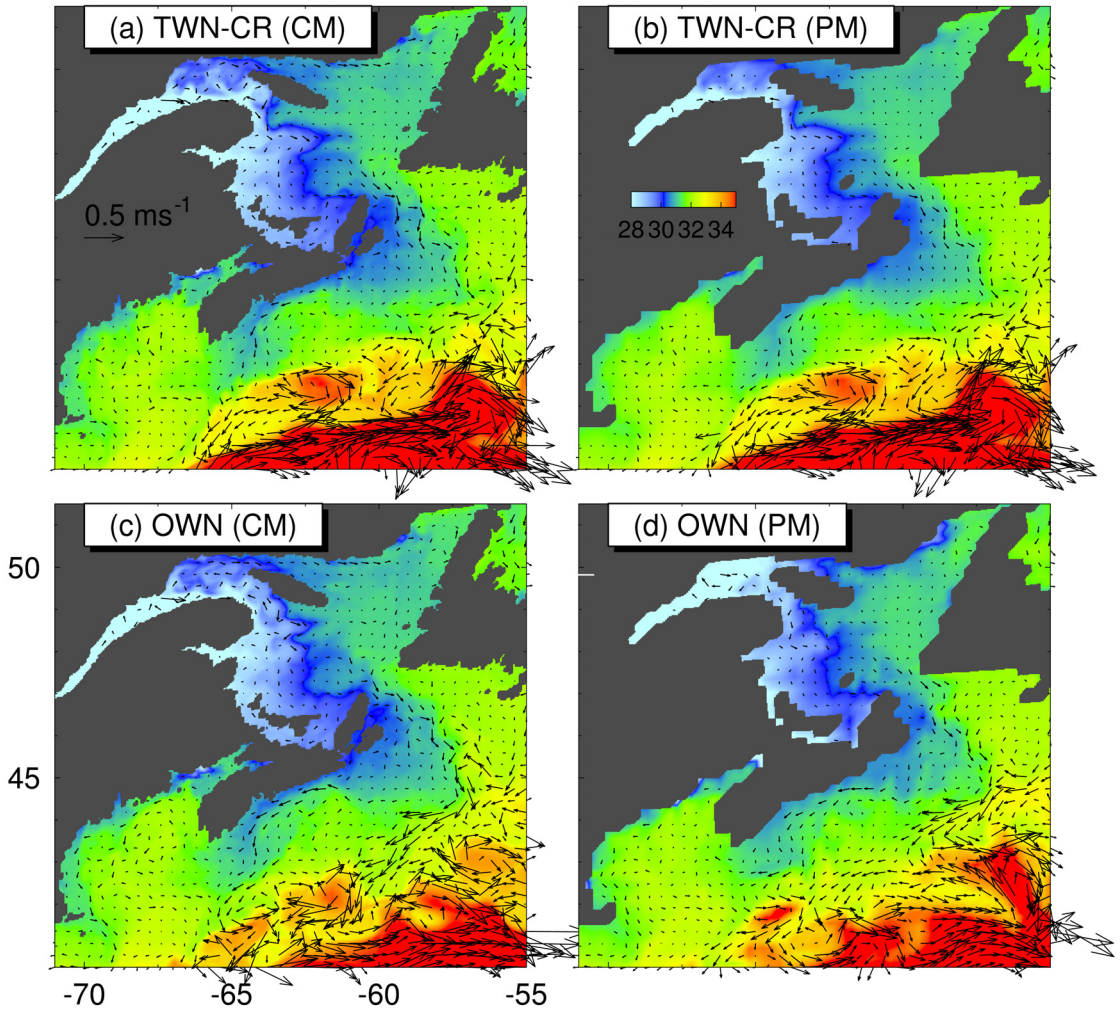

Figure 5.7. Comparison of 5-day mean near-surface (9 m) salinity and currents simulated by the CM (left panels) and PM (right panels) over the CM domain on July 17, 2004 in cases of (a, b) TWN-CR and (c, d) OWN. Velocity vectors are plotted at every 6th child model grid point.

I next examine the effect of data exchange frequencies in two-way nesting on the consistency of model results produced by the CM and PM. Figures 5.8a and b present the 5-day mean near-surface salinity and currents on July 17 produced by the CM and PM,

using the exchange frequency of 20 days in TWN-20D. The large-scale patterns in TWN-20D are characterized by relatively fresher waters over the western Gulf of St. Lawrence and relatively saltier waters over the Slope Water region in the CM and PM. This less frequent data exchange between the CM and PM still produces a large-scale subtidal circulation that is reasonably consistent between the different model components in TWN-20D. For smaller-scale subtidal circulation features, however, the PM and CM model results differ over several regions such as the lower St. Lawrence Estuary, the coastal waters of the Scotian Shelf and estuarine waters in the northern Gulf of St. Lawrence and the Gulf of Maine. It should be noted that the main focus here is the effect of different nesting techniques on the subtidal circulation. For circulation with high-frequency variability, the exchange frequency of 20 days would not ensure consistency between the PM and CM.

Figures 5.8c and d present the results produced by the CM and PM with the feedback taking place only over the feedback interface zone (TWN-BND). There are significant differences in the near-surface salinity fields produced by the PM and CM. In comparison with the CM results, the PM in this case does not reproduce well the influence of the low-salinity estuarine plume which emanates from the western Gulf of St. Lawrence through Cabot Strait and affects the inner Scotian Shelf (Figs. 5.8c and d). The near-surface salinity over the western Gulf of St. Lawrence, central Scotian Shelf and Gulf of Maine in TWN-BND is higher in the PM than in the CM. Finally, the circulation over the Slope Water region simulated by the PM in this case does not agree well with the flow field produced by the CM. Therefore, the interaction between the CM and PM over the feedback interface zone (FIZ) is not sufficient to generate consistent circulation and hydrography between the CM and PM.

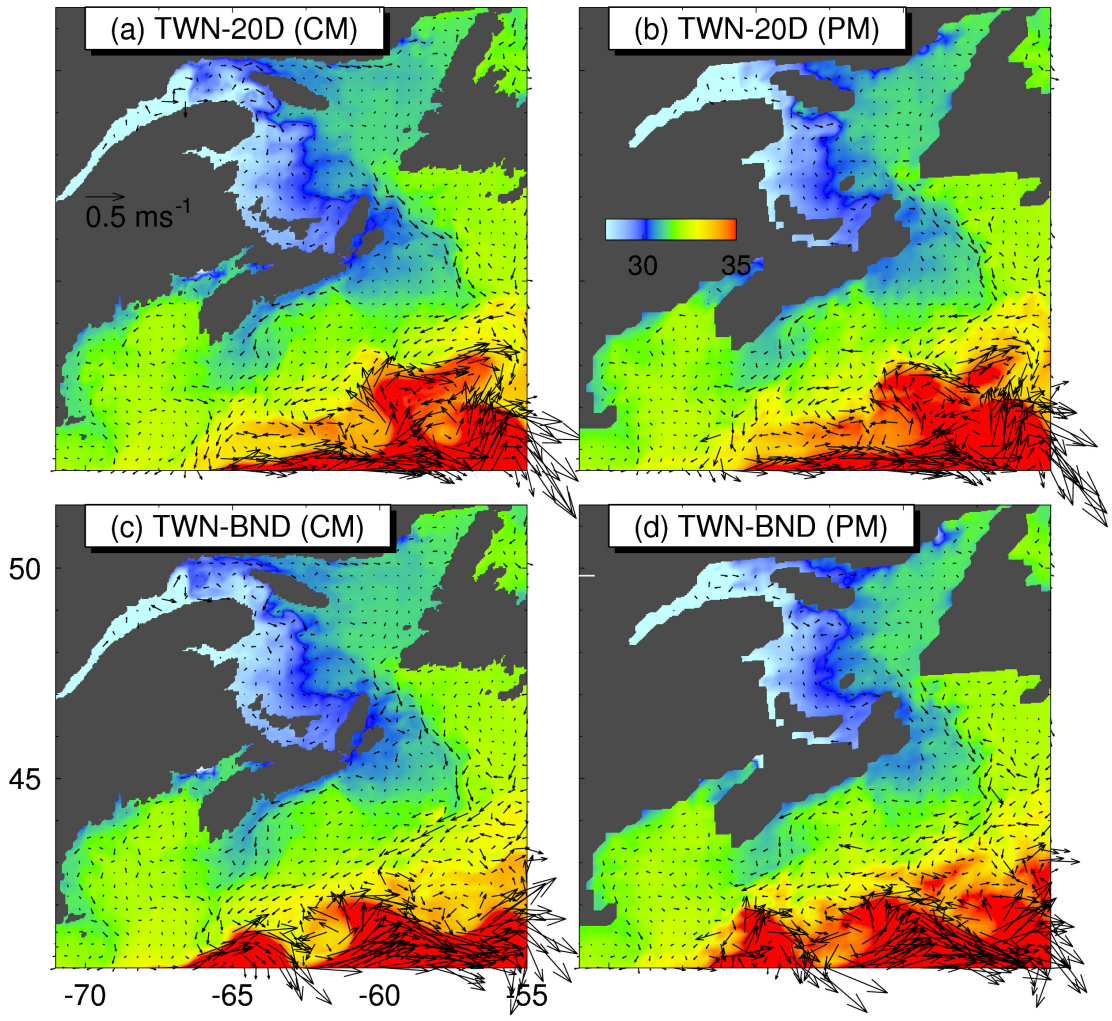

Figure 5.8. Comparison of 5-day mean near-surface (9 m) salinity and currents simulated by the CM (left panels) and the PM (right panels) over the CM domain on July 17, 2004 in cases of (a, b) TWN-20D and (c, d) TWN-BND. Velocity vectors are plotted at every 6th child model grid point.

To quantify the consistency between PM and CM results, I use ε^2 defined in Eq. 4.12, but replacing ϕ_i^O by ϕ_i^{PM} and ϕ_i^M **by** ϕ_i^{CM}, where ϕ_i^{PM} is a PM variable and ϕ_i^{CM} is a CM variable, and N is the number of PM grid points that lie within the CM domain. Again, the agreement between PM and CM is perfect if $\varepsilon^2 = 0$ and the inconsistency between CM and PM results increase as ε^2 increases. Figure 5.9 presents scatterplots of CM and PM results and the corresponding ε^2 values in four different cases (TWN-CR, OWN, TWN-20D, and TWN-BND). The largest values of ε^2 in the four cases shown in Fig. 5.9

occur in OWN, indicating significant inconsistency between PM and CM results if nesting is one-way. In this case ε^2 has values of about 0.104 for salinity and 1.24 for currents. The consistency between the PM and CM results improves significantly in TWN-CR, with ε^2 values of 0.005 for salinity and 0.04 for currents. This improvement is due to the feedback of CM results onto the PM. In comparison with results in OWN, model results in TWN-20D and TWN-BND also improve significantly the consistency between PM and CM with smaller ε^2 values than in OWN.

Figures 5.10 and 5.11 present time series of model salinity and temperature at locations A and B produced by the PM and CM in four numerical experiments (TWN-CR, OWN, TWN-20D, and TWN-BND). These two locations are in the lower St. Lawrence Estuary and in the Slope Water region respectively as marked in Fig. 5.3. In TWN-CR, the sub-surface salinities and temperatures (Fig. 5.10a and 5.11a) in the CM and PM agree well at these two locations as expected. By comparison, the sub-surface salinity at location A produced by the CM in OWN is highly comparable to the results in TWN-CR, but the PM results in OWN differ significantly from the CM results in TWN-CR (Fig. 5.10b). This indicates that in OWN the CM performs reasonably well, but the PM performs less well due to the lack of feedback from the CM to PM in this case. The sub-surface salinity produced by the PM and CM agrees better in TWN-20D (Fig. 5.10c) than in OWN (Fig. 5.10b). There are some discrepancies due to the less frequent information exchange between the PM and CM in TWN-20D. It should be noted that the model results have more high frequency variability in TWN-20D than TWN-CR. In TWN-BND the CM results are similar to the CM results in TWN-CR, but the PM performs less well and drift away from the CM results if only information at the FIZ is exchanged (Fig. 5.10d). At location B situated over the Slope Water region (Fig. 5.3), the time series of sub-surface temperature display significant high frequency variability (Fig. 5.11). The sub-surface time series of temperature produced by the PM differs significantly from CM results in the cases of OWN and TWN-BND (Figs. 5.11b and d), with the largest differences in OWN. The CM results in OWN, TWN-20D and TWN-BND differ from the CM results in TWN-CR, indicating that more frequent information exchange is needed over the whole overlapping area between the CM and PM.

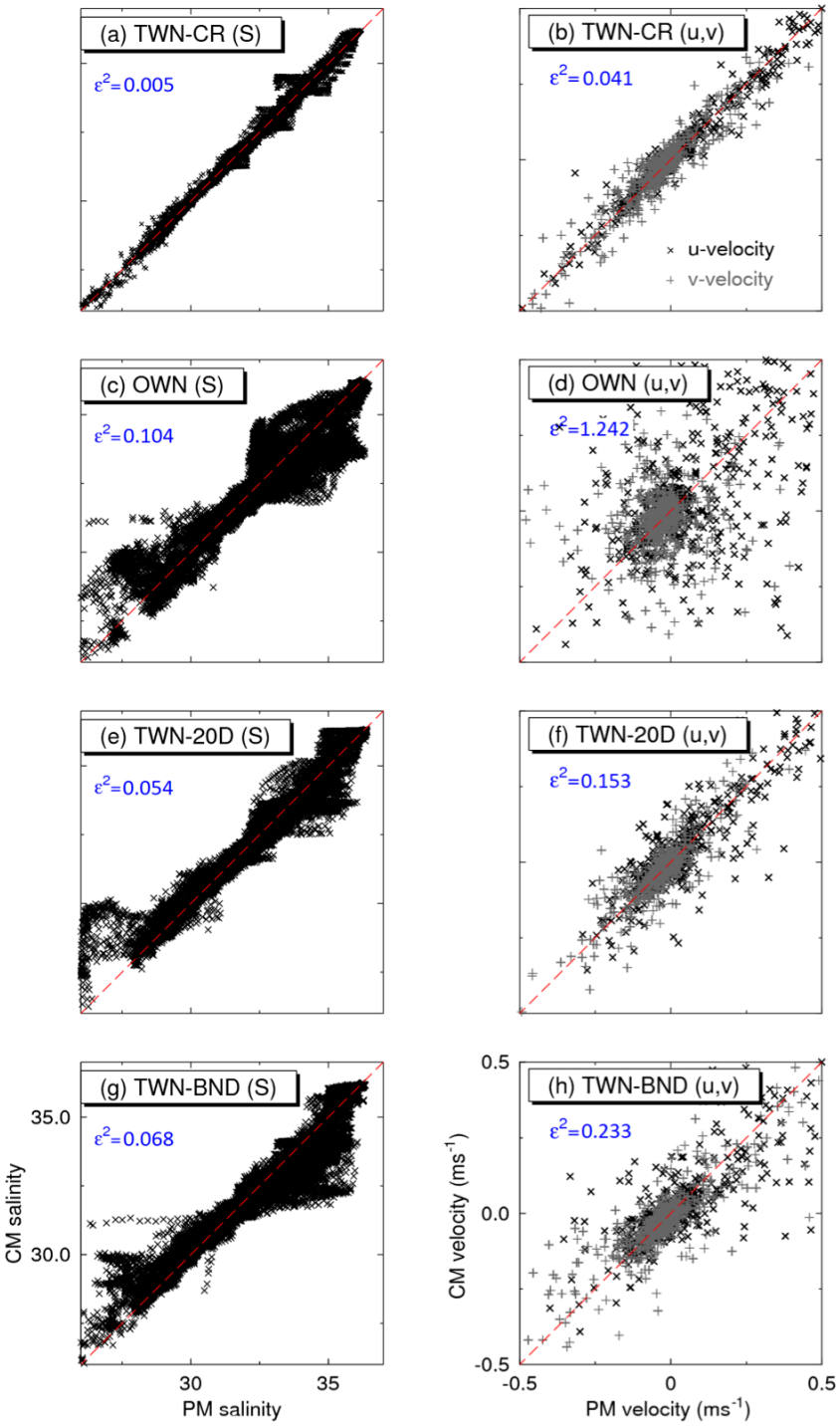

Figure 5.9. Scatterplots of salinity (left panels) and currents (right panels) produced by the PM and CM over the CM domain on July 17, 2004 in cases of (a, b) TWN-CR, (c, d) OWN, (e, f) TWN-20D, and (g, h) TWN-BND.

To further demonstrate the advantage of feedback from the CM to PM, I compare the standard deviation of sea surface elevations produced by the PM in the cases of TWN-CR

and OWN. Figure 5.12 presents the standard deviations of sea surface elevations in years 2001-2004 produced by the PM in the two cases and estimated from altimetry. In comparison with the PM results in OWN (Fig. 5.12b), the PM results in TWN-CR (Fig. 5.12a) have more variability in the sea surface elevation, which is more consistent with the altimetric estimates presented in Fig. 5.12c. The higher variability produced by the PM in TWN-CR occurs not only over the overlapping region between the CM and PM, but also over regions outside the overlapping region, including areas affected directly by the Gulf Stream and the North Atlantic Current. This indicates the effectiveness of TWN in improving the circulation in the PM not only over the overlapping region with the CM but also over areas outside common domain.

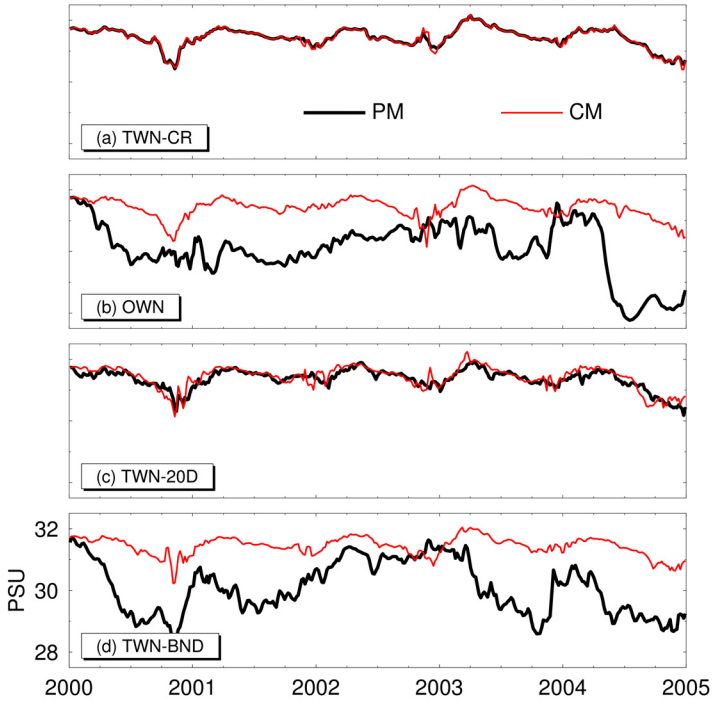

Figure 5.10. Time series of the 5-day mean sub-surface (32 m) salinity at location A over the northwestern Gulf of St. Lawrence produced by the PM (black) and CM (red) in cases of (a) TWN-CR, (b) OWN, (c) TWN-20D, and (d) TWN-BND.

I next examine the improvement of the regional circulation over coastal waters of the eastern Canadian shelf in the PM achieved by using two-way nesting. Figures 5.13a and c show the 2001-2004 time-mean normal currents at Cabot Strait and along the Halifax Line produced by the PM in OWN. The PM results in TWN-CR (Fig. 5.13c and d)

feature generally stronger coastal currents than in OWN (Fig. 5.13a and c). In particular, the inflow into the GSL at the eastern side of Cabot Strait is stronger and the outflow from the GSL at the western side of the Strait extends deeper throughout the water column in TWN-CR (Fig. 5.13b) than OWN (Fig. 5.13a). In TWN-CR, the estimated time-mean outflow at Cabot Strait in the PM is about 0.67 Sv. This value is relatively close to estimates from other modelling studies which suggest that the time-mean outflow at the western Cabot Strait is about 1.02 Sv (Han et al., 1999). By comparison, in OWN the estimated transport in the PM is only 0.38 Sv. The Nova Scotia current in the PM is also stronger in TWN-CR than in OWN. The maximum speeds are about 0.18 ms^{-1} in TWN-CR and about 0.12 ms^{-1} in OWN (Fig. 5.13c and d). The time-mean volume transport of the Nova Scotia Current in TWN-CR is about 0.61 Sv which is in good agreement with the observational estimate of 0.75 Sv of Loder et al. (2003). By comparison, the time-mean transport of the Nova Scotia Current in OWN is only 0.53 Sv.

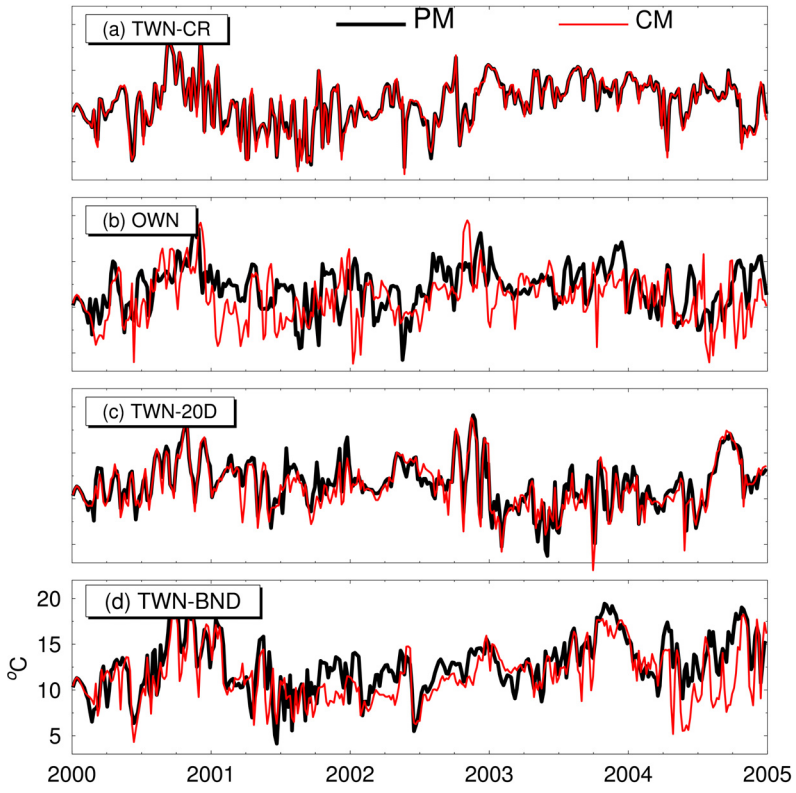

Figure 5.11. Time series of the 5-day mean sub-surface (100 m) temperature at location B over the Slope Water region off the Scotian Shelf produced by the PM (black) and CM (red) in cases of (a) TWN-CR, (b) OWN, (c) TWN-20D, and (d) TWN-BND.

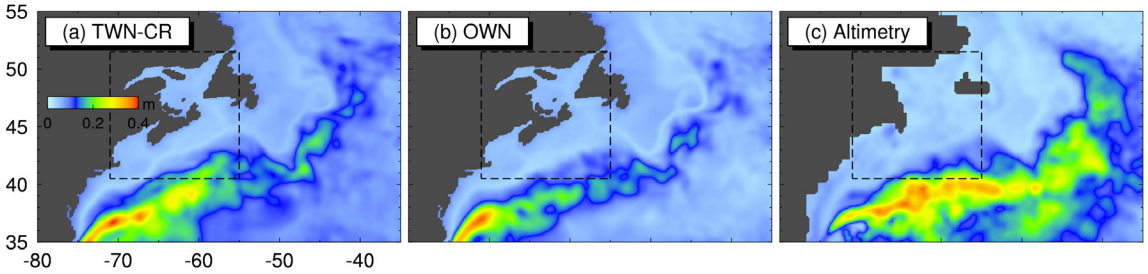

Figure 5.12. Standard deviations of sea surface elevations in the period 2001-2004 produced by the PM in cases of (a) TWN-CR, (b) OWN, and (c) estimated from altimetry. The region marked by dashed lines is the CM domain.

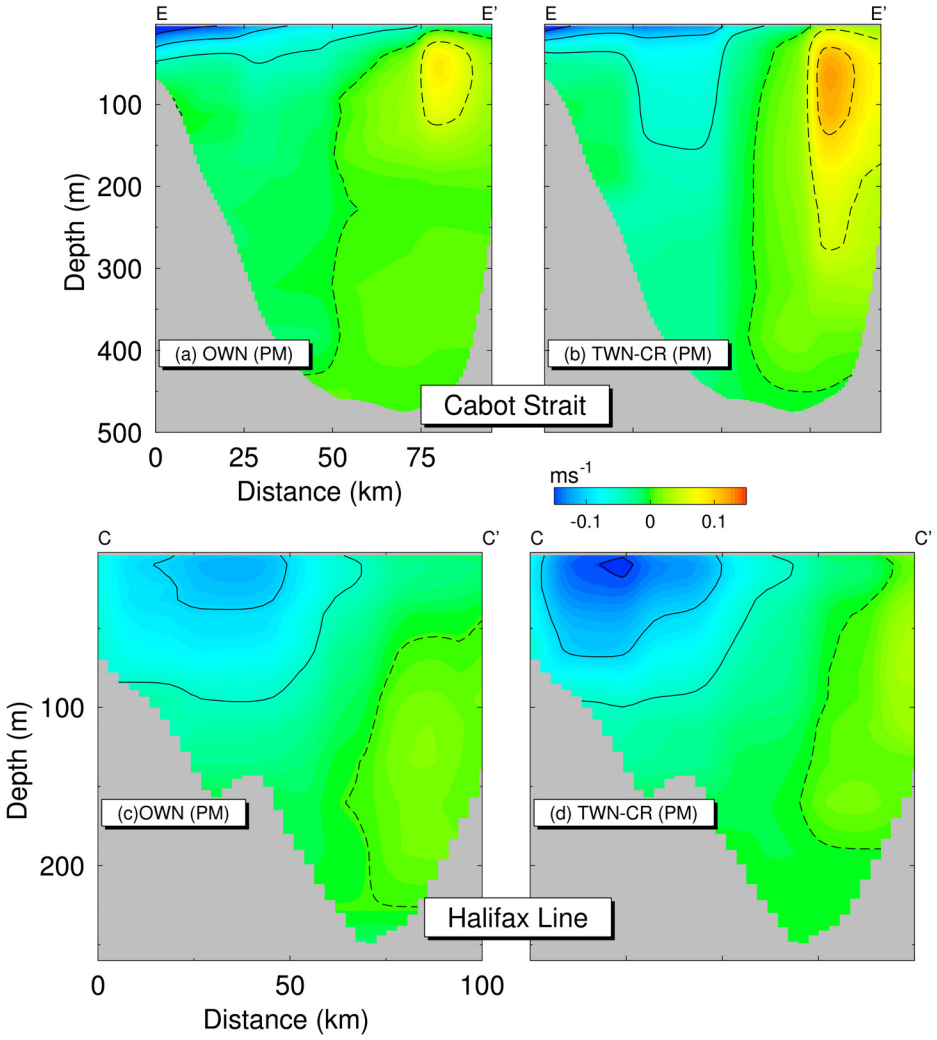

Figure 5.13. Time-mean normal velocities at Cabot Strait and the Halifax Line in the period 2001-2004 produced by the PM in cases of (a, c) OWN and (b, d) TWN-CR. Contour lines are spaced at 0.05 ms^{-1}.

5.4.3 Performance of the Two-Way Nesting Technique Based on the Semi-Prognostic Method

The conventional two-way nesting technique could lead to numerical noise in the PM due to the shock produced during the feedback from the CM to PM. Figures 5.14a and 5.14b show a 30-day time series of simulated subsurface salinity at location B in experiments EXP-CR and EXP-20D, respectively. The shocks introduced during the feedback in EXP-20D are obvious on days 140 and 160 in 2000, but are less obvious in EXP-CR. Figure 5.15 shows the same time series over a 2-day period (shaded interval in Fig. 5.14) in 2000. Although numerical noise also occurs in EXP-CR, the largest amplitudes of numerical noise occur in EXP-20D. However, the effect of the numerical shock persists throughout the entire record in EXP-CR (Fig. 5.15a) and decays faster in EXP-20D (Fig. 5.15b).

I next examine the performance of the two-way nesting technique based on the semi-prognostic method (TWN-SP). In this case the CM temperature and salinity are used to update the hydrostatic pressure equation in the PM, which in turn affects the horizontal pressure gradient terms in the PM.

Figures 5.14c and 5.15c demonstrate that the PM results in TWN-SP do not have numerical noise resulting from the feedback of the CM density to the PM. Because temperature and salinity in the PM are not directly affected by the CM results during the feedback step, the two-way nesting based on the semi-prognostic method has a major advantage over the conventional two-way nesting in simulating tracers by the PM. It should be noted that the TWN-SP method does not guarantee the temperature and salinity to be the same in the PM and CM over the overlapping region since the hydrography in the PM over the overlapping region is not constrained directly by the CM results in this method.

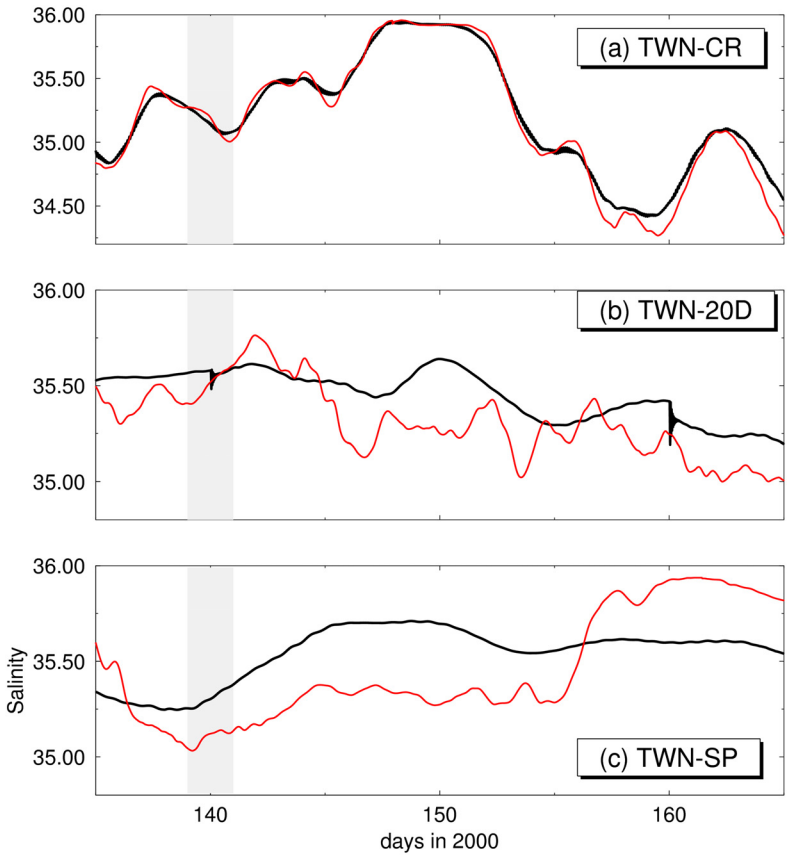

Figure 5.14. Time series of instantaneous sub-surface (100 m) salinity at location B over the Slope Water region off the Scotian Shelf produced by the PM (black) and the CM (red) between June 1, 2000 and June 30, 2000 in cases of (a) TWN-CR, (b) TWN-20D, and (c) TWN-SP.

I next examine the consistence between CM and PM results in TWN-SP. Figures 5.16a and 5.16b show the 5-day mean sub-surface (32 m) temperature on December 29, 2001 produced by the PM and CM, respectively in TWN-SP. The PM and CM results are reasonably consistent in this experiment. The large-scale temperature fields in both the PM and CM in TWN-SP feature cold water of less than 2.5°C over the Gulf of St. Lawrence and the eastern Scotian Shelf. Over the Gulf of Maine and southwestern Scotian Shelf, water temperatures are slightly above ~5°C, and over the deepest part of the Slope Water region, the water reaches temperatures ranging between 13°C and 17°C. The temperature fields in Figs. 5.16a and b show some differences in small-scale structures produced by the PM and CM, which is due mainly to the finer resolution of the CM. For deeper waters, at 100 m, Figs. 5.17a and b show also good agreement of the

large-scale temperature fields in the CM and PM on August 26, 2004, with some minor differences in meso-scale features.

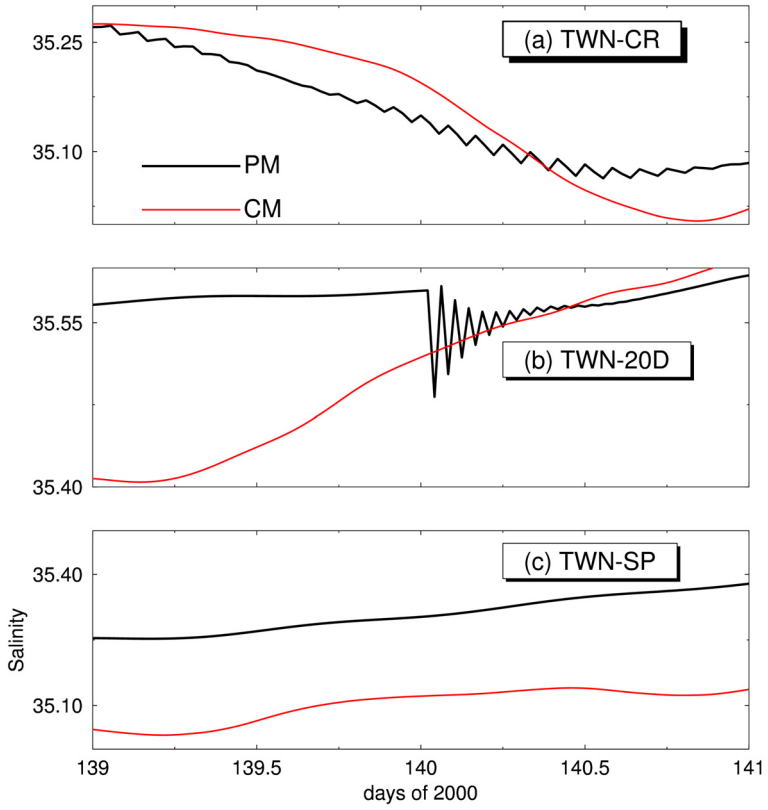

Figure 5.15. Time series of instantaneous sub-surface (100 m) salinity at location B over the Slope Water region off the Scotian Shelf produced by the PM (black) and the CM (red) between May 19, 2000 and May 20, 2000 (shaded period in Fig. 5.14) in cases of (a) TWN-CR, (b) TWN-20D, and (c) TWN-SP.

To quantify the consistency of CM and PM results in TWN-SP in Figs. 5.16 and 5.17, I present scatterplots of CM and PM temperature and their ε^2 values in Fig. 5.18a and b. The scatterplots indicate that the PM and CM results are consistent in TWN-SP (Fig. 5.18a and b) with some relatively small spread about the line of perfect agreement. Figures 5.18c and d shows that the spread of CM and PM results about the line of perfect agreement is still significantly smaller in TWN-SP than in OWN. The ε^2 values in Fig. 5.18 are 0.014 and 0.018 for TWN-SP which are significantly smaller than the ε^2 values of 0.064 and 0.103 for OWN. The ε^2 values in TWN-SP are somewhat higher than the values of about 0.009 in TWN-CR (not shown), indicating that the CM and PM results

are slightly more consistent in the latter experiment. Clearly, the advantage of TWN-SP lies in the skill to produce consistent CM and PM results and to eliminate numerical noise resulting from the interaction of model components.

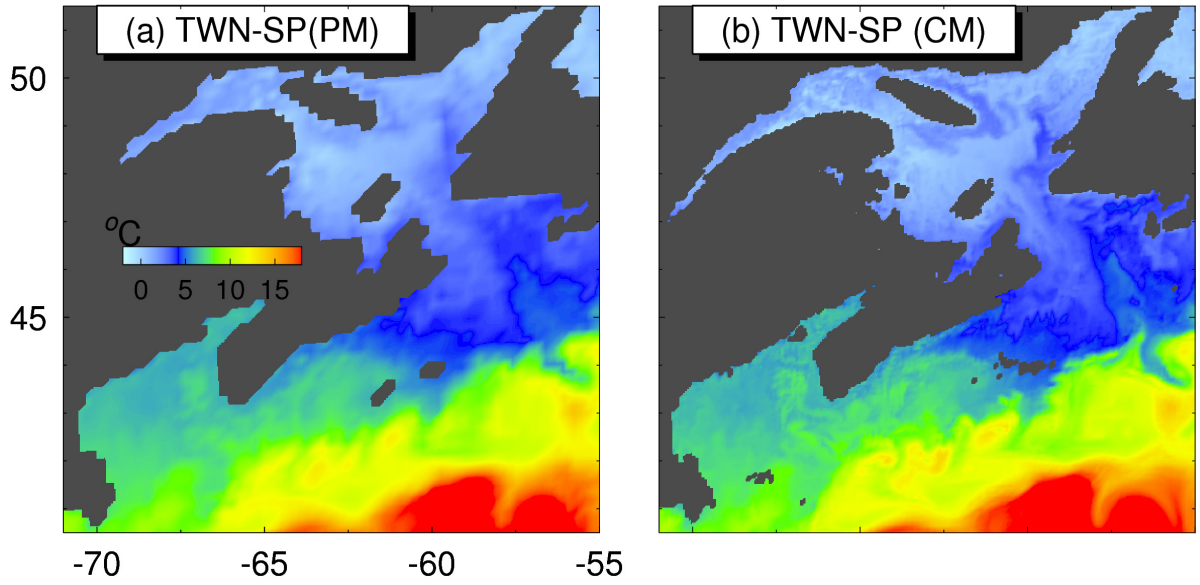

Figure 5.16. Comparison of 5-day mean sub-surface temperature (32 m) on December 29, 2001 over the CM domain produced by (a) the PM and (b) the CM in TWN-SP.

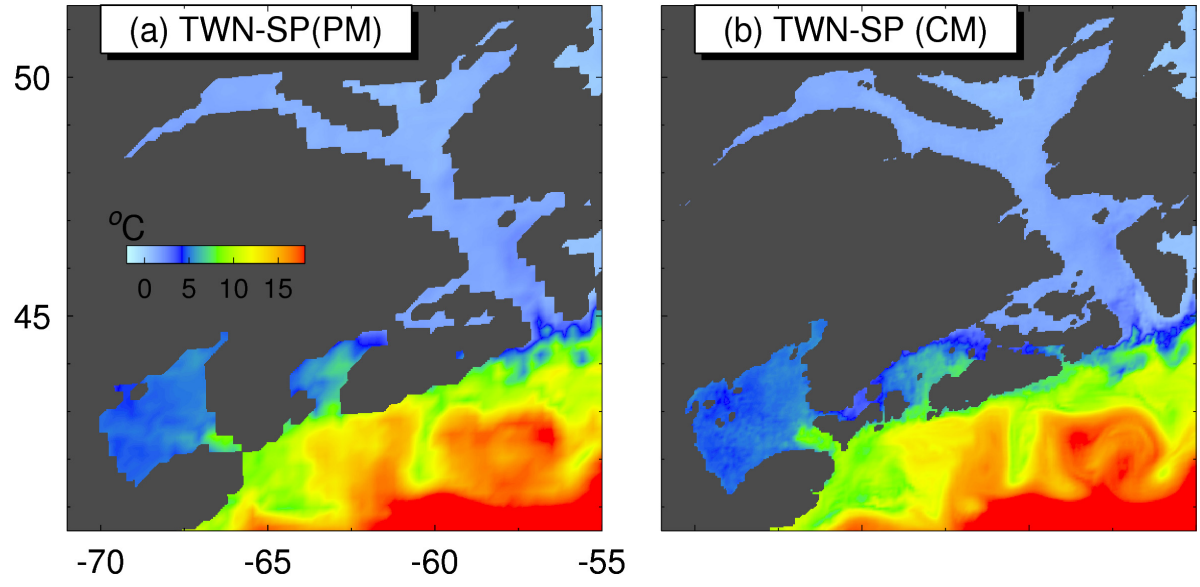

Figure 5.17. Comparison of 5-day mean temperature at 100 m on August 26, 2004 over the CM domain produced by (a) the PM and (b) the CM in experiment TWN-SP.

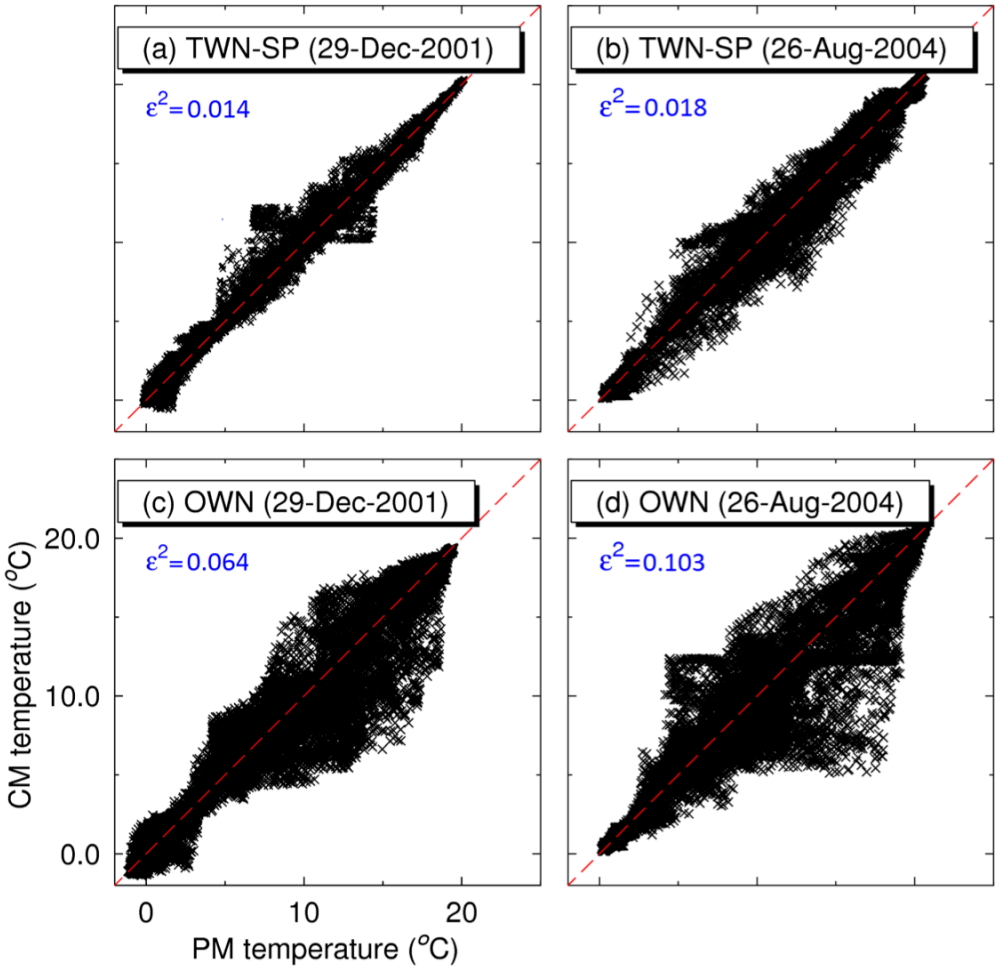

Figure 5.18. Scatterplots of temperature simulated by the PM and the CM on December 29, 2001 (left panels) and August 26, 2004 (right panels) in cases of (a, b) TWN-SP and (c, d) OWN.

5.5 Summary and Conclusions

This study assessed the performance of three different nesting techniques: the conventional two-way nesting (TWN); the one-way nesting (OWN); and the two-way nesting based on the semi-prognostic method (TWN-SP). The assessment was made in terms of four aspects. (a) The consistency between parent (PM) and child (CM) model

results, (b) improvement of the large-scale circulation in the PM, (c) improvement of the regional circulation in the CM, and (d) the reduction of numerical noise in the PM generated by feedback of model variables from the CM to the PM.

The nested-grid circulation modelling system for the eastern Canadian shelf was used in this study. The main circulation features over the eastern Canadian shelf were reproduced reasonably well by the modelling system using the conventional two-way nesting approach (TWN-CR). It was demonstrated that the TWN has better performance than the OWN. In particular, TWN ensures consistency between CM and PM results when feedback from the CM to PM occurs frequently. By comparison, the PM results in the case of OWN drift away from the CM results. I also demonstrated that the two-way coupling between the CM and PM taking place only over the feedback interface zone does not guarantee consistency between PM and CM results. Therefore, nested-grid ocean models should implement two-way coupling between CM and PM over the whole CM domain. It was also shown that the use of a less frequent exchange between the CM and PM in the two-way configuration (TWN-20D) led to a relatively good agreement between CM and PM results for subtidal circulation. However, more frequent exchange between the PM and PM is needed for simulating high frequency variability of the model fields.

The variability of the sea surface elevation produced by the PM in TWN-CR was larger than in OWN indicating that TWN significantly improves the large-scale circulation in nested-grid ocean models. The enhanced sea surface elevation variability in TWN not only occurs over the overlapping region between CM and PM, but also over regions outside the overlapping region, including the Slope Water region and the northwest corner of the North Atlantic Current. Another advantage of using TWN instead of OWN is the improvement of regional circulation features in the PM. In particular, coastal currents are more realistically reproduced by the PM in TWN-CR than in OWN. In TWN the higher horizontal resolution of the CM and the feedback of model results to the PM lead to generally stronger and more realistic coastal currents than in OWN.

It was demonstrated that numerical noise can be generated in the conventional TWN. To eliminate this noise, an alternative TWN technique based on the semi-prognostic method (TWN-SP) was implemented in which the temperature and salinity in the CM are used to add a correction term on the horizontal momentum equations of the PM. The main advantages of the TWN-SP are (1) the elimination of numerical noise during the feedback of CM to the PM, and (2) the consistency between PM and CM results. The TWN-SP is therefore a very attractive method to use in modelling studies of tracers in the ocean.

CHAPTER 6

CONCLUSIONS

This study was motivated by the highly variable oceanographic conditions over the eastern Canadian shelf (ECS) which have important implications for ocean prediction, ecosystem dynamics, and human activities such as fisheries, transportation, or the oil and gas industry. The main goal of my thesis was to improve the understanding of physical processes affecting circulation and associated variability over the ECS, and their relation with the atmospheric variability over the north Atlantic Ocean, the deep ocean (the effect of the Labrador Current and the Gulf Stream), and with shelf processes including river discharge and sea ice formation. The approach included the development, validation, and analysis of model results produced by a nested-grid coupled ocean-ice modelling system based on the Nucleus for the European Modelling of the Ocean (NEMO). The nested-grid model was used to conduct different numerical experiments, and the model results were analyzed using different statistical techniques, including correlation analysis, conventional and complex empirical orthogonal function analysis, and a set of indices to measure the model skill in reproducing observed oceanographic conditions. The nested-grid modelling system consists of a coarse-resolution parent model (PM) of the northwest Atlantic and a fine-resolution child model (CM) of the Gulf of St. Lawrence (GSL), Scotian Shelf (SS), and the Gulf of Maine (GOM). The PM results were first used to examine subtidal variability of circulation and hydrography over the ECS, addressing issues such as the advection of interannual anomalies from high latitudes, or how the interaction between the Gulf Stream and the Labrador Current affects the hydrography over the Newfoundland and Scotian Shelves on interannual time-scales. The model results were also used to examine subtidal variability of circulation and hydrography on a regional scale over the GSL-SS-GOM. Model results were analyzed in different subtidal frequency bands including the time-mean, seasonal cycle, and the low and high frequency variabilities. The analysis was also extended to examine ice dynamics in the St. Lawrence Estuary where surface waters are partially frozen during winter.

Model results demonstrated that interannual variability over the Labrador Shelf is caused mainly by the advection of temperature and salinity anomalies from high latitudes by the Labrador Current (Urrego-Blanco and Sheng, 2012). These hydrographic anomalies at high latitudes are related to the large-scale atmospheric circulation and particularly to the strength of the winds during winter months over the Labrador Sea. Strong winds occur during positive phases of the NAO index, causing significant winter convection and relatively cooler and fresher conditions at high latitudes (Petrie, 2007). A statistical analysis demonstrated that hydrographic anomalies are correlated with the NAO index to a large extent over the Labrador Shelf, but to a lesser extent over the Newfoundland Shelf. The interannual variability over the Newfoundland Shelf is affected significantly by the non-linear interaction between the Labrador Current and the Gulf Stream, and complicated topography in the region. Over the deep waters off the Tail of the Grand Banks, interannual anomalies in the circulation and hydrography are generated due to the competing interaction between the Labrador Current and the Gulf Stream, and appear to be linked to anomalies in the meridional position of the Gulf Stream. The hydrographic anomalies generated off the Tail of the Grand Banks can be advected northwards by the North Atlantic Current, affecting the eastern Newfoundland Shelf, or equatorward as trapped waves along the shelf slope, affecting the Scotian Shelf and the Slope Water region. In addition, those interannual anomalies can affect the Gulf of St. Lawrence through the Laurentian Channel and the inner basins of the Scotian Shelf through the deep channels that favor cross shelf exchanges. These results have provided a more complete picture of the mechanism underlying the high interannual variability over the Scotian Shelf. The interannual variability over the Gulf of Maine was shown to be mainly affected by the cross shelf advection of anomalies from the Slope Water region, which in turn seem to be related to northward shifts of the Gulf Stream.

Further examination of the circulation variability in the model suggested that the temporal variability in atmospheric forcing significantly affects the strength of the time-mean cyclonic circulation over the Gulf of Maine (Urrego-Blanco and Sheng, 2014a). The time-mean circulation in the GSL is affected mainly by the time-mean atmospheric forcing and the inflow through the Strait of Belle Isle. The temporal variability in the

atmospheric forcing affects the outflow through western Cabot Strait, which in turn affects the transport of the Nova Scotian Current and the gulf-wide cyclonic circulation in the GOM. The seasonal salinity variability in the top 30 m of the GSL-SS-GOM in the model is mainly affected by the equatorward advection of low salinity waters emanating from the lower St. Lawrence Estuary to the GOM through the Scotian Shelf, which is consistent with observations. The subtidal high frequency variability of circulation in the GSL is affected by the variability in the estuarine circulation in response to the temporal variability in atmospheric forcing. On the Scotian Shelf, the non-tidal high frequency variability is mainly driven by the variability of wind forcing and mesoscale and non-linear dynamics over the shelf break and slope region. This study also showed that the interannual variability in this region is affected by the interannual anomalies generated near the Tail of the Grand Banks which are advected equatorward by the shelf break jet.The interannual variability in the simulated temperature and salinity were shown to be spatially coherent in intermediate waters in the GSL and partially caused by the local response to atmospheric variability and partially by the variabilities generated near the Tail of the Grand Banks that enter the GSL through eastern Cabot Strait.

I also conducted a study to fill an existing gap in the understanding of the spatial and temporal variations of sea ice over the Gulf of St. Lawrence and adjacent waters. In particular, I examined the patterns of sea ice production and melting, and the role of thermodynamics and dynamics of sea ice which have not been addressed in the past for this region. I showed that sea ice in the GSL is mainly formed over shallow areas, including the coastal waters along Quebéc's northern shore, along the southwestern GSL from the Gaspé Peninsula to the southern Northumberland Strait (Urrego-Blanco and Sheng, 2014b). By contrast, the main areas where sea ice is melted include the central GSL, the eastern side of Esquiman Channel, and waters near Cabot Strait both inside and outside the GSL. The spatial variability of sea ice growth and melting in the model is also affected by the advection of sea ice in the GSL. Advection also plays an important role in redistributing sea ice over different regions in the GSL. On average, during the ice season, net import of sea ice occurs at the eastern side of Esquiman Channel as sea ice is advected mainly from the western Esquiman Channel and from the region between

Anticosti Island and Quebec's northern shore. Net sea ice is imported onto the central GSL and Cabot Strait from the lower St. Lawrence estuary by the action of the Gaspé Current, and from the coastal regions of the western GSL by the action of winds and currents over the Magdalen shallows. An index was developed to quantify the relative importance of dynamics and thermodynamics of sea ice. Based on the value of the index it was found that over the GSL and adjacent waters most of the sea ice is affected by both thermodynamic and dynamic processes. However, over the coastal waters off southwestern Newfoundland, eastern Cabot Strait, and the eastern Scotian Shelf the advection of sea ice plays a dominant role. Analysis of model results also suggested that the capping of the upper ocean layer by the sea ice has a significant effect on the winter currents in the GSL (Urrego-Blanco and Sheng, 2014b). In particular, winter circulation was shown to be significantly weaker than otherwise would be in absence of sea ice, suggesting that changes in the oceanographic regime in the Gulf of St. Lawrence are to be expected in a warming climate, as sea ice coverage is lost. I speculate that over the ECS, changes in the physical environment will manifest more strongly as changes in sea ice distributions, due to its strong sensitivity to atmospheric and oceanic conditions. Other signals related to climate change, particularly those related to changes in hydrography will require long time series to identify due to the highly variable nature of these properties in the region.

The development of the nested-grid modelling system is an important part of my thesis work, which included the implementation of an alternative nesting technique based on the semi-prognostic method and the assessment of one-way and two-way nesting methodologies commonly used in ocean models (Urrego-Blanco et al., 2014). Previous studies examined conservation properties, and consistency and noise control at the interface between the parent (PM) and child (CM) model results (Debreu and Balyo, 2008). I also examined the consistency between the parent (PM) and child (CM) model results ober their overlapping domains, the improvement of the large-scale and regional circulations, and the elimination of numerical noise produced during the interaction of model grids. It was demonstrated that the conventional two-way nesting ensures that the CM and PM results are consistent with each other. By comparison, the one-way nesting

technique produces inconsistencies in the regional circulation between the CM and PM results. Another advantage of two-way nesting over one-way nesting is the improvement of the circulation in the PM. It was shown that by feeding back CM variables onto the PM, the circulation, and particularly the representation of coastal currents, are better simulated by a nested-grid system. This study demonstrated that in conventional two-way nesting significant amounts of numerical noise are produced in the PM when variables are fed back from the CM. The numerical shocks are due to strong interaction between PM and CM. I implemented an alternative two-way nesting technique in the NEMO modelling system based on the semi-prognostic method (Sheng et al., 2005), in which the temperature and salinity are not modified during the feedback from CM to PM. In this alternative technique, the CM density is used to update the PM density, which in turn is used in the calculation of the pressure in the PM. This implies that an adjusted horizontal pressure gradient is used in the horizontal momentum equations of the PM. The use of the semi-prognostic method as an alternative two-way nesting technique was shown to successfully eliminate the numerical noise in the PM while ensuring consistency between CM and PM variables.

The most important findings of my PhD research include:

- Interannual variability of circulation and hydrography over the Newfoundland and Scotian Shelves is strongly related anomalies produced near the Southren Tip of the Grand Banks due to nonlinear dynamics, and the interaction between the Labrador Current and the Gulf Stream over the area south of the Tail of the Grand Banks.
- Interannual variability of circulation and hydrography in subsurface waters in the Gulf of St. Lawrence is mainly affected by anomalies produced near the Southern tip of the Grand Banks, which affect the Gulf through the Laurentian Channel.
- The inflow of the Strait of Belle Isle plays an important role in affecting circulation over the northesatrn GSL, but has a less important role in the the circulation and interannual variability in other areas of the GSL.
- The temporal variability in atmospheric conditions affects the strength of the time-mean circulation in the Scotian Shelf and the Gulf of Maine.

- New insights were made about the sea ice dynamics over the Gulf of St. Lawrence, including the role of sea ice in modulating the strength of the estuarine circulation, and a new index that demonstrated the importance of both dynamics and thermodynamics on sea ice distributions in the GSL.
- The semi-prognostic method was used as a two-way nesting technique produces consistent circulations between PM and CM components. This method has the advantage of reducing numerical noise produced in the tracer fields during feedback from CM to PM.

The results presented in this thesis can be applied to studies of ecosystem dynamics of the ECS or to the design of observation systems over the ECS. For instance, monitoring regions which this study found to be important for the generations of hydrographic anomalies could be useful to anticipate regional changes which can potentially affect fisheries and ecosystems. It should be noted that the coupled ocean-ice model can be further developed by implementing tidal forcing, a more sophisticated multi-category sea ice model, and the use of high-resolution atmospheric forcing. After implementation of tidal forcing, my new circulation model can be used to study other scientific issues such as the interaction between tides and storm surges in coastal regions, or the effect of tides on the formation of sea ice in the Gulf of St. Lawrence. Using high-resolution atmospheric forcing will also allow the study of surface cooling due to the effect of hurricanes, or the horizontal redistribution of sea ice under different storm systems. The use of the model to study regional impacts of climate change on circulation and variability over the ECS will require using atmospheric forcing from climate models run under different scenarios of CO_2 emissions.

APPENDIX A

VERTICAL DISCRETIZATION USED IN THE OCEAN CIRCULATION MODEL

Table A.1. Depth and thickness of z-levels used in the ocean circulation model.

Level	Depth (m)	Thickness (m)
1	3.0	6.2
2	9.4	6.6
3	16.4	7.2
4	23.9	7.9
5	32.2	8.7
6	41.5	9.8
7	51.9	11.1
8	63.9	12.8
9	77.6	14.8
10	93.6	17.2
11	112.3	20.2
12	134.3	23.9
13	160.3	28.3
14	191.1	33.5
15	227.6	39.7
16	270.9	47.0
17	322.0	55.4
18	382.1	65.0
19	452.4	75.8
20	534.0	87.5
21	627.8	100.2
22	734.7	113.6
23	855.1	127.2
24	989.2	140.9

Level	Depth (m)	Thickness (m)
25	1136.9	154.3
26	1297.7	167.1
27	1470.9	179.0
28	1655.5	189.9
29	1850.4	199.7
30	2054.4	208.2
31	2266.4	215.6
32	2485.4	222.0
33	2710.1	227.4
34	2939.8	231.8
35	3173.6	235.6
36	3410.7	238.6
37	3650.7	241.2
38	3892.9	243.2
39	4137.0	244.9
40	4382.6	246.3
41	4629.5	247.3
42	4877.3	248.2
43	5125.9	249.0
44	5375.2	249.5
45	5624.9	250.0
46	5875.1	250.4

APPENDIX B

SPECIFICATION OF RIVER RUNOFF IN THE NESTED-GRID CIRCULATION MODEL

In this study the river runoff is treated as an additional mass flux over a particular area near the mouth of the river in the model. The definition of the area where river runoff is applied is explained below.

The discharge of the St. Lawrence River (SLR) is taken as an example to determine the areas of the other 12 rivers since the SLR it is the largest river in the region. The discharge of the SLR is distributed over a surface area defined by a radius of influence. The choice of this radius is to produce realistic distributions of salinity in the lower St. Lawrence Estuary and the GSL, and also to avoid numerical instabilities caused by large amounts of freshwater distributed over a small area in the model domain.

This was achieved by conducting a sensitivity analysis in which the influence radius for the SLR is varied from 50 km to 400 km downstream of Quebec city. I found that good model results can be obtained with a radius of influence of about 130 km for the SLR. For other rivers in the study region, their radii of influence were calculated by scaling the influence radius for the SLR with the square root of the ratio of their mean discharges to that of the SLR:

$$R = R_{SL}\left(\frac{Q}{Q_{SL}}\right)^{1/2} \tag{B.1}$$

Where R_{SL} is the influence radius from the SLR set to 130 km; Q_{SL} the mean discharge of the St. Lawrence River set to 7.28×10^3 m^3; Q the mean discharge of each individual river; and R the influence radius of each river.

The freshwater mass over the influence area is distributed only over the wet points by using a Gaussian function to determine what portion of the total mass flux should be distributed over the wet cells inside the influence area. The integration of the flow over the influence area equals the total flux and is maximum at the river mouth from where it decays away as a Gaussian function defined as follows:

$$F(r) = \frac{1}{\sigma\sqrt{2\pi}} e^{-\frac{r^2}{2\sigma^2}} \tag{B.2}$$

Where r is the radial distance from the river mouth to the points in the influence area, and σ is a constant based on the influence radius (R) and the assumption that the mass flux at a distance R from the river mouth equals 1% of the mass flux at the mouth itself:

$$\sigma = \sqrt{-\frac{R^2}{2Ln(0.01)}} \approx 0.33R \tag{B.3}$$

The volume flux q_i at every wet grid cell over the influence area around a river mouth is calculated as:

$$q_i = \frac{Q F(r_i)}{\sum a_i F(r_i)} \tag{B.4}$$

Where a_i is the area associated with each model grid cell within the influence area and $F(r_i)$ is calculated according to Eq. B.2 at the distance r_i from each grid cell to the river mouth.

APPENDIX C

COPYRIGHT

1. An edited version of Chapter 2 was published by Taylor and Francis. Copyright (2012) Taylor and Francis. It is reproduced here by permission of Taylor and Francis:

2. Chapter 3 is reproduced here by permission of Springer.

SPRINGER LICENSE
TERMS AND CONDITIONS

May 28, 2014

This is a License Agreement between Jorge Urrego ("You") and Springer ("Springer") provided by Copyright Clearance Center ("CCC"). The license consists of your order details, the terms and conditions provided by Springer, and the payment terms and conditions.

All payments must be made in full to CCC. For payment instructions, please see information listed at the bottom of this form.

License Number	3397700392116
License date	May 28, 2014
Licensed content publisher	Springer
Licensed content publication	Ocean Dynamics
Licensed content title	Study on subtidal circulation and variability in the Gulf of St. Lawrence, Scotian Shelf, and Gulf of Maine using a nested-grid shelf circulation model
Licensed content author	Jorge Urrego-Blanco
Licensed content date	Jan 1, 2014
Volume number	64
Issue number	3
Type of Use	Thesis/Dissertation
Portion	Full text
Number of copies	1
Author of this Springer article	Yes and you are a contributor of the new work
Order reference number	None
Title of your thesis / dissertation	Subtidal circulation, hydrography, sea ice and associated variability over the eastern Canadian shelf using a coupled ocean-ice model
Expected completion date	Jul 2014
Estimated size(pages)	210
Total	0.00 USD
Terms and Conditions	

Introduction
The publisher for this copyrighted material is Springer Science + Business Media. By clicking "accept" in connection with completing this licensing transaction, you agree that the following terms and conditions apply to this transaction (along with the Billing and Payment terms and conditions established by Copyright Clearance Center, Inc. ("CCC"), at the time that you opened your Rightslink account and that are available at any time at http://myaccount.copyright.com).

Limited License

With reference to your request to reprint in your thesis material on which Springer Science and Business Media control the copyright, permission is granted, free of charge, for the use indicated in your enquiry.

Licenses are for one-time use only with a maximum distribution equal to the number that you identified in the licensing process.

This License includes use in an electronic form, provided its password protected or on the university's intranet or repository, including UMI (according to the definition at the Sherpa website: http://www.sherpa.ac.uk/romeo/). For any other electronic use, please contact Springer at (permissions.dordrecht@springer.com or permissions.heidelberg@springer.com).

The material can only be used for the purpose of defending your thesis limited to university-use only. If the thesis is going to be published, permission needs to be re-obtained (selecting "book/textbook" as the type of use).

Although Springer holds copyright to the material and is entitled to negotiate on rights, this license is only valid, subject to a courtesy information to the author (address is given with the article/chapter) and provided it concerns original material which does not carry references to other sources (if material in question appears with credit to another source, authorization from that source is required as well).

Permission free of charge on this occasion does not prejudice any rights we might have to charge for reproduction of our copyrighted material in the future.

Altering/Modifying Material: Not Permitted
You may not alter or modify the material in any manner. Abbreviations, additions, deletions and/or any other alterations shall be made only with prior written authorization of the author(s) and/or Springer Science + Business Media. (Please contact Springer at (permissions.dordrecht@springer.com or permissions.heidelberg@springer.com)

Reservation of Rights
Springer Science + Business Media reserves all rights not specifically granted in the combination of (i) the license details provided by you and accepted in the course of this licensing transaction, (ii) these terms and conditions and (iii) CCC's Billing and Payment terms and conditions.

Copyright Notice:Disclaimer
You must include the following copyright and permission notice in connection with any reproduction of the licensed material: "Springer and the original publisher /journal title, volume, year of publication,

page, chapter/article title, name(s) of author(s), figure number(s), original copyright notice) is given to the publication in which the material was originally published, by adding; with kind permission from Springer Science and Business Media"

Warranties: None

Example 1: Springer Science + Business Media makes no representations or warranties with respect to the licensed material.

Example 2: Springer Science + Business Media makes no representations or warranties with respect to the licensed material and adopts on its own behalf the limitations and disclaimers established by CCC on its behalf in its Billing and Payment terms and conditions for this licensing transaction.

Indemnity
You hereby indemnify and agree to hold harmless Springer Science + Business Media and CCC, and their respective officers, directors, employees and agents, from and against any and all claims arising out of your use of the licensed material other than as specifically authorized pursuant to this license.

No Transfer of License
This license is personal to you and may not be sublicensed, assigned, or transferred by you to any other person without Springer Science + Business Media's written permission.

No Amendment Except in Writing
This license may not be amended except in a writing signed by both parties (or, in the case of Springer Science + Business Media, by CCC on Springer Science + Business Media's behalf).

Objection to Contrary Terms
Springer Science + Business Media hereby objects to any terms contained in any purchase order, acknowledgment, check endorsement or other writing prepared by you, which terms are inconsistent with these terms and conditions or CCC's Billing and Payment terms and conditions. These terms and conditions, together with CCC's Billing and Payment terms and conditions (which are incorporated herein), comprise the entire agreement between you and Springer Science + Business Media (and CCC) concerning this licensing transaction. In the event of any conflict between your obligations established by these terms and conditions and those established by CCC's Billing and Payment terms and conditions, these terms and conditions shall control.

Jurisdiction
All disputes that may arise in connection with this present License, or the breach thereof, shall be settled exclusively by arbitration, to be held

in The Netherlands, in accordance with Dutch law, and to be conducted under the Rules of the 'Netherlands Arbitrage Instituut' (Netherlands Institute of Arbitration).***OR:***

All disputes that may arise in connection with this present License, or the breach thereof, shall be settled exclusively by arbitration, to be held in the Federal Republic of Germany, in accordance with German law.

Other terms and conditions:

v1.3

If you would like to pay for this license now, please remit this license along with your payment made payable to "COPYRIGHT CLEARANCE CENTER" otherwise you will be invoiced within 48 hours of the license date. Payment should be in the form of a check or money order referencing your account number and this invoice number 501314474.
Once you receive your invoice for this order, you may pay your invoice by credit card. Please follow instructions provided at that time.

Make Payment To:
Copyright Clearance Center
Dept 001
P.O. Box 843006
Boston, MA 02284-3006

For suggestions or comments regarding this order, contact RightsLink Customer Support:
customercare@copyright.com or +1-877-622-5543 (toll free in the US) or +1-978-646-2777.

Gratis licenses (referencing $0 in the Total field) are free. Please retain this printable license for your reference. No payment is required.

BIBLIOGRAPHY

[1] Anderson, C. and P.C. Smith, 1989: Oceanographic observations on the Scotian Shelf during CASP. *Atmosphere-Ocean*, 27, 130–156.

[2] Banks, R.E, 1966: The cold intermediate layer of the Gulf of St. Lawrence. *J. Geophys. Res*., 71, 1603–1610.

[3] Barnier, B., B. Madec, B. Penduff, J-M. Molines, A-M. Treguier, J. Le Somer, A. Beckmann, A. Biastoch, C. Böning, J. Dengg, C. Derval, E. Durand, S. Gulev, E. Remy, C. Talandier, T. Theetten, M. Maltrud, J. Mclean and B. De Cuevas, 2006: Impact of partial steps and momentum advection scheme in a global ocean circulation model at eddy-permitting resolution. *Ocean Dyn*., 56, 543–567. doi:10.1007/s10236-006-0082-1.

[4] Bigelow, H.B., 1927: Physical oceanography of the Gulf of Maine. *Bull. U.S. Comm. Bur*., 40, 511-1027.

[5] Brown, W. and R.C. Beardsley, 1978: Winter circulation in the western Gulf of Maine: Part 1. Cooling and water mass formation. *J. Phys. Oceanogr*., 8, 265-277.

[6] Brown, W. and J. Irish, 1992: The annual evolution of geostrophic flow in the Gulf of Maine: 1986-1987. *J. Phys. Oceanogr*., 22, 445-473.

[7] Canadian Ice Service, 2011: Sea ice climatic atlas for the east coast of Canada 1981-2010. Environment Canada. 248 pp. Ottawa, Ontario, Canada.

[8] Canadian Ice Service, 2013: CIS gridded digital charts database: Release 1.0 provided by the Canadian Ice Service. Environment Canada. Ottawa, Ontario, Canada.

[9] Colbourne, E., B. Deyoung, S. Narayanan and J. Helbig, 1997: Comparison of hydrography and circulation on the Newfoundland Shelf during 1990–1993 with the long-term mean. *Can. J. Fish. Aquat. Sci*., 54 (Suppl. 1): 68–80.

[10] Colbourne, E. and K. Foote, 2000: Variability of the stratification and circulation on the Flemish Cap during the decades of the 1950s–1990s. *J. Northw. Atl. Fish. Sci*., 26, 103–122.

[11] Dai, A., T. Qian and K.E. Trenberth, 2009: Changes in continental freshwater discharge from 1948 to 2004. *J. Clim*., 22, 2773–2791.

[12] Danilov, S., Q. Wang, M. Losch, D. Sidorrenko and J. Schoter, 2008: Modeling ocean circulation on unstructured meshes: comparison of two horizontal discretizations. *Ocean Dyn*., 58, 365-374. doi:10.1007/s10236-008-0138-5.

[13] Debreu, L. and E. Blayo, 2002: AGRIF: Adaptive Grid Refinement in Fortran. Tech. Report 0262, INRIA, 16 pp. Montbonnot-St-Martin, France.

[14] Debreu, L. and E. Blayo, 2008: Two-way embedding algorithms: a review. *Ocean Dyn*., 58, 415-428.

[15] Debreu, L., C. Vouland and E. Blayo, 2008: AGRIF: adaptive grid refinement in Fortran. *Comput. Geosci*., 34, 8–13.

[16] Dickson, R., J. Meincke, S. Malmberg and A. Lee, 1988: The "Great Salinity Anomaly" in the northern North Atlantic 1968–1982. *Prog. Oceanogr*., 20, 130–151.

[17] Drinkwater, K.F., D.B. Mountain and A. Herman, 1998: Recent changes in the hydrography of the Scotian Shelf and Gulf of Maine - A return to the conditions of the 1960s? NAFO SCR Doc. No. 37, Serial No. N3024, 16 pp.

[18] Drinkwater, K.F., B. Petrie and H.F. Sutcliffe Jr, 1979: Seasonal geostrophic volume transports along the Scotian Shelf. *Estuar. Coast. Mar. Sci.,* 9,17–27.

[19] Drinkwater, K.F., R.A. Myers, R.G. Pettipas and T.L. Wright, 1994: Climatic data for the Northwest Atlantic: The position of the shelf/slope front and the northern boundary of the Gulf Stream between 50°W and 75° W, 1973–1992. Can. Data Rept. Fish. Ocean. Sci. Report No. 125: 103pp. Bedford Institute of Oceanography, Dartmouth, Nova Scotia, Canada.

[20] Drinkwater, K. F., R. G. Pettipas, G. L. Bugden and P. Langille, 1999: Climatic data for the northwest Atlantic: A sea ice database for the Gulf of St. Lawrence and the Scotian Shelf, *Can. Tech. Rep. Hydrogr. Ocean Sci*. Report No. 199: 134 pp. Bedford Institute of Oceanography, Darmouth, Nova Scotia, Canada.

[21] Drinkwater, K.F. and D. Gilbert, 2004: Hydrographic variability in the waters of the Gulf of St. Lawrence, the Scotian Shelf and the Eastern Gulf of Maine (NAFO Subarea 4) during 1991–2000. *J. Northwest. Atl. Fish. Sci*., 34, 83–99.

[22] Dufour, R. and P. Ouellet, 2007: Estuary and Gulf of St. Lawrence marine ecosystem overview and assessment report. *Can. Tech. Rep. Fish. Aquat. Sci*., Report No. 2744E: 112 pp. Maurice-Lamontagne Institute, Mont-Jolie, Québec, Canada.

[23] Eden, C., R.J. Greatbatch and C.W. Böning, 2004: Adiabatically correcting an eddy-permitting model of the North Atlantic using large-scale hydrographic data: Applications to the Gulf Stream and the North Atlantic Current. *J. Phys. Oceanogr*., 34, 701-719.

[24] El-Sabh, M.I., 1976: Surface circulation pattern in the Gulf of St. Lawrence. *J. Fish. Res. Board. Can*., 33, 124–138.

[25] El-Sabh, M.I., 1977: Oceanographic features, currents and transport in Cabot Strait. *J. Fish. Res. Board. Can*., 34, 516–528.

[26] Fisheries and Oceans Canada, 2012: Atlantic Zone Monitoring Program. Fisheries and Oceans Canada. http://www.meds-sdmm.dfo-mpo.gc.ca/isdm-gdsi/azmp-pmza/index-eng.html . Accessed 16 Sept 2012.

[27] Fichefet, T. and A. Morales-Maqueda, 1997: Sensitivity of a global sea ice model to the treatment of ice thermodynamics and dynamics. *J. Geophys. Res*., 102, 12609-12646.

[28] Fuglister, F. and L. Worthington, 1951: Some results of a multiple ship survey of the Gulf Stream. Tellus, 3,1–14.

[29] Gagné, J.A. and M. Sinclair, 2013: Marine fisheries resources and oceanography of the St. Lawrence Estuary. In Oceanography of a large-scale estuarine system. Eds M.I. El-Sabh and N. Silverberg. Springer-Verlag. New York. doi:10.1002/9781118663783.ch16.

[30] Galbraith, P.F., J. Chassé, D. Gilbert, P. Larouche, B. Pettigrew, A. Gosselin, L. Devine and C. Lafleur C, 2009: Physical oceanographic conditions in the Gulf of St. Lawrence in 2008. DFO Canadian Science advisory secretariat research document 2009/014.

[31] Garrett, C.G., 1972: Tidal resonance in the Bay of Fundy and Gulf of Maine. *Nature*., 238, 441–443.

[32] Gaspar, P., P. Grégoris and J-M. Lefevre, 1990: A simple eddy kinetic energy model for simulations of the oceanic vertical mixing tests at Station Papa and long-term upper ocean study site. *J. Geophys. Res*., 96, 16179-16193.

[33] Gatien, M.G., 1976: A study in the slope water region south of Halifax. *J. Fish. Res. Board of Can*., 33, 2213–2217.

[34] Geshelin, Y., J. Sheng and R.J. Greatbatch, 1999: Monthly mean climatologies of temperature and salinity in the western North Atlantic. Can. Data Rep. Hydrogr. Ocean Sci. Report No. 153, 62 pp. Bedford Institute of Oceanography, Dartmouth, Nova Scotia, Canada.

[35] Gill, A., 1982: Atmosphere-Ocean Dynamics. San Diego: Academic, 662 pp.

[36] Goosse, H. and T. Fichefet, 1999: Importance of ice-ocean interactions for the global ocean circulation: A model study. *J. Geophys. Res.,* 104, 23337-23355.

[37] Greatbatch, R.J., J. Sheng, C. Eden, L. Tang and X. Zhai, 2004: The semi-prognostic method. *Cont. Shelf Res*., 24, 2149–2165.

[38] Gregory, D.N., 2004: Ocean Data Inventory (ODI): a database of ocean current, temperature and salinity time series for the Northwest Atlantic. DFO Canadian Science advisory secretariat research document 2004/097, Dartmouth.

[39] Griffies, S. and R. Hallberg, 2000: Biharmonic friction with a Smagorinsky-like viscosity for use in large-scale eddy-permitting ocean models. *Mon. Weather Rev*., 128, 2935–2946.

[40] Hachey, H.B., F.F. Hermann and W.B. Bailey, 1954: The waters of the ICNAF convention area. In Proc. *Int. Comm. Northwest Atl. Fish. Ann. Proc*.,Vol. 4, pp. 67–102. 8 October 1953, Copenhagen, Denmark.

[41] Han, G., J.W. Loder and P.C. Smith, 1999: Seasonal mean hydrography and circulation in the Gulf of St. Lawrence and on the Eastern Scotian and Newfoundland Shelves. *J. Phys. Oceanogr.,* 29, 1279–1301.

[42] Han, G. and C.L. Tang, 2001: Interannual variations of volume transport in the western Labrador Sea based on TOPEX/Poseidon and WOCE data. *J. Phys. Oceanogr*., 31, 199–211.

[43] Han, G. and J.W. Loder, 2003: Three-dimensional seasonal-mean circulation and hydrography on the eastern Scotian Shelf. *J. Geophys. Res*., 108, 1–21.

[44] Han, G., 2007: Satellite observations of seasonal and interannual changes of sea level and currents over the Scotian Slope. *J. Phys. Oceanogr*., 37, 1051–1065.

[45] Han, G., Z. Lu, Z. Wang, J. Helbig, N. Chen and B. Deyoung, 2008: Seasonal variability of the Labrador Current and shelf circulation off Newfoundland. *J. Geophys. Res*., 113, C10013, doi:10.1029/2007JC004376

[46] Hannachi, A., I.T. Jolliffe and D.B. Stephenson, 2007: Empirical orthogonal functions and related techniques in atmospheric science: A review. *Int. J. Climatol*., 27, 1119–1152.

[47] Hannah, C.G., J.A. Shore, J.W. Loder and C.E. Naime, 2001: Seasonal circulation on the western and central Scotian Shelf. *J. Phys. Oceanogr*., 31, 591–615.

[48] Head, E. and D. Sameoto, 2007: Inter-decadal variability in zooplankton and phytoplankton abundance on the Newfoundland and Scotian Shelves. *Deep-Sea Res*., 54: 2686–2701, doi:10.1016/j.dsr2.2007.08.003.

[49] Herrnstein, A., M. Wickett and O. Rodriguez, 2005: Structured adaptive mesh refinement using leapfrog time integration on a staggered grid for ocean models. *Ocean Modelling,* 9, 283-304.

[50] Hibler III, W.D., 1979: A dynamic thermodynamic sea ice model. *J. Phys. Oceanogr.,* 9, 815-846.

[51] Higginson, S., K.R. Thompson, M. Huang, M. Véronneau and D. Wright, 2011: The mean surface circulation of the North Atlantic subpolar gyre: A comparison of estimates derived from new gravity and oceanographic measurements. *J. Geophys. Res*., 116, CO8016, doi:10.1029/2010JC006877

[52] Horel, J.D., 1984: Complex principal component analysis: Theory and examples. *J. Clim. Appl. Meteorol*., 23: 1660–1673.

[53] Joyce, T.M., C. Deser and M.A. Spall, 2000: The relation between decadal variability of subtropical mode water and the North Atlantic Oscillation. *J. Clim.,* 13, 2550–2569.

[54] Karkoven, J., B. Chen, T. Vihma, M. Arkett, and T. Carrieres, 2012: A method for sea ice thickness and concentration analysis based on SAR data and a thermodynamic model. *The Cryosphere*, 6, 15071526.

[55] Koutitonsky, V.G. and G.L. Bugden, 1991: The physical oceanography of the Gulf of St Lawrence: a review with emphasis on the synoptic variability of the motion. *Can. Spec. Publ. Fish. Aquat. Sci.,* 113, 57–90.

[56] Kurihara, Y., G.J. Tripoli and M.A. Bender, 1979: Design of a movable nested-mesh primitive equation model. *Mon. Wea. Rev*., 107, 239-249.

[57] Large, W. and S. Pond, 1981: Open ocean momentum flux measurements in moderate to strong winds. *J. Phys. Oceanogr*., 11, 324–336.

[58] Large, W. and S. Yeager, 2004: Diurnal to decadal global forcing for ocean and sea-ice models: The data sets and flux climatologies. Tech. Report TN-460+STR, NCAR, 105 pp. Boulder, Colorado, USA.

[59] Lazier, J. and D. Wright, 1993: Annual velocity variations in the Labrador Current. *J. Phys. Oceanogr*., 23, 659–678.

[60] Loder, J.W., 1980: Topographic rectification of tidal currents on the sides of georges Bank. *J. Phys. Oceanogr.,* 10, 1399–1416.

[61] Loder, J.W. and D.A. Greenberg, 1986: Predicted positions of tidal fronts in the Gulf of Maine. *Cont. Shelf. Res*., 6, 397–414.

[62] Loder, J.W., B. Petrie and G. Gawarkiewicz, 1998: The coastal ocean off northeastern North America: A large-scale view. In A.R. Robinson and K.H. Brink (Eds), The Sea. Vol 11., The Global Coastal Studies. Regional Studies and Syntheses (pp. 105–133). USA: John Wiley & Sons, Inc.

[63] Loder, J.W., C.G. Hannah, B.D. Petrie and E.A. Gonzales, 2003: Hydrographic and transport variability on the Halifax section. *J. Geophys. Res*., 108, C118003. doi:10.1029/2001JC001267.

[64] Lynch, D.R., J.T.C. Ip, C.E. Naime and F.E. Werner, 1996: Comprehensive coastal circulation model with application to the Gulf of Maine. *Cont. Shelf Res*., 16, 875–906.

[65] Madec, G, 2008: NEMO Reference Manual, Ocean Dynamics Component: NEMO-OPA, Preliminary Version. Note du Pole de modélisation, Institute Pierre Simon Laplace (IPSL), France, No 27 ISSN: 1288–1619.

[66] Marchesiello, P., J. McWilliams and A. Shchepetkin, 2001: Open boundary conditions for long term integration of regional oceanic models. *Ocean Modelling*, 3, 1–20.

[67] Marsh, R., B. Petrie, C. Weidman, R. Dickson, J. Loder, C. Hannah, K. Frank and K. Drinkwater, 1999: The 1882 tilefish kill - a cold event in shelf waters off the north-eastern United States? *Fish. Oceanogr*., 8, 39–49.

[68] McLellan, H.J., 1957: On the distinctness and origin of the slope water off the Scotian Shelf and its easterly flow south of the Grand Banks. *J. Fish. Res. Board Can*., 14, 4213–4239.

[69] Niiler, P., 2001: The world ocean surface circulation. In J. Church, G. Siedler and J. Gould (Eds), Ocean Circulation and Climate–Observing and Modelling the Global Ocean (pp. 193–204). London: Academic.

[70] Ohashi, K., J. Sheng, K.R. Thompson, C.G. Hannah and H. Ritchie, 2009: Numerical study of three-dimensional shelf circulation on the Scotian Shelf using a shelf circulation model. *Cont. Shelf Res.,* 29, 2138–2156.

[71] Oey, L.Y. and P. Chen, 1992: A nested-grid ocean model: with application to the simulation of meanders and eddies in the Norwegian Coastal Current. *J. Geophys. Res*., 97, 20063-20086.

[72] Parzen, E., 1962: On Estimation of a Probability Density Function and Mode. *Ann. Math. Stat*., 33, 1065.

[73] Petrie, B. and C. Anderson, 1983: Circulation on the Newfoundland Shelf. *Atmosphere-Ocean*, 21, 207–226.

[74] Petrie, B., B. Toulany and C. Garret, 1988: The transport of water, heat and salt through the Strait of Belle Isle. *Atmosphere-Ocean*, 26, 234–251.

[75] Petrie, B., J.W. Loder, J. Lazier and S. Akenhead, 1992: Temperature and salinity variability on the eastern Newfoundland Shelf: The residual field. *Atmosphere-Ocean*, 30, 129–139.

[76] Petrie, B. and K. Drinkwater, 1993: Temperature and salinity variability on the Scotian Shelf and the Gulf of Maine 1945–1990. *J. Geophys. Res*., 98, 20079–20089.

[77] Petrie, B., 2007: Does the North Atlantic Oscillation affect hydrographic properties on the Canadian Atlantic continental shelf? *Atmosphere- Ocean*, 45, 141–151.

[78] Pickart, R. and W. Smethie, Jr, 1998: Temporal evolution of the deep western boundary current where it enters the subtropical domain. *Deep- Sea Res*., 45, 1053–1083.

[79] Rayner, N. A., D. E. Parker, E. B. Horton, C. K. Folland, L. V. Alexander, D. P. Rowell, E. C. Kent, and A. Kaplan, 2003: Global analyses of sea surface temperature, sea ice, and night marine air temperature since the late nineteenth century, *J. Geophys. Res.,* 1058, 4407. doi:10.1029/2002JD002670.

[80] Reynolds, R. W., T. M. Smith, C. Liu, D. B. Chelton, K. S. Casey and M. G. Schlax, 2007: Daily high-resolution-blended analyses for sea surface temperature. *J. Climate*, 20, 5473-5496.

[81] Roullet, G. and G. Madec, 2000: Salt conservation, free surface, and varying levels: a new formulation for ocean general circulation models. *J. Geophys. Res.,* 105, 23927-23942.

[82] Saucier, F.J., F. Roy and D. Gilbert, 2003: Modeling the formation and circulation processes of water masses and sea ice in the Gulf of St Lawrence, Canada. *J. Geophys. Res*., 108, 3269. doi:10.1029/2000JC000686.

[83] Saucier, F.J., F. Roy, S. Senneville, G. Smith, D. Lefaivre, B. Zakardjian and J-F Dumais, 2009: Modelisation de la circulation dans l'estuaire et le golfe du Saint-Laurent en reponse aux variations du debit d'eau douce et des vents. *J. Water. Sci*., 22, 159–176.

[84] Semtner, A. J., 1976: A model for the thermodynamic growth of sea ice in numerical investigations of climate. *J. Phys. Oceanogr.,* 6, 379-389.

[85] Shadwick, E., H. Thomas, A. Comeau, S. Craig, C. Hunt and J. Salisbury, 2010: Air-sea CO_2 fluxes on the Scotian Shelf: seasonal to multi-annual variability. *Biogeosciences*, 7, 3851–3867.

[86] Schwab, D.J., A.H. Clites, J.E. Sandall, L.A. Meadows and G.A. Meadows, 1989: The effect of wind on transport and circulation in lake St. Clair. *J. Geophys. Res*., 94, C4: 4947–4958.

[87] Sheng, J. and K.R. Thompson, 1996: A robust method for diagnosing regional shelf circulation from scattered density profiles. *J. Geophys. Res*., 101, 25647–25659.

[88] Sheng, J., R.J. Greatbatch and D.G. Wright, 2001: Improving the utility of ocean circulation models through adjustment of the momentum balance. *J. Geophys. Res*., 106, 16711–16728.

[89] Sheng, J., 2001: Dynamics of a buoyancy-driven coastal jet: the Gaspé Current. *J. Phys. Oceanogr*., 29, 1279–1301.

[90] Sheng, J. and L. Tang, 2003: A numerical study of circulation in the western Caribbean Sea. *J. Phys. Oceanogr*., 31, 3146–3163.

[91] Sheng, J., R.J. Greatbatch, X. Zhai and L. Tang, 2005: A new two-way nesting technique for ocean modelling based on the smoothed semi-prognostic method. *Ocean Dyn*., 55, 162-177.

[92] Shine, K. P. and A. Henderson-Sellers, 1985: The sensitivity of a thermodynamic sea ice model to changes in surface albedo parameterization. *J. Geophys. Res*., 20, 2243-2250.

[93] Smith, P.C., B. Petrie and C.R. Mann, 1978: Circulation, variability, and dynamics of the Scotian Shelf and Slope. *J. Fish. Aquat. Sci*., 35, 1067-1083.

[94] Smith, P. and F. Schwing, 1991: Mean circulation and variability on the eastern Canadian continental shelf. *Cont. Shelf Res*., 11, 977–1010.

[95] Smith, G.C., F.J. Saucier and D. Straub, 2006: Formation and circulation of the cold intermediate layer in the Gulf of St. Lawrence. *J. Geophys. Res.,* 111, CO6011. doi:10.1029/2005JC003017.

[96] Smith, W.H.F. and D.T. Sandwell, 1997: Global sea floor topography from satellite altimetry and ship depth soundings. *Science*, 277, 1957–1962.

[97] Smith, P.C., C.N. Flagg, R. Limeburner, C. Fuentes-Yaco, C. Hannah, R.C. Beardsley and J.D. Irish, 2003. Scotian Shelf crossovers during winter/spring 1999: *J. Geophys. Res.*, 108, 8013. doi:10.1029/2001JC001288.

[98] Smith, R.D., M.E. Maltrud, F.O. Bryan and M.W. Hecht, 2000: Numerical simulation of the North Atlantic Ocean at 1/10°. *J. Phys. Oceanogr*., 30, 1532–1561.

[99] Smith, G.C., K. Haines, T. Kanzow and S. Cunningham, 2010: Impact of hydrographic data assimilation on the modelled Atlantic meridional overturning circulation. *Ocean Sci*., 6, 761–774.

[100] Smith, G. C., F. Roy and B. Brasnett, 2013: Evaluation of an operational ice-ocean analysis and forecasting system for the Gulf of St. Lawrence. *Q. J. Roy. Meteor. Soc*., 139, 419-433. doi:10.002/qj.1982.

[101] Stevens, D., 1990: On open boundary conditions for three dimensional primitive equations ocean circulation models. *Geophys. Astrophys. Fluid Dyn*., 51, 103–133.

[102] Taylor, A.H., 1996: North-south shifts of the Gulf Stream: ocean-atmosphere interactions in the North Atlantic. *Int. J. Climatol*., 16, 559–583.

[103] Terradas, J., R. Oliver and J.L. Bellester, 2004: Application of statistical techniques to the analysis of solar coronal oscillations. *Astrophys. J*., 614, 435–447.

[104] Thompson, K.R., J.R.N. Lazier and R. Taylor, 1986: Wind-forced changes in Labrador Current transport. *J. Geophys. Res*., 91, 14261–14268.

[105] Thompson, K.R., R.H. Loucks and R.W. Trites, 1988: Sea surface temperature variability in the shelf-slope region of the northwest Atlantic. *Atmosphere-Ocean*, 26, 292–299.

[106] Thompson, K.R., J. Sheng, P.C. Smith and L. Cong, 2003: Prediction of surface currents and drifter trajectories on the inner Scotian Shelf. *J. Geophys. Res*., 108: C9, 3287, doi:10.1029/2001JC001119.

[107] Thompson, K.R., D.G. Wright, Y. Lou and E. Demirov, 2006: A simple method for reducing seasonal bias and drift in eddy resolving ocean models. *Ocean Modelling*, 13, 109–125.

[108] Thompson, K.R., K. Ohashi, J. Sheng, J. Bobanovic and J. Ou, 2007: Suppressing bias and drift of coastal circulation models through the assimilation of seasonal climatologies of temperature and salinity. *Cont. Shelf Res*., 27, 1303–1316.

[109] Thorndike, A.S., 1986: Diffusion of sea ice. *J. Geophys. Res*. 91, 7691-7696.

[110] Timmermann, R., H. Goosse, G. Madec, T. Ficheft, C. Ethe and V. Duliere, 2005: On the representation of high latitude processes in the ORCA-LIM global coupled sea ice-ocean model. *Ocean Modelling*, 8, 175–201.

[111] Trossman, D.S., L. Thompson, K.A. Kelly and Y-O. Kwon, 2009: Estimates of North Atlantic ventilation and model water formation for winters 2002–06. *J. Phys. Oceanogr*., 39, 2600–2917.

[112] Urrego-Blanco, J. and J., Sheng, 2012: Interannual variability of the circulation over the Eastern Canadian Shelf. *Atmosphere-Ocean*, 50, 175–201.

[113] Urrego-Blanco, J. and J. Sheng, 2014a: Study on subtidal circulation and variability in the Gulf of St. Lawrence, Scotian Shelf and Gulf of Maine using a nested-grid shelf circulation model. *Ocean Dyn*., doi: 10.1007/s10236-013-0688-z.

[114] Urrego-Blanco, J. and J. Sheng, 2014b: Formation and distribution of sea ice in the Gulf of St. Lawrence: A process-oriented study using a coupled ocean-ice model. *Submitted to J. Geophys. Res*.

[115] Urrego-Blanco, J., J. Sheng and F. Dupont, 2014: Assessing the performance of one-way and two-way nesting techniques using the shelf circulation modelling system for the eastern Canadian shelf. *Submitted to Ocean Modelling*.

[116] Weare, B.C., 1977: Empirical orthogonal function analysis of Atlantic Ocean surface temperature. *Q. J. R. Meteorol. Soc*., 103, 467–478.

[117] Wright, D.G. and K.R. Thompson, 1982: Time-averaged forms of the nonlinear stress law. *J. Phys. Oceanogr*., 13, 341–345.

[118] Wright, D.G., K.R. Thompson and Y. Lu, 2006: Assimilating long-term hydrographic information into an eddy-permitting model of the north Atlantic. *J. Geophys. Res*., 111: doi:10.1029/2005JC003200.

[119] Xue, H., F. Chai and N. Pettigrew, 2000: A model study of the seasonal circulation in the Gulf of Maine. *J. Phys. Oceanogr*., 30, 1111–1135.

[120] Zhang, S., J. Sheng and R. J. Greatbatch, 2004: A coupled ice-ocean modelling study of the northwest Atlantic Ocean. *J. Geophys. Res*., 109, C04009. doi:10.1029/2003JC001924.

[121] Zhao, J., J. Sheng, R.J. Greatbatch, K. Azetsu-Scott and E.P. Jones, 2006: Simulation of CFCs in the North Atlantic Ocean using an adiabatically corrected ocean circulation model. *J. Geophys. Res*., 111, C06027, doi:10.1029/2004JC002814.